



Tom Lahmer

Herausgeber  
Timon Rabczuk

Carsten Könke

ISM-Bericht 01/2023  
Institut für Strukturmechanik  
Fakultät Bauingenieurwesen  
Bauhaus-Universität Weimar  
Marienstraße 15  
99423 Weimar  
Germany

ISSN: 1610-7381

Tel. +49 3643 584504  
Fax. +49 3643 584514

<http://www.uni-weimar.de/ism>

Electromechanics and Hydrodynamics of Single Vesicles and  
Vesicle Doublet Using Phase-Field Isogeometric Analysis

*Dissertation*

*Zur Erlangung des akademischen Grades eines  
Doktor-Ingenieur (Dr.-Ing.)  
an der Fakultät Bauingenieurwesen  
der Bauhaus-Universität Weimar*

June, 2023

*vorgelegt von*

**Mohammed H. M. Ashour**

*geboren am 06. August 1986 in Riad, Saudi-Arabien,  
aus Gazastreifen, Palästina*

*Mentor*

**Prof. Dr.-Ing. Timon Rabczuk**



*In the loving memory of my father*  
*Hussein M. Ashour*  
*1956-2023*



# EPIGRAPH

*“We are at the very beginning of time for the human race. Our responsibility is to do what we can, learn what we can, improve the solutions, and pass them on. It is our responsibility to leave the men of the future a free hand. In the impetuous youth of humanity, we can make grave errors that can stunt our growth for a long time. This we will do if we say we have the answers now, so young and ignorant; if we suppress all discussion, all criticism, saying, ‘This is it, boys, man is saved!’ and thus doom man for a long time to the chains of authority, confined to the limits of our present imagination. It has been done so many times before.”*

---

Richard P. Feynman,  
*What Do You Care What Other People Think*





# Ehrenwörtliche Erklärung

Ich erkläre hiermit ehrenwörtlich, dass ich die vorliegende Arbeit ohne unzulässige Hilfe Dritter und ohne Benutzung anderer als der angegebenen Hilfsmittel angefertigt habe. Die aus anderen Quellen direkt oder indirekt übernommenen Daten und Konzepte sind unter Angabe der Quelle gekennzeichnet.

Insbesondere habe ich hierfür nicht die entgeltliche Hilfe von Vermittlungs- bzw. Beratungsdiensten (Promotionsberater oder anderer Personen) in Anspruch genommen. Niemand hat von mir unmittelbar oder mittelbar geldwerte Leistungen für Arbeiten erhalten, die im Zusammenhang mit dem Inhalt der vorgelegten Dissertation stehen. Die Arbeit wurde bisher weder im In- noch im Ausland in gleicher oder ähnlicher Form einer anderen Prüfungsbehörde vorgelegt. Ich versichere ehrenwörtlich, dass ich nach bestem Wissen die reine Wahrheit gesagt und nichts verschwiegen habe.

**Ort, Datum:** Weimar, June, 2023

**Unterschrift :**





# Preface

In this dissertation, we include the research that has been carried out at the Institute of Structural Mechanics of the Bauhaus-Universität Weimar between September 2017 and June 2022. The research that has been carried out during this period and included in this dissertation has been published in scientific papers:

- Mohammed Ashour, Navid Valizadeh, Timon Rabczuk, "*Isogeometric analysis for a phase-field constrained optimization problem of morphological evolution of vesicles in electrical fields*", Computer Methods in Applied Mechanics and Engineering, Volume 377, 2021, 113669, ISSN 0045-7825, <https://doi.org/10.1016/j.cma.2021.113669>.
- Mohammed Ashour, Navid Valizadeh, Timon Rabczuk, "*Phase-field Navier–Stokes model for vesicle doublets hydrodynamics in incompressible fluid flow*", Computer Methods in Applied Mechanics and Engineering, Volume 412, 2023, 116063, ISSN 0045-7825, <https://doi.org/10.1016/j.cma.2023.116063>.



# Acknowledgements

On the tenth of October 2017, 10:45, I had my first meeting with my advisor, Prof. Timon Rabczuk. I still remember what went in that meeting. It was like walking through a wall blindfolded. It was supposed to be a two-person discussion about the research topic and the path forward. It ended up with me setting there for 45 minutes, understanding 10-minutes worth of talking at best. Fast forward to 2022, in June, we had a meeting to discuss future research direction. Comparing myself back in 2017 to me in 2022, I can say with confidence that I made a huge leap forward. For this, I'm thankful to Prof. Rabczuk for his supervision, support, and guidance over the years. I would like to also express my deepest gratitude to Dr. Navid Valizadeh for all of his help, insights, and ideas, and for taking a serious interest in my research over the years. I am grateful as well for the administrative staff at ISM, starting with Ms. Terber, Ms. Rosemarie Mayer, Ms. Brömel, and Ms. Kolling for their help with all administrative issues. To my colleagues at ISM, Dr. Cosmin Anitescu, Dr. Ahmed Shabaan, Dr. Jorge Lopez, Dr. Andrea Lück, Dr. Somdatta Goswami, and Dr. Bokai Liu, I would like to say thank you. I am in particular grateful to the ISM Compute Cluster VEGAS administrative team for helping with all the technical issues related to the use of the VEGAS HPC. I would be remiss if I did not thank my colleagues and friends from Ingenieurbüro Dr. Saad and Ingenieurbüro Monig, starting with Dr. Mustapha Saad, Ms. Farak Skerek, Mr. Fayez Khouri, Ms. Suzan Thor and Mr. Falk Monig. For my friends, Dr. I. Baker from Broward College in Florida, Dr. Mohammed Hammad from Leibniz university in Hannover, Dr. Mahmoud Shaqfa from EPFL, and Ramadan El-Hayek from WHU-Otto Beisheim School of Management, I would like to say thank you for all the support, encouragement, and help in this journey. For my wife Heba and my kids Sara, Hussein, and Elias, thank you for your support, and for understanding my absence most of the time from home. Days after my defense, my father passed away, and there are no words to describe it. Thank you dad for everything. To my mother, and my extended family in Gaza, I have been away for so long to the point where the images I have of you started to fade, but I know how much proud of me you are, thank you for all the support.

Weimar, May 2023



# Abstract

Biomembranes are selectively permeable barriers that separate the internal components of the cell from its surroundings. They have remarkable mechanical behavior which is characterized by many phenomena, but most noticeably their fluid-like in-plane behavior and solid-like out-of-plane behavior. Vesicles have been studied in the context of discrete models, such as Molecular Dynamics, Monte Carlo methods, Dissipative Particle Dynamics, and Brownian Dynamics. Those methods, however, tend to have high computational costs, which limited their uses for studying atomistic details. In order to broaden the scope of this research, we resort to the continuum models, where the atomistic details of the vesicles are neglected, and the focus shifts to the overall morphological evolution. Under the umbrella of continuum models, vesicles morphology has been studied extensively. However, most of those studies were limited to the mechanical response of vesicles by considering only the bending energy and aiming for the solution by minimizing the total energy of the system. Most of the literature is divided between two geometrical representation methods; the sharp interface methods and the diffusive interface methods. Both of those methods track the boundaries and interfaces implicitly. In this research, we focus our attention on solving two non-trivial problems. In the first one, we study a constrained Willmore problem coupled with an electrical field, and in the second one, we investigate the hydrodynamics of a vesicle doublet suspended in an external viscous fluid flow.

For the first problem, we solve a constrained Willmore problem coupled with an electrical field using isogeometric analysis to study the morphological evolution of vesicles subjected to static electrical fields. The model comprises two phases, the lipid bilayer, and the electrolyte. This two-phase problem is modeled using the phase-field method, which is a subclass of the diffusive interface methods mentioned earlier. The bending, flexoelectric, and dielectric energies of the model are reformulated using the phase-field parameter. A modified Augmented-Lagrangian (ALM) approach was used to satisfy the constraints while maintaining numerical stability and a relatively large time step. This approach guarantees the satisfaction of the constraints at each time step over the entire temporal domain.

In the second problem, we study the hydrodynamics of vesicle doublet suspended in an external viscous fluid flow. Vesicles in this part of the research are also modeled using the phase-field model. The bending energy and energies associated with enforcing the global volume and area are considered. In addition, the local inextensibility condition is ensured by introducing an additional equation to the system. To prevent the vesicles from numerically overlapping, we deploy an interaction energy definition to maintain a short-range repulsion between the vesicles. The fluid flow is modeled using the incompressible Navier-Stokes equations and the vesicle evolution in time is modeled using two advection equations describing the process of advecting each vesicle by the fluid flow. To overcome the velocity-pressure saddle point system, we apply the Residual-Based Variational MultiScale (RBVMS) method to the Navier-Stokes equations and solve the coupled systems using isogeometric analysis. We study vesicle doublet hydrodynamics in shear flow, planar extensional flow, and parabolic flow under various configurations and boundary conditions.

The results reveal several interesting points about the electrostatics and hydrodynamics responses of single vesicles and vesicle doublets. But first, it can be seen that isogeometric analysis as a numerical tool has the ability to model and solve 4<sup>th</sup>-order PDEs in a primal variational framework at extreme efficiency and accuracy due to the abilities embedded within the NURBS functions without the need to reduce the order of the PDE by creating an intermediate environment. Refinement whether by knot insertion, order increasing or both is far easier to obtain than traditional mesh-based methods. Given the wide variety of phenomena in natural sciences and engineering that are mathematically modeled by high-order PDEs, the isogeometric analysis is among the most robust methods to address such problems as the basis functions can easily attain high global continuity.

On the applicational side, we study the vesicle morphological evolution based on the electromechanical liquid-crystal model in 3D settings. This model describing the evolution of vesicles is composed of time-dependent, highly nonlinear, high-order PDEs, which are nontrivial to solve. Solving this problem requires robust numerical methods, such as isogeometric analysis. We concluded that the vesicle tends to deform under increasing magnitudes of electric fields from the original sphere shape to an oblate-like shape. This evolution is affected by many factors and requires fine-tuning of several parameters, mainly the regularization parameter which controls the thickness of the diffusive interface width. But it is most affected by the method used for enforcing the constraints. The penalty method in presence of an electrical field tends to lock on the initial phase-field and prevent any evolution while a modified version of the ALM has proven to be sufficiently stable and accurate to let the phase-field evolve while satisfying the constraints over time at each time step. We show additionally the effect of including the flexoelectric



nature of the Biomembranes in the computation and how it affects the shape evolution as well as the effect of having different conductivity ratios. All the examples were solved based on a staggered scheme, which reduces the computational cost significantly.

For the second part of the research, we consider vesicle doublet suspended in a shear flow, in a planar extensional flow, and in a parabolic flow. When the vesicle doublet is suspended in a shear flow, it can either slip past each other or slide on top of each other based on the value of the vertical displacement, that is the vertical distance between the center of masses between the two vesicles, and the velocity profile applied. When the vesicle doublet is suspended in a planar extensional flow in a configuration that resembles a junction, the time in which both vesicles separate depends largely on the value of the vertical displacement after displacing as much fluid from between the two vesicles. However, when the vesicles are suspended in a tubular channel with a parabolic fluid flow, they develop a parachute-like shape upon converging towards each other before exiting the computational domain from the predetermined outlets. This shape however is affected largely by the height of the tubular channel in which the vesicle is suspended. The velocity essential boundary conditions are imposed weakly and strongly. The weak implementation of the boundary conditions was used when the velocity profile was defined on the entire boundary, while the strong implementation was used when the velocity profile was defined on a part of the boundary. The strong implementation of the essential boundary conditions was done by selectively applying it to the predetermined set of elements in a parallel-based code. This allowed us to simulate vesicle hydrodynamics in a computational domain with multiple inlets and outlets. We also investigate the hydrodynamics of oblate-like shape vesicles in a parabolic flow. This work has been done in 2D configuration because of the immense computational load resulting from a large number of degrees of freedom, but we are actively seeking to expand it to 3D settings and test a broader set of parameters and geometrical configurations.



# Zusammenfassung

Biomembranen sind selektiv durchlässige Barrieren, die die inneren Bestandteile der Zelle von ihrer Umgebung trennen. Sie haben ein bemerkenswertes mechanisches Verhalten, das durch viele Phänomene gekennzeichnet ist: Vor allem durch ihr flüssigkeit-sähnliches Verhalten in der Ebene und ihr festkörperähnliches Verhalten außerhalb der Ebene. Vesikel wurden im Zusammenhang mit diskreten Modellen wie Molekulardynamik, Monte-Carlo-Methoden, dissipativer Partikeldynamik und Brownscher Dynamik untersucht. Diese Methoden sind jedoch in der Regel sehr rechenintensiv, was ihre Anwendung auf die Untersuchung atomistischer Details beschränkt. Um den Anwendungsbereich dieser Forschung zu erweitern, wurde in dieser Dissertation auf Kontinuumsmodelle zurückgegriffen, bei denen die atomistischen Details der Vesikel vernachlässigt werden und sich der Schwerpunkt auf die allgemeine morphologische Entwicklung verlagert.

In Kontinuumsmodellen anderer wissenschaftlicher Arbeiten wurde die Morphologie von Vesikeln bereits ausgiebig untersucht. Die meisten dieser Studien beschränkten sich jedoch auf die mechanische Reaktion von Vesikeln, indem sie nur die Biegeenergie berücksichtigten und eine Lösung durch Minimierung der Gesamtenergie des Systems anstrebten. In der Literatur wird überwiegend zwischen zwei geometrischen Darstellungsmethoden unterschieden: Der scharfen Grenzflächenmethode und der diffusiven Grenzflächenmethode. Beide Methoden verfolgen die Grenzen und Grenzflächen implizit. In dieser Arbeit wurde sich auf die Lösung von zwei nicht-trivialen Problemen konzentriert. Im ersten Fall wurde ein eingeschränktes Willmore-Problem untersucht, das mit einem elektrischen Feld gekoppelt ist. Im zweiten Fall erfolgte die Untersuchung der Hydrodynamik eines Vesikel-Doubles, das in einer externen viskosen Flüssigkeitsströmung schwebt.

Für das erste Problem wurde ein eingeschränktes Willmore-Problem unter Verwendung der isogeometrischen Analyse gelöst, das mit einem elektrischen Feld gekoppelt ist. Dies dient der Untersuchung der morphologischen Entwicklung von Vesikeln, die statischen elektrischen Feldern ausgesetzt sind. Das Modell besteht aus zwei Phasen: Der Lipiddoppelschicht und den Elektrolyten. Das Zwei-Phasen-Problem wird mit der Phasenfeldmethode modelliert, die eine Unterklasse der bereits erwähnten diffusiven Grenzflächenmethoden ist. Die Biegeenergie sowie die flexoelektrischen und die dielektrischen Energien

des Modells wurden mit Hilfe des Phasenfeldparameters umformuliert. Ein modifizierter Augmented-Lagrangian-Ansatz (ALM) wurde verwendet, um die Nebenbedingungen zu erfüllen und gleichzeitig die numerische Stabilität und einen relativ großen Zeitschritt beizubehalten. Dieser Ansatz garantiert die Erfüllung der Nebenbedingungen bei jedem Zeitschritt über den gesamten Zeitbereich.

Im zweiten Problem wurde die Hydrodynamik von Vesikeldoubletten betrachtet, die in einer externen viskosen Flüssigkeitsströmung schweben. Die Vesikel wurden in diesem Teil der Untersuchung ebenfalls mit dem Phasenfeldmodell modelliert. Die Biegeenergie und die mit der Durchsetzung des globalen Volumens und der Fläche verbundenen Energien wurden berücksichtigt. Darüber hinaus wurde die Bedingung der lokalen Undehnbarkeit durch die Einführung einer zusätzlichen Gleichung in das System sichergestellt. Um zu verhindern, dass sich die Bläschen numerisch überlappen, wurde eine Definition der Wechselwirkungsenergie verwendet, um eine kurzreichweitige Abstoßung zwischen den Bläschen aufrechtzuerhalten. Die Flüssigkeitsströmung wurde durch inkompressible Navier-Stokes-Gleichungen modelliert. Die zeitliche Entwicklung der Vesikel wurde durch zwei Advektionsgleichungen beschrieben, die den Prozess der Vorwärtsbewegung jedes Vesikels durch die Flüssigkeitsströmung beschreiben. Um das Geschwindigkeits-Druck-Sattelpunktsystem zu überwinden, wurde die Residual-Based Variational Multi-Scale (RBVMS)-Methode auf die Navier-Stokes-Gleichungen angewandt. Zur Lösung der gekoppelten Systeme wird die isogeometrische Analyse genutzt. Mithin wird die Hydrodynamik von Vesikel-Doubletten in Scherströmung, planarer Dehnungsströmung und parabolischer Strömung unter verschiedenen Konfigurationen und Randbedingungen untersucht.

Die Ergebnisse zeigen mehrere interessante Punkte über die elektro- und hydrodynamischen Reaktionen von einzelnen Vesikeln und Vesikeldoubletten. Zunächst aber zeigt sich, dass die isogeometrische Analyse als numerisches Werkzeug in der Lage ist, PDEs der Ordnung  $4^{th}$  in einem primären Variationsrahmen mit extremer Effizienz und Genauigkeit zu modellieren und zu lösen. Dies liegt an den in NURBS-Funktionen eingebetteten Fähigkeiten, ohne dass die Ordnung der PDE durch Schaffung einer Zwischenumgebung reduziert werden muss. Die Verfeinerung durch Einfügen von Knoten, Erhöhen der Ordnung oder beides ist viel einfacher zu erreichen als bei traditionellen netzbasierten Methoden. Angesichts der Vielzahl von Phänomenen in den Natur- und Ingenieurwissenschaften, die mathematisch durch PDEs hoher Ordnung modelliert werden können, gehört die isogeometrische Analyse zu den robustesten Methoden zur Lösung solcher Probleme, da die Basisfunktionen leicht eine hohe globale Kontinuität erreichen können. Auf der Anwendungsseite wurde die morphologische Entwicklung von Vesikeln auf der Grundlage des elektromechanischen Flüssigkristallmodells in 3D-Umgebungen untersucht. Dieses Modell, das die Entwicklung von Vesikeln beschreibt, besteht aus zeitabhängigen,

hochgradig nichtlinearen PDEs hoher Ordnung, die nicht trivial zu lösen sind. Die Lösung dieses Problems erfordert robuste numerische Methoden, wie die isogeometrische Analyse. Es kann geschlussfolgert werden, dass das Vesikel dazu neigt, sich unter zunehmenden elektrischen Feldern von der ursprünglichen Kugelform zu einer abgeflachten Form zu verformen. Diese Entwicklung wird von vielen Faktoren beeinflusst und erfordert eine Feinabstimmung mehrerer Parameter, vor allem des Regularisierungsparameters, der die Dicke der diffusiven Grenzfläche steuert. Am stärksten wird sie jedoch von der Methode beeinflusst, die zur Durchsetzung der Beschränkungen verwendet wird. Die Strafmethode neigt bei Vorhandensein eines elektrischen Feldes dazu, das anfängliche Phasenfeld zu fixieren und jegliche Entwicklung zu verhindern. Demgegenüber hat sich eine modifizierte Version des ALM als ausreichend stabil und genau erwiesen, um das Phasenfeld sich entwickeln zu lassen, während es in jedem Zeitschritt die Randbedingungen erfüllt. Außerdem wurde gezeigt, wie sich die Einbeziehung der flexoelektrischen Natur der Biomembran in die Berechnung auswirkt und wie sie die Formentwicklung beeinflusst sowie die Auswirkungen unterschiedlicher Leitfähigkeitsverhältnisse. Alle Beispiele wurden auf der Grundlage eines gestaffelten Schemas gelöst, was die Rechenkosten erheblich reduziert.

Im zweiten Teil der Untersuchung wurden Vesikel-Doubletten betrachtet, die in einer Scherströmung, in einer ebenen Dehnungsströmung und in einer parabolischen Strömung schweben. Wenn die Vesikel-Doublette in einer Scherströmung aufgehängt ist, kann es entweder aneinander vorbeigleiten oder übereinander gleiten, je nach dem Wert der vertikalen Verschiebung, d. h. dem vertikalen Abstand zwischen den Masseschwerpunkten der beiden Vesikel, und dem angewandten Geschwindigkeitsprofil. Wenn die Vesikeldoublette in einer ebenen Dehnungsströmung in einer Konfiguration aufgehängt ist, die einer Kreuzung ähnelt, hängt die Zeit, in der sich beide Vesikel trennen, weitgehend vom Wert der vertikalen Verschiebung ab, nachdem so viel Flüssigkeit wie möglich zwischen den beiden Vesikeln verdrängt wurde. Wenn die Bläschen jedoch in einem röhrenförmigen Kanal mit einer parabolischen Flüssigkeitsströmung aufgehängt sind, entwickeln sie bei gegenseitiger Annäherung eine fallschirmähnliche Form, bevor sie das Berechnungsgebiet an den vorbestimmten Auslässen verlassen. Diese Form wird jedoch in hohem Maße von der Höhe des röhrenförmigen Kanals beeinflusst, in dem die Bläschen schweben. Die für die Geschwindigkeit wesentlichen Randbedingungen wurden schwach und stark implementiert. Die schwache Implementierung der Randbedingungen wurde verwendet, wenn das Geschwindigkeitsprofil auf dem gesamten Rand definiert war. Die starke Implementierung fand Anwendung, wenn das Geschwindigkeitsprofil auf einem Teil des Randes definiert war. Die starke Implementierung der wesentlichen Randbedingungen erfolgte durch selektive Anwendung auf die vorgegebene Menge von Elementen in einem parallelbasierten Code. Auf diese Weise konnte die Hydrodynamik von Vesikeln in einem Berech-

nungsgebiet mit mehreren Ein- und Auslässen simulieren werden. Ebenfalls untersucht wurde die Hydrodynamik von Bläschen mit abgeflachter Form in einer parabolischen Strömung. Diese Arbeit wurde aufgrund der immensen Rechenlast, die sich aus der großen Anzahl von Freiheitsgraden ergibt, in einer 2D-Konfiguration durchgeführt. Die Ausweitung 3D-Einstellungen wird zukünftig angestrebt, um eine breitere Palette von Parametern und geometrischen Konfigurationen zu testen

# Contents

DEDICATION . . . . .	iii
EPIGRAPH . . . . .	v
Ehrenwörtliche Erklärung . . . . .	vii
Preface . . . . .	viii
Acknowledgements . . . . .	xi
Abstract . . . . .	xii
Zusammenfassung . . . . .	xvi
Nomenclature . . . . .	xxx
<b>1 Summary</b>	<b>1</b>
1.1 Motivation . . . . .	1
1.2 Phase-Field method . . . . .	3
1.3 Isogeometric analysis . . . . .	5
1.4 Vesicles and lipid bilayer membranes in computational mechanics . . . . .	7
1.4.1 Vesicles morphology using discrete models . . . . .	8
1.4.2 Vesicles morphology using continuum models . . . . .	9
1.4.2.1 Vesicles studies in the context of Level-Set method . . . . .	10
1.4.2.2 Vesicles studies in the context of Phase-Field method . . . . .	10
1.5 The electrodynamics and hydrodynamics of vesicles . . . . .	11
1.5.1 Vesicles Electrodynamics . . . . .	12
1.5.2 Vesicles Hydrodynamics . . . . .	14
1.6 Outline . . . . .	16
<b>2 Phase-Field Method</b>	<b>19</b>
2.1 Introduction . . . . .	19
2.2 Thermodynamics of Phase-Field method . . . . .	21
2.3 Single vesicle electrodynamics in the context of the phase-field method . . . . .	24

2.3.1	Mathematical model . . . . .	24
2.3.2	Phase-Field formulation . . . . .	26
2.4	Vesicle doublet hydrodynamics in the context of the phase-field method . . . . .	30
2.4.1	Mathematical model . . . . .	31
2.4.2	Phase-Field formulation . . . . .	32
<b>3</b>	<b>Isogeometric Analysis</b>	<b>37</b>
3.1	Introduction . . . . .	37
3.2	B-splines basis functions . . . . .	38
3.3	B-splines Curves and Surfaces . . . . .	40
3.3.1	B-Spline Curves . . . . .	40
3.3.2	B-Spline Surfaces . . . . .	41
3.4	The Non-Uniform Rational B-splines (NURBS) . . . . .	42
3.5	<i>hpk</i> -Refinement . . . . .	42
3.6	Preliminary IGA Work: Rectangular plate with a circular hole . . . . .	43
3.6.1	Problem's equations . . . . .	43
3.6.2	The Strong form of the problem . . . . .	44
3.6.3	The Weak form of the problem . . . . .	44
3.6.4	Numerical results . . . . .	45
<b>4</b>	<b>A Constrained Optimization Problem of Morphological Evolution of Vesicles in Electric Fields</b>	<b>53</b>
4.1	Introduction . . . . .	53
4.2	The strong form . . . . .	54
4.3	The weak form and numerical formulation . . . . .	55
4.3.1	Continuous problem in the weak form . . . . .	55
4.3.2	The semidiscrete formulation . . . . .	56
4.3.3	Time discretization and numerical implementation . . . . .	56
4.3.4	Modified ALM implementation . . . . .	59
4.4	Numerical results . . . . .	61
4.4.1	Constrained Willmore flow problem . . . . .	62
4.4.2	Electrical response of vesicles . . . . .	62
4.4.3	Evolution of Vesicles in presence of flexoelectric effect . . . . .	67
4.4.4	Conductivity role in morphological evolution . . . . .	72
4.5	Summary . . . . .	75



<b>5</b>	<b>Phase-Field Navier-Stokes model for vesicle doublets hydrodynamics in incompressible fluid flow</b>	<b>77</b>
5.1	Introduction . . . . .	77
5.2	The strong form . . . . .	78
5.3	Numerical formulation and RBVMS implementation . . . . .	79
5.4	The weak form . . . . .	83
5.4.1	The semi-discrete formulation . . . . .	84
5.4.2	Time discretization and numerical implementation . . . . .	85
5.5	Numerical examples . . . . .	89
5.5.1	Vesicle doublet in stationary fluid . . . . .	92
5.5.2	Effect of Interaction Number . . . . .	93
5.5.3	Vesicle doublet suspended in a shear flow . . . . .	94
5.5.4	Vesicle doublet suspended in a planar extensional flow . . . . .	100
5.6	Summary . . . . .	107
<b>6</b>	<b>Summary, conclusions, and future research</b>	<b>113</b>
6.1	Summary . . . . .	113
6.2	Conclusions . . . . .	115
6.3	Future research . . . . .	117
<b>A</b>	<b>Phase-Field formulation of Bending, Flexoelectric and Dielectric energies</b>	<b>119</b>
A.1	Bending Energy . . . . .	120
A.2	Flexoelectric Energy . . . . .	121
A.3	Dielectric Energy of the Membrane . . . . .	121
	Curriculum Vitae . . . . .	140



# List of Figures

1.1	The lipid bilayer consists of a polar hydrophilic phosphate head, and a non-polar hydrophobic lipid tail. The lipid bilayer consists of two adjacent sheets of phospholipids, arranged tail to tail. The hydrophobic tails associate with one another, forming the interior of the membrane. The polar heads contact the fluid inside and outside of the cell. (Source: [76]).	8
1.2	Surface charge distribution induced by the time-varying magnetic field. (A): The plot demonstrated an instant pattern of surface charge distribution. The color represented the amount of the charge density ( $C/m^2$ ). Field frequency was 10 KHz. $\sigma_o = 1.2$ S/m. $\sigma_i = 0.3$ S/m. (B): There was no accumulation of surface charges if the two media were set to be electrically identical ( $\sigma_o = \sigma_i$ and $\epsilon_o = \epsilon_i$ ). (Source: [111]). . . . .	13
1.3	The evolution of a single vesicle in an unbounded shear flow. The viscosity contrast $\nu = .01, 1, \text{ and } 100$ , bending modulus $\kappa_b = 1$ , reduced area = $.75$ , and the temporal domain = $9$ . When $\nu < \nu_c$ , the vesicle reaches an equilibrium and then undergoes tank-treading motion. When $\nu$ is large, the vesicle tumbles. (Reproduced from Ref. [118] with permission from Elsevier and Copyright Clearance Center's RightsLink®). . . . .	15
2.1	A graphical representation of the interface based on the diffusive interface methods (left), and the sharp-interface methods (right). . . . .	22
2.2	A schematic diagram shows the system of vesicle doublet suspension. . .	32
3.1	The quadratic basis functions, i.e., ( $p = 2$ ) for the open uniform knot vector $\xi = \{0, 0, 0, 0.25, 0.5, 0.75, 1, 1, 1\}$ . The number of basis functions is $n - p - 1$ , yielding 6 basis functions over the entire knot vector. . . . .	40
3.2	A second order B-spline curve constructed using the knot vector of Fig. (3.3), with a control polygon $\{\mathbf{P}_i\}$ coordinates of $\{(1.5,1), (2,4), (4,4.5), (3,-1), (6,-1), (5,1.8), (6,1.7)\}$ . . . . .	41

3.3	The quadratic basis functions, i.e., ( $p = 2$ ) for the open uniform knot vector $\xi = \{0, 0, 0, 0.20, 0.40, 0.60, 0.80, 1, 1, 1\}$ . The number of basis functions is $n - p - 1$ , yielding 7 basis functions over the entire knot vector.	41
3.4	A schematic diagram of the rectangular plate under in-plane load. . . . .	44
3.5	The computational domain corresponding to the two second-order knot vectors $\xi$ and $\eta$ with a) control points projected on the computational domain (black dots), and b) elements and nodes (black dots). . . . .	47
3.6	First (a-b), second (c-d), and third (e-f) refinement orders of initial computational domain. Figures (a), (c), and (e) shows the control points distribution, while figures (b), (d), and (f) shows the mesh and the spatial discretization of the initial computational domain. . . . .	48
3.7	Third (a-b), fourth (c-d), and fifth (e-f) order-based control points distribution and corresponding initial mesh. . . . .	49
3.8	A $k$ -refinement for the initial knot vector by elevating the original order by one degree, e.g., 3 and increasing the continuity across element boundaries.	50
3.9	Stress fields based on a geometry and a solution approximation using initial knot vector. . . . .	50
3.10	Stress fields based on geometry and a solution approximation using a second-order knot vector and a refinement of $5^{th}$ order. . . . .	51
3.11	Stress fields based on geometry and a solution approximation using a fifth-order knot vector an a refinement of $5^{th}$ order. . . . .	51
3.12	A comparison between the error in the Energy-norm between versus $h_{MAX}$ , the largest element diameter in the mesh, for the solutions approximated for degrees ranging from $p = 2$ to $p = 6$ , and refinement orders ranging from 0 to 7. . . . .	52
3.13	A comparison between the stress error in the $L^2$ versus $h_{MAX}$ , for the solutions approximated for degrees ranging from $p = 2$ to $p = 6$ , and refinement orders ranging from 0 to 7. . . . .	52
4.1	Evolution of a sphere from initial state (4.1a) to the stationary state (4.1c)	63
4.2	Evolution of a prolate spheroid from initial state (4.2a) to the stationary state (4.2c) . . . . .	63
4.3	(4.3a)Willmore flow of a spherical vesicle, (4.3b) Area ratio and Volume ratio. $R_0 = 10\mu\text{m}$ . . . . .	64
4.5	Stationary states of a vesicle subjected to electrical field ranging between (4.5b) 1 kV/m and (4.5i) 50 kV/m. Flexoelectric effect is neglected. . . . .	64

4.4	Total Energy corresponding to: (4.4a) 10 kV/m, (4.4b) 15 kV/m, (4.4c) 20 kV/m, (4.4d) 30 kV/m, (4.4e) 40 kV/m and (4.4f) 50 kV/m. Flexoelectric response of the biomembrane was neglected. Time is expressed in seconds on x-axis. Energy is expressed in electronvolt unit [eV] on y-axis. . . . .	65
4.6	A planar section shows the temporal evolution of vesicle in absence of flexoelectric response. Electrical field with values ranging between 1-50 kV/m. Both x and y axes are limited to [-11,11] $\mu\text{m}$ for more distinction. . . . .	66
4.7	(4.7a) A streamline interpolation of the electric field shows a reorientation in direction due to the presence of the membrane. (4.7b) A planar section shows a spike in the electric field intensity at the top and the bottom of the vesicle. . . . .	67
4.8	Electrical potential projected on 0-Level set of phase field at (4.8a) initial state, (4.8b) stationary state and (4.8c) tubule formation in vesicles [188]. Electric field intensity = 10 kV/m. Flexoelectric response of the biomembrane neglected. . . . .	68
4.9	Phase field profile along: (4.9a) Y-axis, (4.9b) X-axis. Both profiles correspond to the 50 kV/m models. Red corresponds to the initial phase field profile along the axis, and blue corresponds to the phase field profile at the stationary state. The X-Axis is limited to [-15,15] $\mu\text{m}$ for comparison purposes. . . . .	69
4.10	Vesicle at stationary state with flexoelectric effect included subjected to (4.10a) $E_0 = 10$ kV/m, and (4.10b) $E_0 = 50$ kV/m. . . . .	69
4.11	(a) PF-based interpolation of the conductivity according to Eq. 2.20, and (b) the corresponding profile. . . . .	70
4.12	(4.12a): 0.3 and -0.3 PF-level sets with electric potential projection. Wireframe represents 0 PF-level set, (4.12b) -0.3 PF-level set, and (4.12c) 0.3 PF-level set. . . . .	70
4.13	Temporal evolution of system's energies: (4.13a) Bending energy, (4.13b) Flexoelectric energy, (4.13c) Dielectric energy of the biomembrane, (4.13d) Dielectric energy of the electrolyte (Blue) and total energy of the system (Red). All energies are expressed in $eV = 1.602 \times 10^{-19}$ Joule. . . . .	72
4.14	Vesicle subjected to an electric field $E_0 = 50$ kV/m with varying conductivity ratio. Green represents a sphere-to-prolate morphological evolution with largest ratio value of 4, red represents a sphere-to-oblate morphological evolution with smallest value of 0.25. Dotted black profile depicts a vesicle with a conductivity ratio of 1. . . . .	73

4.15	Vesicle subjected to an electric field $E_0 = 50$ kV/m with varying conductivity ratio $\sigma_{in}\backslash\sigma_{out}$ ranging between 4.0 and 0.25. Vesicles in green have a sphere-to-prolate evolution at stationary state. Vesicles in red have an sphere-to-oblate evolution at stationary state. Initial profile in yellow is shown in Figure 4.15e. Corresponding planer values are plotted in Figure (4.14.) . . . . .	74
4.16	The stationary state for the extreme tested values of 0.25 and 4.0 conductivity ratios. (4.16a) shows a sphere-oblate evolution and (4.16c) shows a sphere-prolate evolution. Figures (4.16b) and (4.16d) shows the corresponding experimental observations [189] (Reproduced from Ref. [189] with permission from the Centre National de la Recherche Scientifique (CNRS) and The Royal Society of Chemistry). . . . .	75
5.1	Temporal evolution of a single vesicle from (5.1a) the spheroidal shape to the (5.1b) well-known peanut-like shape in absence of external forces. Fig. (5.1c) shows the velocity profile during the evolution. . . . .	92
5.2	Velocity Streamlines of vesicle doublet suspended in planar extensional flow with various interaction number ( $JN$ ) of: (5.2a) 0.05, (5.2b) 0.5, and (5.2c) 5.0. $\lambda_1$ and $\lambda_2$ projected on the zero level-set of phase-field variables $\phi_1$ and $\phi_2$ , and interpreted as the surface tension on both vesicles. In figure (5.2f), the pressure projected on the zero-level set of the phase field shows increased values on both sides facing the inlet and facing the other vesicle. . . . .	94
5.3	(5.3a) Vesicles suspended in a shear flow, and (5.3b) their corresponding inclination angles. $\phi_1$ denotes the vesicle on the left and $\phi_2$ denotes the vesicle on the right. Fluid flow motion is shown by the velocity streamlines. . . . .	96
5.4	Vesicle doublet suspended in a shear flow with no initial vertical displacement at (5.4a) initial state and (5.4b) equilibrium state. Vesicle doublet <i>lock</i> in position due to the absence of initial vertical displacement. Fluid flow motion is shown by velocity streamlines. . . . .	97
5.5	Vesicle doublet suspended in a shear flow with initial vertical displacement of 0.04 unit length at (5.5a) initial state, (5.5b) $t = 0.1$ , (5.5c) $t = 0.2$ , (5.5c) $t = 0.2$ , (5.5d) $t = 0.4$ , (5.5e) $t = 1$ , and (5.5f) $t = 2$ . Fluid flow motion is shown by velocity streamlines. . . . .	98

5.6	(5.6a) Interaction energy of vesicle doublet system in a shear flow with initial vertical displacement of 0.04 unit length and a velocity vector $\mathbf{u}_{b_{top}} = 15\vec{\mathbf{e}}_1$ and $\mathbf{u}_{b_{bottom}} = -15\vec{\mathbf{e}}_1$ , and (5.6b) interaction energy of vesicle doublet system in a shear flow with an initial vertical displacement of 0.06 unit length and a velocity vector $\mathbf{u}_{b_{top}} = 30\vec{\mathbf{e}}_1$ and $\mathbf{u}_{b_{bottom}} = -30\vec{\mathbf{e}}_1$ . . . . .	100
5.7	Vesicle doublet suspended in a shear flow with vertical displacement of 0.06 unit length and a horizontal displacement of 1.6 unit length at (5.5a) initial state and (5.71) $t = 3.5$ . Fluid flow motion shown by velocity streamlines, and a velocity profile $\mathbf{u}_{b_{top}} = 30\vec{\mathbf{e}}_1$ and $\mathbf{u}_{b_{bottom}} = -30\vec{\mathbf{e}}_1$ . . . . .	101
5.8	(5.8a) Initial state of vesicle doublet suspended in planar extensional flow at $t = 0$ with velocity streamlines showing fluid flowing in the x-direction, and (5.8b) and the corresponding velocity profile at $t = 0.01$ . . . . .	102
5.9	(5.9a) Vesicle doublet temporal evolution suspended in a planar extensional flow at $t = 0.8$ with initial vertical displacement of 0.02, (5.9b) the corresponding X-Direction velocity profile, and (5.9c) the corresponding Y-Direction velocity profile. (5.9d-5.9f) Ditto, at $t = 0.60$ with initial vertical displacement of 0.1, and (5.9g-5.9i) Ditto, at $t = 0.52$ with initial vertical displacement of 0.2. . . . .	104
5.10	A not-to-scale representation of the computational domain with two vesicles suspended in a planar extensional flow in a tubular channel with two side inlets and two outlets. . . . .	105
5.11	A representation of the computational domain $\Omega$ being distributed on 8 processes, which corresponds to <code>mpiexec -n 8</code> . . . . .	106
5.12	Snippets of the temporal evolution of two vesicles suspended in a planar extensional flow with an initial vertical displacement of 0.2. The velocity vector is projected as streamlines. The X- and Y-components of the velocity vector are shown in Figures (5.12h) and (5.12i). . . . .	109
5.13	The temporal evolution of the left vesicle in Fig. (5.12) in a parabolic extensional flow with an initial vertical displacement of 0.2. . . . .	110
5.14	A comparison between the morphological evolution of two vesicles suspended in a planar extensional flow. The blue vesicle is suspended in a tubular channel with a width of 6 unit length, while the red one is suspended in a channel of 4 unit length. . . . .	110
5.15	The temporal evolution of an oblate spheroid vesicle suspended in a planar extensional flow with a parabolic velocity profile. Fig. (5.15a) shows the initial oblate-like shape, while Fig. (5.15f) shows the final shape of the vesicle as it exits through the top outlet. Domain configurations are similar to Fig. (5.10). . . . .	111

## Nomenclature

In the following table, we list the most used symbols and abbreviations throughout this dissertation, sorted in alphabetical order. Unlisted symbols are defined after their introduction.

### Acronyms

ALM	Augmented-Lagrangian Method
CAD	Computer-Aided Design
FEA	Finite Element Analysis
IGA	Isogeometric Analysis
KSP	Krylov Subspace
NURBS	Non-Uniform Rational B-Spline
PDE	Partial Differential Equation
PHT	Polynomials splines over Hierarchical T-meshes
RHT	Rational splines over Hierarchical T-meshes
SNEs	System of Nonlinear Equations
VOL	Volume Of Fluid

### Latin symbols

$c$	The concentration field
$c_1$	Flexoelectric constant
$\mathbf{D}^e$	Electric displacement
$d_m$	membrane thickness
$\mathbf{E}$	Electric field intensity
$\mathcal{E}_B$	Bending energy of biomembrane
$\mathcal{E}_{DE}$	Dielectric energy of electrolyte
$\mathcal{E}_{DM}$	Dielectric energy of biomembrane
$\mathcal{E}_F$	Flexoelectric energy of biomembrane
$f_c$	Free energy density
$f_g$	Gradient of interfacial energy density
$f_{lr}$	Long-range interaction energy density
$\dot{g}_i$	Rate of generation in Cahn-Hilliard equation
$H$	Total curvature of the membrane
$H_{sp}$	Spontaneous curvature of the membrane
$h_n$	Wall-normal element size parameter



$K$	Gaussian curvature
$L_\rho$	Interface mobility
$M_{ij}$	Chemical mobility tensor
$\Delta p$	Pressure difference
$\mathbf{P}$	Tangential projection operator
$\mathbf{P}^f$	Bending-induced Polarization
$\mathcal{R}_0$	Effective radius of Vesicle
$R_e$	Reynolds number
$\dot{S}_i$	Rate of sink in Cahn-Hilliard equation

## Greek symbols

$\alpha$	Repulsion parameter
$\beta$	Viscosity ratio
$\dot{\gamma}_i$	Rate of reaction in Cahn-Hilliard equation
$\varepsilon$	Diffusive interface regularization parameter
$\varepsilon_i$	Dielectric constant of inner electrolyte
$\varepsilon_m$	Dielectric constant of the biomembrane
$\varepsilon_o$	Dielectric constant of outer electrolyte
$\zeta$	Thermal fluctuation
$\kappa$	Bending rigidity of the membrane
$\kappa_G$	Gaussian bending rigidity of the membrane
$\lambda$	Surface tension
$\lambda_g, \lambda_v$	Lagrange Multipliers
$\mu^*$	Dynamics viscosity
$\sigma_i$	Conductivity of electrolyte
$\sigma_m$	Conductivity of biomembrane
$\zeta_i$	Chemical potential of the interaction energy
$\tau_B$	Stabilization parameter of RBVMS method
$\phi$	Phase-Field Variable
$\chi$	Reduced Areal
$\psi$	Electric potential
$\Omega$	Domain
$\partial\Omega$	Boundary of the domain $\Omega$

# 1

## Summary

### 1.1 Motivation

Vesicle behavior is among the most complicated natural phenomenon in the human body [1]. They - among other things - serve the purpose of intra-extra cellular communication in prokaryotes and eukaryotes, as they can transfer proteins, lipids, and nucleic acids between the two mediums. This has a significant influence on the various physiological and pathological functions of both recipient and parent cells [2]. In nature, vesicles are selectively permeable barriers that separate the internal components of the cell from its surroundings [3]. They have remarkable mechanical behavior that is characterized by many phenomena, most noticeably their fluid-like in-plane behavior and solid-like out-of-plane behavior [4]. Vesicles can exhibit various shape transitions depending on their ambient environment. Among the most notable are: budding, discocyte-stomatocyte, reentrant dumbbell-pear-dumbbell, and spontaneous blebbing [5]. Those transitions are attributed to surface tension [6], osmotic pressure [4], and pressure difference in a fluid flow [7], which plays crucial roles in shape evolution, e.g., budding happens when a neg-

ative effective surface tension attained, and a transition from a discocyte into a prolate ellipsoidal shape occurs in capillary flow in presence of pressure difference. In addition to the surrounding environment, both the mean-curvature bending stiffness and the spontaneous curvature driven by the lipid composition can contribute significantly to the final resting shape of vesicles [8].

Vesicles have been studied in the context of discrete models such as molecular dynamics [9–11], Monte Carlo methods [12], Dissipative Particle Dynamics [13], and Brownian Dynamics [14]. Those methods, however, tend to have high computational costs, which limited their uses to studying atomistic details such as vesicle budding, fission, and fusion. To study a broader set of phenomena, the continuum models, in which, vesicles are treated as a continuum by neglecting the atomistic details, have the advantage, mainly the low computational costs when compared to the discrete methods as they are very expensive to scale up for large domains [15]. Using continuum models, vesicles hydrodynamics [16, 17], electromechanics [18], electrohydrodynamics [19], multicomponent vesicles [20] and shape dynamics of vesicles [21] have been studied.

Following this path, and for the work conducted in this thesis, we are employing the IsoGeometric Analysis (IGA) to study single vesicle electrodynamics and vesicle doublets hydrodynamics. Isogeometric analysis was first theorized in [22] and later expanded in [23]. Isogeometric analysis was motivated by the existing gap between Finite Element Analysis (FEA) and Computer-Aided Design (CAD) [22], as it seeks to unify the fields of CAD and FEA. The basic idea of isogeometric analysis is to use the CAD basis functions to model both geometry and field variables in the analysis stage instead of the Lagrange basis function. The origin of IGA was by using Non-Uniform Rational B-splines (NURBS) basis functions but was later expanded to use T-splines [24], PHT-splines [25, 26], and RHT-splines [27]. Isogeometric analysis has proven to show superiority when compared to classical mesh-based methods due to their limited continuity which necessitate a need for additional intermediate equations to account for such limitation, as it possesses the unique ability to solve high-order differential operators since a  $\mathcal{C}^1$ , or even higher order continuities can easily be implemented and achieved. In addition, Isogeometric analysis has the unique ability to precisely interpret geometrical shapes, especially in the case of nonlinear geometries. It has been used in a wide range of mathematical and engineering problems, such as biomembranes and vesicles morphology [28–31], fluid-structure inter-

action [32–35], acoustic problems [36–39], topology optimization [40, 41], and many other fields.

In this work, we are leveraging the advantages and efficiency of isogeometric analysis, especially, the ability to attain higher-order continuity basis functions, to study and investigate in detail the following:

1. Solving a constrained Willmore problem coupled with an electrical field to simulate the morphological evolution of vesicles subjected to static electrical fields. The model consists of two phases, the lipid bilayer, and the electrolyte. The two-phase problem is modeled using the phase-field method, a subclass of the diffusive interface models. The bending, flexoelectric, and dielectric energies of the model are reformulated using the phase-field parameter. In a primal variational framework, the resulting Euler-Lagrange equation is a 4<sup>th</sup>-order PDE which requires  $\mathcal{C}^1$  basis function to be solved numerically. For this reason, we use IGA to numerically approximate the solution of the examples we intend to study,
2. Studying the hydrodynamics of vesicle doublet suspended in an external viscous fluid flow. Vesicle doublets are also modeled using the phase-field method. The bending energy and energies associated with enforcing the global volume and area are considered. In addition, the local inextensibility condition is ensured by introducing an additional equation to the system. To prevent the vesicles from numerically overlapping, we deploy an interaction energy definition to maintain a short-range repulsion between the vesicles. The fluid flow is modeled using the incompressible Navier-Stokes equations and the vesicle evolution in time is modeled using two advection equations describing the process of advecting each vesicle by the fluid flow. The Residual-Based Variational MultiScale (RBVMS) method was used to overcome the velocity-pressure saddle point system and solve the Navier-Stokes equations.

## 1.2 Phase-Field method

The phase-field method is a mathematical method for solving interfacial problems by tracing the zero level-set of an order parameter with a distinctive, bounded value, which,

in the limit of the order parameter, i.e., the sharp interface limit, the interfacial dynamics is recovered. It was first theorized in [42] to study the thermodynamic description of a solidifying system in a part of a broader pattern formation in the first-order phase transitions study. Since then, the method has been used in a wide variety of research fields like single vesicles hydrodynamics [19, 43, 44], single vesicles electrodynamics [18, 45], fracture mechanics [46, 47], phase-separation [48, 49], microstructures evolution [50, 51], void formation and evolution [52, 53], precipitation [54, 55], and many other fields. The phase-field method is a thermodynamically-based method with multiple advantages, i.e., it does not require a pre-defined morphological evolution pattern or shape, and since the phase-field is an implicit method, there is no need to track the interfacial region explicitly, but rather by extracting the zero-level set which defines the interface between multiple phases. In addition, it is easy to implement and can easily be extended from a 2D to a 3D formulation with minimal work.

The phase-field formulation can be either a variational or non-variational formulation. Under the variational formulation, the system's equations are formulated based on a free energy functional, which is rewritten as a function of the order parameter. This formulation includes the order parameter describing the location of the interface and another parameter that *regulates* the interface width. For the non-variational formulation, the system's equations are derived directly without referring to any energy functional, however, when the asymptotic expansion is performed, the sharp-interface model is recovered [56, 57]. Generally speaking, the phase-field formulation includes two sets of scalar variables, i.e., the concentration and the order parameter. The former variable addresses the spatial distribution of the field of interest in time, like - *for example* - the chemical concentration of a substance within the computational domain over the entire temporal domain. The latter variable describes the temporal evolution of the interface between phases, which is manifested by the spatial location of the zero-level set [58]. In the realm of the implicit geometrical description of vesicles, the physical phenomena associated with its morphology can be mathematically represented as free boundary problems, in which, the boundary  $\Gamma \subseteq \partial\Omega$  of a domain  $\Omega$  is unknown and subjected to evolution over time. The surface is *diffused* over a predetermined distance - using a regularization parameter  $\varepsilon$  - from the zero level-set of the function describing the profile of the domain, e.g., the hyperbolic tangent function in the case of phase-field method, which means that the in-

terface has a thin thickness nonetheless, diffused over  $\varepsilon\Gamma \subset \Omega$ , and all fields of interest change smoothly across the diffused interface.

In this work, we are using a variational energy-based thermodynamically consistent approach to *rederive* the energy functional describing the electromechanical behavior of single vesicles in terms of the phase-field variable, for which, and within a primal variational framework, the strong form of the problems is obtained and solved using the isogeometric analysis. But different from the electromechanical model of single vesicles, the system of equations describing the hydrodynamics of a vesicle doublet system is a non-variational based, which is also solved using the isogeometric analysis.

### 1.3 Isogeometric analysis

The isogeometric analysis was first introduced by Hughes *et al.*, [22] and later expanded in [59–61] with the purpose of surpassing the CAD-CAE bottleneck manifested by the disconnected-from-CAD meshes, from which it was originally made, and to integrate the CAD-FEM into a unified modeling-analysis process. Prior to NURBS-based FEM (referred to as **isogeometric analysis**), the ratio of modeling to analysis, time-wise, was 80%-20% [23] with extreme difficulties to develop simulation-specific geometrical models, in which, the FEM meshes were at best an approximation to the CAD geometries. This approximation is the most frequent cause for errors in numerical results, where mesh imperfections, unsuitable elements, small aspect ratios, penetration, and other problems can lead to a significant degradation in the solution's accuracy. For those reasons, isogeometric analysis was introduced on the basis of using the same geometry description in the design and analysis processes. Isogeometric analysis began with the use of non-uniform rational B-splines (NURBS) - the fundamental building block of most commercial CAD programs - to represent the geometry of the model and approximate the solution's control variable. With this at hand, refinement, which requires access to the exact geometry of the model was made available by either knot insertion - *h*-refinement - or order elevation - *p*-refinement - or both, i.e., *k*-refinement.

Different from the classical finite element method, there are no nodal points and nodal variables, but control points and control variables, and the geometry is an "*exact*", while it is an approximation in the classical FEM. In addition, in classical FEM, the continu-

ity across elements boundaries is fixed to  $\mathcal{C}^0$  continuity, while in isogeometric analysis, higher-order continuities can be easily attained across elements boundaries. In addition to this, and different from FEM, isogeometric analysis by design has two definitions of mesh, i.e., the control mesh and the physical mesh, which, unlike the FEM, has only one mesh. The control points are spatially scattered *points* that define the control mesh, which in turn control the geometry of the model, and the control mesh interpolates the control points. Besides that, the basis functions are usually not interpolatory, and the control variables are the degrees of freedom per control point.

In our work, and for the Willmore problem mentioned in the previous section, we are considering Helfrich [62] elastic energy, which, after reformulating using the phase-field variable  $\phi$  produces an energy functional with a  $2^{nd}$  order spatial derivative of the phase-field variable, for which, the Euler-Lagrangian PDE is of  $4^{th}$  order. In the context of Galerkin-based numerical methods, upon multiplying by a weighting function, integrating by parts, and dropping the boundary terms, we end up with a weak form, for which, the highest spatial derivative is of  $2^{nd}$  order. In the classical finite element method, the Lagrange basis functions are globally fixed  $\mathcal{C}^0$  continuous. This makes the method best fitted to solve PDEs with second-order spatial operators where their primal variational form necessitates the integration of first-order derivatives which are well-defined and integrable if the basis functions are piece-wise smooth and globally  $\mathcal{C}^0$  continuous, and hence, it is not possible to simulate the electromechanical response of the vesicles by considering Helfrich elastic energy while using the classical finite element method, unless one resorts to a mixed formulation as in [18, 63] or strong form meshfree methods to compute a discretized higher-order derivative operators [64–67]. Alternatively, isogeometric analysis possesses the ability to solve  $4^{th}$ -order PDEs in a primal variational framework as it incorporates *k*-Refinement, i.e., the ability to increase the order and continuity. And hence, the NURBS-based IGA can easily attain  $\mathcal{C}^1$  or higher order continuities, which makes it suitable for simulating a phase-field model based on Helfrich elastic bending energy. The ability to solve high-order PDEs in an isogeometric analysis framework was exploited extensively. Aside from better results when compared to the mixed formulation or any other techniques used to solve high-order PDEs, the easiness of the computational implementation, speed, and efficiency make the isogeometric analysis far better than any other numerical methods [20, 28, 45, 61, 68–70].

## 1.4 Vesicles and lipid bilayer membranes in computational mechanics

Vesicles are cellular organelles self-contained lipid bilayer membrane-surrounded pockets generated by most cells for the purpose of transporting materials and destroying toxic substances and pathogens. They serve as a communicator to transmit biological signals between cells [71, 72] and they play a vital role in metabolism and enzyme storage as well [73]. Vesicles are composed of proteins, lipid bilayers, and nucleic acids, and they vary significantly in type and functionality. Lipid bilayers are fatty—molecules that make up about 50% of the mass of most human cell membranes, nearly all of the remainder being protein. There are approximately  $5 \times 10^6$  lipid molecules in a  $1 \mu\text{m} \times 1 \mu\text{m}$  area of lipid bilayer, or about  $10^9$  lipid molecules in the plasma membrane. As shown in Fig. (1.1), all of the lipid molecules in cell membranes are amphipathic (or amphiphilic), and they have a hydrophilic, i.e., water-loving, or polar end, and a hydrophobic, i.e., water-fearing, or nonpolar end [74]. Vesicles have peculiar mechanical behavior like their fluid-like in-plane behavior and solid-like out-of-plane behavior [4]. Their morphology depends highly on their surrounding environment [5]. For example, and depending on the spontaneous curvature, vesicles can evolve from a prolate-like shape to a dumbbell, which in turn can develop into an outward budding or a tube-like vesicle, depending on the volume change rate. Vesicles can also evolve from an oblate-like shape into a biconcave into a stomatocyte into an inward budding when the spontaneous curvature has a negative value [75]. In addition, the mean-curvature bending stiffness [8], the surface tension [6], osmotic pressure [4] and pressure difference in a fluid flow [7] play crucial roles in shape evolution. The presence of electric fields can also alter the morphology of vesicles in a quasi-static state, which triggers a flexoelectric response in the biomembrane, causing the vesicle to evolve into counter-intuitive shapes [45].

Lipid bilayers have been studied in the context of discrete models. However, when the atomistic details are not the primary concern of the study, but the overall morphology, the continuum models are more suitable.



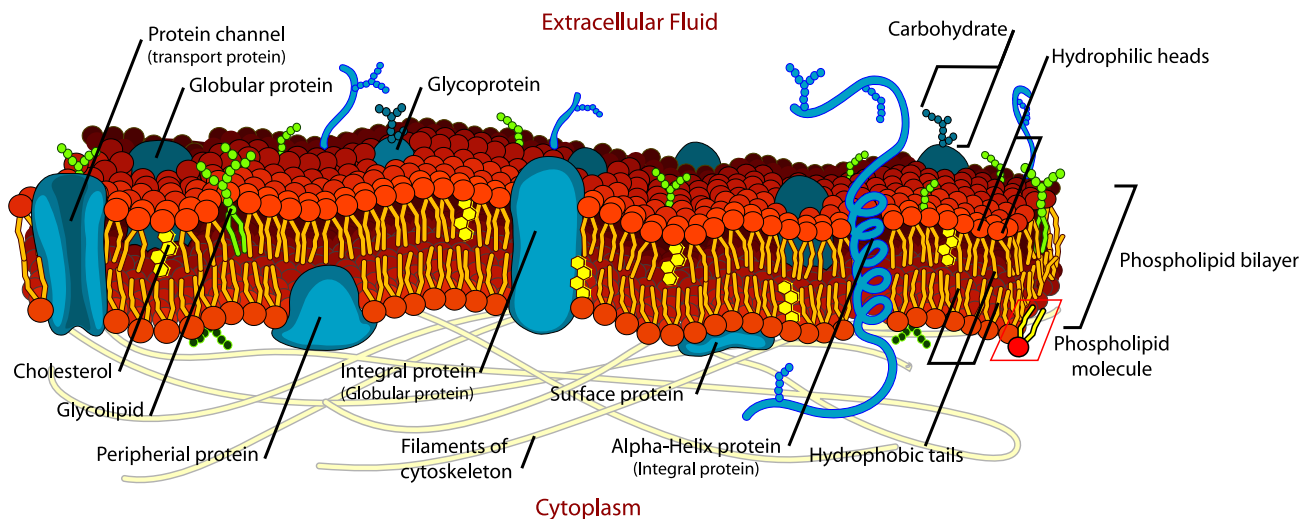


Figure 1.1: The lipid bilayer consists of a polar hydrophilic phosphate head, and a non-polar hydrophobic lipid tail. The lipid bilayer consists of two adjacent sheets of phospholipids, arranged tail to tail. The hydrophobic tails associate with one another, forming the interior of the membrane. The polar heads contact the fluid inside and outside of the cell. (Source: [76]).

#### 1.4.1 Vesicles morphology using discrete models

Various discrete models have been used to study the atomistic details of lipid bilayers, among the most notable is Molecular Dynamics [77–79]. Other models such as Monte Carlo methods [80–82], Coarse-Grained model [83–85], and Dissipative Particle Dynamics [86–88] have also been used extensively in the context of lipid bilayer studies. Those studies in general focused on comparing and validating numerical-based results to experimental ones by studying various settings related to the mechanical behavior of the lipid bilayers as in [78], in which, the lipid areas, bilayer area compressibilities, bending constants, and monolayer spontaneous curvatures were studied in depth. Whereas [79] studied the Protein ion channels and the Potassium-Calcium pump. The increase in research using those discrete models can be attributed to the massive increase in computational power, the development of reliable molecular dynamics simulation algorithms, and the development of well-validated empirical molecular mechanical force fields. For more details about the current state-of-the-art of lipid bilayer simulations using molecular dynamics, please refer to the review of Moradi *et. al.* [89].

### 1.4.2 Vesicles morphology using continuum models

Unlike the discrete models, the continuum models are used to study the overall morphology of vesicles under various conditions. Conceptually, a Vesicle can be simulated as a 2D surface embedded in 3D space that could be represented either explicitly or implicitly. Explicit surfaces map a vector-valued parameterization function  $f : \Omega \rightarrow \mathcal{S}$  from a two-dimensional parameter domain  $\Omega \subset \mathbb{R}^2$  to a surface  $\mathcal{S} = f(x,y) \subset \mathbb{R}^3$ . Implicit surfaces are defined by the zero set of a scalar-valued function  $f : \mathbb{R}^3 \rightarrow \mathbb{R}$  such that  $\mathcal{S} = \{x \in \mathbb{R}^3 \mid F(x) = 0\}$ . For complex geometries that feature splitting or merging phenomena during deformation, consistent definition without overlapping and/or self-intersection is difficult to maintain, therefore, ad-hoc cut-and-connect techniques (See Ref. [90]) need to be deployed to track the topology changes on the vesicle's surface mesh, which by itself is a very difficult task to perform, not to mention the immense computational load associated with such techniques. For such cases, implicit surface representation has been used successfully as their volumetric definition implies a consistent, closed manifold. Numerous techniques have been used to track interfaces implicitly. Those techniques can be categorized into two main groups: sharp interface, and diffuse interface methods. For sharp interface models involving two phases [91–94], the governing equations for each phase are written separately and additional jump conditions are considered at the interface to satisfy conservation/continuity of some physical quantities, e.g., conservation of mass, momentum and/or energy [95], continuity of the traction vector [96], and conservation of current density across the membrane [19]. The interface between different phases of the system is considered to be infinitely sharp, i.e., the slope of the scalar-valued function at the interface is undefined, and the boundaries between the different domains are described by the interfacial boundaries. For diffuse interface methods, the interface is smeared out and therefore has a non-zero thickness and the quantities of interest are distributed throughout the interfacial region [97–99]. The domain is represented by a phase-field variable function that is continuous in space and time. For multicomponent domains, the phase-field variable has the same value for each phase and the transition at the interface is continuous [100]. Consequently, the interface can be tracked implicitly by a contour of constant phase-field values, and the energy of the system is defined over the entire domain. Different from the sharp interface methods,

jump conditions are included in the governing equations and the interface thickness spans over a few spatial elements [21, 101].

#### 1.4.2.1 Vesicles studies in the context of Level-Set method

The level-set method is an implicit surface tracking method, in which, a real-valued surface function takes on a given constant value representing the tracked surface. The method was first introduced by Stanley *et. al.* in [102] in an attempt to capture the moving interface by tracking the zero-level set of an auxiliary field, which distinguished between multiple phases. The method - like most of the implicit methods - is highly robust, as it does not require a mesh re-generation at each time step and can be used on a fixed mesh. Using the level-set method, Salac *et. al.* [103] studied the motion of lipid vesicles in shear flow and a pressure-driven flow. Doyeux *et. al.* [104] simulated vesicles in fluid flow using the level-set method by writing the membrane properties as interfacial forces between the intra- and extracellular fluids. The method when compared to the phase-field method is computationally less expensive but at the expense of the fact that it is more suitable for larger scale simulations, where the interface is not well resolved by the mesh, and where the problem at hand has only two phases.

#### 1.4.2.2 Vesicles studies in the context of Phase-Field method

Vesicle's morphology in the context of the phase-field method has been the highlight of this research field in the last decade. The phase-field method is an implicit method to solve moving boundary problems. The reason for the method's popularity can be attributed to its relative easiness of scalability, where the numerical formulation can be extended from 2D to 3D settings with minimal work. A phase-field model has been developed by Aland [105] to investigate biomembranes inhomogeneities due to inserted proteins, absorbed molecules, or different compositions of lipids and cholesterol. Lázaro *et al.* [106] presented a phase-field formulation to simulate complex phenomena related to the dynamics and morphology of biological membranes such as pearling, tubulation, and RBCs hydrodynamics in microchannels. Rosolen *et al.* [101] presented an adaptive meshfree method based on the maximum-entropy approximants for simulating phase-field models of biomembranes based on Helfrich curvature elastic energy. Kim *et al.* [107] presented a finite-element formulation using Nitsche's method for the phase-field

model of a single component vesicle by minimizing the curvature energy and deriving a nonconforming finite-element formulation which is applied to  $\mathcal{C}^0$ -elements. The proposed continuous-discontinuous Galerkin formulation weakly imposes the continuity of first derivatives across the element boundaries and uses a Nitsche’s method to achieve stability. Wang *et al.* [21] combined exponential time differencing Runge–Kutta approximations for time integration with spectral discretizations for spatial operators on regular meshes to solve unconstrained and constrained Willmore flow problem using the phase-field method. They also proposed a modified augmented Lagrange multiplier approach to avoid numerical instabilities caused by large penalty terms imposed on the system to penalize the violations in surface area and volume constraints.

Simulation of the electromechanics of vesicles and their corresponding evolution have been an ongoing effort in the field of biomechanics. Steigmann *et al.* [108] proposed a two-dimensional model based on a three-dimensional liquid-crystal theory framework to simulate the response of electrically polarized lipid bilayers by an applied electric fields generated by a remote source. Even before this work, Gao *et al.* [109] proposed an electromechanical liquid crystal model of vesicles. Soon later, they proposed a phase-field model for investigating the morphological evolution of vesicles subjected to an external electrical field [18], where they used a monolithic finite element-based mixed-formulation to solve a system of second-order PDEs. Only axisymmetric vesicles were considered in their work.

## 1.5 The electrostatics and hydrodynamics of vesicles

The dynamics of vesicles and hence, the morphology, can be described accurately by the free energy functional of the Canham-Helfrich [62, 110], of which, the vesicle can be treated as a two-dimensional surface embedded into three-dimensional space and defined by the two radii of curvature at each point. To this end, the Canham-Helfrich free energy of the lipid bilayer that describes the bending energy of a homogeneous membrane can be expressed as follows:

$$E = \frac{\kappa}{2} \int_{\Gamma} [(H - H_{sp})^2 + \kappa_G K] d\Gamma \quad (1.1)$$

where  $\kappa$  is the bending rigidity,  $\kappa_G$  is the Gaussian bending rigidity, and  $H$ ,  $H_{sp}$ ,  $K$  are the total curvature, the spontaneous and Gaussian curvatures, respectively. Based on the Gauss–Bonnet theorem, the Gaussian curvature term which is integrated over a closed surface is considered a topological invariant, and since most studies in the field of lipid bilayers are not concerned with topological changes, this term will be a constant contribution in the total free energy and will drop out. This Cahnham-Helfrich model of Eq. (1.1) is a sharp interface model with an Euler-Lagrangian PDE is of 4<sup>th</sup> order, which can be solved implicitly using the phase-field isogeometric analysis as shown later.

### 1.5.1 Vesicles Electrodynamics

The research focused on the electrostatics of vesicles is less frequent than the one focused on the hydrodynamics of vesicles. This is mainly because of the complexity associated with the electric response of the biomembranes as it incorporates flexoelectric properties, which makes modeling biomembranes a non-trivial problem to solve. Ye *et al.* [111] used electromagnetic induction with a time-varying magnetic field to develop an analytical theory to investigate the biomechanics of a modeled vesicle. The suspending media is treated as a lossy dielectric, with a membrane thickness equal to zero, and the electric resistance of the membrane is assumed to be negligible. This work provided an analytical solution for the surface charges (Fig. 1.2), electric field, radial pressure, overall transnational forces, and rotational torques introduced on a vesicle by the time-varying magnetic field. Gao *et al.* [18] developed a phase-field model to investigate the morphology of vesicles in static electric fields. His model accounted for the flexoelectric response of the biomembrane. The energies of the system were reformulated in terms of the phase-field variable, and the global surface area and volume constraints were dealt with locally by introducing two Lagrange multipliers to enforce them. The study was conducted under 2D-axisymmetric assumptions. Various evolution patterns emerged from the study under various conditions, most notably the complexity of the shape evolution when the flexoelectric response is considered. It is worth mentioning that the system was solved using a mixed-formulation finite element method, which introduced a new variable to the system in order to address the  $\mathcal{C}^0$  issue associated with the classical finite element method. Li *et al.* [112] presented a way to simulate the electroformation process of giant unilamellar vesicles (GUV) in saline solution. They showed that the formation

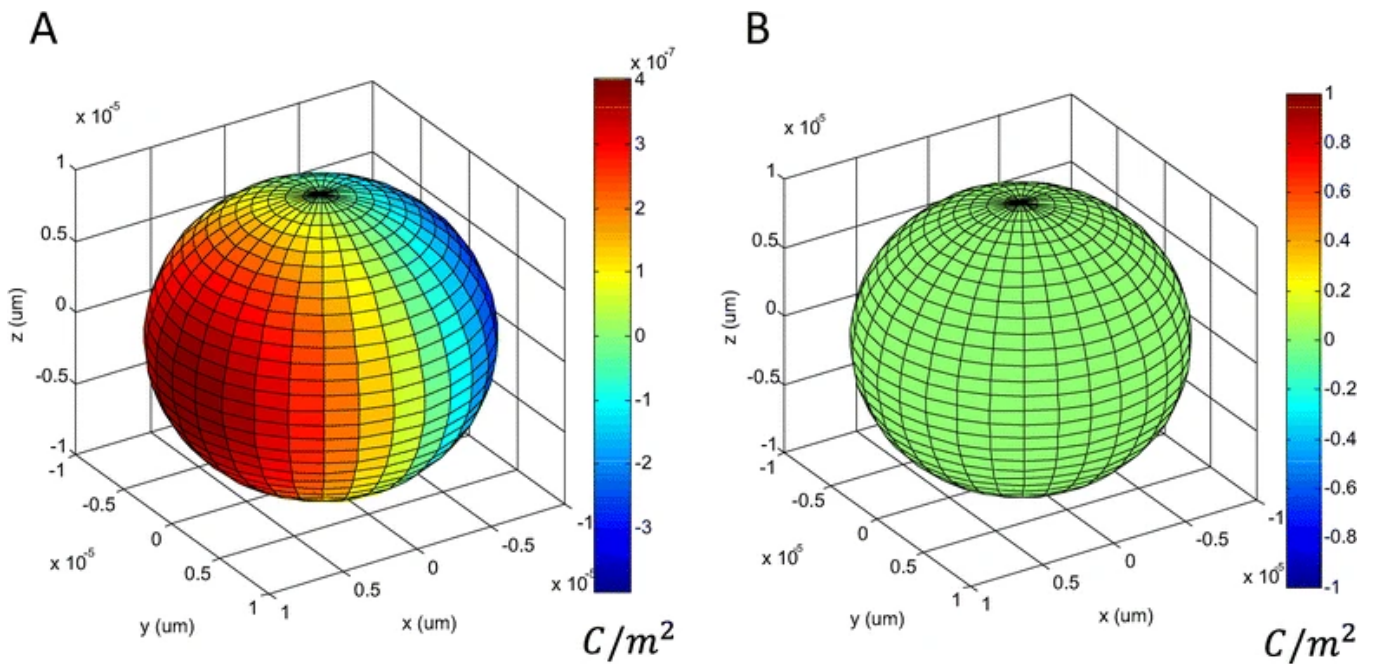


Figure 1.2: Surface charge distribution induced by the time-varying magnetic field. (A): The plot demonstrated an instant pattern of surface charge distribution. The color represented the amount of the charge density ( $C/m^2$ ). Field frequency was 10 KHz.  $\sigma_o = 1.2$  S/m.  $\sigma_i = 0.3$  S/m. (B): There was no accumulation of surface charges if the two media were set to be electrically identical ( $\sigma_o = \sigma_i$  and  $\epsilon_o = \epsilon_i$ ). (Source: [111]).

of GUVs in saline solution is in fact affected by many factors, like the amplitude and frequency of the AC fields, the temperature, and the NaCl concentration. Liu *et. al.* [113] studied the phenomena of electroporation and electrofusion and the effect of the vesicle shape and medium on those two phenomena. They also studied the effect of the transmembrane voltage and pore density on the possibility of vesicle fusion. Among the findings of the research, the authors found out that electric pulse can induce a selective electroporation at the contact area between two vesicles regardless of the vesicle shape. Nodargi *et. al.* [114] conducted an isogeometric analysis to study red-blood cells electro-deformation. A surface shell model has been proposed for capturing the RBC kinematics, with Helfrich model being used to describe the bending behavior of the biological membrane. The enclosed-volume conservation constraint has been enforced at the structural level to model the volumetric behavior arising from the nearly incompressible fluid inside the biomembrane. The authors used a staggered fixed-point iteration scheme that has been presented for performing the electro-mechanical strong coupling, in such a way that electrical and mechanical problems can be solved in an uncoupled way by means of respective reliable solvers. Specifically. The numerical simulations reproduced RBC large

deformation by optical tweezers and RBC electro-deformation have been performed.

## 1.5.2 Vesicles Hydrodynamics

Unlike the vesicle electrodynamics, the hydrodynamics of vesicles has been studied extensively from different perspectives, and using different implicit - and sometimes explicit - geometrical description methods, and this, in fact, is part of a larger effort to push the boundaries of biomechanics further in understanding some of the most complex and fundamental phenomena inside the human body. To this end, and in an early study in the field of computational mechanics, Kraus *et. al.* [115] studied fluid vesicles in a shear flow. In this study, the authors present a coupling model between the flow within the membrane and the hydrodynamics of the surrounding bulk fluid. The study is built on the use of the Oseen tensor to compute the disturbance in flow due to the presence of the vesicle. Several parameters have been studied like, e.g., linear shear flow and shear rate. Although the study presented a novelty at the time it was conducted, it does not address several major issues as the local inextensibility of vesicles and global surface area and volume conservation. Sukumaran *et. al.* [116] conducted a study of the dynamics of three-dimensional fluid vesicles in a bounded and unbounded steady shear flow in the vicinity of a wall, within the context of the boundary element method. Three cases were investigated in detail at low Reynolds number, i.e., a neutrally buoyant vesicle, a vesicle filled with a denser fluid, and the dynamics in the case of additional adhesive forces exerted by the wall on the vesicle. The researchers in their conclusion point out to a very important issue, which is the need to address the contrast in viscosities between the intra- and extracellular mediums. Ghigliotti *et. al.* [117] studied the rheology of a dilute two-dimensional suspension of vesicles. The numerical method used in this study was based on the boundary integral formulation, i.e., Green's function technique, and the phase-field approach. The flow considered was an unbounded linear shear flow, with the aim of establishing a link between the rheology of vesicle suspensions and the microscopic dynamics of the constituent particles, e.g., tanktreading and tumbling motions. Rahimian *et. al.* [118] did a boundary integral analysis of inextensible vesicles suspended in a viscous Stokesian fluid. In their research, the authors considered different viscosities for the fluid within and outside the vesicles, i.e., viscosity contrast. The research covers the dependence of the inclination on the ratio of the viscosity contrast, the effect of the

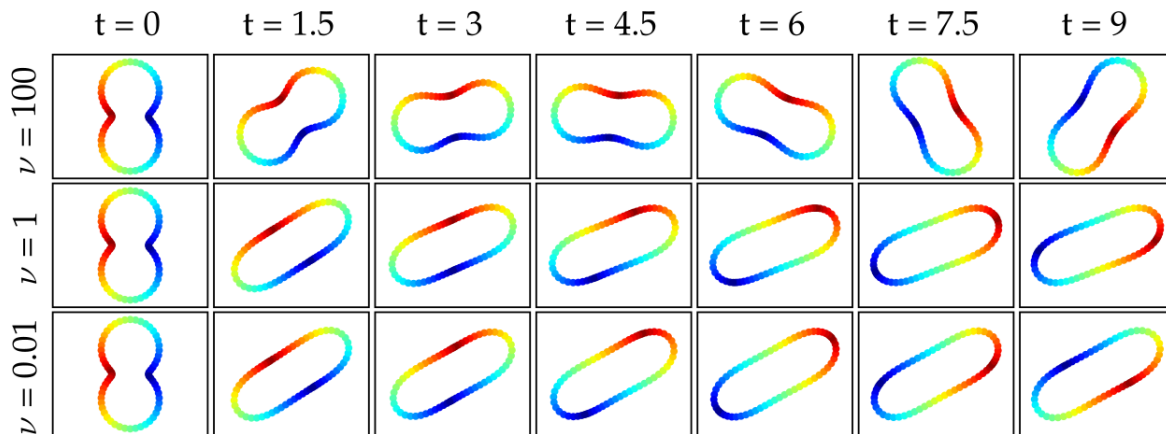


Figure 1.3: The evolution of a single vesicle in an unbounded shear flow. The viscosity contrast  $\nu = .01, 1, \text{ and } 100$ , bending modulus  $\kappa_b = 1$ , reduced area = .75, and the temporal domain = 9. When  $\nu < \nu_c$ , the vesicle reaches an equilibrium and then undergoes tank-treading motion. When  $\nu$  is large, the vesicle tumbles. (Reproduced from Ref. [118] with permission from Elsevier and Copyright Clearance Center's RightsLink®).

reduced area of the vesicle on the overall hydrodynamics of vesicles, the effective viscosity of a dilute suspension of vesicles, the lateral migration of vesicles in shear flow, and the dispersion of two vesicles. Aland et. al. [119] proposed a diffusive interface model for the dynamics of inextensible vesicles in viscous fluid with inertial forces by including an additional equation to account for local inextensibility in the vicinity of the vesicle interface. The model also includes novel parameters related to the regularization, relaxation rate, and novel diffusion coefficient. In the field of multi-vesicle and vesicle doublet systems in a fluid flow, Quaife et. al. [44] studied the dynamics of adhesive vesicle doublet suspended in a quiescent flow. Two vesicles were placed apart and moved towards each other to form a vesicle doublet by pushing the fluid between them. Various configurations of flow were considered, like shear flow and extensional flow. Marth et. al. [120] investigated the margination of white blood cells and their behavior dependency on a set of factors like haematocrit, cells' deformability, and Reynolds number. Their approach accounts for the short interaction between white and red blood cells by including an interaction energy definition in the variational formulation, which we borrow to maintain separation between vesicles in the current study. As a summarization, vesicles tend to lock in a tank-treading motion in a planner shear flow at low viscosity contrast and low shear rate, while at high viscosity, vesicles transition to a tumbling motion [43, 121, 122]. Vesicle trembling has also been noticed [123, 124]. The reduced area/volume in 2D/3D of vesicles plays a significant role in the morphology and hydrodynamics [43, 44, 125].



At a low Reynolds number regime, the inertial forces can be neglected and the Stokes limit is considered. Under those circumstances, the vesicles undergo small deformations which result in the aforementioned shape transitions [43, 121–124]. However, the inertial effects can become significant in vesicles and vesicle doublet hydrodynamics in certain situations, i.e., margination of WBC and vesicles flow in large blood vessels like arteries, in which, Reynolds numbers might be equal to or greater than 1.0 [126]. At those limits, and when the inertial terms of the Navier-Stokes equation are included, the tumbling motion of vesicles in fluid flow within the Stokes limit is no longer observed [119].

On the experimental side, there also has been extensive research regarding vesicles' rheology and hydrodynamics (see e.g. [127–129] and the references therein), and for most numerical research, the experimental data were used as benchmarking studies to validate the numerical results.

## 1.6 Outline

This thesis is divided into 6 chapters. The first one was devoted to a general literature review of the current state-of-the-art of lipid bilayer research and the motivation behind this work. In chapter 2, we present a research-oriented introduction to the phase-field method and the applications in which it was used. We also present a detailed reformulation of energy functional used in this work into the phase-field framework. In chapter 3, we discuss the isogeometric analysis, the core numerical tool that has been used in this work. We highlight - in detail - its advantages and the role it plays in solving higher-order PDEs. In chapter 4, we speak about the Willmore constrained optimization problem coupled with an electrical field. We also present a modified Augmented-Lagrangian approach we used to satisfy the constraints while maintaining numerical stability and a relatively large time step. We present our findings on the morphological evolution of the vesicles under static electric fields and the effect of several factors on the overall morphology of the vesicles. In chapter 5, we study the hydrodynamics of vesicle doublet suspended in an external viscous fluid flow. Vesicles, in this part of the research, are modeled using the phase-field model. The bending energy and energies associated with enforcing the global volume and area are considered. In addition, the local inextensibility condition is ensured by introducing an additional equation to the system. To prevent the vesicles

from numerically overlapping, we deploy an interaction energy definition to maintain a short-range repulsion between the vesicles. The fluid flow is modeled using the incompressible Navier-Stokes equations and the vesicle evolution in time is modeled using two advection equations describing the process of advecting each vesicle by the fluid flow. To overcome the velocity-pressure saddle point system, we apply the Residual-Based Variational MultiScale (RBVMS) method to the Navier-Stokes equations and solve the coupled systems using isogeometric analysis. We study vesicle doublet hydrodynamics in shear flow, planar extensional flow, and parabolic flow under various configurations and boundary conditions. The results show phenomenal dynamics of vesicle doublet under those various conditions. In chapter 6, we summarize our work and present our conclusions. In addition, we highlight the research topics we would like to study in the future.



# 2

## Phase-Field Method

### 2.1 Introduction

The temporal morphological evolution of vesicles is a moving-boundary problem. This class of problems is challenging to solve using computational methods due to the severely deformed boundaries between interfaces, nonlinearity arising from the coupling of the interface dynamics with the material dynamics, and the different time and length scales. Methods for tracking the interface position can be generally speaking classified into the so-called Lagrangian and Eulerian methods. Lagrangian methods - often referred to as *front-tracking* methods - track the interface explicitly, while Eulerian methods - often referred to as *front-capturing* methods - track the interface implicitly. In the former case, the interface is tracked by the motion of particles on the interface and accurate calculation of the curvature [130]. For the implicit methods, the location of the interface is captured with an additional scalar field [131].

In the explicit geometrical description approach, the governing equations within each field

are solved on a mesh that deforms in accordance with the moving boundary, and the interfaces are continuously updated. The methods under this definition provide an accurate estimation of the shape's morphology at the expense of complexity, as they are limited to simple cases. On the other hand, implicit methods can accurately track interfaces of complex geometries. Those methods are based on incorporating of the interface boundary conditions as sources in the momentum and energy equations. Among the most notable sub-classes of the Eulerian methods are the Volume Of Fluid (VOF) and the Level-Set (LS) methods. The first of those methods, i.e., the VOF, has been used to track and locate the free surfaces in the case of multiple-phase fluid and fluid-fluid interaction, in which, the interface is treated as a step-wise function and reconstructed by volume fraction values [132, 133]. The level set methods (LSM) are Eulerian methods that implicitly track the location of the boundary surface. LSM has been used to solve solidification of binary alloys [134, 135], computational fluid dynamics [136, 137] and also to model vesicle morphology [138–140], among other applications. The solution of an additional differential equation is required to track the interface. The numerical approach to solving the partial differential equations (PDEs) in the context of LSM depends on the degree of PDEs. For higher-order PDEs, IGA is widely used, while for first and second-order PDEs, FEM has often been used. Phase-field method belongs to Eulerian methods and similar to LSM, phase-field models also involve solving an additional differential equation. In contrast to the LSM, which allows a sharp, i.e. exact, description of the interface, the phase-field method smears the interface over a small area. This mitigates the need for the time-consuming re-initialization process of the level-set function, which significantly simplifies the implementation.

The phase-field method is one of the most popular methods in solving free-boundary problems and tracking interfaces between different materials. It is a multi-scale method that can be used on a nano-, micro-, meso- and macro-scale levels, and revolves around capturing surfaces and interfaces implicitly by introducing an auxiliary field called the *phase-field variable*, denoted  $\phi$  hereinafter, and tracking the zero level-set of this field which represents the interface between the multiple phases. The method can describe the morphological evolution of interfaces using a set of conserved and non-conserved field variables that are continuous across the interfacial regions. It has multiple features that make it attractive in the realm of implicit geometrical description, like its multidimen-

sional implementation applicability, i.e., 2D and 3D, and the absence of prior morphological assumptions, with extreme computational efficiency and scalability [141]. In the field of vesicles electrohydrodynamics, where the boundaries between multiple phases, i.e., vesicle's surface and ambient fluid or electrolyte, are time-dependant and prone to evolution over time, solving the set of partial differential equations (PDEs) describing the system is a non-trivial problem as it involves coupling a set PDEs on the boundaries and within the computational domain with the PDEs on the evolving interface and/or surface. This class of problems is called free-boundary problems, and it was - prior to the phase-field era - solved using moving mesh methods, in which, the interface was actually spatially discretized to allow for the boundary conditions on the interface to be imposed correctly and then the PDE describing the system to be solved [See Ref. ([142, 143]) for more on adaptive meshing across boundary interface]. As shown in Fig. (2.1), the order parameter - e.g., *the phase-field variable* - takes a constant value within the bulk of each phase and experiences a smooth transition across the interface, with the interfacial region being small enough to resemble the physical interface, and yet, have a non-zero thickness to allow to order parameter and all the quantities defined on the interface to *transition* smoothly.

The phase-field method has been applied in various fields such as solidification [144], grain growth [145–147], evolution of thin films [148, 149], crack propagation [150, 151], electromigration [152, 153] and biomechanics as pointed out in the summary chapter. The temporal evolution of the interface can be accurately described by the two well-known continuum equations of Cahn-Hilliard diffusion equation [154] and Allen-Cahn equation [155], and the models are derived based on the laws of thermodynamics and kinetics as will be discussed in the next section.

## 2.2 Thermodynamics of Phase-Field method

The phase-field model can be derived from classical irreversible thermodynamics. It describes the compositional and structural domain of any considered system and the interface across multiple phases using a set of variables that are continuous across the interface. Those variables are classified into two categories, i.e., conserved and non-conserved. In chemically closed systems, the concentration field represented by the concentration vector

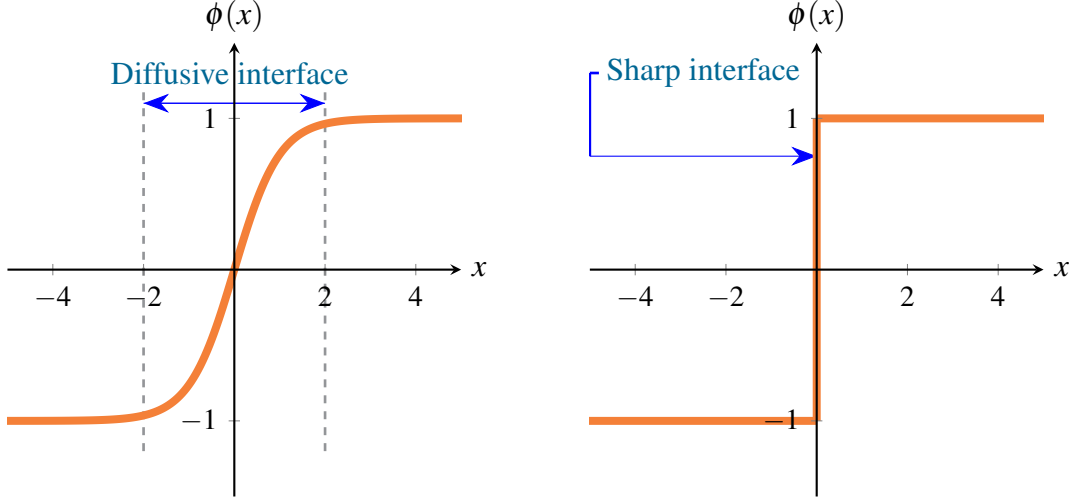


Figure 2.1: A graphical representation of the interface based on the diffusive interface methods (left), and the sharp-interface methods (right).

$\mathbf{c} = \{c_1(\mathbf{x}, t), c_2(\mathbf{x}, t), \dots, c_M(\mathbf{x}, t)\}$  is conserved, while the order parameter field represented by an order parameter vector  $\boldsymbol{\phi} = \{\phi_1(\mathbf{x}, t), \phi_2(\mathbf{x}, t), \dots, \phi_N(\mathbf{x}, t)\}$  is not. The total free energy of the system is then expressed in terms of the phase-field variables as an integration of the entire volume  $V$  of the system, as follows:

$$F = \int_V [f_c(\mathbf{c}; \boldsymbol{\phi}) + f_g(\mathbf{c}; \boldsymbol{\phi}) + f_{lr}(\mathbf{c}; \boldsymbol{\phi})] dV \quad (2.1)$$

where  $f_c$  is the free energy density,  $f_g$  is the gradient of the interfacial energy density which includes the gradient coefficients of the concentration and the order parameter and gives the model its diffusive nature.  $f_{lr}$  is the long-range interaction energy density. The evaluation procedures of the concentration  $\mathbf{c}$  and the order parameter  $\boldsymbol{\phi}$  vectors involve solving Cahn-Hilliard and Allen-Cahn equations, respectively, as follows:

$$\frac{\partial c_i}{\partial t} = \nabla \cdot \sum_j \left( M_{ij} \nabla \frac{\delta F}{\delta c_j} \right) + \zeta_i + \dot{g}_i + \dot{\gamma}_i + \dot{S}_i \quad (i = 1, 2, \dots, M) \quad (2.2)$$

$$\frac{\partial \phi_i}{\partial t} = -L_\rho \frac{\delta F}{\delta \phi_\rho} + \zeta_\rho \quad (\rho = 1, 2, \dots, N) \quad (2.3)$$

where  $M_{ij}$  and  $L_\rho$  are the chemical mobility tensor, and the interface mobility, respectively.  $\zeta_i$  and  $\zeta_\rho$  are the thermal fluctuations. The constants  $\dot{g}_i$ ,  $\dot{\gamma}_i$  and  $\dot{S}_i$  are the rates of generation, reaction, and sink of species  $i$ , respectively. The term  $f_g$  in Eq. (2.1) is

defined as following:

$$f_g(\mathbf{c}; \phi) = \sum_m \frac{1}{2} \kappa_{cm} (\nabla c_m)^2 + \sum_n \frac{1}{2} \kappa_{\phi n} (\nabla \phi_n)^2 \quad (m, n) = 1, 2, \dots, (M, N) \quad (2.4)$$

The aforementioned set of equations, e.g. Eqs. (2.1-2.4), gives a general description of the phase-field model. Those equations can be used to simulate the morphology of a multi-components multi-phases system. The free energy definition of Eq. (2.1) can take many forms as it depends on the definition of the problems. For example, an Entropy-based formulation can be used for isolated non-isothermal systems, while Gibbs free energy can be used when the system is isothermal with constant pressure. For systems with constant temperature and volume, Helmholtz free energy can be used to describe the free energy functional. Accordingly, the definition of the free energy functional and the phase-field variables can set the rule for the evolution equations of the phase-field model, which can be either one of four cases as follows (See Ref. [141]):

- **Cahn-Hilliard phase-field model** [155]:

This model can be used if the free energy of the system can be described in terms of the concentration field  $\mathbf{c}$ , where the temporal evolution is the time derivative of concentration. Here, the morphology can be obtained by solving the Cahn-Hilliard equation (See Ref. [61, 156]).

- **Allen-Cahn phase-field model** [157]:

Unlike the previous model, if the free energy of the system can be described in terms of the order parameter  $\phi$ , where the temporal evolution is the time derivative of the order parameter, i.e., the phase-field variable. In this case, the morphology can be obtained by solving Ginzburg-Landau or Allen-Cahn equation.

- **Wheeler, Boettinger, and McFadden (WBM) phase-field model** [158]:

In this model, the free energy is a function of both the concentration field  $\mathbf{c}$  and the order parameter field  $\phi$ . for a multi-phases system of  $\alpha$  and  $\beta$ , the free energies of the two phases are defined as  $f_\alpha(c)$  and  $f_\beta(c)$  with a single order parameter field  $\phi$  used to distinguish the two phases. A key feature of this model is that the model assumes that both phases  $\alpha$  and  $\beta$  have the same concentration at the same spatial point  $\mathbf{x}$  but different volume fractions. The temporal evolution is given as the solution of the Cahn-Hilliard and Allen-Cahn equations.



- **SG Kim, WT Kim, and Suzuki (KKS) phase-field model [159]:**

This model is a multi-phases model as the previous one, with the difference being that both phases  $\alpha$  and  $\beta$  have different concentrations at any spatial point  $\mathbf{x}=(x_1, x_2, x_3)$  within the computational domain, however, the concentration fields have the same chemical potential definition.

## 2.3 Single vesicle electrodynamics in the context of the phase-field method

In the following subsections, we present our mathematical model for a single vesicle subjected to a static electric field and the corresponding phase-field formulation. We start by defining the free energy functional that accounts for the mechanical and electric response of the vesicle membrane, from which we derive the phase-field formulation of the problem at hand.

### 2.3.1 Mathematical model

Based on the electromechanical model proposed in [18, 109] and [160], Helmholtz free energy of the lipid bilayer system consists of the elastic bending energy denoted henceforth  $\mathcal{E}_B$ , the flexoelectric energy  $\mathcal{E}_F$ , the dielectric energy which can be decomposed into two phase-based domains: of the membrane  $\mathcal{E}_{DM}$  and of the electrolyte  $\mathcal{E}_{DE}$ , and the energies associated with enforcing global area and volume constraints using a Lagrange multiplier method. The Lagrange multipliers are imposed on the system to maintain a constant volume and surface area and their physical interpretation is the osmotic pressure and the surface tension, respectively. The total energy functional is expressed as following [109]:

$$\mathcal{E} = \mathcal{E}_B + \mathcal{E}_F + \mathcal{E}_{DM} + \mathcal{E}_{DE} + \Delta p (\int_{\Omega} d\Omega - V_0) + \lambda (\oint d\Gamma - A_0) \quad (2.5)$$

with  $\mathcal{E}_B$ ,  $\mathcal{E}_F$ ,  $\mathcal{E}_{DM}$ , and  $\mathcal{E}_{DE}$  defined as following:

$$\mathcal{E}_B = \oint \frac{1}{2} \kappa (2H + H_{sp})^2 d\Gamma + \oint \kappa_G K d\Gamma \quad (2.6)$$

$$\mathcal{E}_F = - \oint \int_0^{d_m} \mathbf{P}^f \cdot \mathbf{E} dr d\Gamma \quad (2.7)$$

$$\mathcal{E}_{DM} = - \frac{1}{2} \oint \int_0^{d_m} \mathbf{D}^e \cdot \mathbf{E} dr d\Gamma \quad (2.8)$$

$$\mathcal{E}_{DE} = - \int \frac{1}{2} \varepsilon_r |\nabla \psi|^2 d\Omega \quad (2.9)$$

where  $d\Omega$  is the volume element of the bulk,  $d\Gamma$  is the area element of the surface,  $d_m$  the membrane thickness,  $\Delta p$  is the pressure difference,  $\lambda$  is the surface tension,  $\kappa$  is the bending rigidity,  $\kappa_G$  is Gaussian bending rigidity,  $H$  the mean curvature,  $H_{sp}$  is the spontaneous curvature,  $K$  is the Gaussian curvature,  $\mathbf{P}^f = -c_1(\nabla \cdot \mathbf{m}) \mathbf{m}$  is the bending-induced polarization,  $c_1$  is the flexoelectric constant,  $\mathbf{m}$  the unit normal vector of the membrane surface,  $\psi$  the electric potential,  $\mathbf{E}$  is the electric field intensity, and  $\mathbf{D}^e$  is the electric displacement [161], defined as  $\mathbf{D}^e = \varepsilon_m \mathbf{E} = \varepsilon_m (E_u \mathbf{Y}_{,u} + E_v \mathbf{Y}_{,v} + E_m \mathbf{m})$ , where  $\varepsilon_m$  is the dielectric constant of the vesicle. Here,  $\mathbf{Y}_{,u}$  and  $\mathbf{Y}_{,v}$  are tangential vectors of the surface that along with  $\mathbf{m}$  form an orthogonal coordinate system on the surface of the membrane. Considering a system where the vesicle is subjected to a static electrical field, then the electric potential is governed by the following linear elliptic PDE of second-order:

$$\nabla \cdot (\sigma \nabla \psi) = 0 \quad (2.10)$$

where the conductivity is defined as  $\sigma = \sigma_m$  on the membrane,  $\sigma = \sigma_i$  in the electrolyte inside the membrane, and  $\sigma = \sigma_o$  in the electrolyte outside the membrane.

By taking the first variation of Eq. (2.6) and using integration by parts, the following shape equation emerges:

$$\Delta \left[ 2\kappa H + \kappa H_{sp} - c_1 \int_0^{d_m} E_m dr \right] + f = 0 \quad (2.11)$$

where the last term on the left-hand side  $f$  is defined as:

$$\begin{aligned} f = & \kappa(2H + H_{sp})(2H^2 - H_{sp}H - 2K) + \Delta p \\ & - 2\lambda H + H \int_0^{d_m} \varepsilon_m [E_m^2 + g_{uu} E_u^2 + g_{vv} E_v^2] dr \\ & + 2c_1 K \int_0^{d_m} E_m dr + \varepsilon_i (E_i^2 - \frac{1}{2} \mathbf{E}_i \cdot \mathbf{E}_i) - \varepsilon_o (E_o^2 - \frac{1}{2} \mathbf{E}_o \cdot \mathbf{E}_o) \end{aligned} \quad (2.12)$$

The operator  $\Delta = \nabla^2 = \nabla \cdot \nabla$  is the Laplace operator,  $\varepsilon_i$  and  $\varepsilon_o$  are the dielectric constants of the inner and outer electrolytes,  $\mathbf{E}_i$  and  $\mathbf{E}_o$  are the electric field intensities in the inner and outer electrolytes,  $E_i = \mathbf{E}_i \cdot \mathbf{m}$ ,  $E_o = \mathbf{E}_o \cdot \mathbf{m}$ ,  $\int_0^{d_m} E_m dr = \psi_{in} - \psi_{out}$  being the trans-membrane voltage drop in the  $\mathbf{m}$  direction and  $g_{uu}, g_{vv}$  are surface metrics defined as  $\mathbf{Y}_{,u} \cdot \mathbf{Y}_{,u}$  and  $\mathbf{Y}_{,v} \cdot \mathbf{Y}_{,v}$ , respectively.

### 2.3.2 Phase-Field formulation

Next, we review the phase field model for the above electromechanical model of vesicles as proposed in [18]. The phase-field approximation of the energy functional in Eq. (2.5) is obtained by introducing an auxiliary phase field variable  $\phi$  taking constant values in each of the phases and experiencing rapid but smooth transition across the interfacial region. We are defining the profile of the phase field variable by the hyperbolic tangent function such that:  $\phi(\mathbf{x}) = \tanh(\frac{d(\mathbf{x})}{\sqrt{2}\epsilon})$  with  $d(\mathbf{x})$  being a signed distance function between a point in the computational domain and the surface of the vesicle. Values of  $\phi(\mathbf{x})$  range between -1 and 1 with  $\phi(\mathbf{x}) > 0$  represents the electrolyte domain outside the vesicle,  $\phi(\mathbf{x}) < 0$  represents electrolyte domain inside the vesicle and  $\phi(\mathbf{x}) = 0$  represents the surface of the vesicle.

Following the ideas in Wang work [162], the following expressions after some arrangement emerge:

$$\mathbf{m} = \nabla d(\mathbf{x}) = \frac{\sqrt{2}\epsilon}{1-\phi^2} \nabla \phi \quad (2.13a)$$

$$\nabla d(\mathbf{x}) \cdot \nabla d(\mathbf{x}) = \mathbf{m} \cdot \mathbf{m} = 1 \quad (2.13b)$$

$$\nabla \cdot \mathbf{m} = \Delta d(\mathbf{x}) = \frac{\sqrt{2}\epsilon}{1-\phi^2} [\Delta \phi + \frac{\phi}{\epsilon^2} (1-\phi^2)] \quad (2.13c)$$

$$H = -\frac{1}{2} \nabla \cdot \mathbf{m} = \frac{-\sqrt{2}\epsilon}{2(1-\phi^2)} [\Delta \phi + \frac{\phi}{\epsilon^2} (1-\phi^2)] \quad (2.13d)$$

$$\lim_{\epsilon \rightarrow 0} \frac{1}{\epsilon} \int_{\Omega} p(\frac{d(x)}{\epsilon}) f(x) dx = \int_{-\infty}^{\infty} p(t) dt \int_{\Gamma} f(s) ds \quad (2.13e)$$

$$\int_{-\infty}^{\infty} [1 - \tanh^2(\frac{x}{\sqrt{2}\epsilon})]^2 dx = \frac{4}{3} \sqrt{2}\epsilon \quad (2.13f)$$

Using Eqs. (2.13), we can transform all the surface integrals in Eqs. (2.6-2.8) into volume integrals and reformulate all the energies in terms of the phase field variable. The energies of the system recasted in phase field variable are as follows:

#### 1. Bending Energy

For surfaces of constant topology, the second integral in the curvature energy is a constant, and for this reason, it is often ignored [101]. The bending energy in terms

of phase field variable is:

$$\begin{aligned}\mathcal{E}_B &= \int_{\Gamma} \frac{1}{2} \kappa [2H + H_{sp}]^2 d\Gamma \approx \left( \int_{\Gamma} \frac{1}{2} \kappa [2H + H_{sp}]^2 d\Gamma \right) \left( \frac{3}{4\sqrt{2}\varepsilon} \int_{-\infty}^{\infty} [1 - \phi^2]^2 dx \right) \\ E_B(\phi) &= \frac{3\kappa}{4\sqrt{2}\varepsilon} \int_{\Omega} \left[ \varepsilon \Delta \phi + \left( \frac{\phi}{\varepsilon} - \frac{H_{sp}}{\sqrt{2}} \right) (1 - \phi^2) \right]^2 d\Omega\end{aligned}\tag{2.14}$$

## 2. Flexoelectric Energy

Assuming a constant membrane thickness  $d_m$ , and since the bending-induced polarization  $\mathbf{P}^f = -c_1 (\nabla \cdot \mathbf{m}) \mathbf{m}$ , the flexoelectric energy in terms of phase field variable is:

$$\begin{aligned}\mathcal{E}_F &= - \int_{\Gamma} \int_0^{d_m} \mathbf{P}^f \cdot \mathbf{E} dr d\Gamma = -2c_1 d_m \int_{\Gamma} H \mathbf{E} \cdot \mathbf{m} d\Gamma \\ &\approx (-2c_1 d_m \int_{\Gamma} H \mathbf{E} \cdot \mathbf{m} d\Gamma) \left( \frac{3}{4\sqrt{2}\varepsilon} \int_{-\infty}^{\infty} [1 - \phi^2]^2 dx \right) \\ E_F(\phi) &= -\frac{3c_1 d_m}{2\sqrt{2}} \int_{\Omega} \left[ \varepsilon \Delta \phi + \frac{\phi}{\varepsilon} (1 - \phi^2) \right] \nabla \phi \cdot \nabla \psi d\Omega\end{aligned}\tag{2.15}$$

## 3. Dielectric Energies of Membrane and Electrolyte

$$\begin{aligned}\mathcal{E}_{DM} &= -\frac{1}{2} \int_{\Gamma} \int_0^{d_m} \mathbf{D}^e \cdot \mathbf{E} dr = -\frac{d_m \varepsilon_m}{2} \int_{\Gamma} |\nabla \psi|^2 d\Gamma \\ &\approx \left( -\frac{d_m \varepsilon_m}{2} \int_{\Gamma} |\nabla \psi|^2 d\Gamma \right) \left( \frac{3}{4\sqrt{2}\varepsilon} \int_{-\infty}^{\infty} [1 - \phi^2]^2 dx \right) \\ E_{DM}(\phi) &= -\frac{3d_m \varepsilon_m}{8\sqrt{2}\varepsilon} \int_{\Omega} (1 - \phi^2)^2 |\nabla \psi|^2 d\Omega\end{aligned}\tag{2.16}$$

$$\begin{aligned}E_{DE}(\phi) &= \frac{-1}{2} \int_{\Omega} \varepsilon_r(\phi) |\nabla \psi|^2 d\Omega \\ \varepsilon(\phi) &= \frac{\varepsilon_{in}}{2} (1 - \phi) + \frac{\varepsilon_{out}}{2} (1 + \phi)\end{aligned}\tag{2.17}$$

## 4. Surface Area and Volume

$$\begin{aligned}A(\phi) &= \frac{3}{2\sqrt{2}} \int_{\Omega} \left( \frac{\varepsilon}{2} |\nabla \phi|^2 + \frac{1}{4\varepsilon} (\phi^2 - 1)^2 \right) d\Omega \\ V(\phi) &= \int_{\Omega} \frac{1}{2} (1 - \phi) d\Omega\end{aligned}\tag{2.18}$$

A full version of the aforementioned formulation can be found in Appendix A. Under a static electric field, the equation governing the electric potential recasted in terms of the phase field variable is given as

$$\nabla \cdot (\sigma_{\phi} \nabla \psi) = 0\tag{2.19}$$

where  $\sigma_\phi$  is the conductivity expressed in terms of the phase field variable. Due to Ion impermeability of the biomembrane, charges tend to pile up on both sides of the membrane which make it resemble a capacitor, leading to a discontinuity of the electrical potential across the membrane [91]. In addition, the scalar value of the conductivity  $\sigma_\phi$  across a line profile in the domain passes through the axis of the vesicle, i.e., normal to the vesicle surface, shows that it experiences a discontinuity, characterized by a value jump at the vesicle-electrolyte interface due to the order of magnitude difference between the conductivity values for membrane and electrolyte. Hence, an interpolating function [18] that smooths out this discontinuity and can accurately represent the conductivity in the intra- and extracellular domains, is as follows

$$\sigma_\phi = \frac{\sigma_i}{4}(1-\phi)^2\phi^8 + \frac{\sigma_m}{4}(1-\phi)^2(1+\phi)^2 + \frac{\sigma_o}{4}(1+\phi)^2\phi^8 \quad (2.20)$$

The constrained optimization problem of the system is written as follows:

$$\min_{\phi} E(\phi) = E_B(\phi) + E_F(\phi) + E_{DM}(\phi) + E_{DE}(\phi) \quad (2.21)$$

subjected to  $V(\phi) \approx \alpha_0$  to preserve the initial volume and  $A(\phi) \approx \beta_0$  to preserve the initial surface area. Several constrained optimization solving algorithms have been considered. Among the most known is the penalty method. After intensive testing, we conclude that the penalty method is not suitable for the given problem as the penalization coefficients need to be very large to penalize the violations in the constraints, which leads inevitably to a very stiff system, preventing any evolution of the phase field variable in time. Alternatively, the Lagrange multiplier approach can be used to evaluate the time-dependent multipliers. However, as shown in [163], the time step size must be taken very small to maintain numerical stability and convergence.

Wang *et al.* [21] built on the traditional augmented Lagrange multiplier approach and developed a modified augmented Lagrange multiplier algorithm to repeatedly solve the unconstrained objective energy functional while maintaining numerical stability and relatively large time step size, ranging from  $10^{-4}$  to  $10^{-2}$  where the steady state is reached at about  $t = 10$ . The proposed algorithm was tested for the constrained phase field Willmore problem. We are borrowing the idea and implementing it for the phase field model of electromechanics of vesicles.

The ALM version of the unconstrained objective functional in Eq. (2.21) reads as follows:

$$\begin{aligned} \min_{\phi} E_{tot}(\phi) &= E(\phi) + \frac{1}{2}M_1(V(\phi) - \alpha_0)^2 + \frac{1}{2}M_2(A(\phi) - \beta_0)^2 \\ &+ \lambda_1(V(\phi) - \alpha_0) + \lambda_2(A(\phi) - \beta_0) \end{aligned} \quad (2.22)$$

This way, the penalty parameters can be taken as constants with relatively small values over the run time. The time-dependent Lagrange multipliers  $\lambda_1$  and  $\lambda_2$  are updated after each iteration as following:

$$\begin{aligned} \lambda_1 &\leftarrow \lambda_1 + M_1(V(\phi) - \alpha_0) \\ \lambda_2 &\leftarrow \lambda_2 + M_2(A(\phi) - \beta_0) \end{aligned} \quad (2.23)$$

and the gradient flow characterizing the evolution of the phase field in Eq. (2.22) is as the following:

$$\begin{aligned} \frac{\partial \phi}{\partial t} + \frac{\delta E_{tot}(\phi)}{\delta \phi} &= 0 \\ \frac{\partial \phi}{\partial t} + \frac{\delta E(\phi)}{\delta \phi} + M_1(V(\phi) - \alpha_0 + \lambda_1(t)) \frac{\delta V(\phi)}{\delta \phi} + M_2(A(\phi) - \beta_0 + \lambda_2(t)) \frac{\delta A(\phi)}{\delta \phi} &= 0 \end{aligned} \quad (2.24)$$

where the variational derivatives are obtained by taking the first variation of the functionals, performing integration by parts and dropping the boundary integrals by assuming zero-flux boundary conditions on the phase field and electric potential. Doing these steps results in:

$$\begin{aligned} \delta E(\phi) &= \int_{\Omega} \left[ \frac{3\kappa}{2\sqrt{2}\epsilon} (\epsilon \Delta \phi + (\frac{\phi}{\epsilon} - \frac{H_{sp}}{\sqrt{2}})(1 - \phi^2)) (\frac{1 - 3\phi^2}{\epsilon} + \sqrt{2}H_{sp}\phi) \right] \delta \phi \, d\Omega \\ &+ \int_{\Omega} \left[ \frac{3\kappa}{2\sqrt{2}} \Delta (\epsilon \Delta \phi + (\frac{\phi}{\epsilon} - \frac{H_{sp}}{\sqrt{2}})(1 - \phi^2)) \right] \delta \phi \, d\Omega \\ &+ \int_{\Omega} \left[ \frac{-3c_1 d_m}{2\sqrt{2}} \left( (\frac{1 - 3\phi^2}{\epsilon}) \nabla \phi \cdot \nabla \psi - \nabla \cdot \left( (\epsilon \Delta \phi + \frac{\phi}{\epsilon}(1 - \phi^2)) \nabla \psi \right) + \Delta (\epsilon \nabla \phi \cdot \nabla \psi) \right) \right] \delta \phi \, d\Omega \\ &+ \int_{\Omega} \left[ \frac{3d_m}{2\sqrt{2}\epsilon} \epsilon_m (\phi - \phi^3) |\nabla \psi|^2 \right] \delta \phi \, d\Omega + \int_{\Omega} \left[ \frac{1}{4} (\epsilon_{in} - \epsilon_{out}) |\nabla \psi|^2 \right] \delta \phi \, d\Omega \end{aligned} \quad (2.25)$$

$$\delta V(\phi) = \int_{\Omega} \left[ -\frac{1}{2} \right] \delta \phi \, d\Omega \quad (2.26)$$

$$\begin{aligned} \delta A(\phi) &= \int_{\Omega} \frac{3}{2\sqrt{2}} (\epsilon \nabla \phi \cdot \nabla \delta \phi + \frac{1}{\epsilon} (\phi^2 - 1) \phi \delta \phi) \, d\Omega \\ &= \int_{\Omega} \left[ \frac{3\epsilon}{2\sqrt{2}} (-\Delta \phi + \frac{1}{\epsilon^2} (\phi^3 - \phi)) \right] \delta \phi \, d\Omega \end{aligned} \quad (2.27)$$

By the fundamental lemma of variational calculus,  $\delta\phi(\mathbf{x})$  is an arbitrary continuous function for all  $\mathbf{x} \in \Omega$ , then it follows that the functional derivatives of the energy contributions in the aforementioned equations are the terms inside the brackets. Finally, we can write the functional derivative of the total energy as the following:

$$\begin{aligned} \frac{\delta E_{tot}(\phi)}{\delta\phi} = & \frac{3\kappa}{2\sqrt{2}\varepsilon} \left( \varepsilon\Delta\phi + \left( \frac{\phi}{\varepsilon} - \frac{H_{sp}}{\sqrt{2}} \right) (1 - \phi^2) \right) \left( \frac{1 - 3\phi^2}{\varepsilon} + \sqrt{2}H_{sp}\phi \right) + \frac{3\kappa}{2\sqrt{2}} \Delta \left( \varepsilon\Delta\phi + \left( \frac{\phi}{\varepsilon} - \frac{H_{sp}}{\sqrt{2}} \right) (1 - \phi^2) \right) \\ & - \frac{3c_1 d_m}{2\sqrt{2}} \left( -\varepsilon\Delta\phi\Delta\psi - \left( \frac{\phi - \phi^3}{\varepsilon} \right) \Delta\psi + 2\varepsilon\nabla\nabla\phi : \nabla\nabla\psi + \varepsilon\nabla\phi \cdot \nabla(\Delta\psi) \right) \\ & + \frac{3d_m}{2\sqrt{2}\varepsilon} \varepsilon_m (\phi - \phi^3) |\nabla\psi|^2 + \frac{1}{4} (\varepsilon_{in} - \varepsilon_{out}) |\nabla\psi|^2 \\ & - \frac{M_1}{2} (V(\phi) - \bar{\alpha}(t)) + \frac{3\varepsilon M_2}{2\sqrt{2}} (A(\phi) - \bar{\beta}(t)) \left( -\Delta\phi + \frac{1}{\varepsilon^2} (\phi^3 - \phi) \right) \end{aligned} \quad (2.28)$$

where  $\bar{\alpha}(t) = \alpha_0 - \lambda_1(t)$  and  $\bar{\beta}(t) = \beta_0 - \lambda_2(t)$ . Here,  $\nabla\nabla\phi$  and  $\nabla\nabla\psi$  are second-order tensors of the second-order partial derivatives of the phase field and electric potential, respectively, which their components are expressed as following

$$\begin{pmatrix} \phi_{,xx} & \phi_{,xy} & \phi_{,xz} \\ \phi_{,yx} & \phi_{,yy} & \phi_{,yz} \\ \phi_{,zx} & \phi_{,zy} & \phi_{,zz} \end{pmatrix} \text{ and } \begin{pmatrix} \psi_{,xx} & \psi_{,xy} & \psi_{,xz} \\ \psi_{,yx} & \psi_{,yy} & \psi_{,yz} \\ \psi_{,zx} & \psi_{,zy} & \psi_{,zz} \end{pmatrix}$$

and  $(:)$  denotes the double contraction of the two tensors defined as  $\mathbf{A} : \mathbf{B} = \sum_{i,j=1}^3 A_{ij} B_{ij}$ .

## 2.4 Vesicle doublet hydrodynamics in the context of the phase-field method

The mathematical model for vesicle doublet suspended in an external viscous fluid flow and the corresponding phase-field formulation are presented in the following two subsections. The bending energy and energies associated with enforcing the global volume and area are considered. The vesicle's local inextensibility condition is ensured by introducing an additional constraint equation to the system. A phase-field-based interaction energy definition is also considered to maintain a short-range repulsion between the vesicles. The fluid flow is modeled using the incompressible Navier-Stokes equations and the vesicle evolution in time is modeled using two advection equations describing the process of advecting each vesicle by the fluid flow. To overcome the velocity-pressure saddle point

system, we apply the Residual-Based Variational MultiScale (RBVMS) method to the Navier-Stokes equations and solve the coupled systems using isogeometric analysis.

### 2.4.1 Mathematical model

The mathematical model of a system consist of an inextensible vesicle doublet suspended in an incompressible fluid flow is given by the sharp interface model. The mathematical model consists of two transport equations with the purpose of describing how a scalar field, which in this case is the phase-field variable  $\phi$ , is transported through space and evolves through time with the appropriate boundary conditions. In addition to this, the Navier-Stokes equations are considered to study the motion of the viscous fluid flow. Following the work of Valizadeh *et. al.* [43], and considering the sharp interface model presented in Laadhari *et. al* [164], we can formulate the mathematical model as following: Let  $\Omega \in \mathbb{R}^d$ , where  $d = 2,3$ , denote the computational domain dimensionality in which the system of the vesicle doublet is suspended. The vesicle doublet is suspended in an incompressible flow. The vesicle intracellular domain and membrane are denoted by  $\Lambda_i$  and  $\partial\Lambda_i$ , respectively, where  $i = 1,2$ , corresponding to the first and second vesicles. The outward normal vector to the surface of the vesicle is denoted by  $\mathbf{n}_i$ , while the outward normal vector to the computational domain is denoted by  $\mathbf{m}$  [See Fig. 2.2]. Let  $\mathbf{u}$  denote the velocity profile defined on the boundary, and  $\phi_i$  denote the level-set function which represents the spatial location of the interface and let  $p$  denote the pressure, and let  $\lambda_i$  to be the Lagrange multiplier mimicking the surface tension of each vesicle. The strong form of the problem in the context of the sharp-interface model becomes:

Find  $\mathbf{u}$ ,  $p$ ,  $\phi_1, \phi_2$ ,  $\lambda_1$ , and  $\lambda_2$  such that:

$$\frac{\partial \phi_1}{\partial t} + \mathbf{u} \cdot \nabla \phi_1 = 0, \quad \text{in } \Omega \times (0, T), \quad (2.29)$$

$$\frac{\partial \phi_2}{\partial t} + \mathbf{u} \cdot \nabla \phi_2 = 0, \quad \text{in } \Omega \times (0, T), \quad (2.30)$$

$$\frac{\partial \mathbf{u}}{\partial t} + \mathbf{u} \cdot \nabla \mathbf{u} + \nabla p - \frac{1}{Re} \nabla \cdot (2\mu \mathbf{D}(\mathbf{u})) = 0, \quad \text{in } (\Omega \setminus (\partial\Lambda_1 \cup \Lambda_2)) \times (0, T), \quad (2.31)$$

$$\nabla \cdot \mathbf{u} = 0, \quad \text{in } \Omega \times (0, T), \quad (2.32)$$

$$\nabla_s \cdot \mathbf{u} = 0, \quad \text{on } \partial\Lambda_1 \times (0, T), \quad (2.33)$$

$$\nabla_s \cdot \mathbf{u} = 0, \quad \text{on } \partial\Lambda_2 \times (0, T), \quad (2.34)$$

$$[[\mathbf{u}]] = 0, \quad \text{on } \partial\Lambda_1 \times (0, T), \quad (2.35)$$



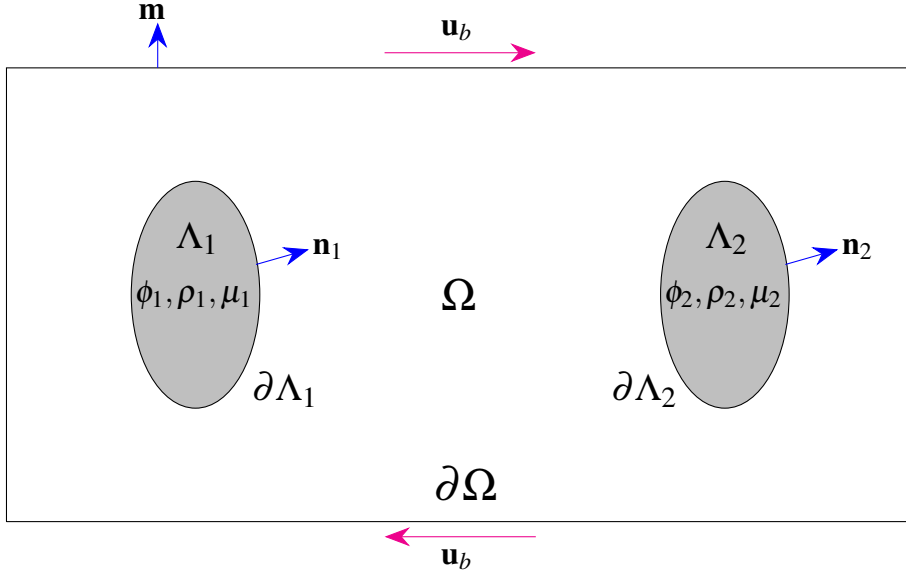


Figure 2.2: A schematic diagram shows the system of vesicle doublet suspension.

$$[[\mathbf{u}]] = 0, \quad \text{on } \partial\Lambda_2 \times (0, T), \quad (2.36)$$

$$- \kappa_1 \left( \Delta_s H_1 + H_1 \left( \frac{H_1^2}{2} - 2K_1 \right) \right) \mathbf{n}_1 \quad (2.37)$$

$$+ H_1 \lambda_1 \mathbf{n}_1 - \nabla_s \lambda_1 + [[2\mu^* \mathbf{D}(\mathbf{u}) - p\mathbf{I}]] \cdot \mathbf{n}_1 = 0 \quad \text{on } \partial\Lambda_1 \times (0, T)$$

$$- \kappa_2 \left( \Delta_s H_2 + H_2 \left( \frac{H_2^2}{2} - 2K_2 \right) \right) \mathbf{n}_2 \quad (2.38)$$

$$+ H_2 \lambda_1 \mathbf{n}_2 - \nabla_s \lambda_2 + [[2\mu^* \mathbf{D}(\mathbf{u}) - p\mathbf{I}]] \cdot \mathbf{n}_2 = 0 \quad \text{on } \partial\Lambda_2 \times (0, T)$$

$$\phi_1 = \phi_2 = \phi_n, \quad \text{on } \partial\Omega_- \times (0, T) \quad (2.39)$$

$$\mathbf{u} = \mathbf{u}_b, \quad \text{on } \partial\Omega_D \times (0, T) \quad (2.40)$$

$$(2\mu \mathbf{D}(\mathbf{u}) - p\mathbf{I}) \cdot \mathbf{m} = 0, \quad \text{on } \partial\Omega_N \times (0, T) \quad (2.41)$$

$$\phi_1(0) = \phi_2(0) = \phi_0, \quad \text{in } \Omega \times (0, T) \quad (2.42)$$

$$\mathbf{u}(0) = \mathbf{u}_0, \quad \text{in } \Omega \times (0, T) \quad (2.43)$$

## 2.4.2 Phase-Field formulation

To attain thermodynamic consistency, the first law of thermodynamics must be satisfied. That is, a global mass conservation, i.e.,  $\frac{d}{dt} \int_{\partial\Lambda_i} \mathbf{u} \, dA = 0$ , and negative energy dissipation, i.e.,  $\frac{d}{dt} E[\Lambda_i, \mathbf{u}] \leq 0$  for an advecting system. The interface of the vesicle doublet  $\partial\Lambda_i$  is the zero level set of the phase-field function  $\phi$  defined by the tangent hyperbolic function such that  $\phi(\mathbf{x}, t) = \tanh \frac{-d(\mathbf{x}, t)}{\sqrt{2\varepsilon}}$ , with  $d(\mathbf{x}, t)$  being a signed distance function to the membrane interface and  $\varepsilon$  being a regularization parameter. By choosing  $d(\mathbf{x}, t)$  to be negative inside the membrane and positive outside, we render  $\phi \approx 1$  inside and  $\phi \approx -1$  outside.

Stemming from this definition the outward normal vector to the membrane  $\mathbf{n} = -\frac{\nabla\phi}{|\nabla\phi|}$  and the total curvature  $\mathbf{H} = \nabla \cdot \mathbf{n}$ .

To this extent, and based on the phase-field model for vesicle hydrodynamics proposed by Du et al. [165, 166] that accounts for global volume and surface area, and by including the inextensibility constraint proposed by Aland et. al [119] and the interaction energy defined as in Marth et. al [120] work, and considering two advection-diffusion equations describing the time evolution of vesicle doublet in a viscous fluid flow with inertial forces, the evolution equation of the phase-field variables  $\phi_i$  for  $i = 1, 2$  is written as follows:

$$\frac{\partial \phi_i}{\partial t} + \mathbf{u} \cdot \nabla \phi_i = -\eta_\phi (g_i - \lambda_{g(i)} f_i - \lambda_{v(i)} + \zeta_i) \quad (2.44)$$

where  $\mathbf{u}$  is the velocity vector. Both  $g_i$  and  $f_i$  are defined as following:

$$g_i = (1/(Re Ca))[\Delta f_i - (1/\varepsilon^2)(3\phi_i^2 - 1)f_i],$$

$$f_i = \varepsilon \Delta \phi_i - (1/\varepsilon)(\phi_i^2 - 1)\phi_i.$$

$\lambda_{g(i)}$  and  $\lambda_{v(i)}$  are spatially constant Lagrange multipliers to enforce the conservation of the total surface area and total volume, respectively. The dimensionless chemical potentials  $\zeta_i$  being defined as the variational derivative of the interaction energy  $\mathcal{E}(\phi_i)$  w.r.t the phase-field variable  $\phi_i$  is defined as:

$$\zeta_i = \frac{\delta \mathcal{E}(\phi_i)}{\delta \phi_i} \quad (2.45)$$

while the interaction energy of the vesicles is the overall sum of the interaction energy associated with each vesicle individually, and defined in the context of the phase-field model as follows:

$$\mathcal{E}_i(\phi_1, \dots, \phi_n) = \frac{1}{Re \mathcal{JN}} \int_{\Omega} B(\phi_i) \sum_{\substack{j=1 \\ j \neq i}}^n w_j d\Omega \quad (2.46)$$

with  $B(\phi_i) = (1/\varepsilon)(\phi_i^2 - 1)^2$  and  $\mathcal{JN}$  being a dimensionless interaction number defined as:  $(4\sqrt{2}/3)(v_0 U/\alpha)$ , where  $\alpha$  is the interaction parameter determining the strength of the repulsive interaction between the two vesicles,  $v_0$  is the fluid dynamic viscosity and  $U$  is the characteristic velocity. The variational derivative of the non-dimensional interaction energy is as follows:

$$\frac{\delta \mathcal{E}_{int}(\phi_i, \dots, \phi_n)}{\delta \phi_i} = \frac{1}{Re \mathcal{JN}} \left( \frac{4\phi_i}{\varepsilon} (\phi_i^2 - 1) \sum_{\substack{j=1 \\ j \neq i}}^n w_j + w'_i \sum_{\substack{j=1 \\ j \neq i}}^n \frac{1}{\varepsilon} (\phi_i^2 - 1)^2 \right) \quad (2.47)$$

Where the short-range interaction function  $w_j$  is:

$$w_j = \begin{cases} \exp\left(-\frac{1}{2}\left(\ln \frac{1+\phi_j}{1-\phi_j}\right)^2\right) & \text{if } |\phi_j(\mathbf{x})| < 1 \\ 0 & \text{otherwise} \end{cases} \quad (2.48)$$

and its derivative w.r.t. the phase field variable is:

$$w_j' = \begin{cases} \frac{2 \exp(\frac{-1}{2} (\ln \frac{1+\phi_j}{1-\phi_j})^2) \ln \frac{1+\phi_j}{1-\phi_j}}{\phi_j^2 - 1} & \text{if } |\phi_j(\mathbf{x})| < 1 \\ 0 & \text{otherwise} \end{cases} \quad (2.49)$$

The evolution equation (2.44) of the first vesicle has two cases depending on  $\phi_1$  and  $\phi_2$ , and reads as following:

$$\frac{\partial \phi_1}{\partial t} + \mathbf{u} \cdot \nabla \phi_1 = -\eta_\phi (g_1 - \lambda_{g1} f_1 - \lambda_{v1} + \zeta_1) \quad (2.50)$$

However, only when the vesicles are in close proximity, the interaction terms comes into effect. Otherwise, when  $|\phi_1(\mathbf{x})| \geq 1$  and/or  $|\phi_2(\mathbf{x})| \geq 1$ , the term completely drops, and the evolution equation reduces to

$$\frac{\partial \phi_1}{\partial t} + \mathbf{u} \cdot \nabla \phi_1 = -\eta_\phi (g_1 - \lambda_{g1} f_1 - \lambda_{v1}) \quad (2.51)$$

The second evolution equation of the second vesicle follows the same principle and reads as follows:

$$\frac{\partial \phi_2}{\partial t} + \mathbf{u} \cdot \nabla \phi_2 = -\eta_\phi (g_2 - \lambda_{g2} f_2 - \lambda_{v2} + \zeta_2) \quad (2.52)$$

and reduces to an evolution equation without the interaction term when the vesicles are apart away as follows:

$$\frac{\partial \phi_2}{\partial t} + \mathbf{u} \cdot \nabla \phi_2 = -\eta_\phi (g_2 - \lambda_{g2} f_2 - \lambda_{v2}) \quad (2.53)$$

Where  $\zeta_1$  and  $\zeta_2$  are defined as following:

$$\zeta_1 = \frac{1}{Re \mathcal{JN}} \left[ \frac{4\phi_1}{\varepsilon} (\phi_1^2 - 1) \exp\left(-\frac{1}{2} \left(\ln \frac{1+\phi_2}{1-\phi_2}\right)^2\right) + \frac{2 \exp(\frac{-1}{2} (\ln \frac{1+\phi_1}{1-\phi_1})^2) \ln \frac{1+\phi_1}{1-\phi_1}}{\phi_1^2 - 1} \left(\frac{1}{\varepsilon} (\phi_2^2 - 1)^2\right) \right] \quad (2.54)$$

$$\zeta_2 = \frac{1}{Re \mathcal{JN}} \left[ \frac{4\phi_2}{\varepsilon} (\phi_2^2 - 1) \exp\left(-\frac{1}{2} \left(\ln \frac{1+\phi_1}{1-\phi_1}\right)^2\right) + \frac{2 \exp(\frac{-1}{2} (\ln \frac{1+\phi_2}{1-\phi_2})^2) \ln \frac{1+\phi_2}{1-\phi_2}}{\phi_2^2 - 1} \left(\frac{1}{\varepsilon} (\phi_1^2 - 1)^2\right) \right] \quad (2.55)$$

The non-dimensional Navier-Stokes equation reads:

$$\frac{\partial \mathbf{u}}{\partial t} + \mathbf{u} \cdot \nabla \mathbf{u} + \nabla p - \frac{1}{Re} \nabla \cdot (2\mu^* \mathbf{D}(\mathbf{u})) = \sum_{i=1}^n \phi_i^\# \nabla \phi_i \quad (2.56)$$

with  $\mu^*$  is the dynamic viscosity and expressed as a function of the phase-field variable  $\mu^*(\phi)$  and calculated based on a normalized value of the unified phase-field  $\phi = \phi_1 + \phi_2 + 1$  such that  $\mu^*(\phi) = 0.5(1 + \phi)\beta + 0.5(1 - \phi)$ , where  $\beta$  is the viscosity ratio between the intracellular  $\mu_i$  and the extracellular fluids  $\mu_o$ .  $\mathbf{D}(\mathbf{u})$  is strain rate tensor that describes the rate of stretching and shearing and defined as  $(1/2)(\nabla \mathbf{u} + \nabla^T \mathbf{u})$ . The right-hand side

is defined as follows:

$$\begin{aligned} \sum_{i=1}^n \phi_i^\sharp \nabla \phi_i &= \nabla \cdot (\delta_{\varepsilon_1} \mathbf{P} \lambda_1) + (g_1 - \lambda_{g1} f_1 - \lambda_{v1} + \zeta_1) \nabla \phi_1 + \\ &+ \nabla \cdot (\delta_{\varepsilon_2} \mathbf{P} \lambda_2) + (g_2 - \lambda_{g2} f_2 - \lambda_{v2} + \zeta_2) \nabla \phi_2 \end{aligned} \quad (2.57)$$

where  $\mathbf{P}$  is the tangential projection operator and  $\delta_\varepsilon$  is the diffusive interface approximation of the surface delta function.



# 3

## Isogeometric Analysis

### 3.1 Introduction

The IsoGeometric Analysis (IGA) was first theorized by Hughes, Cottrell, and Bazilevs [22] back in 2005 with the aim of bridging the gap between the Computer-Aided Design (CAD) part of any simulation process and the analysis part, especially when the method in use is the Finite Element Method (FEM). In the industrial world, CAD systems are the most used technologies to generate geometries using Non-Uniform Rational B-splines (NURBS), subdivision surfaces, T-splines, and other techniques, to be later used in the analysis, whether in static structural, dynamic, hydrodynamic, mechanical, thermal or other types of analysis. In doing so, some features of the CAD-based geometries would be lost upon transferring those models to Computer-Aided Engineering (CAE) software as a result of the reparametrization process due to the use of linear Lagrange polynomials used in FEM to approximate the geometry. The reparametrization process is labor-cost intensive and leads to poor and unsatisfactory results analysis-wise. This is where the

IGA comes to address. Instead of using different basis functions to describe the geometry and approximate the solution, IGA unifies the design-analysis process by using the same basis functions used in the geometrical description of the model to also approximate the solution. Building on this idea, the B-splines and NURBS were used to construct the geometry of the model as well as approximating the solution of the PDEs in the weak form within the context of the Galerkin method. NURBS major advantages come from their ability to generate an *exact* replica of the CAD geometry, whereas the finite element mesh is merely an approximation of the CAD geometry. Therefore, NURBS-based geometry can be used to represent exact circles, spheres, ellipsoids, and many other geometrical shapes. In addition to that, the NURBS possess the ability to be k-refined, a property unique to NURBS over the classical Lagrange polynomials used in FEM. The k-refinement is the order elevation procedure carried out using two steps; order elevation of the original knot vector, then knot insertion. Unlike the hp-refinement, the k-refinement is limited to NURBS-based FEM, i.e., IGA, and does not have an analog in the standard FEM [23].

## 3.2 B-splines basis functions

In the world of Computer-Aided Design (CAD), the NURBS are the industry standards in geometry generation. NURBS are an extended version of B-splines. A B-spline is a piecewise polynomial function, in which the pieces constructing the curve are joint together at spatial points called knots. Let  $\Xi = \{\xi_0, \xi_1, \xi_2, \dots, \xi_m, \}$  be a one dimensional knot vector, consisting of  $m+1$  nondecreasing set of real numbers, i.e.,  $\xi_i \leq \xi_{i+1}$ , where each  $\xi_i \in \mathbb{R}$ , and  $i = 1, 2, \dots, m-1$ , then the  $i^{th}$  B-spline basis function with a polynomial order  $p$ , denoted by  $N_{i,p}(\xi)$  is defined recursively using the Cox-de-Boor [167, 168] formula as following:

$$p = 0$$

$$N_{i,0}(\xi) = \begin{cases} 1, & \xi_i \leq \xi < \xi_{i+1} \\ 0, & \text{otherwise} \end{cases} \quad (3.1)$$

and for  $p \geq 1$

$$N_{i,p}(\xi) = \frac{\xi - \xi_i}{\xi_{i+p} - \xi_i} N_{i,p-1}(\xi) + \frac{\xi_{i+p+1} - \xi}{\xi_{i+p+1} - \xi_{i+1}} N_{i+1,p-1}(\xi) \quad (3.2)$$

The knot vector  $\Xi$  can be *uniform* if all knots are equally spaced in the parametric space, or non-uniform otherwise. In addition to this, the knot vector can be open if the first and last entities are  $p+1$  repeated. From Eqs. (3.1-3.2), we can see that zeroth order of any basis function is a step function, whereas, for the first order onward, the basis function for any knot is a linear combination of two  $(p-1)$ -degree basis functions. In addition to this, the  $i^{\text{th}}$ -knot span defined as the open interval  $[\xi_i, \xi_{i+1})$  can have a zero-length due to knot multiplicity. The B-splines basis functions have a set of properties that control the geometric characteristics of curves and surfaces, such as:

- Any basis function has a local support property, in that,  $N_{i,p}(\xi) = 0$  if  $\xi$  is outside the open interval  $[\xi_i, \xi_{i+p+1})$ . An example of this can be seen in Fig. (3.1), where  $N_{4,2}$  is only defined on the interval  $[\xi_4, \xi_7)$  spanning from  $[0.5, 1)$  in the knot vector,
- There are only  $p+1$  nonzero basis functions  $N_{i-p,p}, \dots, N_{i,p}$  on the knot span  $[\xi_i, \xi_{i+1})$ . This is due to the fact that the only nonzero zeroth-basis function of the given interval is  $N_{i,0}$ , which leads to  $N_{i-p,p}, \dots, N_{i,p}$  being the only nonzero basis function on the aforementioned knot span. To illustrate this,  $\xi$  of 0.625 in the knot vector of Fig. (3.1) is located in the 4<sup>th</sup> knot span, and therefore, for the given knot span, only the basis functions  $N_{2,2}, N_{3,2}$ , and  $N_{4,2}$  are nonzero,
- The basis functions attain a nonnegativity property, i.e.,  $N_{i,p}(\xi) \geq 0$ , over the entire knot vector of order  $p$ , and for any arbitrary knot span  $i$  and  $\xi$  values. This can be easily seen in Fig. (3.1), where all basis function has nonnegative values ranging between 0 and 1,
- The basis functions attain a portion of unity property, that is, for an arbitrary knot span  $[\xi_i, \xi_{i+1})$ , we have:

$$\sum_{j=i-p}^i N_{j,p}(\xi) = 1 \quad \forall \xi \in [\xi_i, \xi_{i+1}) \quad (3.3)$$

An example of this can be drawn using Eq. (3.2) for  $\xi = 0.625$ , where we have the basis functions  $N_{2,2}, N_{3,2}$ , and  $N_{4,2}$  operating on the knot span  $\xi$  is located in. The values of those basis functions are 0.125, 0.75, and 0.125, respectively,

- By default, the derivatives of  $N_{i,p}(\xi)$  are defined within the borders of the knot span on which the basis function sub-polynomials are defined. It follows that at any arbitrary knot within the knot vector  $\xi$ , the nonzero basis functions  $N_{i,p}(\xi)$



are  $p - k$  continuously differentiable, where  $k$  is the multiplicity of the knot. We can conclude from this that increasing the degree of the knot vector increases the continuity while increasing the knot multiplicity decreases the continuity.

For more details on the B-splines basis function, the reader is referred to [169].

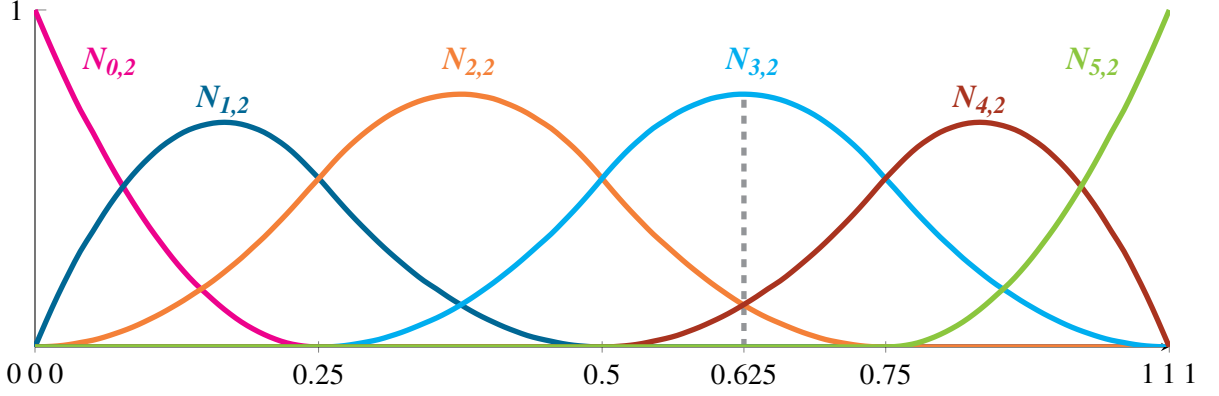


Figure 3.1: The quadratic basis functions, i.e., ( $p = 2$ ) for the open uniform knot vector  $\xi = \{0, 0, 0, 0.25, 0.5, 0.75, 1, 1, 1\}$ . The number of basis functions is  $n - p - 1$ , yielding 6 basis functions over the entire knot vector.

### 3.3 B-splines Curves and Surfaces

#### 3.3.1 B-Spline Curves

The B-splines based curves are defined as a linear combination of the control point set, e.g., *control polygon*,  $\{\mathbf{P}_i\}$  and the basis functions  $N_{i,p}$ , as following:

$$C(\xi) = \sum_{i=0}^n N_{i,p}(\xi) \mathbf{P}_i. \quad (3.4)$$

where  $i$  is the B-spline basis function index,  $N_{i,p}$  is the  $i^{\text{th}}$  B-spline basis function, and  $p$  is the polynomial orders in the  $\xi$  parametric direction. Any B-spline curve, however, reduces to a Bézier curve in the case of  $n = p$ , where the number of basis functions equals  $n + 1$ , and  $p$  is the basis function order. The number of control points per parametric direction is controlled by the size of the knot vector in that direction, such that the number of the control points equals the number of the basis function. In addition to this, the B-spline curve has a convex hull property where the curve is contained within its control polygon, which leads to the endpoints of the curve coinciding with the endpoints of the control polygon. A graphical representation of a B-spline curve can be seen in Fig. (3.2). The curve has 7 spatial control points, which in turn constructs the control polygon

containing the B-spline curve. The second-order knot vector has seven basis functions as shown in Fig. (3.3), which is the same number as the control points.

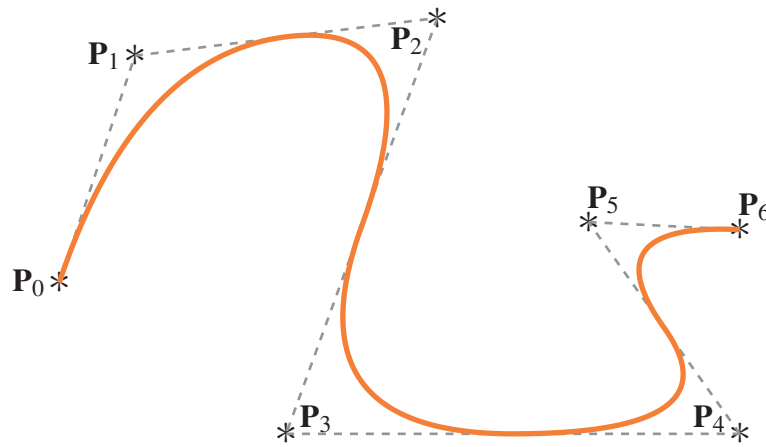


Figure 3.2: A second order B-spline curve constructed using the knot vector of Fig. (3.3), with a control polygon  $\{P_i\}$  coordinates of  $\{(1.5,1), (2,4), (4,4.5), (3,-1), (6,-1), (5,1.8), (6,1.7)\}$ .

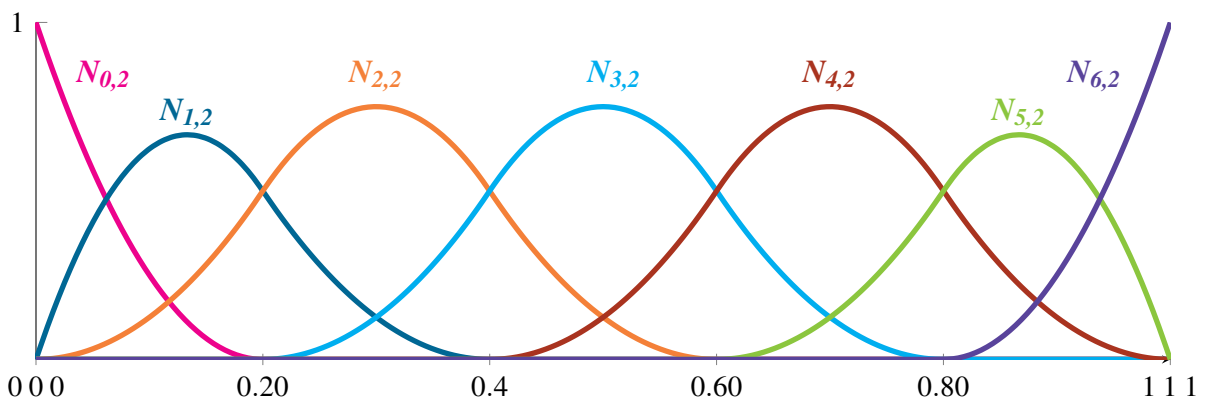


Figure 3.3: The quadratic basis functions, i.e.,  $(p = 2)$  for the open uniform knot vector  $\xi = \{0, 0, 0, 0.20, 0.40, 0.60, 0.80, 1, 1, 1\}$ . The number of basis functions is  $n - p - 1$ , yielding 7 basis functions over the entire knot vector.

### 3.3.2 B-Spline Surfaces

Similar to B-spline curves, but in bidirectional settings, the B-spline surface is constructed from a net of control points. Each physical direction has a parametric knot vector which sets the element number and length of each element in this direction. The B-spline curve is defined as the summation of univariate products of the basis functions with the control point corresponding to the basis functions as follows:

$$S(\xi, \eta) = \sum_{i=0}^n \sum_{j=0}^m N_{i,p}(\xi) N_{j,q}(\eta) P_{i,j}. \quad (3.5)$$

where  $i, j$  are the B-splines function indices,  $N_{i,p}, N_{j,q}$  are the  $i^{th}, j^{th}$  B-spline basis function, and  $p, q$  are the polynomial orders in the  $\xi, \eta$  directions. Assuming the knot vectors  $U(\xi)$  and  $V(\eta)$  have  $r + 1$  and  $s + 1$  knots, respectively, then it follows that  $n = r - p - 1$  and  $m = s - q - 1$ .

### 3.4 The Non-Uniform Rational B-splines (NURBS)

NURBS curves and surfaces are the gold standard of Computer-Aided Design (CAD) for their ability to represent very complex geometrical shapes [22]. They attain the same properties of the B-spline from which they are constructed and provide more flexibility to control surfaces and curves due to the embedded feature of control points weights [170].

A univariate NURBS function is defined as follows:

$$R_{i,p}(\xi) = \frac{N_{i,p}(\xi)w_i}{\sum_{j=0}^n N_{j,p}(\xi)w_j} \quad (3.6)$$

where  $w_{\bar{j}}$ s are the set of weights of the control points, with the same size. Eq. (3.6) can easily be extended for 2D and 3D configuration. For example, a trivariate NURBS function defined recursively over the parametric space is given by:

$$R_{i,j,k}(\xi, \eta, \zeta) = \frac{N_{i,p}(\xi)N_{j,q}(\eta)N_{k,r}(\zeta)w_{i,j,k}}{\sum_{\bar{i}=1}^n \sum_{\bar{j}=1}^m \sum_{\bar{k}=1}^t N_{\bar{i},p}N_{\bar{j},q}(\eta)N_{\bar{k},r}(\zeta)w_{(\bar{i},\bar{j},\bar{k})}} \quad \text{for trivariate cases.} \quad (3.7)$$

with  $i, j, k$  are the NURBS function indices, the  $N_{i,p}, N_{j,q}$  and  $N_{k,r}$  are the  $i^{th}, j^{th}$  and  $k^{th}$  B-spline basis function and  $p, q, r$  are the polynomial orders in the  $\xi, \eta, \zeta$  directions, respectively.  $w_{i,j,k}$  being the weight associated with the control point  $\mathbf{P}_{i,k,j}$ .

Following this, a NURBS surface can be defined as follows:

$$\mathbf{S}(\xi, \eta) = \sum_{i=0}^n \sum_{j=0}^m R_{i,j}^{p,q}(\xi, \eta) \mathbf{P}_{i,j} \quad (3.8)$$

This equation can easily be extended to a trivariate form to produce a NURBS-based volume object.

### 3.5 hpk-Refinement

B-spline basis function can be refined by various mechanisms without changing the geometry and the corresponding parameterization. This can be done in three ways: a) Knot insertion, b) order elevation, and c) higher order and higher continuity. The first method of refinement is the knot insertion, in which the knot vector is *extended* to include the

additional knot/s. In the case of a B-spline curve or surface, the new control points set is also extended by a linear combination of the original control points. This form of refinement is analog to the  $h$ -refinement of the FEM. The second method of refinement is the order elevation, e.g., from quadratic to cubic, cubic to quartic .. etc. When this mechanism is implemented, attention must be paid to preserving the discontinuities in the various derivatives existing in the original curve. During order elevation, the multiplicity of each knot value is increased by one, but no new knot values are added. Similar to the knot insertion method, neither the geometry nor the parameterization is changed. This type of refinement is analog to the  $p$ -refinement of the FEM. Thirdly, a knot vector can also be refined by augmenting its order and continuity. This involves elevating the order of the original knot vector, and afterward, a unique knot is inserted. This leads to the order and continuity elevation at each  $\bar{\xi}$  in the new knot vector. This is called  $k$ -refinement, and it is unique to IGA and does not have an analog in the classical FEM [22, 170].

## 3.6 Preliminary IGA Work: Rectangular plate with a circular hole

In This section, we present our preliminary work. We solved a linear elasticity problem for a rectangular plate with a central circular hole under an in-plane load. This example has been extensively studied in the literature and it does not have any novelty, it only serves as an example of IGA-based analysis.

### 3.6.1 Problem's equations

Let  $\boldsymbol{\sigma} = [\sigma_{ij}]$ ,  $\boldsymbol{\varepsilon} = [\varepsilon_{ij}]$ , and  $u_i$  be the Cartesian components of the Cauchy stress tensor, strain tensor, and the displacement vector, respectively. Where the strain tensor is the symmetric part of the displacement gradient as follows:

$$\varepsilon_{ij} = \frac{u_{i,j} + u_{j,i}}{2} \quad (3.9)$$

By Hook's law, which relates the stress tensor to the strain tensor, we have

$$\sigma_{ij} = c_{ijkl} \varepsilon_{kl} \quad (3.10)$$

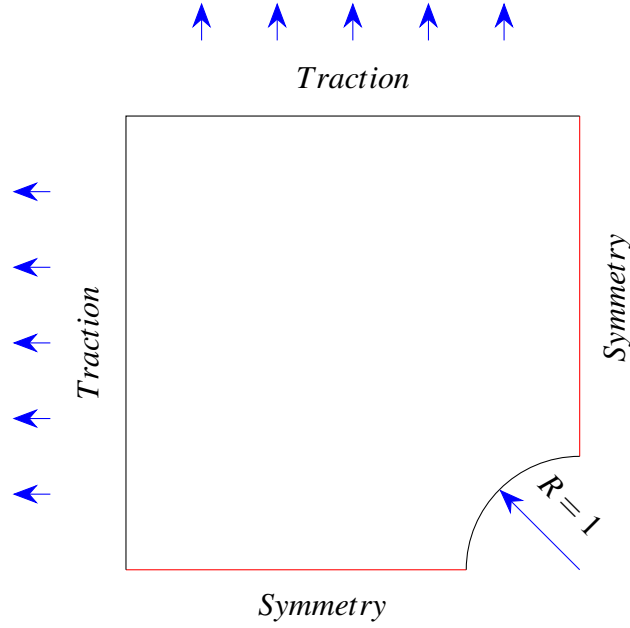


Figure 3.4: A schematic diagram of the rectangular plate under in-plane load.

where the  $c_{ijkl}$  are elastic coefficients, better known as the modulus of elasticity, for which, constant values over the domain constitute a homogeneous material.

### 3.6.2 The Strong form of the problem

Let  $f_i : \Omega \in \mathbb{R}^d$ ,  $g_i : \Gamma_{D_i} \in \mathbb{R}$ , and  $h_i : \Gamma_{N_i} \in \mathbb{R}$ , then the strong form of the problem is as follows: find  $u_i : \overline{\Omega} \rightarrow \mathbb{R}$  such that:

$$\sigma_{ij,j} + f_i = 0 \quad \text{in } \Omega \quad (3.11)$$

$$u_i = g_i \quad \text{on } \Gamma_{D_i} \quad (3.12)$$

$$\sigma_{ij} \mathbf{n}_j = h_i \quad \text{on } \Gamma_{N_i} \quad (3.13)$$

where,  $g_i$  and  $h_i$  are the prescribed boundary conditions and traction, respectively.  $\Gamma = \overline{\Gamma_{D_i} \cup \Gamma_{N_i}}$  and  $\Gamma_{D_i} \cap \Gamma_{N_i} = \emptyset$ .

### 3.6.3 The Weak form of the problem

Let  $\mathcal{V} = \mathcal{H}^1$  be the Sobolev space of scalar-valued square-integrable functions with square integrable first derivatives and let  $\mathcal{S}$  be the trial solution space, and the weighting function spaces  $\mathcal{W}$ . The weak form of the problem then reads: find  $u_i \in \mathcal{S} \subset \mathcal{V}$  such that:  $\forall w_i \in \mathcal{W} \subset \mathcal{V}$

$$\int_{\Omega} w(i, j) \sigma_{ij} d\Omega = \int_{\Omega} w_i f_i d\Omega + \sum_{i=1}^d \left( \int_{\Gamma_{N_i}} w_i h_j d\Gamma \right) \quad (3.14)$$

The continuous form of the problem states that for  $\mathbf{S} = \{\mathbf{u} | u_i \in \mathcal{S}_i\}$ , and let  $\mathbf{V} = \{\mathbf{w} | w_i \in \mathcal{V}_i\}$ , then the weak form of the problem becomes:

$$\mathbf{a}(\mathbf{w}, \mathbf{u}) = L(\mathbf{w}) \quad (3.15)$$

where

$$\mathbf{a}(\mathbf{w}, \mathbf{u}) = \int_{\omega} w_{(i,j)} c_{ijkl} u_{(k,l)} \quad (3.16)$$

$$L(\mathbf{w}) = \int_{\Omega} w_i f_i d\Omega + \sum_{i=1}^d \left( \int_{\Gamma_{N_i}} w_i h_j d\Gamma \right) \quad (3.17)$$

The finite-dimensional trial solution functions spaces  $\mathcal{S}^h \in \mathcal{S}$  and  $\mathcal{V}^h \in \mathcal{V}$  are defined using the isoparametric NURBS basis with vector-valued control variables. Assuming  $\mathbf{g}^h \in \mathcal{S}^h$ , then it follows that:  $\forall \mathbf{u}^h \in \mathcal{S}^h$ , we have:

$$\mathbf{u}^h = \mathbf{v}^h + \mathbf{g}^h \quad (3.18)$$

Where  $\mathbf{v}^h \in \mathcal{V}^h$ , and the Galerkin formulation is then reads: find  $\mathbf{u}^h = \mathbf{v}^h + \mathbf{h}^h \in \mathcal{S}^h$ , such that  $\forall \mathbf{w}^h \in \mathcal{V}^h$ :

$$a(\mathbf{w}^h, \mathbf{v}^h) = L(\mathbf{w}^h) - a(\mathbf{w}^h, \mathbf{g}^h) \quad (3.19)$$

where the  $i^h$  component of  $\mathbf{u}^h$  and  $\mathbf{w}^h$  are expressed as following:

$$\begin{aligned} u_i^h &= \sum_{A=1}^{n_{eq}} = N_A d_{iA} + g_i^h \\ w_i^h &= \sum_{A=1}^{n_{eq}} = N_A c_{iA} \end{aligned} \quad (3.20)$$

We solve for  $\mathbf{d}$  the following equation:

$$\mathbf{Kd} = \mathbf{F} \quad (3.21)$$

With the global stiffness matrix is defined as follows:

$$K = \mathbf{e}_i^T \int_{\Omega} \mathbf{B}_A^T \mathbf{D} \mathbf{B}_B d\Omega \mathbf{e}_j \quad (3.22)$$

In this equation,  $\mathbf{D}$  is the elasticity coefficients tensor, and  $\mathbf{B}_A$  is the strain displacement matrix.

### 3.6.4 Numerical results

We solved Eq. (3.21) using a Matlab hand-written code designed for this problem. The initial parametric space is defined by two second-order knot vectors,  $\xi = \{0, 0, 0, 0.5, 1,$

1, 1} and  $\boldsymbol{\eta} = \{0, 0, 0, 1, 1, 1\}$ , which gives an initial elements number count of 2. For the first knot vector, we have a total of 4 basis functions, while for the second one, we have a total of 3 basis functions. As mentioned in subsection (3.3.1), the corresponding 2-D control net and associated weights are defined as a matrix with the same dimensions as the basis functions, i.e.,  $4 \times 3$ , as following:

$$\mathbf{P}_i = \begin{bmatrix} (-1, 0, 1) & (-1, \sqrt{2} - 1, 1 + \frac{1}{\sqrt{2}}) & (1 - \sqrt{2}, 1, 1 + \frac{1}{\sqrt{2}}) & (0, 1, 1) \\ (-2.5, 0, 1) & (-2.5, 0.75, 1) & (-0.75, 2.5, 1) & (0, 2.5, 1) \\ (-4, 0, 1) & (-4, 4, 1) & (-4, 4, 1) & (0, 4, 1) \end{bmatrix} \quad (3.23)$$

The matrix  $\mathbf{D}$  has a plain-stress definition, with a modulus of elasticity  $\mathbf{E}$  equals to  $1 \times 10^5$  and a Poisson's ratio  $\nu$  of 0.3. The geometrical description of the problem can be seen in Fig. (3.4). The plate is  $8 \times 8$  unit length, with a hole at the center of radius 1 unit length. Taking advantage of the axes of symmetries, we can reduce the whole plate to a quarter around the vertical and horizontal lines passing through the center of the circle by fixing the displacement in the direction parallel to the symmetry lines. As shown in Fig. (3.5), the initial mesh shows that the computational domain is discretized into two elements as per the definition of the initial knot vectors  $\boldsymbol{\xi}$  and  $\boldsymbol{\eta}$ . We can see from Fig. (3.5a), that there are two non-polar control points close to the circumference of the hole but not exactly on the circumference. This is achieved by manipulating the weights of those two control points as shown in the control points matrix  $\mathbf{P}_i$  of Eq. (3.23).

An  $h$ -refinement of the knot vectors  $\boldsymbol{\xi}$  and  $\boldsymbol{\eta}$  would increase the element count in both directions, by inserting new unique knots within each knot vector, thus, increasing the span count of each knot vector and consequently the number of the elements in each direction. This can be seen in Fig. (3.6), where each element from the previous refinement order is split in half, thus doubling the element numbers.

In a similar manner, a  $p$ -refinement can also be implemented to increase the order of the initial knot vector. However, different from the  $h$ -refinement, and when implemented on the initial knot vector, the  $p$ -refinement does not change the spatial discretization. Only the number of the basis functions is increased and the number of the control points per direction. To maintain the continuity of the original knot vector, duplicated knots are inserted across element boundaries. As shown in Fig (3.7), the initial mesh is still the same as in Fig. (3.5b) since no  $h$ -refinement was applied to the initial knot vector, however, the control points number has increased by each  $p$ -refinement by the same number the basis

function increased by. Alternatively, a  $k$ -refinement can also be implemented to refine the initial knot vector. As mentioned in section 3.5, the  $k$ -refinement is unique to isogeometric analysis and does not have an analog in the standard FEM. When implementing this technique to the initial knot vector, we end up with the results shown in Fig. (3.8).

One interesting fact about this model and its configuration is the repeated control point on the top left corner of the plate. From the control points matrix of Eq. (3.23), we see that there are two control points with the same spatial coordinates. This results in a  $\mathcal{C}^0$  continuity, given that upon implementing any type of refinement, the corresponding knot span will always have a continuity of  $\mathcal{C}^0$  on both sides of the element. But in all cases, it is evident that the exact geometry can be obtained with the coarsest mesh considered.

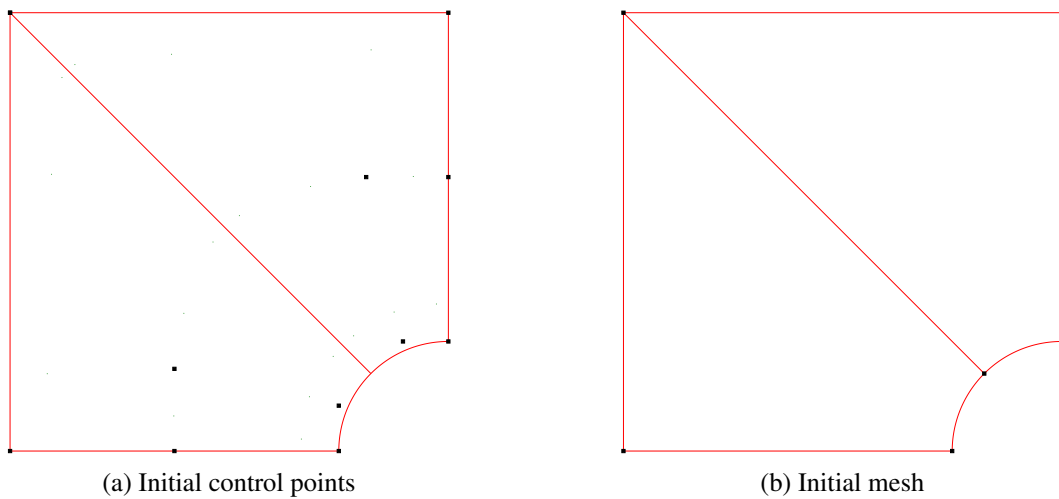


Figure 3.5: The computational domain corresponding to the two second-order knot vectors  $\xi$  and  $\eta$  with a) control points projected on the computational domain (black dots), and b) elements and nodes (black dots).



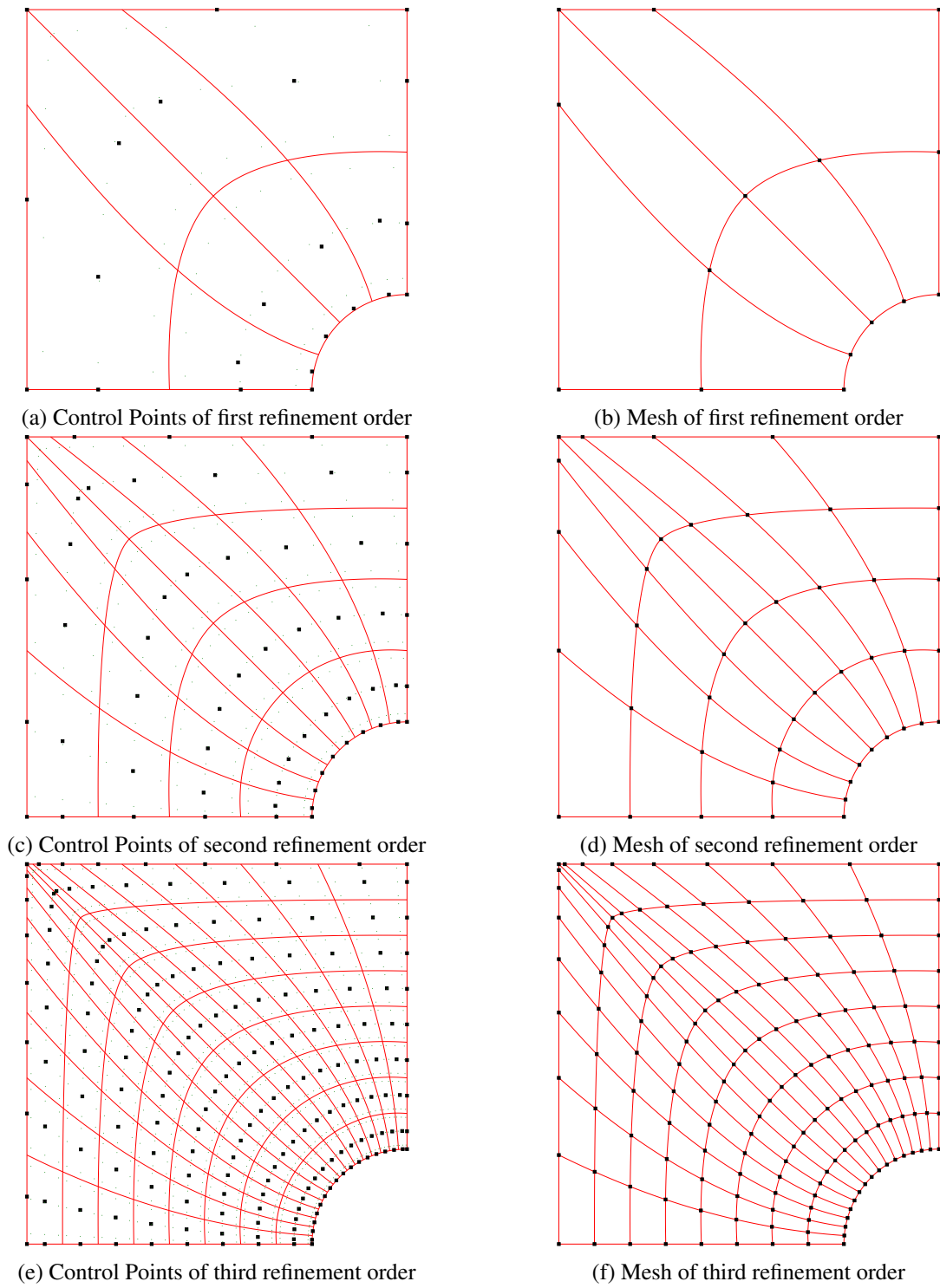


Figure 3.6: First (a-b), second (c-d), and third (e-f) refinement orders of initial computational domain. Figures (a), (c), and (e) shows the control points distribution, while figures (b), (d), and (f) shows the mesh and the spatial discretization of the initial computational domain.

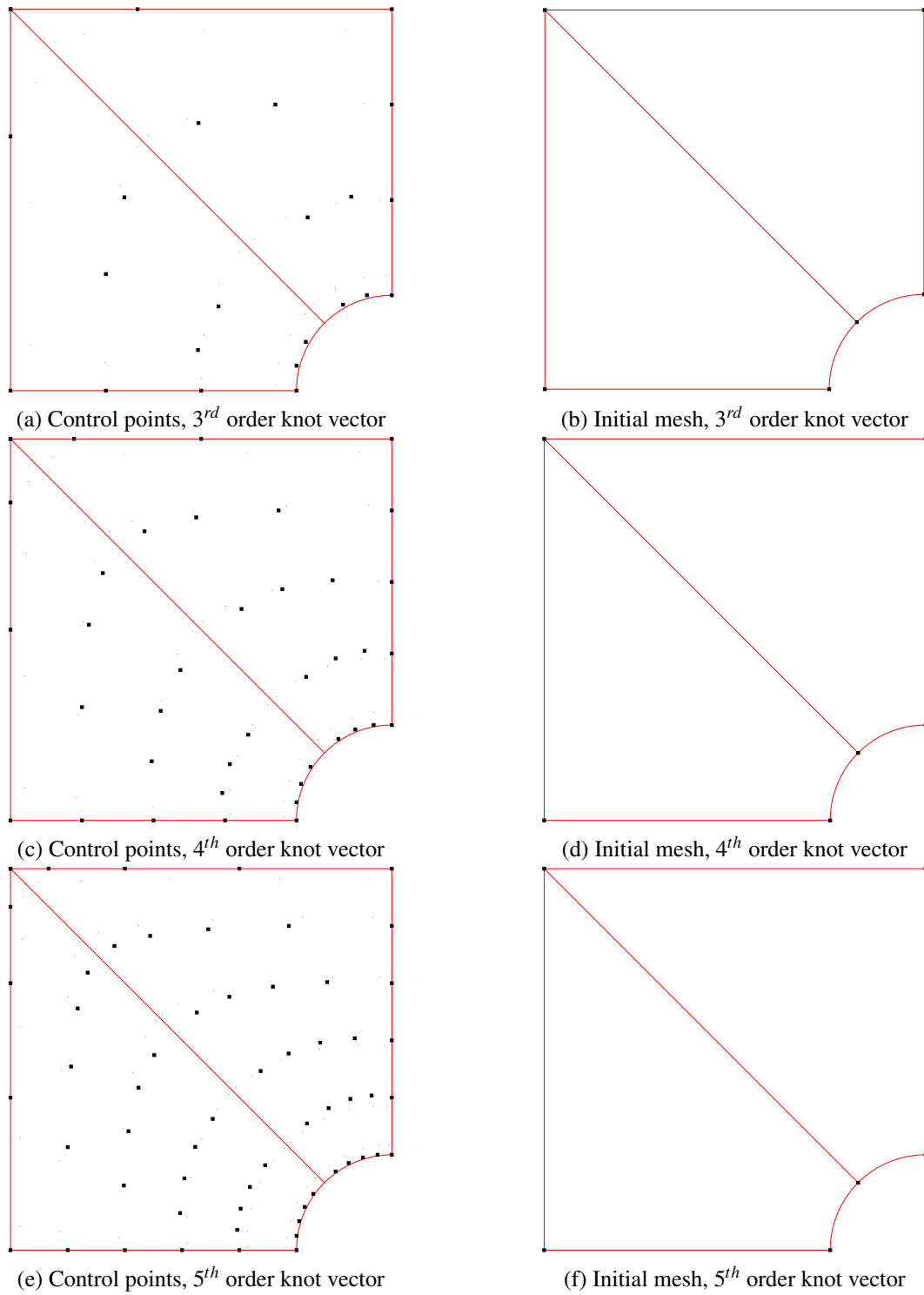


Figure 3.7: Third (a-b), fourth (c-d), and fifth (e-f) order-based control points distribution and corresponding initial mesh.

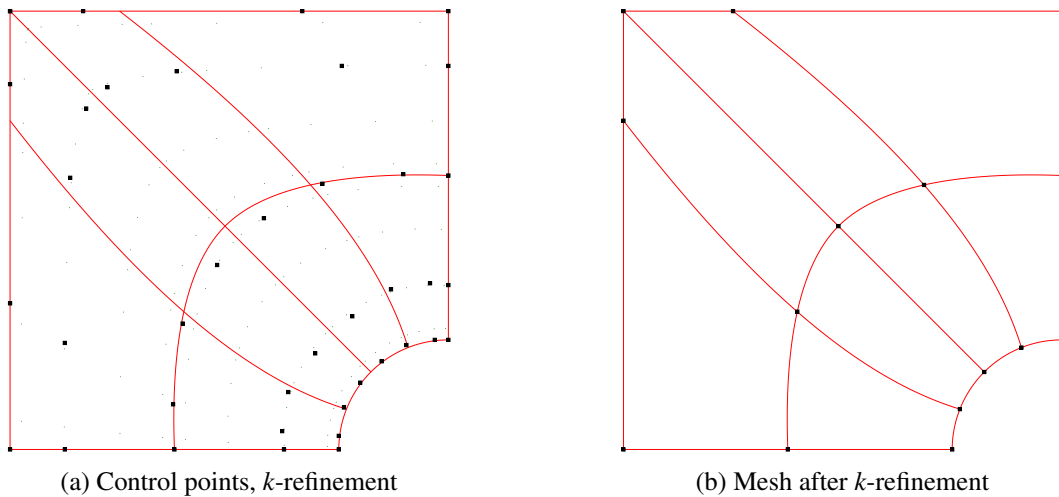


Figure 3.8: A  $k$ -refinement for the initial knot vector by elevating the original order by one degree, e.g., 3 and increasing the continuity across element boundaries.

The X- and Y-components of stress fields based on the initial knot vector are shown in Fig (3.9), while in Fig. (3.10), we had a second-order knot vector with a refinement order of 5, e.g., an  $h$ -refinement implemented on the initial knot vector, and in Fig. (3.11), we elevated the degree of the knot vector to 5.

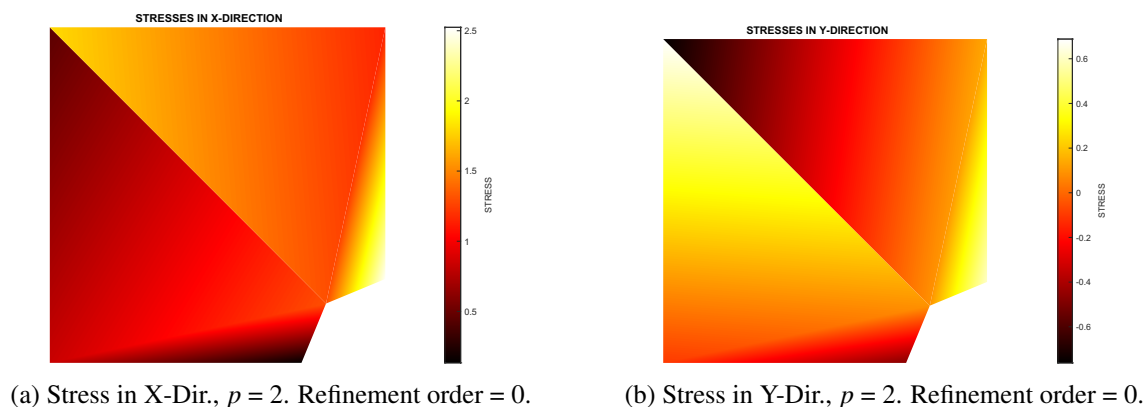


Figure 3.9: Stress fields based on a geometry and a solution approximation using initial knot vector.

From a visual perspective, we can see the results are improving when an  $h$ -refinement is implemented as shown in the difference between Fig. (3.9) and Fig. (3.10). But at this point, when elevating the degree of the knot vector from a second-order one to a fifth-order one, the visuals are almost similar, and the accuracy of the solution approximated using order-varying knot vectors can only be measured using the norms-based error. As shown in Figs (3.12-3.13), an  $h$ -refinement for the knot vector while maintaining the same degree would reduce the error noticeably, but a more effective method is to apply a  $p$ -refinement or a mix of both, i.e., a  $k$ -refinement, as it would reduce the error by 100%

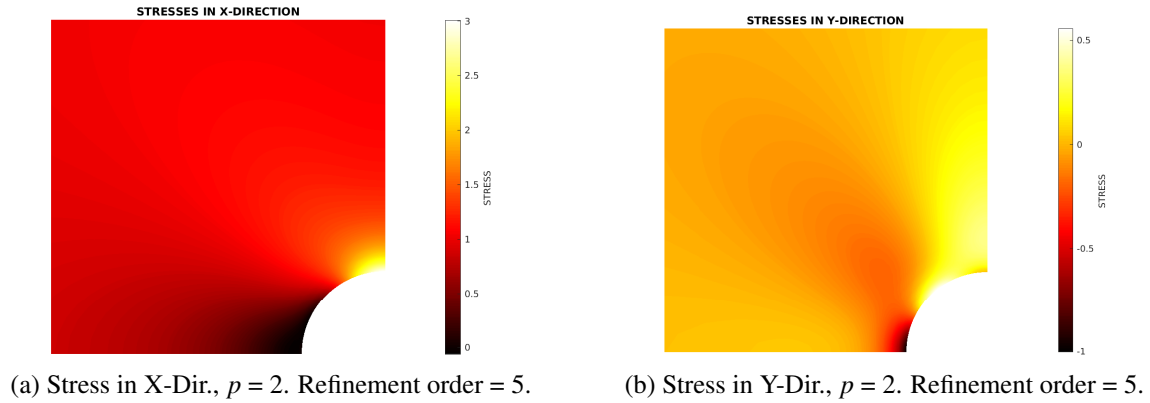


Figure 3.10: Stress fields based on geometry and a solution approximation using a second-order knot vector and a refinement of  $5^{th}$  order.

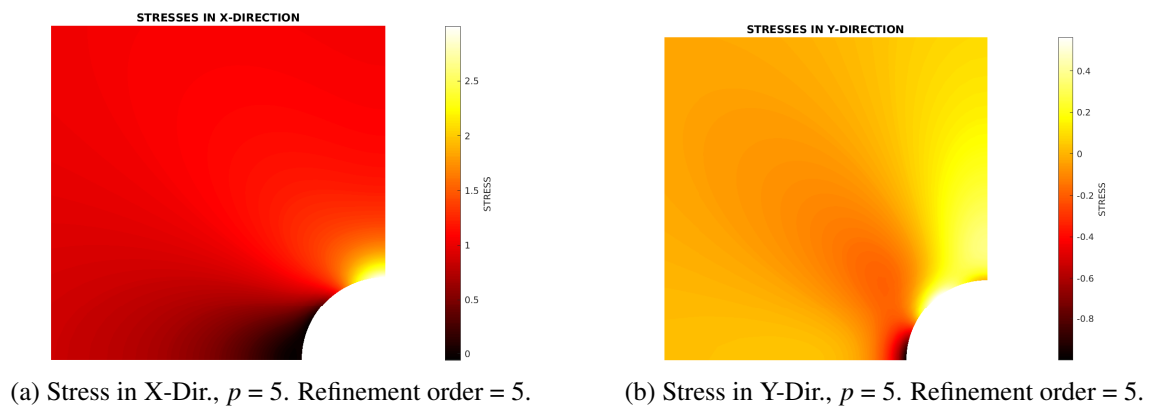


Figure 3.11: Stress fields based on geometry and a solution approximation using a fifth-order knot vector and a refinement of  $5^{th}$  order.

after a certain threshold of refinement has been passed. For example, a quadratic knot vector refined 7 times would have an error in the energy norm of  $7.22428 \times 10^{-07}$ , while it would have an error in the energy norm of  $3.57773 \times 10^{-13}$  in case the order of the knot vector was elevated to the sixth degree, e.g., Hexic, with the same  $h$ -refinement order. The same thing can also be seen when comparing the stress error in the  $L^2$ -norm as shown in Fig. (3.13). Those findings are similar to the results in [22, 171].

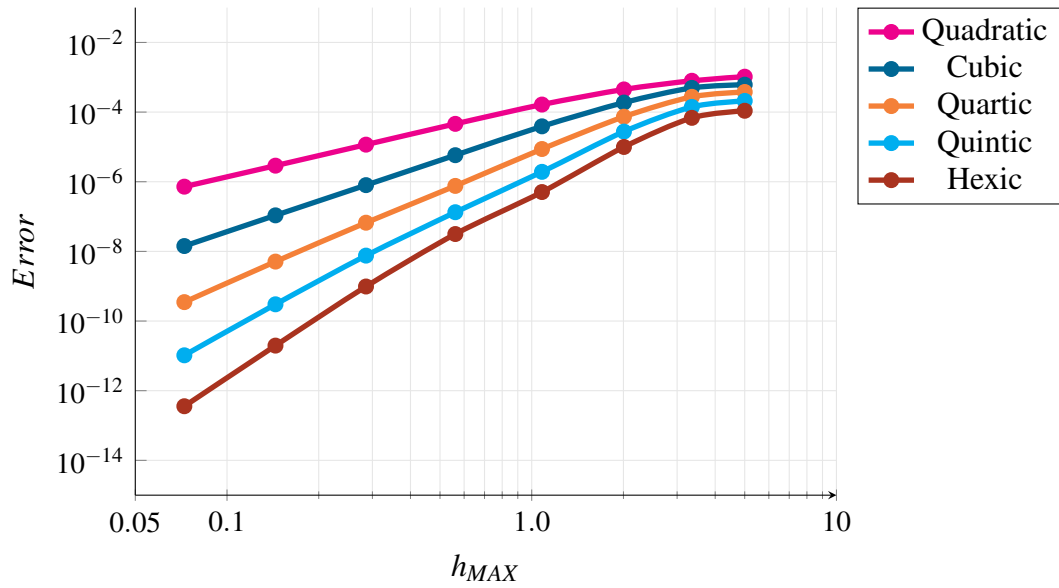


Figure 3.12: A comparison between the error in the Energy-norm between versus  $h_{MAX}$ , the largest element diameter in the mesh, for the solutions approximated for degrees ranging from  $p = 2$  to  $p = 6$ , and refinement orders ranging from 0 to 7.

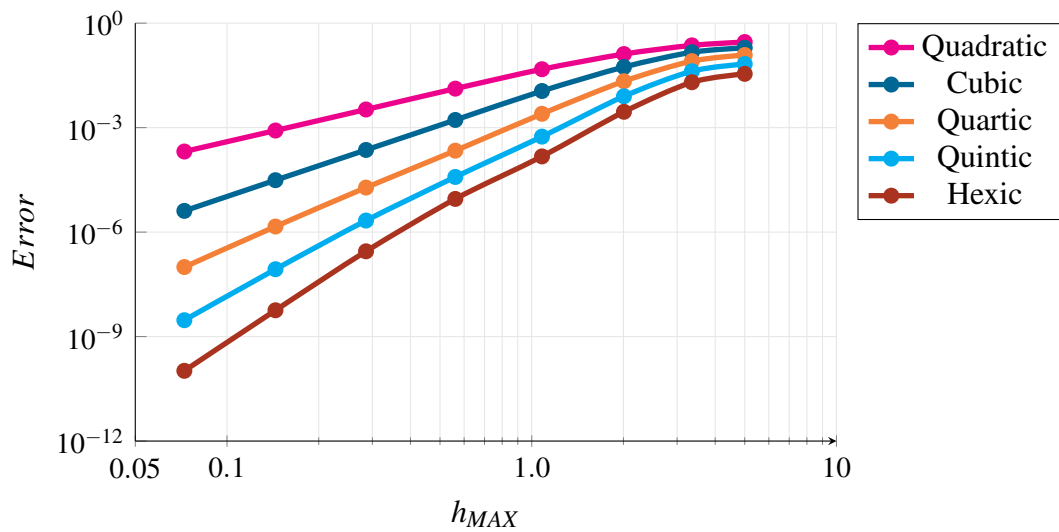


Figure 3.13: A comparison between the stress error in the  $L^2$  versus  $h_{MAX}$ , for the solutions approximated for degrees ranging from  $p = 2$  to  $p = 6$ , and refinement orders ranging from 0 to 7.

# 4

## A Constrained Optimization Problem of Morphological Evolution of Vesicles in Electric Fields

### 4.1 Introduction

In this chapter, we build up on the mathematical model and the phase-field formulation presented in section 2.3 to formulate the strong form of the problem, which consists of two PDEs; one describes the time evolution of the vesicle, while the other one describes the electric potential within the computational domain. The first PDE is a fourth-order equation, hence, we solve it within the framework of isogeometric analysis due to the need for higher than  $\mathcal{C}^0$  continuity as explained in section 1.3, which can not be achieved using standard FEM, and therefore, we resort to isogeometric analysis to solve the problem given the ability to attain higher-order continuity required to solve

the problem. After introducing the strong form of the problem, we then introduce the weak form, and afterward, we solve multiple examples under various conditions, e.g., a constrained Willmore flow problem, the effect of flexoelectricity on vesicles morphology, and the membrane conductivity role.

## 4.2 The strong form

Let  $\Omega \subset \mathbb{R}^3$  be an open set representing the computational domain. The boundary of  $\Omega$  denoted as  $\partial\Omega$  is assumed to be sufficiently smooth. The unit outward normal vector to  $\partial\Omega$  denoted  $\mathbf{n}$ . For the initial boundary problem of the phase field approximation of the electromechanical model, where  $\bar{\Omega}$  is the closure of  $\Omega$ ,  $\partial\Omega_{-y}$  and  $\partial\Omega_{+y}$  are bottom and top sides of  $\Omega$  respectively, the strong form is stated as the following: find  $\phi : \bar{\Omega} \times (0, T) \mapsto \mathbb{R}$ , such that

$$\begin{aligned}
& \frac{\partial \phi}{\partial t} + \frac{3\kappa_b}{2\sqrt{2}}(\Delta\phi)\left(\frac{1-3\phi^2}{\varepsilon} + \sqrt{2}H_{sp}\phi\right) + \frac{3\kappa_b}{2\sqrt{2}\varepsilon}\left(\frac{\phi}{\varepsilon} - \frac{H_{sp}}{\sqrt{2}}\right)(1-\phi^2)\left(\frac{1-3\phi^2}{\varepsilon} + \sqrt{2}H_{sp}\phi\right) \\
& + \frac{3\kappa_b}{2\sqrt{2}}\Delta\left(\varepsilon\Delta\phi + \left(\frac{\phi}{\varepsilon} - \frac{H_{sp}}{\sqrt{2}}\right)(1-\phi^2)\right) - \frac{3c_1d_m}{2\sqrt{2}}\left(-\varepsilon\Delta\phi\Delta\psi - \left(\frac{\phi-\phi^3}{\varepsilon}\right)\Delta\psi\right. \\
& \left. + 2\varepsilon\nabla\nabla\phi : \nabla\nabla\psi + \varepsilon\nabla\phi \cdot \nabla(\Delta\psi)\right) + \frac{3d_m}{2\sqrt{2}\varepsilon}\varepsilon_m(\phi-\phi^3)|\nabla\psi|^2 + \frac{1}{4}(\varepsilon_{in} - \varepsilon_{out})|\nabla\psi|^2 \\
& - \frac{M_1}{2}(V(\phi) - \bar{\alpha}(t)) + \frac{3\varepsilon M_2}{2\sqrt{2}}(A(\phi) - \bar{\beta}(t))\left(-\Delta\phi + \frac{1}{\varepsilon^2}(\phi^3 - \phi)\right) = 0 \quad \text{in } \Omega \times (0, T) \\
& \phi = 1 \quad \text{on } \partial\Omega \times (0, T) \\
& \nabla\phi \cdot \mathbf{n} = 0 \quad \text{on } \partial\Omega \times (0, T) \\
& \phi(\mathbf{x}, 0) = \phi_0(\mathbf{x}) \quad \text{in } \Omega
\end{aligned} \tag{4.1}$$

For the electric potential, we have

$$\begin{aligned}
& \nabla \cdot (\sigma_\phi \nabla \psi) = 0 \quad \text{in } \Omega \times (0, T) \\
& \psi = +V \quad \text{on } \partial\Omega_{-y} \times (0, T) \\
& \psi = -V \quad \text{on } \partial\Omega_{+y} \times (0, T) \\
& \nabla\psi \cdot \mathbf{n} = 0 \quad \text{on } \partial\Omega_t \times (0, T) \\
& \psi(\mathbf{x}, 0) = \psi_0 \quad \text{in } \Omega
\end{aligned} \tag{4.2}$$

### 4.3 The weak form and numerical formulation

The continuous problem in the weak form can be formulated in two ways, a monolithic approach or a staggered approach. In the monolithic formulation, we are formulating the weak form of the problem and solving for two degrees-of-freedom per control point, simultaneously. Another way of approaching the problem is by solving the weak form of Eq. (4.2) by assuming the phase-field is given and then solve the weak form of Eq. (4.1) by considering the electric potential from the previous step at each iteration to evaluate the phase field. For the problem at hand, both formulations yield nearly the same results, however, the staggered scheme is computationally less expensive since the linear Laplacian Eq. (4.2) can be efficiently solved using an iterative linear solver such as Generalized Minimal Residual (GMRES) method, which reduces significantly the nonlinear solver computational load. In the following, we are presenting the weak form for the staggered scheme.

#### 4.3.1 Continuous problem in the weak form

Let  $\mathcal{V} = \mathcal{H}^2$  being the Sobolev space of square-integrable functions with square integrable first and second derivatives and denote the trial solution space by  $\mathcal{S}$  and weighting function space by  $\mathcal{W}$  spaces. Multiplying Eq. (4.1) by the weighting function and integrating by parts gives the weak form as follows: find  $\phi \in \mathcal{S} \subset \mathcal{V}$ , such that  $\forall w \in \mathcal{W} \subset \mathcal{V}$ ,

$$B(w, \phi) = 0, \quad \text{where} \quad (4.3)$$

$$\begin{aligned} B(w, \phi) = & \left( w, \dot{\phi} \right)_{\Omega} + \left( w, \frac{3\kappa_b}{2\sqrt{2}\varepsilon} (\varepsilon \Delta \phi) \left( \frac{1-3\phi^2}{\varepsilon} + \sqrt{2} H_{sp} \phi \right) \right)_{\Omega} \\ & + \left( w, \frac{3\kappa_b}{2\sqrt{2}\varepsilon} \left( \frac{\phi}{\varepsilon} - \frac{H_{sp}}{\sqrt{2}} \right) (1-\phi^2) \left( \frac{1-3\phi^2}{\varepsilon} + \sqrt{2} H_{sp} \phi \right) \right)_{\Omega} \\ & + \left( \Delta w, \frac{3\kappa_b}{2\sqrt{2}} \left[ \varepsilon \Delta \phi + \left( \frac{\phi}{\varepsilon} - \frac{H_{sp}}{\sqrt{2}} \right) (1-\phi^2) \right] \right)_{\Omega} \\ & + \left( w, \frac{3c_1 d_m}{\sqrt{2}} \varepsilon \Delta \phi \Delta \psi \right)_{\Omega} + \left( w, \frac{3c_1 d_m}{2\sqrt{2}} \left( \frac{\phi - \phi^3}{\varepsilon} \right) \Delta \psi \right)_{\Omega} \\ & - \left( w, \frac{3c_1 d_m}{\sqrt{2}} \varepsilon \nabla \nabla \phi : \nabla \nabla \psi \right)_{\Omega} + \left( \nabla w, \frac{3c_1 d_m}{2\sqrt{2}} \varepsilon \Delta \psi \nabla \phi \right)_{\Omega} \\ & + \left( w, \frac{3d_m \varepsilon_m}{2\sqrt{2}\varepsilon} (\phi - \phi^3) |\nabla \psi|^2 \right)_{\Omega} + \left( w, \frac{1}{4} (\varepsilon_{in} - \varepsilon_{out}) |\nabla \psi|^2 \right)_{\Omega} \\ & - \left( w, \frac{M_1}{2} (V(\phi) - \bar{\alpha}) \right)_{\Omega} - \left( w, \frac{3\varepsilon M_2}{2\sqrt{2}} (A(\phi) - \bar{\beta}) \left( \Delta \phi - \frac{1}{\varepsilon^2} (\phi^3 - \phi) \right) \right)_{\Omega} \end{aligned} \quad (4.4)$$



$(\cdot, \cdot)_\Omega$  is the  $\mathcal{L}^2$  inner product with respect to the domain  $\Omega$ .

### 4.3.2 The semidiscrete formulation

Find  $\phi^h \in \mathcal{S}^h \subset \mathcal{S} \subset \mathcal{V}$  such that  $\forall w^h \in \mathcal{W}^h \subset \mathcal{W} \subset \mathcal{V}$

$$B(w^h, \phi^h) = 0 \quad (4.5)$$

where  $w^h$  and  $\phi^h$  are defined as the following

$$w^h = \sum_{A=1}^{n_b} N_A(x) w_A, \quad \phi^h = \sum_{A=1}^{n_b} N_A(x) \phi_A \quad (4.6)$$

where  $N_A(x)$  is NURBS function [169], defined recursively over the parametric space as

$$N_{i,j,k}(\xi, \eta, \zeta) = \frac{N_{i,p}(\xi)N_{j,q}(\eta)N_{k,r}(\zeta)w_{i,j,k}}{\sum_{\bar{i}=1}^n \sum_{\bar{j}=1}^m \sum_{\bar{k}=1}^l N_{\bar{i},p}(\xi)N_{\bar{j},q}(\eta)N_{\bar{k},r}(\zeta)w_{(\bar{i},\bar{j},\bar{k})}} \quad \text{for trivariate cases.} \quad (4.7)$$

with  $i, j, k$  are the NURBS function indices, the  $N_{i,p}$ ,  $N_{j,q}$  and  $N_{k,r}$  are the  $i^{\text{th}}$ ,  $j^{\text{th}}$  and  $k^{\text{th}}$  B-spline basis function and  $p, q, r$  are the polynomial orders in the  $\xi, \eta, \zeta$  directions, respectively.  $w_{i,j,k}$  being the weight associated with the control point  $\mathbf{P}_{i,j,k}$ . For simplicity, we are denoting the trivariate basis function by  $N_A(x)$ . The NURBS functions are of non-interpolatory nature. This prevents strictly interpolating control variables as opposed to Lagrangian finite element methods [23].

### 4.3.3 Time discretization and numerical implementation

The Generalized- $\alpha$  method has been used to implement the time discretization of the semi-discrete Galerkin formulation from the previous subsection. Generalized- $\alpha$  contains a parameter to control the degree of damping of high frequencies, which gives the method the advantage accuracy-wise over other time implicit integration schemes like the Backward Differentiation Formula (BDF). Nonetheless, numerical testing revealed both time integrators produce identical results for the problem at hand, except for the Generalized- $\alpha$  method being faster in reaching the stationary state of the system.

Let  $\phi$  and  $\dot{\phi}$  denote the vector of degrees of freedom of phase field and phase field time derivative, respectively. We start by defining the residual vector as:

$$\begin{aligned} \mathbf{R} &= \{R_A\}, \\ R_A &= B(N_A, \phi^h) \end{aligned} \quad (4.8)$$

Given  $\phi$  and  $\dot{\phi}$  and  $\Delta t_n = t_{n+1} - t_n$ , the time integration algorithm can be formulated as

following: find  $\dot{\phi}_{n+1}$ ,  $\phi_{n+1}$ ,  $\dot{\phi}_{n+\alpha_m}$  and  $\phi_{n+\alpha_f}$  such that:

$$\mathbf{R}(\dot{\phi}_{n+\alpha_m}, \phi_{n+\alpha_f}) = 0 \quad (4.9)$$

$$\phi_{n+1} = \phi_n + \Delta t_n \dot{\phi}_n + \gamma \Delta t_n (\dot{\phi}_{n+1} - \dot{\phi}_n) \quad (4.10)$$

$$\dot{\phi}_{n+\alpha_m} = \dot{\phi}_n + \alpha_m (\dot{\phi}_{n+1} - \dot{\phi}_n) \quad (4.11)$$

$$\phi_{n+\alpha_f} = \phi_n + \alpha_f (\phi_{n+1} - \phi_n) \quad (4.12)$$

where  $\alpha_f$ ,  $\alpha_m$ , and  $\gamma$  are real-valued parameters that define the method. For a linear first-order system of ODEs, the Generalized- $\alpha$  method is second-order accurate in time [172] if

$$\gamma = \frac{1}{2} + \alpha_m - \alpha_f \quad (4.13)$$

and unconditionally stable if:

$$\alpha_m \geq \alpha_f \geq \frac{1}{2} \quad (4.14)$$

where  $\alpha_m$  and  $\alpha_f$  are as following

$$\alpha_m = \frac{1}{2} \left( \frac{3 - \rho_\infty}{1 + \rho_\infty} \right), \quad \alpha_f = \left( \frac{1}{1 + \rho_\infty} \right). \quad (4.15)$$

The spectral radius of the amplification matrix at an infinitely large time step,  $\rho_\infty \in [0, 1]$ , which controls the high-frequency damping, was set to 0.5, which results in  $\alpha_f = 0.66\bar{6}$  and  $\alpha_m = 0.83\bar{3}$  and hence, satisfying Eq. (4.14) for unconditionally stable time integration for a system of linear ODEs. The situation is, however, more complicated for nonlinear problems, as the notion of stability is problem-dependent. For nonlinear phase-field problems, there is still little known about the stability of the generalized- $\alpha$  method [172, 173]. Nonetheless, based on our numerical experience, the method is *computationally* stable [174, 175] for the range of time-step sizes we considered in this paper. The nonlinear system of Eqs. (4.9)–(4.12) is solved using Newton's method, according to a two-stage predictor-multicorrector approach as the following:

1. Predictor stage

$$\phi_{n+1}^{(0)} = \phi_n \quad (4.16)$$

$$\dot{\phi}_{n+1}^{(0)} = \frac{\gamma - 1}{\gamma} \dot{\phi}_n \quad (4.17)$$

with the superscript denoting the iteration index of the nonlinear solver.

2. Multicorrector stage Repeat the following steps for  $i = 1, 2, 3, \dots, i_{max}$ , or until con-

vergence is reached.

- Evaluate iterates at  $\alpha$ -levels:

$$\dot{\phi}_{n+\alpha_m}^{(i)} = \dot{\phi}_n + \alpha_m(\dot{\phi}_{n+1}^{(i-1)} - \dot{\phi}_n) \quad (4.18)$$

$$\phi_{n+\alpha_f}^{(i)} = \phi_n + \alpha_f(\phi_{n+1}^{(i-1)} - \phi_n) \quad (4.19)$$

- Use  $\alpha$ -level iterates to assemble the linear system of equations corresponding to the linearization of Equation (4.9)

$$\mathbf{R}_{n+1}^{(i+1)} = \mathbf{R}_{n+1}^{(i)} + \mathbf{K}^{(i)}\Delta\dot{\phi}_{n+1}^{(i)} = 0 \quad (4.20)$$

This linearized system is solved using GMRES method available through KSP solvers in PETSc [176–179].

- Update the solution

$$\dot{\phi}_{n+1}^{(i)} = \dot{\phi}_{n+1}^{(i-1)} + \Delta\dot{\phi}_{n+1}^{(i)} \quad (4.21)$$

$$\phi_{n+1}^{(i)} = \phi_{n+1}^{(i-1)} + \gamma\Delta t_n \dot{\phi}_{n+1}^{(i)} \quad (4.22)$$

The tangent matrix in Eq. 4.20 is evaluated as following:

$$\begin{aligned} \mathbf{K} &= \frac{\partial \mathbf{R}(\dot{\phi}_{n+\alpha_m}, \phi_{n+\alpha_f})}{\partial \dot{\phi}_{n+\alpha_m}} \frac{\partial \dot{\phi}_{n+\alpha_m}}{\partial \dot{\phi}_{n+1}} + \frac{\partial \mathbf{R}(\dot{\phi}_{n+\alpha_m}, \phi_{n+\alpha_f})}{\partial \phi_{n+\alpha_f}} \frac{\partial \phi_{n+\alpha_f}}{\partial \dot{\phi}_{n+1}} \\ &= \alpha_m \frac{\partial \mathbf{R}(\dot{\phi}_{n+\alpha_m}, \phi_{n+\alpha_f})}{\partial \dot{\phi}_{n+\alpha_m}} + \alpha_f \gamma \Delta t_n \frac{\partial \mathbf{R}(\dot{\phi}_{n+\alpha_m}, \phi_{n+\alpha_f})}{\partial \phi_{n+\alpha_f}} \end{aligned} \quad (4.23)$$

where the iteration index  $i$  has been dropped for simplicity, and the tangent matrix  $\mathbf{K} = \{K_{AB}\}$  is formulated as the following:

$$\begin{aligned}
K_{AB} = & \alpha_m(N_A, N_B)_\Omega \\
& + \alpha_f \gamma \Delta t_n \left[ \left( N_A, \frac{3\kappa_b}{2\sqrt{2}\varepsilon} [(\varepsilon \Delta N_B + N_B \frac{1-\phi^2}{\varepsilon} + (\frac{\phi}{\varepsilon} - \frac{H_{sp}}{\sqrt{2}})(-2\phi N_B)) \right. \right. \\
& \quad \left. \left( \frac{1-3\phi^2}{\varepsilon} + \sqrt{2}H_{sp}\phi \right) + (\varepsilon \Delta \phi + (\frac{\phi}{\varepsilon} - \frac{H_{sp}}{\sqrt{2}})(1-\phi^2)) \right. \\
& \quad \left. \left. \left( \frac{-6\phi N_B}{\varepsilon} + \sqrt{2}H_{sp}N_B \right) \right]_\Omega + \left( \Delta N_A, \frac{3\kappa_b}{2\sqrt{2}} [\varepsilon \Delta N_B + N_B \frac{1-\phi^2}{\varepsilon} \right. \right. \\
& \quad \left. \left. + (\frac{\phi}{\varepsilon} - \frac{H_{sp}}{\sqrt{2}})(-2\phi N_B) \right] \right)_\Omega + \left( N_A, \frac{3c_1 d_m}{\sqrt{2}} \varepsilon \Delta N_B \Delta \psi \right)_\Omega \\
& + \left( N_A, \frac{3c_1 d_m}{2\sqrt{2}} \left( \frac{N_B - 3\phi^2 N_B}{\varepsilon} \right) \Delta \psi \right)_\Omega - \left( N_A, \frac{3c_1 d_m}{\sqrt{2}} \varepsilon \nabla \nabla N_B : \nabla \nabla \psi \right)_\Omega \\
& + \left( \nabla N_A, \frac{3c_1 d_m}{2\sqrt{2}} \varepsilon \Delta \psi \nabla N_B \right)_\Omega + \left( N_A, \frac{3d_m \varepsilon_m}{2\sqrt{2}} (N_B - 3\phi^2 N_B) |\nabla \psi|^2 \right)_\Omega \\
& - \left. \left( N_A, \frac{3\varepsilon M_2}{2\sqrt{2}} (A(\phi) - \bar{\beta}) \left( \Delta N_B - \frac{1}{\varepsilon^2} (3\phi^2 N_B - N_B) \right) \right)_\Omega \right]
\end{aligned} \tag{4.24}$$

where  $\nabla \nabla N_B$  is a second-order tensor of the second-order partial derivatives of the NURBS function, which its components is expressed as the following

$$\begin{pmatrix} N_{B,xx} & N_{B,xy} & N_{B,xz} \\ N_{B,yx} & N_{B,yy} & N_{B,yz} \\ N_{B,zx} & N_{B,zy} & N_{B,zz} \end{pmatrix}$$

**Remark.** To save computational time, we treat the non-local terms of the residual vector,  $A(\phi)$  and  $V(\phi)$ , explicitly. Therefore, instead of evaluating these terms in (4.9) at  $t_{n+\alpha_f}$ , they are evaluated at  $t_n$ .

#### 4.3.4 Modified ALM implementation

We are employing the algorithm in [21] to calculate the Lagrange multipliers in Eqs. (4.9) and (4.24). The proposed modified ALM overcomes the setbacks of the penalty method and has proven to be sufficiently stable with relatively large time steps. The idea is to repeatedly solve Eq. (4.20) using an updated set of the Lagrangian multipliers  $\bar{\alpha}$  and  $\bar{\beta}$  so the solution vector is converging to an admissible one, i.e., satisfying all constraints simultaneously. Considering the  $k^{th}$  iterations, the multipliers are updated according to the following update mechanism:

$$\begin{pmatrix} \bar{\alpha} \\ \bar{\beta} \end{pmatrix} \leftarrow \begin{pmatrix} \bar{\alpha} \\ \bar{\beta} \end{pmatrix} - \mathbf{T}_{AV}^{-1} \begin{pmatrix} V(\phi^{n+1}) - \alpha_0 \\ A(\phi^{n+1}) - \beta_0 \end{pmatrix} \quad (4.25)$$

where  $T_{AV}$  is a  $2 \times 2$  Jacobian of  $v$  and  $a$  at  $\bar{\alpha}_{k-1}$  and  $\bar{\beta}_{k-1}$ , and are approximated such that after updating the solution vector according to Eq. (4.22) at  $t_{n+1}$ , it still upholds the constraints  $v := V(\phi^{n+1}) = \alpha_0$ ,  $a := A(\phi^{n+1}) = \beta_0$ . Algorithm 1 shows the solution procedures of the phase field electromechanical problem with fixed volume and surface area. It ensures that the solution vector will converge gradually to an admissible set by upholding the two constraints.

---

**Algorithm 1** Modified ALM for constrained PF electromechanical problem with 2 Lagrange multipliers

---

**Input:** Initial phase field configuration  $\phi_0$   
Initial electrical field configuration  $\psi_0$   
The end time  $T > 0$  and the initial time step size  $\Delta t_n$   
Target Volume  $\alpha_0$  and Area  $\beta_0$   
Small termination tolerance  $\text{tol} > 0$   
Constant penalty parameters  $M_1, M_2 > 0$

**Procedures:**

- 1: Set  $\bar{\alpha} = \alpha_0, \bar{\beta} = \beta_0$
- 2: Initialize the  $2 \times 2$  Jacobian matrices,  $\mathbf{T}_{AV}^{-1} = \mathbf{I}$
- 3: Evaluate the solution vector at initialization  $\phi_0$
- 4: **for** ( $n = 0, 1, \dots, N_t - 1$ ) **do**
- 5:     **for** ( $i = 1, 2, 3$ ) **do**
- 6:         Update  $(\bar{\alpha}, \bar{\beta})$  according to Eq. (4.25), use  $\phi_n$  instead of  $\phi_{n+1}$  when  $i = 1$
- 7:         Evaluate  $\phi_{n+1}$  according to Eq. (4.22)
- 8:         **if**  $\max[ |V(\phi_{n+1}) - \alpha_0|/\alpha_0, |A(\phi_{n+1}) - \beta_0|/\beta_0 ] \leq \text{tol}$ , pass control to next  $n$
- 9:         Set  $\bar{\alpha}_i = \bar{\alpha}$ ,  $\bar{\beta}_i = \bar{\beta}$ ,  $\bar{v}_i = \bar{v}$ , and  $\bar{a}_i = \bar{a}$
- 10:     **end**
- 10:     **while true do**
- 11:         Set  $\mathbf{T}_{AV}^{-1} = \begin{pmatrix} \bar{\alpha}_2 - \bar{\alpha}_1 & \bar{\alpha}_3 - \bar{\alpha}_1 \\ \bar{\beta}_2 - \bar{\beta}_1 & \bar{\beta}_3 - \bar{\beta}_1 \end{pmatrix} \begin{pmatrix} \bar{v}_2 - \bar{v}_1 & \bar{v}_3 - \bar{v}_1 \\ \bar{a}_2 - \bar{a}_1 & \bar{a}_3 - \bar{a}_1 \end{pmatrix}^{-1}$
- 12:         Update  $(\bar{\alpha}, \bar{\beta})$  according to Eq. (4.25)
- 13:         Evaluate  $\phi^{n+1}$  according to Eq. (4.22)
- 14:         **if**  $\max[ |V(\phi_{n+1}) - \alpha_0|/\alpha_0, |A(\phi_{n+1}) - \beta_0|/\beta_0 ] \leq \text{tol}$ , pass control to next  $n$
- 15:         Set respectively  $\bar{\alpha}_1, \bar{\alpha}_2, \bar{\alpha}_3, \bar{\beta}_1, \bar{\beta}_2, \bar{\beta}_3$ , **to**  $\bar{\alpha}_2, \bar{\alpha}_3, \bar{\alpha}, \bar{\beta}_2, \bar{\beta}_3, \bar{\beta}$
- 16:         Set  $\bar{v}_1, \bar{v}_2, \bar{v}_3, \bar{a}_1, \bar{a}_2, \bar{a}_3$ , **to**  $\bar{v}_2, \bar{v}_3, V(\phi_{n+1}), \bar{a}_2, \bar{a}_3, A(\phi_{n+1})$
- 16:     **end**
- 16: **end**

---

## 4.4 Numerical results

The numerical results presented in this section are implemented using NURBS-based PetIGA [180], a high-performance isogeometric analysis software. PetIGA uses intensively algorithms and data structures from PETSc [176–179], the *Portable, Extensible Toolkit for Scientific Computation*. For the details of the cost estimates and the computational efficiency of PetIGA for different methods and problems, we refer to [180–185]. We consider a 3D configuration. The spatial domain is discretized by uniform elements in all spatial directions. The temporal discretization is done by Generalized- $\alpha$  method. The time adaptivity scheme Digital Signal Processing (DSP) [174, 175] implemented in PETSc is considered in all examples. Numerical examples are initiated with a time step size of  $\Delta t = 1.0 \times 10^{-10}$ . A cap is placed on the time-step controller so the time step would not exceed 1.0 seconds in any of the iterations. This is to maintain stability and numerical accuracy. In addition, if chosen, PETSc implements a delay on increasing a converged time-step  $\Delta t$  after a decreased one due to convergence failure. This is to prevent the adaptor from bouncing back and forth between two nearby time-steps. We are delaying the increase until three consecutive steps converge successfully to start increasing  $\Delta t$  once again. This option provides an additional layer of stability in reaching the maximum time step size specified. To check the correctness of the hand-coded Jacobian, we compare it with the finite difference’s Jacobian. The relative difference is less than  $1.0 \times 10^{-09}$  and the absolute difference was less than  $1.0 \times 10^{-25}$ , this is to be tested using quad-precision and it virtually implies the correctness of the hand-derived Jacobian. The initial condition of the phase field variable is generated using the hyperbolic tangent function as the following

$$\phi_0 = \tanh \left( \frac{\sqrt{x^2 + y^2 + z^2} - R_0}{\sqrt{2}\epsilon} \right) \quad (4.26)$$

Unless otherwise stated, we use cubic NURBS elements, each with 6 integration points per direction. In models where the electrical response of the vesicle is under investigation, the dielectric constant for electrolytes inside  $\epsilon_{in}$  and outside  $\epsilon_{out}$  the vesicle is taken as  $6.4 \times 10^{-10} \text{As/Vm}$ , and  $4.4 \times 10^{-11} \text{As/Vm}$  for the membrane  $\epsilon_m$ . The bending rigidity  $\kappa_b$  is  $1.0 \times 10^{-19} \text{J}$ . The conductivity of electrolyte inside  $\sigma_{in}$  is taken as  $0.3 \text{Sm}^{-1}$ ,  $1.2 \text{Sm}^{-1}$  for outside  $\sigma_{out}$ , and  $3.0 \times 10^{-7} \text{Sm}^{-1}$  for membrane  $\sigma_m$ . The flexoelectric constant of

the membrane  $c_1$  is taken as  $1.0 \times 10^{-10} C/m$ . These parameters are adopted based on Kotnik *et al.* [186] work. It is worth mentioning that the units to be used in all models henceforth are SI-Based normalized units in order to avoid the large order-of-magnitude difference between the variables.

We note that a detailed convergence study of a Willmore flow problem was conducted in our previous work [20] which should be consulted for more details about the convergence behavior of isogeometric analysis for this class of problems.

#### 4.4.1 Constrained Willmore flow problem

We start by considering a Willmore problem. A sphere and a prolate spheroid are modeled. For the sphere, we take the geometrical settings of the model to be later investigated for the electromechanical response. The initial 3D profile of the vesicle was constructed using Eq. (4.26) with  $R_0 = 10 \mu\text{m}$  on a computational domain  $\Omega$  of  $[-30, 30] \mu\text{m} \times [-15, 15] \mu\text{m} \times [-30, 30] \mu\text{m}$  and element count of  $[60]^3$ . We consider cubic NURBS functions and 6 integration points in each direction per element. The regularization parameter  $\varepsilon$  is set to  $2h$ , where  $h$  is the element length. In the absence of an electric field, the sphere is expected to maintain its original shape, giving it the lowest possible surface area-to-volume ratio when compared to other geometrical shapes. The energy at the stationary state converges to the exact Willmore energy, that is  $8\pi$  as shown in Fig. (4.3a). It can be seen from Fig. (4.3b) that both the surface area and the volume are kept constant over time. For the prolate spheroid model, we are considering a dimensionless setting on the computational domain  $[-7, 7]^3$ . The semi-major and minor axes are set to 2.0 and 0.5, respectively. In the absence of any additional external fields, the vesicle evolves to a dumbbell shape at the stationary state, which matches the profiles of prolate vesicles in the numerical work of Yuan *et al.* [75] and experimental observations of Yanagisawa *et al.* [187].

#### 4.4.2 Electrical response of vesicles

Here, we test the electromechanical behavior of vesicles in the absence of flexoelectricity. An approximately uniform electric field with varying magnitudes ranging from 1 to 50  $kV/m$  is applied. The initial phase field is constructed using the same settings for the Willmore problem. The computational domain is  $\Omega := [-30, 30] \mu\text{m} \times [-15, 15] \mu\text{m} \times [-30, 30] \mu\text{m}$ .

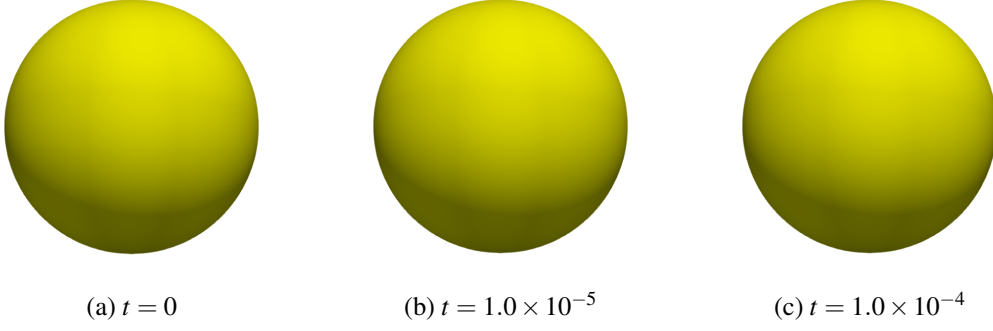


Figure 4.1: Evolution of a sphere from initial state (4.1a) to the stationary state (4.1c)

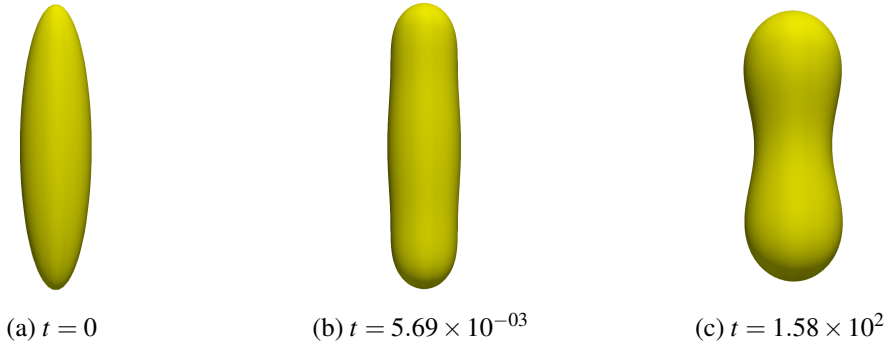


Figure 4.2: Evolution of a prolate spheroid from initial state (4.2a) to the stationary state (4.2c)

In the presence of an electric field, the vesicle is expected to deform from its original spherical shape. Numerical testing shows that the vesicle is morphologically evolving towards an oblate-like shape under the increasing magnitude of electric fields. As shown in Fig. (4.4), the total energy of the system is decreasing monotonically for  $E_0$  up to 10 kV/m, due to the absence of flexoelectric effect, which is not the case as shown later when the flexoelectric response is included. Interestingly, the bending energy of the system increases slightly as the vesicle deforms to its stationary state. This observation is also recorded, but more bluntly, as shown later for models when the flexoelectric is included. The values of  $E_0$  for which the vesicle is tested are shown in Fig. (4.5) with the corresponding values of x-y planar sections shown in Fig. (4.6). It can be seen that with increasing magnitudes of the static electric field, the vesicle semi-minor axis in the direction of the electric field decreases while the semi-major axis increases in the lateral dimension, mimicking an evolution towards an oblate setting. Although the deformations up to 10 kV/m are barely noticeable, any increase of the electric field intensity  $E_0$  beyond this value tends to significantly accelerate evolution towards an oblate-like shape. For an electric field intensity of  $E_0 = 1$  kV/m, the vesicle deforms to an oblate-like shape with



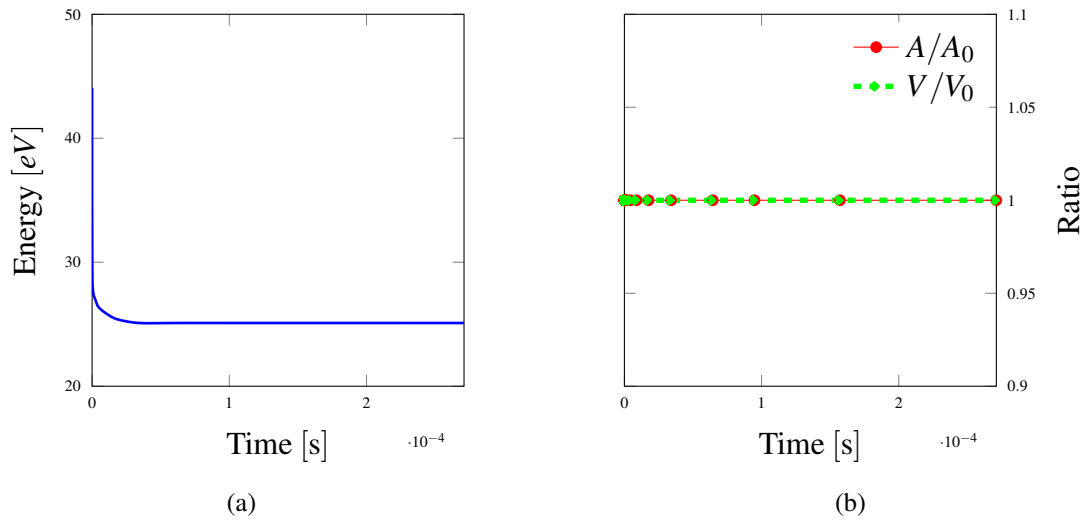


Figure 4.3: (4.3a) Willmore flow of a spherical vesicle, (4.3b) Area ratio and Volume ratio.  $R_0 = 10\mu\text{m}$  a minor axis of  $19.5275\mu\text{m}$  and a major axis of  $20.6850\mu\text{m}$ , where for  $E_0 = 50\text{ kV/m}$ , it deforms to  $17.6821\mu\text{m} \times 21.4628\mu\text{m}$  for the minor and major axes, respectively.

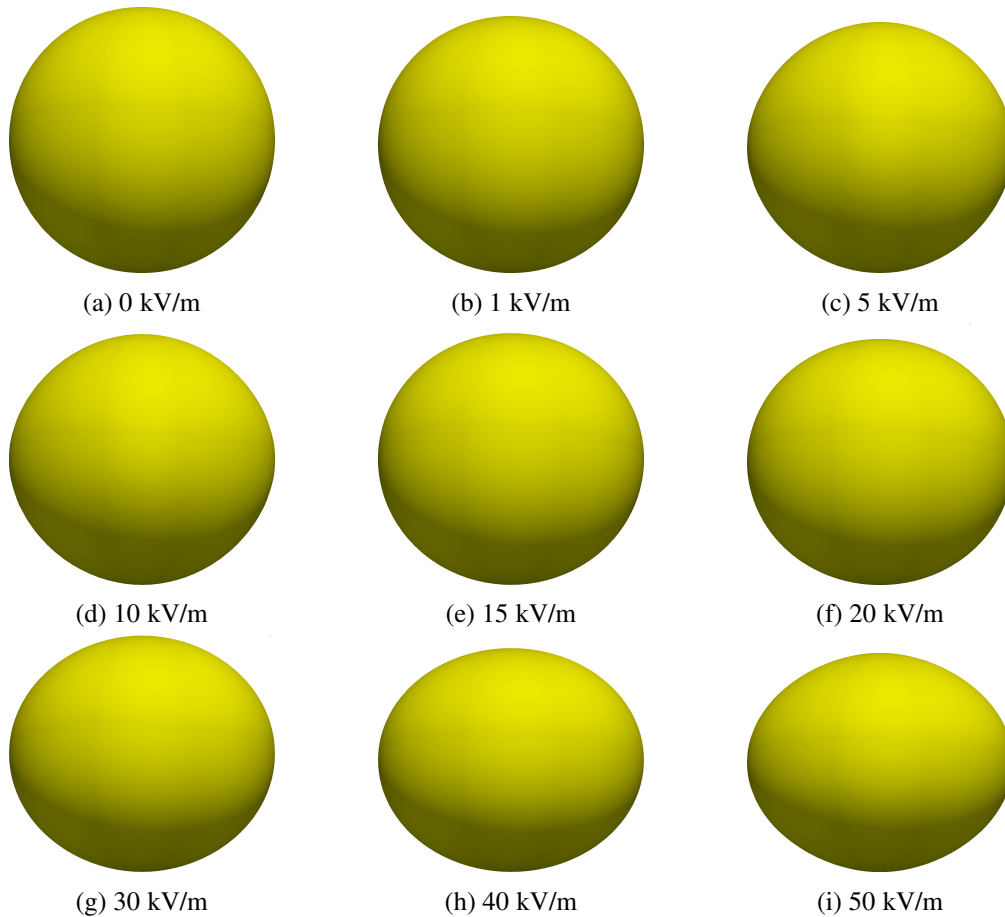


Figure 4.5: Stationary states of a vesicle subjected to electrical field ranging between (4.5b) 1 kV/m and (4.5i) 50 kV/m. Flexoelectric effect is neglected.

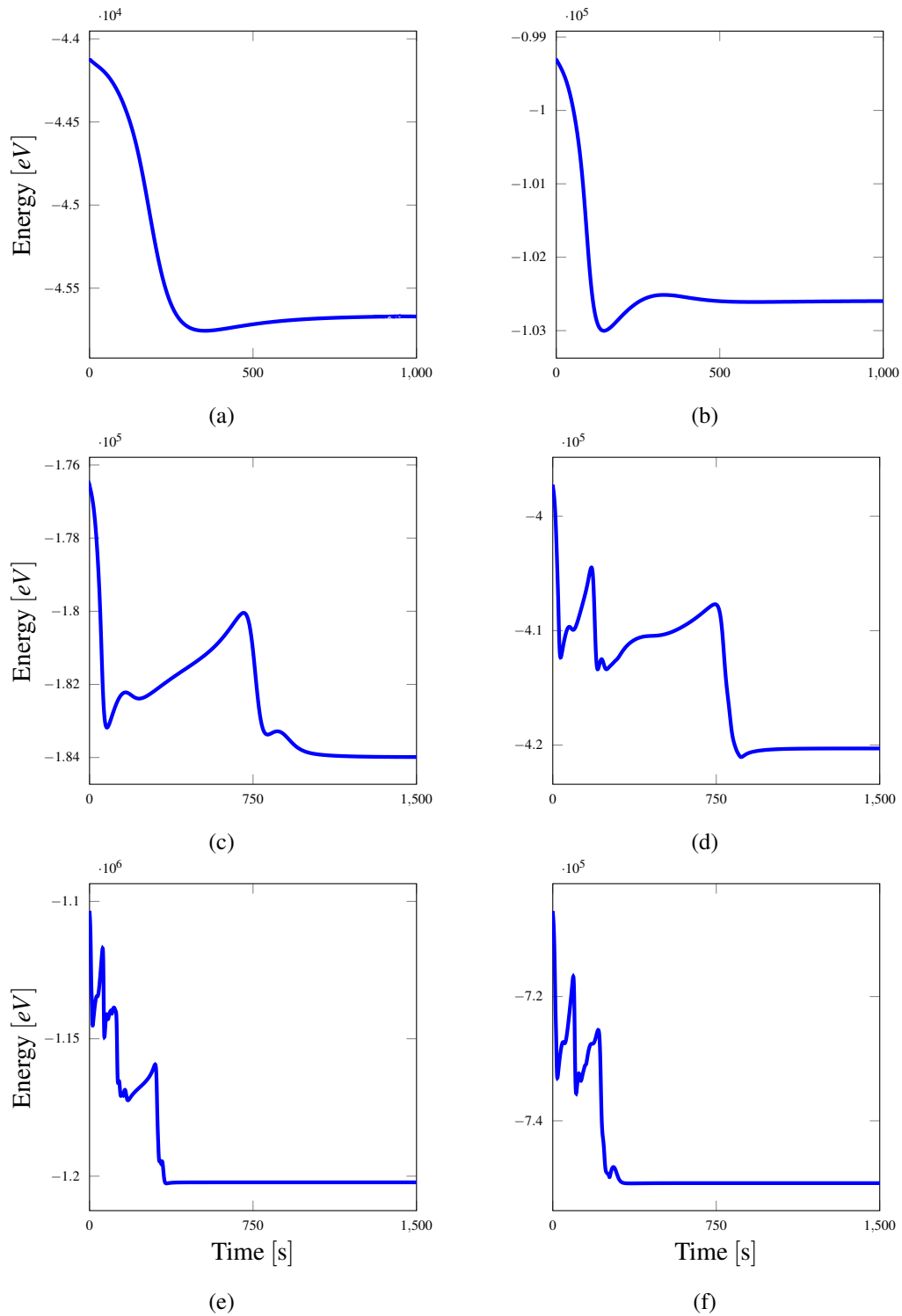


Figure 4.4: Total Energy corresponding to: (4.4a) 10 kV/m, (4.4b) 15 kV/m, (4.4c) 20 kV/m, (4.4d) 30 kV/m, (4.4e) 40 kV/m and (4.4f) 50 kV/m. Flexoelectric response of the biomembrane was neglected. Time is expressed in seconds on x-axis. Energy is expressed in electronvolt unit [eV] on y-axis.

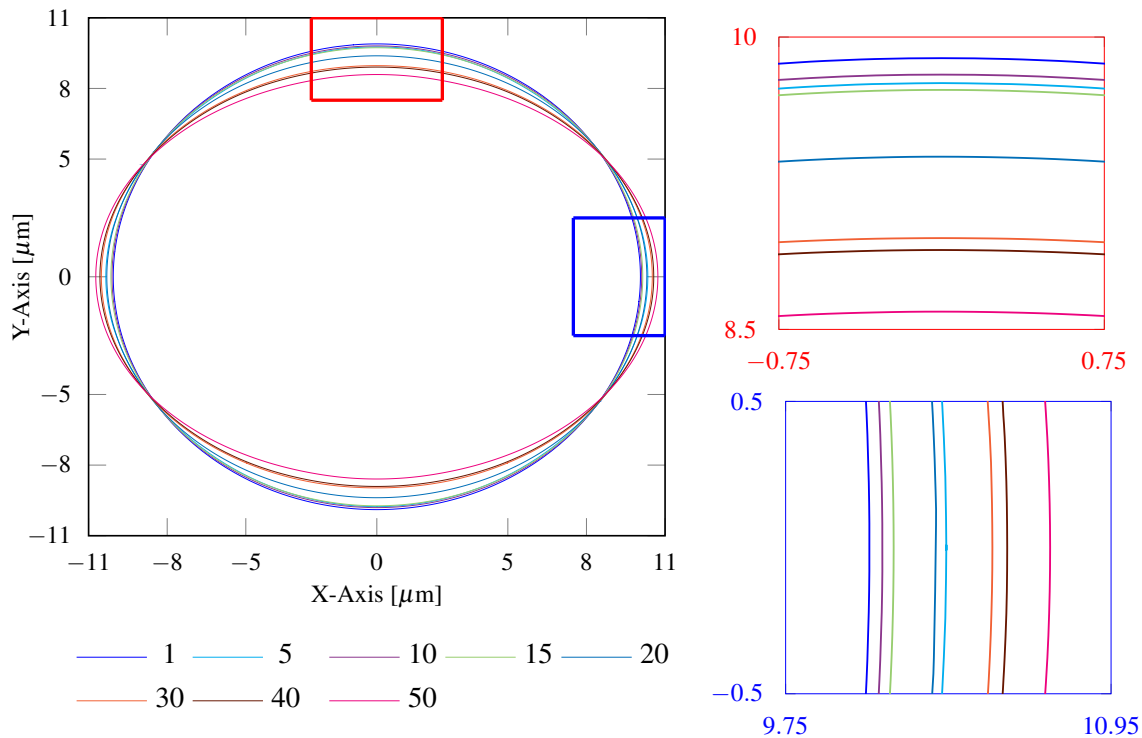


Figure 4.6: A planar section shows the temporal evolution of vesicle in absence of flexoelectric response. Electrical field with values ranging between 1-50  $kV/m$ . Both x and y axes are limited to  $[-11,11]$   $\mu m$  for more distinction.

A streamline interpolation shown in Fig. (4.7a) of the results shows that despite an initial uniform electrical field, the vesicle membrane tends to deflect the electrical charges away from the vesicle. This observation is consistent with the physical understanding of the membrane as it behaves like a capacitor, preventing charges from moving freely from the extracellular to the intracellular medium. We find out that the electric field intensity away from the vesicle is as assigned in the initial condition of the problem, while it nearly vanishes inside the vesicle as shown in Fig. (4.7b). Additionally, there is a spike in the electric field intensity at the top and the bottom of the vesicle in the direction of the electric field. This depicts an accumulation of the electric charges in those regions. Given the nature of the membrane, this observation is expected, and it indicates a good solution as it validates the physics of the biomembrane regarding its impermeable nature to ions and electric charges. Fig. (4.8) shows a projection of the electrical potential on a semi-spherical zero-level set of the phase field, i.e., the vesicle surface. Certain locations of the interface are experiencing higher values due to the rippled overlapping distribution of the electric potential. Perrier *et. al* [188] reported tubule formation in vesicles with an electric field intensity of  $90 V/mm$ , as shown in Fig. (4.8c) which might be the case for

Fig. (4.8b), however, we have not tested this beyond this point.

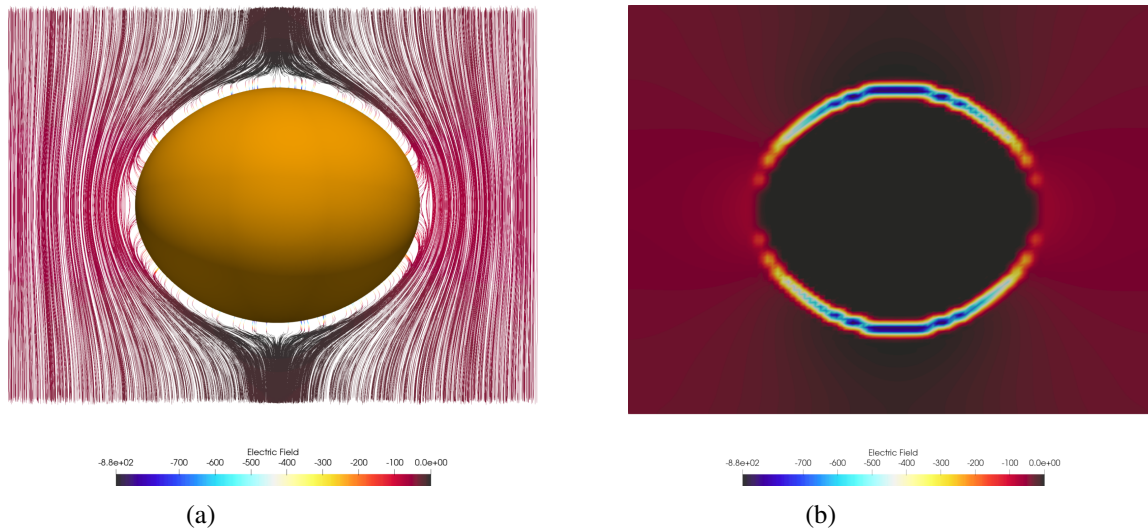


Figure 4.7: (4.7a) A streamline interpolation of the electric field shows a reorientation in direction due to the presence of the membrane. (4.7b) A planar section shows a spike in the electric field intensity at the top and the bottom of the vesicle.

The algorithm in 4.3.4 manages to accurately satisfy the constraints on surface area and volume of vesicle over the entire temporal domain. During the vesicle shape evolution, no rigid body motion or transitional movement, laterally or vertically, has been noticed. A correct implementation of the algorithm 4.3.4 ensures that the phase field profile is maintained during the simulation as shown in Figures 4.9b and 4.9a. Usually, it takes between 2-4 outer iterations to optimize the solution vector in order to satisfy the constraints within a predetermined tolerance. In addition, when implementing time adaptivity with the parameters explained previously, the time step size can be easily seen to increase steadily, indicating a significant improvement over the penalty method-based formulation. For the model with  $E_0 = 10$  kV/m, the timestep size  $\Delta t$  reaches the cap time limit of 1 second exactly after 34 steps starting from  $\Delta t = 1.0 \times 10^{-10}$ .

#### 4.4.3 Evolution of Vesicles in presence of flexoelectric effect

In this section, we test the full model by incorporating the effect of flexoelectricity. Due to a higher computational load characterized by more iterations per time step to meet the tolerances, we are considering two cases only: a)  $E_0 = 10$  and b)  $E_0 = 50$  kV/m. We solve this example in 3D Cartesian space using the same settings as in the previous examples. The polynomial order of the NURBS functions was set to 3, which are  $\mathcal{C}^2$  globally

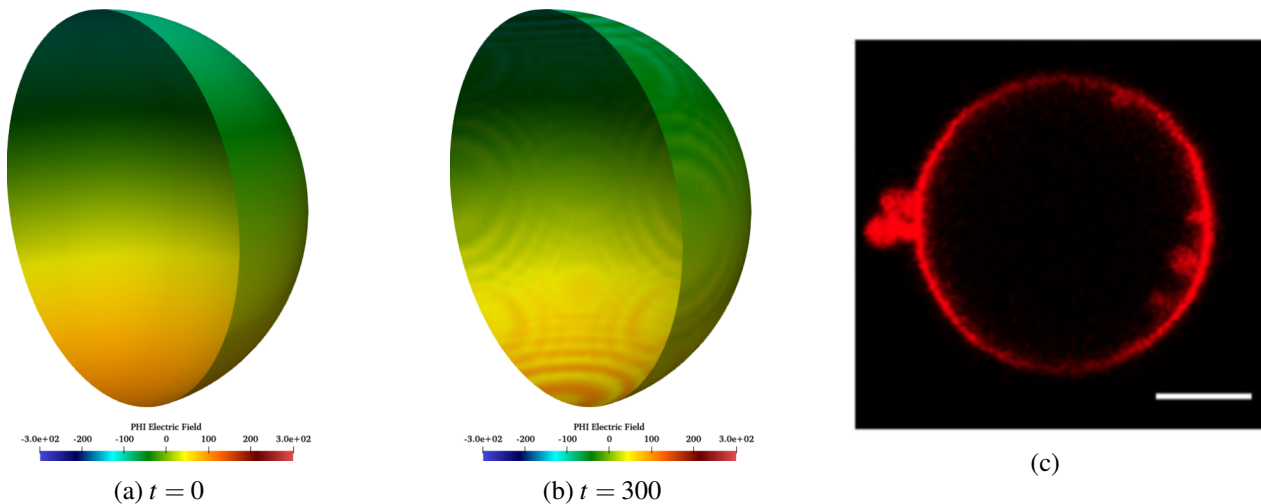


Figure 4.8: Electrical potential projected on 0-Level set of phase field at (4.8a) initial state, (4.8b) stationary state and (4.8c) tubule formation in vesicles [188]. Electric field intensity =  $10 \text{ kV/m}$ . Flexoelectric response of the biomembrane neglected.

continuous across element boundaries in absence of repeated knots. The regularization parameter  $\varepsilon$  was set to  $2h$ . This way, we ensure the diffusive region will span over 4 spatial elements on each side of the interface, and hence there is a smooth transition in phase field variable values across the interface.

The computational domain is  $\Omega := [-30, 30]\mu\text{m} \times [-15, 15]\mu\text{m} \times [-30, 30]\mu\text{m}$  which is discretized by  $80 \times 40 \times 80$  elements. Given that the solution vector ranges between -1 and 1 as defined by the hyperbolic tangent function, it is of paramount importance to run the model using extended quad-precision to mitigate any round-off errors, a feature that can be easily implemented in PETSc.

We begin by testing a vesicle subjected to  $E_0 = 10 \text{ kV/m}$  while considering the flexoelectric response of the membrane. The result revealed that the symmetry of the vesicle evolution over time breaks to form an asymmetrical shape. Asymmetric vesicle shapes in the direction of the electric field were also reported in [18] where only axisymmetric vesicles were studied.

Given that this example and the corresponding one without the flexoelectric effect – see section 4.4.2 – were run using the same parameters reveals the impact of including the flexoelectric nature of the biomembrane in the calculations. Numerical results show that the modified ALM can satisfy the constraints imposed on the system. The asymmetry of the evolution is more obvious in the case of  $E_0 = 50 \text{ kV/m}$  as shown in Fig. (4.10b).

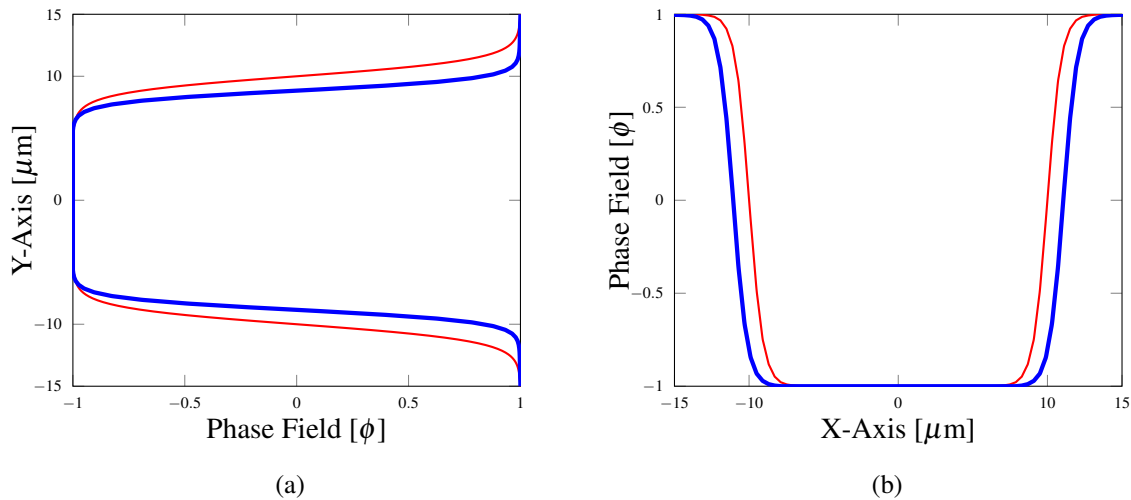


Figure 4.9: Phase field profile along: (4.9a) Y-axis, (4.9b) X-axis. Both profiles correspond to the 50 kV/m models. Red corresponds to the initial phase field profile along the axis, and blue corresponds to the phase field profile at the stationary state. The X-Axis is limited to  $[-15,15]$   $\mu\text{m}$  for comparison purposes.

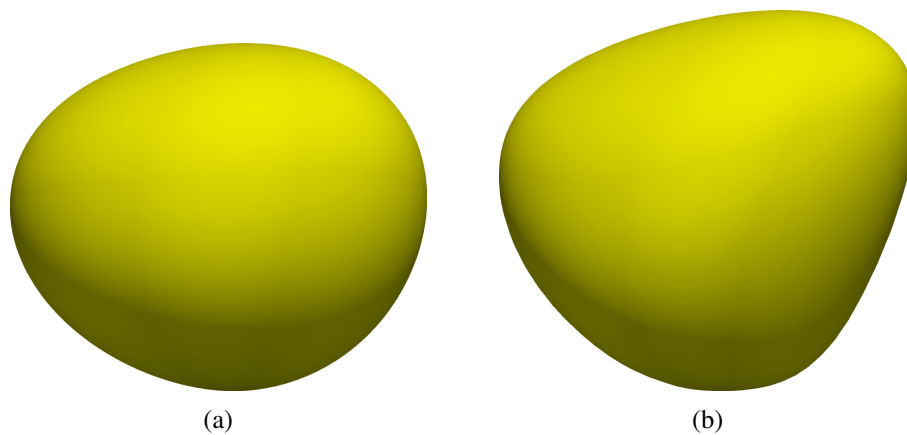


Figure 4.10: Vesicle at stationary state with flexoelectric effect included subjected to (4.10a)  $E_0 = 10$  kV/m, and (4.10b)  $E_0 = 50$  kV/m.

The impermeability nature of the biomembrane can be seen from the electrical potential across the computational domain. This phenomenon can easily be spotted by the high electric potential concentration on the outer layer of the biomembrane, where the values vary depending on the relative proximity from the source but remain relatively higher than the electrical potential inside the biomembrane. This, in turn, can be attributed to the order-of-magnitude difference between the conductivities of the biomembrane and the surrounding medium. A phase field-based interpolation of the conductivity within  $\Omega$  based on Eq. (2.20) can be seen in Fig. (4.11a), and the corresponding profile can be seen in Fig. (4.11b). It is clear from the interpolated values the capacitor-like nature of the biomembrane. One additional remark regarding the dielectric energies is that the

membrane energy is always somewhere between 0.01196% and 0.0122% of the electrolyte energy regardless of whether or not the flexoelectric response is included. To further explain the spike in the electric field magnitude as shown in Fig. (4.7b), a set of electric potential projections as shown in Fig. (4.12a) on a PF-level set of 0.3 (vesicle exterior) and -0.3 (vesicle interior) reveals that due to the impermeability of the biomembrane, the electric potential inside the vesicle is in the vicinity of zero as shown in Fig. (4.12b). Using the same scale, one can see a high concentration of electric potential on the outer side of the vesicle at the top and bottom tips, as shown in Fig. (4.12c). As expected, the electric potential mid-domain in the direction of the electric field is zero, as shown by the magenta strip in Fig. (4.12c).

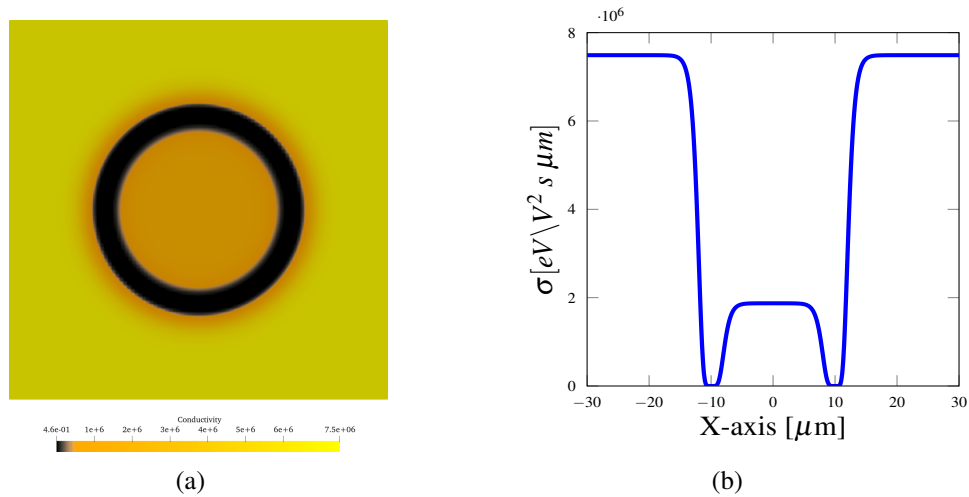


Figure 4.11: (a) PF-based interpolation of the conductivity according to Eq. 2.20, and (b) the corresponding profile.

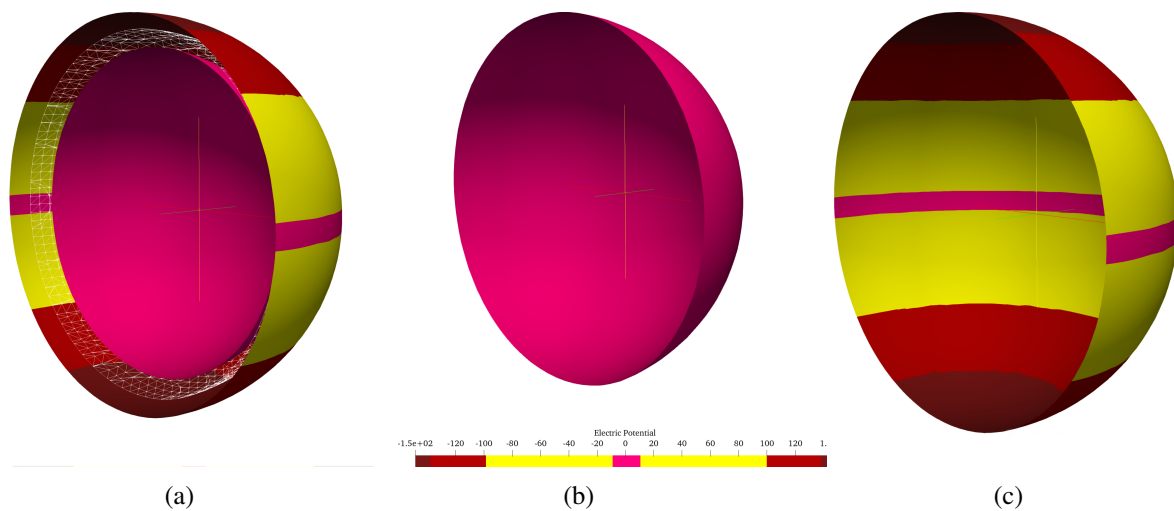


Figure 4.12: (4.12a): 0.3 and -0.3 PF-level sets with electric potential projection. Wireframe represents 0 PF-level set, (4.12b) -0.3 PF-level set, and (4.12c) 0.3 PF-level set.

We consider the vesicle has reached a stationary state when there is no more change in the total energy of the system with time. The temporal evolution of energies is plotted in  $eV$  unit in Fig. (4.13). Although the flexoelectric energy contributes slightly to the overall energy of the system, the flexoelectric response of the biomembrane plays a crucial role in the morphological evolution of the vesicles. Initially, the flexoelectric energy of the system increases quadratically over a small period of time to  $-25.21 eV$  as a reflex to the applied electric field. In the absence of an external electric field, the flexoelectric effect of the biomembrane is neglected per Equation 2.15. Considering the fundamental definition of the flexoelectricity, in the absence of any deformation, the flexoelectricity is supposed to vanish after reaching the equilibrium position, which is the case for our model as seen in Fig. (4.13b), as it drops to  $4.0256 eV$  and keeps dissipating by  $0.001 eV$  for each timestep onward. Interestingly, the bending energy of the system is increasing while the overall energy of the system is decreasing. This counter-intuitive observation can be attributed to the fact that the vesicle tends to diverge from its original spherical shape to a more compressed-shaped due to the external electric field, as shown in Fig. (4.10). By comparison, we can see from Fig. (4.13d) (Red curve), that including the flexoelectricity in the formulation tends to change the overall behavior of the vesicle over time, and hence the total energy, compared to when the flexoelectricity is neglected as shown in Fig. (4.4a) for the case of the electric field  $E_0 = 10 \text{ kV/m}$ .



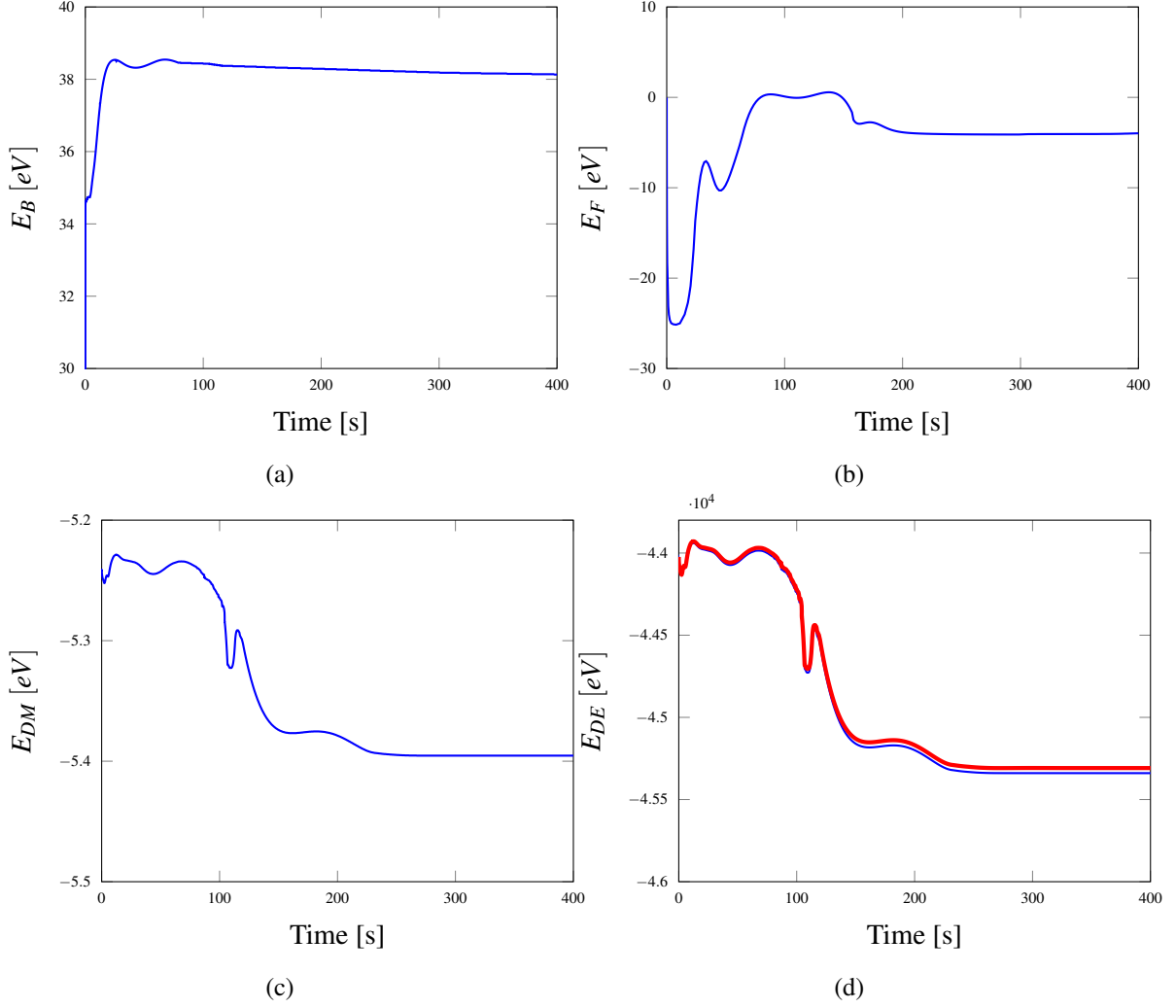


Figure 4.13: Temporal evolution of system's energies: (4.13a) Bending energy, (4.13b) Flexoelectric energy, (4.13c) Dielectric energy of the biomembrane, (4.13d) Dielectric energy of the electrolyte (Blue) and total energy of the system (Red). All energies are expressed in  $eV = 1.602 \times 10^{-19}$  Joule.

#### 4.4.4 Conductivity role in morphological evolution

Several experimental studies addressed the effect of the conductivity values of the electrolyte inside and outside the vesicle on the morphological evolution of the giant vesicles. In the context of the phase field formulation, and regardless of the conductivities values, the conductivity scalar field is affected largely by regularization parameter  $\varepsilon$  as depicted by Fig. (4.11b). For large values of  $h$  and hence  $\varepsilon$ , the numerically evaluated conductivity field would not capture the physical interpretation of the conductivity, i.e., a step drop across the membrane. For small values of  $h$ , the diffusive interface region itself is manifested by a steep transition in values representing the outside and inside of the vesicle across a smaller number of spatial elements, and hence, the phase field evolution

can not be accurately evaluated. One way to address this issue is to use local refinement that spans outward and inward of the interface as seen in [101], or by just simply increasing the mesh density over the entire computational domain. To test the effect of the ratio of the conductivity of the intracellular and extracellular electrolytes  $\sigma_{in} \setminus \sigma_{out}$ , we are fixing the value of  $\varepsilon = 2h$  and varying the ratio from 0.25 to 4.0, which represents a flipping of the values mentioned in section introductory by increasing the intracellular value by 0.1  $S/m$  and decreasing the extracellular value by the same amount. Accounting for a sphere-prolate transition, we have modified the computational domain such that  $\Omega = [-30, 30] \mu m \times [-20, 20] \mu m \times [-30, 30] \mu m$  in 3D Cartesian space with an element count of  $80 \times 60 \times 80$ . Testing with  $E_0 = 50 \text{ kV}/m$ , we can see that vesicle evolves to two stationary states depending on the conductivity ratio, i.e., to a sphere-oblate as shown in Fig. (4.16a) when the ratio is less than one, and a sphere-prolate 4.16c when the ratio is larger than one. Those observations are in good agreement with the experimental work of Dimova *et.al.* [189] as shown in Fig. (4.16).

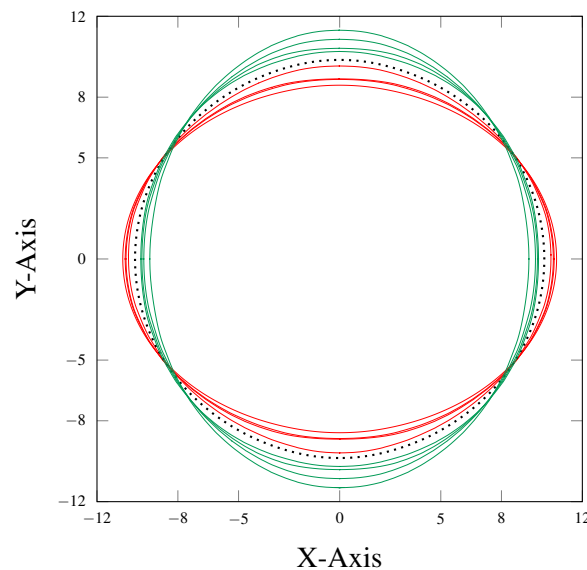


Figure 4.14: Vesicle subjected to an electric field  $E_0 = 50 \text{ kV}/m$  with varying conductivity ratio. Green represents a sphere-to-prolate morphological evolution with largest ratio value of 4, red represents a sphere-to-oblate morphological evolution with smallest value of 0.25. Dotted black profile depicts a vesicle with a conductivity ratio of 1.

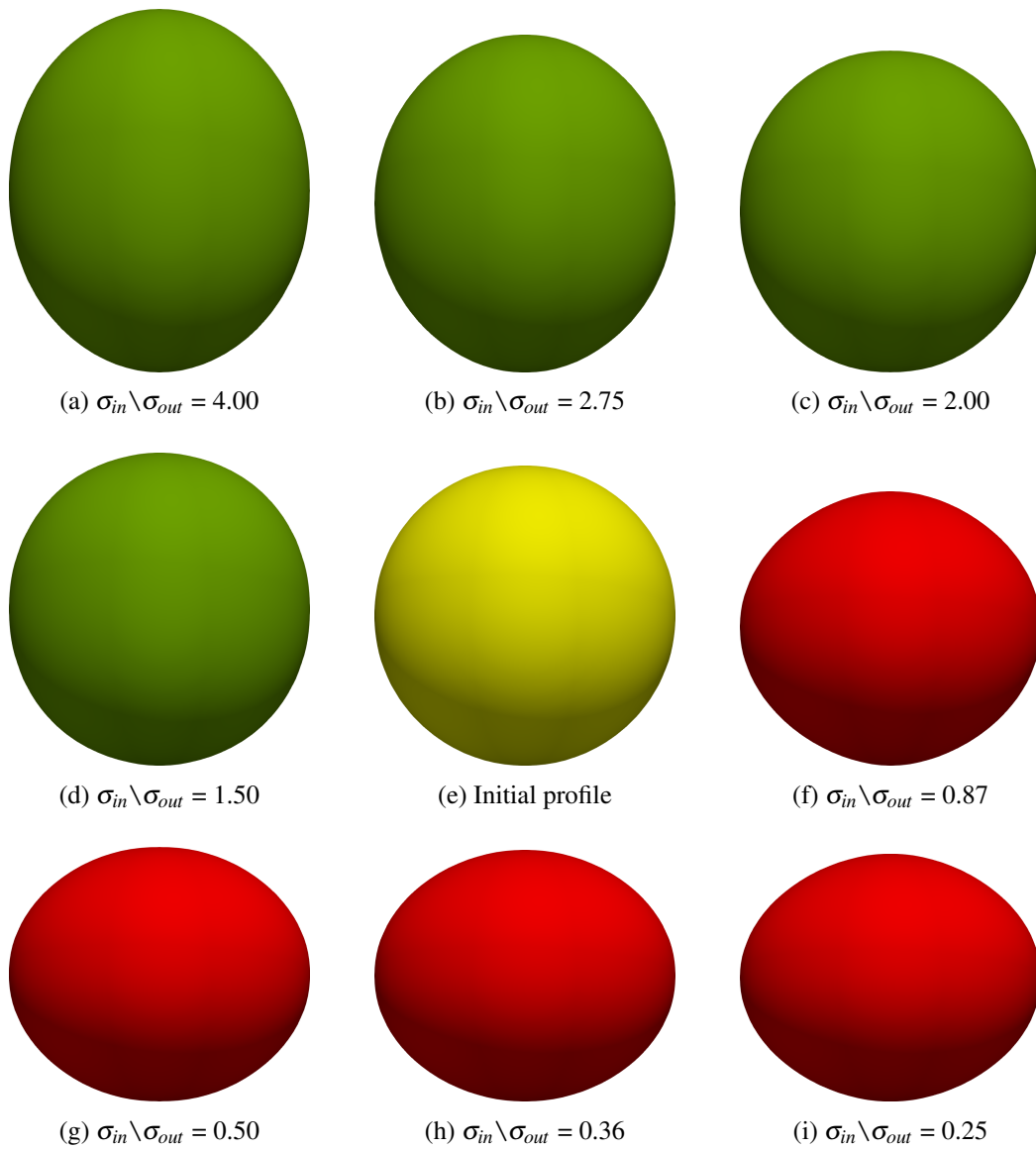


Figure 4.15: Vesicle subjected to an electric field  $E_0 = 50$  kV/m with varying conductivity ratio  $\sigma_{in} \setminus \sigma_{out}$  ranging between 4.0 and 0.25. Vesicles in green have a sphere-to-prolate evolution at stationary state. Vesicles in red have an sphere-to-oblate evolution at stationary state. Initial profile in yellow is shown in Figure 4.15e. Corresponding planer values are plotted in Figure (4.14.)

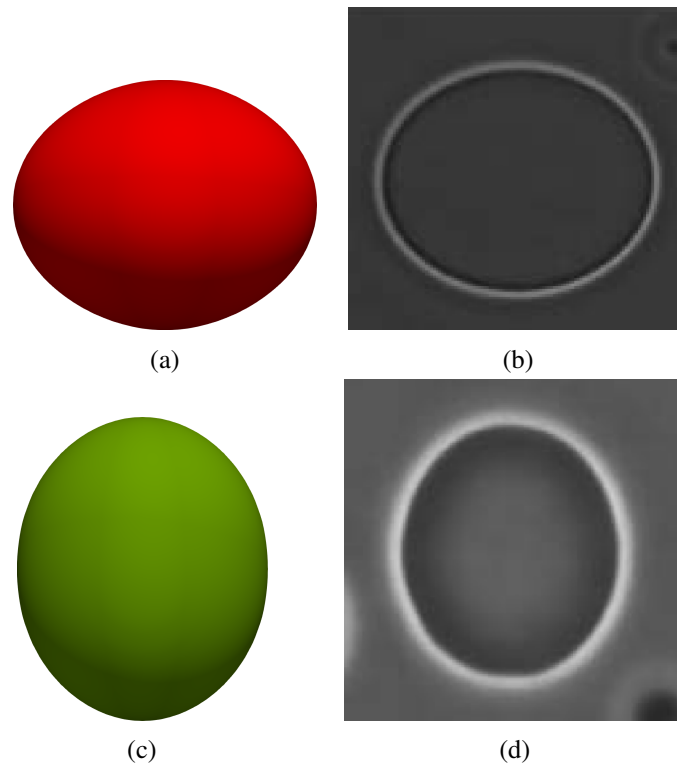


Figure 4.16: The stationary state for the extreme tested values of 0.25 and 4.0 conductivity ratios. (4.16a) shows a sphere-oblate evolution and (4.16c) shows a sphere-prolate evolution. Figures (4.16b) and (4.16d) shows the corresponding experimental observations [189] (Reproduced from Ref. [189] with permission from the Centre National de la Recherche Scientifique (CNRS) and The Royal Society of Chemistry).

We would like to mention that the data extracting for the curves, the vesicle snapshots, phase field profiles, and the conductivity profiles were done using VTK [190] files exported as binary files using PETSc writing functionalities and converted using the igakit [191].

## 4.5 Summary

In this chapter, we address several points. First, it can be seen that isogeometric analysis as a numerical tool has the ability to model and solve 4<sup>th</sup>-order PDEs in a primal variational framework at extreme efficiency and accuracy due to the abilities embedded within the NURBS functions without the need to reduce the order by creating an intermediate environment. Refinement whether by knot insertion, order increasing or both is far easier to obtain than traditional mesh-based methods. Given the wide variety of phenomena in natural sciences and engineering that are mathematically modeled by high-order PDEs, the isogeometric analysis is among the most robust methods to address such problems as the basis functions can easily attain high global continuity. On the applicational side, we

study the vesicle morphological evolution based on the electromechanical liquid-crystal model in 3D settings. This model describing the evolution of vesicles is composed of time-dependent, highly nonlinear, high-order PDEs, which are nontrivial to solve. Solving this problem requires robust numerical methods, such as isogeometric analysis. We concluded that the vesicle tends to deform under increasing magnitudes of electric fields from the original sphere shape to an oblate-like shape. This evolution is affected by many factors and requires fine-tuning several parameters, mainly the regularization parameter. But it is most affected by the method used for enforcing the constraints. The penalty method in presence of an electrical field tends to lock on the initial phase-field and prevent any evolution while a modified version of the ALM has proven to be sufficiently stable and accurate to let the phase-field evolve while satisfying the constraints over time at each time step. We show additionally the effect of including the flexoelectric nature of the biomembrane in the computation and how it affects the shape evolution as well as the effect of having different conductivity ratios. All the examples were solved based on a staggered scheme, which reduces the computational cost significantly.

# 5

## Phase-Field Navier-Stokes model for vesicle doublets hydrodynamics in incompressible fluid flow

### 5.1 Introduction

In this chapter, we study the hydrodynamics of vesicle doublet suspended in incompressible fluid flow. In section 2.4, we presented the mathematical model and the corresponding phase-field formulation for the problem, and in this chapter, we present the set of equations representing the strong form of the problem. Given that the system of Navier-Stokes equations is solved using the Residual-Based Variational MultiScale (RBVMS) method, we are presenting the RBVMS full implementation alongside the numerical formulation. The weak form of the problem is then solved within the isogeometric analysis framework. We study several configurations of vesicle doublet and investigate the effect of the inter-

action number on the vesicle doublet hydrodynamics. In addition, we study the vesicle doublet hydrodynamics in a shear flow and in a planar extensional flow. We also *fork* the well-known PetIGA [180] library to strongly impose velocity boundary conditions of certain portions of the domain to simulate a fluid junction with two inlets and two outlets.

## 5.2 The strong form

The strong form of the non-dimensional phase-field Navier-Stokes model then reads as follows:

$$\frac{\partial \phi_1}{\partial t} + \mathbf{u} \cdot \nabla \phi_1 = -\eta_\phi (g_1 - \lambda_{g1} f_1 - \lambda_{v1} + \zeta_1), \quad \text{in } \Omega \times (0, T), \quad (5.1)$$

$$\frac{\partial \phi_2}{\partial t} + \mathbf{u} \cdot \nabla \phi_2 = -\eta_\phi (g_2 - \lambda_{g2} f_2 - \lambda_{v2} + \zeta_2), \quad \text{in } \Omega \times (0, T), \quad (5.2)$$

$$\begin{aligned} \frac{\partial \mathbf{u}}{\partial t} + \mathbf{u} \cdot \nabla \mathbf{u} + \nabla p - \frac{1}{Re} \nabla \cdot (2\mu^* \mathbf{D}(\mathbf{u})) = \\ \nabla \cdot (\delta_{\varepsilon_1} \mathbf{P} \lambda_1) + (g_1 - \lambda_{g1} f_1 - \lambda_{v1} + \zeta_1) \nabla \phi_1 + \\ \nabla \cdot (\delta_{\varepsilon_2} \mathbf{P} \lambda_2) + (g_2 - \lambda_{g2} f_2 - \lambda_{v2} + \zeta_2) \nabla \phi_2, \end{aligned} \quad (5.3)$$

$$\text{in } \Omega \times (0, T),$$

$$f_1 = \varepsilon \Delta \phi_1 - \frac{1}{\varepsilon_1} (\phi_1^2 - 1) \phi_1, \quad \text{in } \Omega \times (0, T), \quad (5.4)$$

$$f_2 = \varepsilon \Delta \phi_2 - \frac{1}{\varepsilon_2} (\phi_2^2 - 1) \phi_2, \quad \text{in } \Omega \times (0, T), \quad (5.5)$$

$$g_1 = \frac{1}{Re Ca} \left( \Delta f_1 - \frac{1}{\varepsilon_1^2} (3\phi_1^2 - 1) f_1 \right), \quad \text{in } \Omega \times (0, T), \quad (5.6)$$

$$g_2 = \frac{1}{Re Ca} \left( \Delta f_2 - \frac{1}{\varepsilon_2^2} (3\phi_2^2 - 1) f_2 \right), \quad \text{in } \Omega \times (0, T), \quad (5.7)$$

$$\nabla \cdot \mathbf{u} = 0, \quad \text{in } \Omega \times (0, T), \quad (5.8)$$

$$\xi \varepsilon_1^2 \nabla \cdot (\phi_1^2 \nabla \lambda_1) + \delta_{\varepsilon_1} \mathbf{P} : \nabla \mathbf{u} = 0, \quad \text{in } \Omega \times (0, T), \quad (5.9)$$

$$\xi \varepsilon_2^2 \nabla \cdot (\phi_2^2 \nabla \lambda_2) + \delta_{\varepsilon_2} \mathbf{P} : \nabla \mathbf{u} = 0, \quad \text{in } \Omega \times (0, T), \quad (5.10)$$

$$A_1 = A_2 = A_0 \quad \text{for } (0, T), \quad (5.11)$$

$$V_1 = V_2 = V_0 \quad \text{for} \quad (0, T), \quad (5.12)$$

$$\phi_1 = \phi_2 = \phi_b \quad \text{on} \quad \partial\Omega_\phi \times (0, T), \quad (5.13)$$

$$\mathbf{u} = \mathbf{u}_b \quad \text{on} \quad \partial\Omega_D \times (0, T), \quad (5.14)$$

$$f_1 = f_2 = f_b \quad \text{on} \quad \partial\Omega_f \times (0, T), \quad (5.15)$$

$$\lambda_1 = \lambda_2 = \lambda_b \quad \text{on} \quad \partial\Omega_\lambda \times (0, T), \quad (5.16)$$

$$(2\mu \mathbf{D}(\mathbf{u}) - p\mathbf{I}) \cdot \mathbf{m} = 0 \quad \text{in} \quad \partial\Omega_N \times (0, T), \quad (5.17)$$

$$\phi_1(0) = \phi_2(0) = \phi_0 \quad \text{in} \quad \Omega, \quad (5.18)$$

$$\mathbf{u}(0) = \mathbf{u}_0 \quad \text{in} \quad \Omega, \quad (5.19)$$

where the Lagrange multipliers  $\lambda_{g_i}$  and  $\lambda_{v_i}$  in equations [5.1], [5.2] and [5.3] can be calculated such that the time derivative of the volume and the global area constraint are zeros, which gives the following system of equations:

$$\lambda_{v_i} \int_{\Omega} d\Omega + \lambda_{g_i} \int_{\Omega} f_i d\Omega = \int_{\Omega} \left( \frac{1}{\eta_\phi} \mathbf{u} \cdot \nabla \phi_i + g_i + \varsigma_i \right) d\Omega + \frac{1}{2\Delta t} (V_0 - V) \quad (5.20)$$

$$\lambda_{v_i} \int_{\Omega} f_i d\Omega + \lambda_{g_i} \int_{\Omega} f_i^2 d\Omega = \int_{\Omega} \left( \frac{1}{\eta_\phi} \mathbf{u} \cdot \nabla \phi_i + g_i + \varsigma_i \right) f_i d\Omega - \frac{1}{2\Delta t} (A_0 - A) \quad (5.21)$$

Those two equations then can be solved after each converged time step to update the multipliers, where the penalty terms on the RHS are added to prevent error accumulation and provide more accuracy to the solution [43, 119, 163]. The parameter  $\xi$  in Equations (5.9-5.10) is a regularization spatially constant parameter with a positive value, which based on the conclusions and recommendations of [119] will be set to 1.0 throughout the entire research.

### 5.3 Numerical formulation and RBVMS implementation

The strong form in the previous section is solved using the isogeometric analysis. The Galerkin NURBS-based IGA is used to solve the set of advection-diffusion equations. Isogeometric analysis is a superclass of finite element analysis. It incorporates the *hpk*-



Refinement, i.e., the ability to increase both continuity and order, in addition to a set of advantages like the ability to present the exact geometry of the model compared to an approximate geometry in classical FEA. On the other hand, Navier-Stokes equations are solved using the residual-based variational multiscale method (RBVMS) proposed by Bazilevs et. al. [192]. The idea of RBVMS is that the decomposition of the fine and coarse scale equations is exact, in the sense that the solution to those equations will give the exact solution to the original variational problem of Navier-Stokes equations. The process starts by approximating the fine-scale equations analytically and then substituting them into the coarse-scale equations which are in turn solved numerically. We start with a direct-sum decomposition of the trial solution and weighting function spaces  $\mathcal{S}$  into coarse-scale and fine-scale subspaces,  $\bar{\mathcal{S}}$  and  $\mathcal{S}'$ , respectively,

$$\mathcal{S} = \bar{\mathcal{S}} \oplus \mathcal{S}' \quad (5.22)$$

where  $\bar{\mathcal{S}}$  is assumed to be a finite-dimensional space of the coarse-scale and  $\mathcal{S}'$  is the infinite-dimensional space of the fine-scale subspaces. The trial solution functions of the velocity and pressure fields  $\bar{\mathcal{S}}_{\mathbf{u}}$  and  $\bar{\mathcal{S}}_p$  are defined as

$$\bar{\mathcal{S}}_{\mathbf{u}} = \{\mathbf{u} | \mathbf{u}(\cdot, t) \in (H^1(\Omega))^d, \quad \mathbf{u} = \mathbf{u}_b \quad \text{on} \quad \partial\Omega_D\} \quad (5.23)$$

$$\bar{\mathcal{S}}_p = \{p | p(\cdot, t) \in L^2(\Omega), \quad \int_{\Omega} p \, d\Omega = 0 \quad \text{if} \quad \partial\Omega = \partial\Omega_D\} \quad (5.24)$$

where  $L^2(\Omega)$  is the space of scalar-valued functions that are square-integrable on  $\Omega$  with square integrable first derivative, and  $(H^1(\Omega))^d$  being the Sobolev space of vector-valued square-integrable functions on  $\Omega$  with square integrable first derivatives, respectively. The test functions for the velocity and pressure  $\bar{\mathcal{V}}_{\mathbf{u}}$  and  $\bar{\mathcal{V}}_p$  are identical to the trial solution functions spaces, except for the fact that the weighting functions for the velocity field  $\mathbf{w}$  vanish on the essential boundary.

Assuming  $\mathbf{U} = \{\mathbf{u}, p\} \in \mathcal{S}$ , the variational formulation of Navier-Stokes equations reads as follows: Find  $\mathbf{U} = \{\mathbf{u}, p\} \in \mathcal{S}$  such that  $\forall \mathbf{V} = \{\mathbf{w}, q\} \in \mathcal{S}$ :

$$\int_{\Omega} \mathbf{w} \cdot \left( \frac{\partial \mathbf{u}}{\partial t} + \mathbf{u} \cdot \nabla \mathbf{u} - \mathbf{b} \right) d\Omega + \int_{\Omega} \mathbf{D}(\mathbf{w}) : \mathcal{S}(\mathbf{u}, p) d\Omega + \int_{\Omega} \nabla \mathbf{w} : \mathbf{B} d\Omega + \int_{\Omega} q \nabla \cdot \mathbf{u} d\Omega = 0 \quad (5.25)$$

where  $\mathbf{S}(\mathbf{u}, p) = \frac{2\mu^*}{Re} \mathbf{D}(\mathbf{u}) - p\mathbf{I}$  is the stress tensor. The given body force  $\mathbf{b}$  defined per unit volume, is decomposed into two components, i.e., the gradient of the phase field scaled by the source term in the evolution equation,  $(g - \lambda_{g_i} f - \lambda_{v_i} + \zeta_i) \nabla \phi$  as in the first term of Eq. [5.25], and the gradient of  $\mathbf{B} = \delta_\varepsilon \mathbf{P} \lambda$ , which after expressed in the weak form results in the third term of the aforementioned equation. If existed, an additional term can be included in Eq. [5.25] to account for prescribed traction on the boundary.

By virtue of Eq. [5.22], both the velocity and pressure fields and the corresponding weighting functions can also be decomposed into their coarse and fine-scale components, that is:

$$\mathbf{u} = \bar{\mathbf{u}} + \mathbf{u}', \quad p = \bar{p} + p', \quad \mathbf{w} = \bar{\mathbf{w}} + \mathbf{w}', \quad q = \bar{q} + q'. \quad (5.26)$$

Using a linear  $H^1$ -projector, the trial solution  $\mathbf{U} = \{\mathbf{u}, p\}$  can be decomposed into its coarse and fine-scale approximation as follows:

$$\bar{\mathbf{U}} = \bar{\mathbb{P}} \mathbf{U}, \quad \mathbf{U}' = \mathbf{U} - \bar{\mathbb{P}} \mathbf{U} = (\mathbb{I} - \bar{\mathbb{P}}) \mathbf{U}. \quad (5.27)$$

where  $\bar{\mathbb{I}}$  is the identity operator and  $\bar{\mathbb{P}}$  is the projection operator. Similarly, the weighting functions can be decomposed into the coarse and fine-scale as follows:

$$\bar{\mathbf{W}} = \bar{\mathbb{P}} \mathbf{W}, \quad \mathbf{W}' = \mathbf{W} - \bar{\mathbb{P}} \mathbf{W} = (\mathbb{I} - \bar{\mathbb{P}}) \mathbf{W}. \quad (5.28)$$

The solution  $\mathbf{U} = \{\mathbf{u}, p\}$  can then be obtained by approximating the fine-scale solution analytically as a function of the coarse-scale residual and the coarse-scale solution and then substituted into the coarse-scale equations, which are to be solved numerically. The approximation of the fine-scale solution can be written as follows:

$$\tilde{\mathbf{U}}' = \begin{Bmatrix} \tilde{\mathbf{u}}' \\ \tilde{p}' \end{Bmatrix} = -\tau \mathbf{Res}(\mathbf{U}^h) \quad (5.29)$$

where  $\mathbf{U}^h$  replaced  $\bar{\mathbf{U}}$ . In Eq. [5.29],  $\tau$  is an element-wise matrix-valued stabilization parameter defined on the diagonal with two components, i.e.,  $\tau_m$  and  $\tau_c$ , such that:

$$\tau = \begin{bmatrix} \tau_m \mathbf{I}_{3 \times 3} & \mathbf{0}_3 \\ \mathbf{0}_3^T & \tau_c \end{bmatrix}$$

The residual of  $\mathbf{U}^h$  is defined by the two components  $r_m(\mathbf{u}^h, p^h)$  and  $r_c(\mathbf{u}^h)$ , corresponding

to the linear momentum and continuity residuals, respectively. Following this, the fine-scale velocity field can be defined as:

$$\mathbf{u}' = -\tau_m r_m(\mathbf{u}^h, p^h) \quad (5.30)$$

with  $\tau_m$  being:

$$\tau_m = \left( \frac{4}{\Delta t^2} + \mathbf{u}^h \cdot \mathbf{G} \mathbf{u}^h + \mathcal{C}_1 \left( \frac{\mu_o}{Re} \right)^2 \mathbf{G} : \mathbf{G} \right)^{-1/2} \quad (5.31)$$

and  $r_m(\mathbf{u}^h, p^h)$  being:

$$r_m(\mathbf{u}^h, p^h) = \left( \frac{\partial \mathbf{u}^h}{\partial t} + \mathbf{u}^h \cdot \nabla \mathbf{u}^h - \mathbf{b}^h \right) - \nabla \cdot \mathbf{S}(\mathbf{u}^h, p^h) - \nabla \cdot \mathbf{B}^h \quad (5.32)$$

The fine-scale pressure field can also be defined as:

$$p' = -\tau_c r_c(\mathbf{u}^h) \quad (5.33)$$

with  $\tau_c$  defined as:

$$\tau_c = (\text{tr}(\mathbf{G}) \tau_m)^{-1}, \quad \text{where } \text{tr}(\mathbf{G}) \text{ is the trace of matrix } \mathbf{G}, \quad (5.34)$$

and  $r_c(\mathbf{u}^h)$  defined as:

$$r_c(\mathbf{u}^h) = \nabla \cdot \mathbf{u}^h \quad (5.35)$$

In Eq. [5.31],  $\mathbf{G}$  is the element metric tensor [193], and  $\mathcal{C}_1$  is a positive mesh-independent constant, which will be set to  $6\mathcal{P}^4$  throughout this study, where  $\mathcal{P}$  is the order of the NURBS-basis function. Further details about RBVMS method and its implementation can be found in Bazilevs et. al. [192]. The equations (5.9) and (5.10) serve the purpose of ensuring local inextensibility constraint of vesicles doublet, i.e., preventing the membrane from stretching and preserving the surface area. This was first theorized by Aland et. al. [119], by introducing a spatially varying Lagrange multiplier  $\lambda_i$  which resembles the tension forces on the membrane interface in the form of  $\nabla \cdot (\delta_\varepsilon \mathbf{P} \lambda_i)$ , where  $\mathbf{P}$  is the tangential projection operator and  $\delta_\varepsilon$  is the diffusive interface approximation of the surface delta function. The inextensibility constraint  $\nabla_s \cdot \mathbf{u} = \mathbf{P} : \nabla \mathbf{u} = 0$  is extended to the whole domain away from the interface by equations (5.9) and (5.10), in which, both equations reduces to  $\Delta \lambda_i$  away from the vesicle interface since  $\delta_\varepsilon \approx 0$ , and reduces to the

inextensibility constraint  $\mathbf{P} : \nabla \mathbf{u} = \mathbf{0}$  in the vicinity of the interface, hence, ensuring the local inextensibility.

As shown later, the weak form of Navier-Stokes equations will consist of terms obtained using the standard Galerkin method, in addition to stabilization terms and terms produced by the RBVMS method itself. On the other hand, the weak forms for the evolution equations (5.1) and (5.2), the intermediate equations (5.4) and (5.5), and the local inextensibility equations (5.9) and (5.10) are obtained using standard Galerkin method. The infinite-dimensional trial solution functions spaces  $\bar{\mathcal{S}}_f$ ,  $\bar{\mathcal{S}}_\phi$  and  $\bar{\mathcal{S}}_\lambda$  are defined as

$$\bar{\mathcal{S}}_f = \{f | f(.,t) \in H^2(\Omega), \quad f = f_b \quad \text{on } \partial\Omega_f\} \quad (5.36)$$

$$\bar{\mathcal{S}}_\phi = \{\phi | \phi(.,t) \in H^1(\Omega), \quad \phi = \phi_b \quad \text{on } \partial\Omega_\phi\} \quad (5.37)$$

$$\bar{\mathcal{S}}_\lambda = \{\lambda | \lambda(.,t) \in H^1(\Omega), \quad \lambda = \lambda_b \quad \text{on } \partial\Omega_\lambda\} \quad (5.38)$$

and the test functions  $\bar{\mathcal{V}}_f$ ,  $\bar{\mathcal{V}}_\phi$  and  $\bar{\mathcal{V}}_\lambda$  are defined similarly to the trial solution functions spaces but with homogeneous Dirichlet boundary conditions. Note that in what follows, the finite-dimensional approximation of a function space  $\square$  will be denoted by  $\square^h$ .

## 5.4 The weak form

The weak form of the transport equations, the Navier-Stokes equation, and the local inextensibility constraint equations are written as follows: Find  $\mathbf{u} \in \bar{\mathcal{S}}_{\mathbf{u}}$ ,  $p \in \bar{\mathcal{S}}_p$ ,  $f_1, f_2 \in \bar{\mathcal{S}}_f$ ,  $\phi_1, \phi_2 \in \bar{\mathcal{S}}_\phi$ , and  $\lambda_1, \lambda_2 \in \bar{\mathcal{S}}_\lambda$ , such that:  $\forall \mathbf{w} \in \bar{\mathcal{V}}_{\mathbf{u}}$ ,  $q \in \bar{\mathcal{V}}_p$ ,  $l_1, l_2 \in \bar{\mathcal{V}}_f$ ,  $r_1, r_2 \in \bar{\mathcal{V}}_\phi$ , and  $s_1, s_2 \in \bar{\mathcal{V}}_\lambda$ :

$$B(\{\mathbf{w}, q, l_1, l_2, r_1, r_2, s_1, s_2\}, \{\mathbf{u}, p, f_1, f_2, \phi_1, \phi_2, \lambda_1, \lambda_2\}) = L(\{\mathbf{w}, r\}), \quad \text{and} \quad (5.39)$$

$$\begin{aligned}
B(\{\mathbf{w}, q, l_1, l_2, r_1, r_2, s_1, s_2\}, \{\mathbf{u}, p, f_1, f_2, \phi_1, \phi_2, \lambda_1, \lambda_2\}) = & \\
& \left( \mathbf{w}, \frac{\partial \mathbf{u}}{\partial t} + \mathbf{u} \cdot \nabla \mathbf{u} \right)_{\Omega} + \left( \mathbf{D}(\mathbf{w}) : \mathcal{S}(\mathbf{u}, p) \right)_{\Omega} + \left( q, \nabla \cdot \mathbf{u} \right)_{\Omega} + \\
& \left( \mathbf{u} \cdot \nabla \mathbf{w} + \nabla q, \tau_m r_m(\mathbf{u}, p) \right)_{\Omega} + \left( \nabla \cdot \mathbf{w}, \tau_c r_c(\mathbf{u}) \right)_{\Omega} - \left( \mathbf{w} \cdot \nabla \mathbf{u}, \tau_m r_m(\mathbf{u}, p) \right)_{\Omega} - \\
& \left( \nabla \mathbf{w}, \tau_m r_m(\mathbf{u}, p) \otimes \tau_m r_m(\mathbf{u}, p) \right)_{\Omega} + \\
& \left( l_1, f_1 \right)_{\Omega} + \left( \nabla l_1, \varepsilon_1 \nabla \phi_1 \right)_{\Omega} + \left( l_1, \frac{1}{\varepsilon_1} (\phi_1^2 - 1) \phi_1 \right)_{\Omega} + \\
& \left( l_2, f_2 \right)_{\Omega} + \left( \nabla l_2, \varepsilon_2 \nabla \phi_2 \right)_{\Omega} + \left( l_2, \frac{1}{\varepsilon_2} (\phi_2^2 - 1) \phi_2 \right)_{\Omega} - \\
& \left( r_1, \frac{\partial \phi_1}{\partial t} + \mathbf{u} \cdot \nabla \phi_1 \right)_{\Omega} + \left( r_1, \eta_{\phi 1} (g_1 - \lambda_{g 1} f_1 + \psi_1) \right)_{\Omega} + \\
& \left( r_2, \frac{\partial \phi_2}{\partial t} + \mathbf{u} \cdot \nabla \phi_2 \right)_{\Omega} + \left( r_2, \eta_{\phi 2} (g_2 - \lambda_{g 2} f_2 + \psi_2) \right)_{\Omega} + \\
& \left( \nabla \mathbf{s}_1, \xi \varepsilon_1^2 \phi_1^2 \nabla \lambda_1 \right)_{\Omega} + \left( s_1, \delta_{\varepsilon 1} \mathbf{P} : \nabla \mathbf{u} \right)_{\Omega} - \left( \nabla \mathbf{s}_2, \xi \varepsilon_2^2 \phi_2^2 \nabla \lambda_2 \right)_{\Omega} + \left( s_2, \delta_{\varepsilon 2} \mathbf{P} : \nabla \mathbf{u} \right)_{\Omega}
\end{aligned} \tag{5.40}$$

$$\begin{aligned}
L(\{\mathbf{w}, r\}) = & \left( \mathbf{w} \cdot \mathbf{b}_1 \right)_{\Omega} + \left( \mathbf{w} \cdot \mathbf{b}_2 \right)_{\Omega} - \left( \nabla \mathbf{w} : \mathbf{B}_1 \right)_{\Omega} - \left( \nabla \mathbf{w} : \mathbf{B}_2 \right)_{\Omega} + \\
& \left( r, \eta_{\phi 1} \lambda_{v 1} \right)_{\Omega} + \left( r, \eta_{\phi 2} \lambda_{v 2} \right)_{\Omega}
\end{aligned} \tag{5.41}$$

where  $(\cdot, \cdot)_{\Omega}$  is the  $\mathcal{L}^2$  inner product with respect to the domain  $\Omega$ ,  $\mathbf{A} : \mathbf{B}$  denotes the double contraction of the two tensors  $\mathbf{A}$  and  $\mathbf{B}$ , and  $\mathbf{a} \otimes \mathbf{b}$  is the tensor product of vectors  $\mathbf{a}$  and  $\mathbf{b}$ .

### 5.4.1 The semi-discrete formulation

The semi-discrete formulation of Eq. (5.39) can be stated as following:

find  $\mathbf{u}^h \in \overline{\mathcal{S}}_{\mathbf{u}}^h$ ,  $p^h \in \overline{\mathcal{S}}_p^h$ ,  $f_1^h, f_2^h \in \overline{\mathcal{S}}_f^h$ ,  $\phi_1^h, \phi_2^h \in \overline{\mathcal{S}}_{\phi}^h$ , and  $\lambda_1^h, \lambda_2^h \in \overline{\mathcal{S}}_{\lambda}^h$ , such that:  $\forall \mathbf{w}^h \in \overline{\mathcal{V}}_{\mathbf{u}}^h$ ,  $q^h \in \overline{\mathcal{V}}_p^h$ ,  $l_1^h, l_2^h \in \overline{\mathcal{V}}_f^h$ ,  $r_1^h, r_2^h \in \overline{\mathcal{V}}_{\phi}^h$ , and  $s_1^h, s_2^h \in \overline{\mathcal{V}}_{\lambda}^h$ :

$$B(\{\mathbf{w}^h, q^h, l_1^h, l_2^h, r_1^h, r_2^h, s_1^h, s_2^h\}, \{\mathbf{u}^h, p^h, f_1^h, f_2^h, \phi_1^h, \phi_2^h, \lambda_1^h, \lambda_2^h\}) - L(\{\mathbf{w}^h, r^h\}) = 0 \tag{5.42}$$

with the test function and the corresponding trial solution functions defined as follows:

$$\begin{aligned}
\mathbf{w}^h &= \sum_{A=1}^{n_b} N_A(x) \mathbf{w}_A, & \mathbf{u}^h &= \sum_{A=1}^{n_b} N_A(x) \mathbf{u}_A \\
q^h &= \sum_{A=1}^{n_b} N_A(x) q_A, & p^h &= \sum_{A=1}^{n_b} N_A(x) p_A \\
f_i^h &= \sum_{A=1}^{n_b} N_A(x) f_{Ai}, & l^h &= \sum_{A=1}^{n_b} N_A(x) l_A \\
\phi_i^h &= \sum_{A=1}^{n_b} N_A(x) \phi_{Ai}, & r^h &= \sum_{A=1}^{n_b} N_A(x) r \\
\lambda_i^h &= \sum_{A=1}^{n_b} N_A(x) \lambda_{Ai}, & s^h &= \sum_{A=1}^{n_b} N_A(x) s
\end{aligned} \tag{5.43}$$

where  $N_A(x)$  is NURBS function [169], defined recursively over the parametric space, and  $\phi_i^h$  - for example - is the control variable for the phase-field parameter, and  $n_b$  is the number of the basis function. Those NURBS functions are non-interpolatory functions, in that, for an open knot vector, they are interpolatory at the end of the parametric space where the first and the last knots must appear  $p + 1$  times, where  $p$  is the order of the knot vector, and at the corner of patches in multiple dimensions. This means that the control mesh interpolates the physical mesh at those locations, but they are not interpolatory functions at the interior knots, where the physical mesh might not conform to the control mesh [23].

### 5.4.2 Time discretization and numerical implementation

In order to get a system of ordinary differential equations to be solved using a time-integration scheme, the vector form of Eq. (5.42) should be formulated. By virtue of the arbitrariness of the control variables of the test function listed in Eq. (5.43), the vector form can be formulated as follows:

$$\mathbf{R}^M(\dot{\mathbf{U}}, \mathbf{U}, \mathbf{P}, \mathbf{F}_1, \mathbf{F}_2, \Phi_1, \Phi_2, \Lambda_1, \Lambda_2) = 0, \tag{5.44}$$

$$\mathbf{R}^C(\dot{\mathbf{U}}, \mathbf{U}, \mathbf{P}, \mathbf{F}_1, \mathbf{F}_2, \Phi_1, \Phi_2, \Lambda_1, \Lambda_2) = 0, \tag{5.45}$$

$$\mathbf{R}^{F_1}(\mathbf{F}_1, \Phi_1) = 0, \quad \mathbf{R}^{F_2}(\mathbf{F}_2, \Phi_2) = 0, \tag{5.46}$$

$$\mathbf{R}^{\Phi_1}(\mathbf{U}, \mathbf{F}_1, \dot{\Phi}_1, \Phi_1) = 0, \quad \mathbf{R}^{\Phi_2}(\mathbf{U}, \mathbf{F}_2, \dot{\Phi}_2, \Phi_2) = 0, \quad (5.47)$$

$$\mathbf{R}^{\Lambda_1}(\mathbf{U}, \Phi_1, \Lambda_1) = 0, \quad \mathbf{R}^{\Lambda_2}(\mathbf{U}, \Phi_2, \Lambda_2) = 0, \quad (5.48)$$

The residual vectors of the system, consisting of  $\mathbf{R}^M$  and  $\mathbf{R}^C$  of the linear momentum and continuity equations,  $\mathbf{R}^{F_1}$  and  $\mathbf{R}^{F_2}$  for the intermediate equations,  $\mathbf{R}^{\Phi_1}$  and  $\mathbf{R}^{\Phi_2}$  for the phase-field variables, and  $\mathbf{R}^{\Lambda_1}$ ,  $\mathbf{R}^{\Lambda_2}$  for the local inextensibility equations are defined as following:

$$\begin{aligned} \mathbf{R}^M &= [R_{A,i}^M], & \mathbf{R}^C &= [R_A^C], & \mathbf{R}^{F_1} &= [R_A^{F_1}], & \mathbf{R}^{F_2} &= [R_A^{F_2}], & \mathbf{R}^{\Phi_1} &= [R_A^{\Phi_1}], \\ \mathbf{R}^{\Phi_2} &= [R_A^{\Phi_2}], & \mathbf{R}^{\Lambda_1} &= [R_A^{\Lambda_1}], & \mathbf{R}^{\Lambda_2} &= [R_A^{\Lambda_2}], \end{aligned} \quad (5.49)$$

where,

$$\begin{aligned} R_{A,i}^M &= B(\{N_A \mathbf{e}_i, 0, 0, 0, 0, 0, 0, 0\}, \{\mathbf{u}^h, p^h, f_1^h, f_2^h, \phi_1, \phi_2, \lambda_1, \lambda_2\}) && -L(\{N_A \mathbf{e}_i, 0\}) \\ R_A^C &= B(\{0, N_A, 0, 0, 0, 0, 0, 0\}, \{\mathbf{u}^h, p^h, f_1^h, f_2^h, \phi_1, \phi_2, \lambda_1, \lambda_2\}) && -L(\{N_A \mathbf{e}_i, 0\}) \\ R_A^{F_1} &= B(\{0, 0, N_A, 0, 0, 0, 0, 0\}, \{\mathbf{u}^h, p^h, f_1^h, f_2^h, \phi_1, \phi_2, \lambda_1, \lambda_2\}) \\ R_A^{F_2} &= B(\{0, 0, 0, N_A, 0, 0, 0, 0\}, \{\mathbf{u}^h, p^h, f_1^h, f_2^h, \phi_1, \phi_2, \lambda_1, \lambda_2\}) \\ R_A^{\Phi_1} &= B(\{0, 0, 0, 0, N_A, 0, 0, 0\}, \{\mathbf{u}^h, p^h, f_1^h, f_2^h, \phi_1, \phi_2, \lambda_1, \lambda_2\}) && -L(\{0, N_A\}) \\ R_A^{\Phi_2} &= B(\{0, 0, 0, 0, 0, N_A, 0, 0\}, \{\mathbf{u}^h, p^h, f_1^h, f_2^h, \phi_1, \phi_2, \lambda_1, \lambda_2\}) && -L(\{0, N_A\}) \\ R_A^{\lambda_1} &= B(\{0, 0, 0, 0, 0, 0, N_A, 0\}, \{\mathbf{u}^h, p^h, f_1^h, f_2^h, \phi_1, \phi_2, \lambda_1, \lambda_2\}) \\ R_A^{\lambda_2} &= B(\{0, 0, 0, 0, 0, 0, 0, N_A\}, \{\mathbf{u}^h, p^h, f_1^h, f_2^h, \phi_1, \phi_2, \lambda_1, \lambda_2\}) \end{aligned} \quad (5.50)$$

where  $A$  is the control point index in isogeometric analysis, similar to the nodal index in classical finite element, and  $\mathbf{e}_i$  is a unit Cartesian basis vector.

The Generalized- $\alpha$  method has been used to implement the temporal discretization of the semi-discrete Galerkin RBVMS formulation above. We discretize the temporal domain  $[0, T]$  into segments of  $\Delta t_n = t_{n+1} - t_n$ , with  $t_n$  being the current time step and  $t_{n+1}$  the next time step. Let  $\dot{\mathbf{U}}^n$ ,  $\mathbf{U}^n$ ,  $\mathbf{P}^n$ ,  $\mathbf{F}_1^n$ ,  $\mathbf{F}_2^n$ ,  $\dot{\Phi}_1^n$ ,  $\Phi_1^n$ ,  $\dot{\Phi}_2^n$ ,  $\Phi_2^n$ ,  $\Lambda_1^n$  and  $\Lambda_2^n$  denote the global vectors of the control variables at  $t_n$ . Given  $\Delta t$ , the problem can be stated as following: find  $\dot{\mathbf{U}}^{n+1}$ ,  $\mathbf{U}^{n+1}$ ,  $\mathbf{P}^{n+1}$ ,  $\mathbf{F}_1^{n+1}$ ,  $\mathbf{F}_2^{n+1}$ ,  $\dot{\Phi}_1^{n+1}$ ,  $\Phi_1^{n+1}$ ,  $\dot{\Phi}_2^{n+1}$ ,  $\Phi_2^{n+1}$ ,  $\Lambda_1^{n+1}$ ,  $\Lambda_2^{n+1}$  at  $t_{n+1}$  such that

$$\mathbf{R}^M(\dot{\mathbf{U}}^{n+\alpha_m}, \mathbf{U}^{n+\alpha_f}, \mathbf{P}^{n+1}, \mathbf{F}_1^{n+1}, \mathbf{F}_2^{n+1}, \Phi_1^{n+\alpha_f}, \Phi_2^{n+\alpha_f}, \Lambda_1^{n+1}, \Lambda_2^{n+1}) = 0, \quad (5.51)$$

$$\mathbf{R}^C \left( \dot{\mathbf{U}}^{n+\alpha_m}, \mathbf{U}^{n+\alpha_f}, \mathbf{P}^{n+1}, \mathbf{F}_1^{n+1}, \mathbf{F}_2^{n+1}, \Phi_1^{n+\alpha_f}, \Phi_2^{n+\alpha_f}, \Lambda_1^{n+1}, \Lambda_2^{n+1} \right) = 0, \quad (5.52)$$

$$\mathbf{R}^{F_1} \left( \mathbf{F}_1^{n+1}, \Phi_1^{n+\alpha_f} \right) = 0, \quad \mathbf{R}^{F_2} \left( \mathbf{F}_2^{n+1}, \Phi_2^{n+\alpha_f} \right) = 0, \quad (5.53)$$

$$\mathbf{R}^{\Phi_1} \left( \mathbf{U}^{n+\alpha_f}, \mathbf{F}_1^{n+1}, \dot{\Phi}_1^{n+\alpha_m}, \Phi_1^{n+\alpha_f} \right) = 0, \quad (5.54)$$

$$\mathbf{R}^{\Phi_2} \left( \mathbf{U}^{n+\alpha_f}, \mathbf{F}_2^{n+1}, \dot{\Phi}_2^{n+\alpha_m}, \Phi_2^{n+\alpha_f} \right) = 0, \quad (5.55)$$

$$\mathbf{R}^{\Lambda_1} \left( \mathbf{U}^{n+\alpha_f}, \Phi_1^{n+\alpha_f}, \Lambda_1^{n+1} \right) = 0, \quad (5.56)$$

$$\mathbf{R}^{\Lambda_2} \left( \mathbf{U}^{n+\alpha_f}, \Phi_2^{n+\alpha_f}, \Lambda_2^{n+1} \right) = 0, \quad (5.57)$$

where - for example - for the first phase-field variable  $\Phi_1$ , we have:

$$\begin{aligned} \Phi_{1_{n+1}} &= \Phi_{1_n} + \Delta t_n \dot{\Phi}_{1_n} + \gamma \Delta t_n (\dot{\Phi}_{1_{n+1}} - \dot{\Phi}_{1_n}) \\ \dot{\Phi}_{1_{n+\alpha_m}} &= \dot{\Phi}_{1_n} + \alpha_m (\dot{\Phi}_{1_{n+1}} - \dot{\Phi}_{1_n}) \\ \Phi_{n+\alpha_f} &= \Phi_n + \alpha_f (\Phi_{n+1} - \Phi_n) \end{aligned} \quad (5.58)$$

Eq. (5.58) can also be extended for the remaining fields of velocity, pressure, intermediate equation variables, phase-field variables and local inextensibility Lagrangian multiplier. The variables  $\alpha_f$ ,  $\alpha_m$ , and  $\gamma$  are real-valued parameters that define the method. For a linear first-order system of ODEs, the Generalized- $\alpha$  method is second-order accurate in time [172] if

$$\gamma = \frac{1}{2} + \alpha_m - \alpha_f \quad (5.59)$$

and unconditionally stable if:

$$\alpha_m \geq \alpha_f \geq \frac{1}{2} \quad (5.60)$$

where  $\alpha_m$  and  $\alpha_f$  are as following

$$\alpha_m = \frac{1}{2} \left( \frac{3 - \rho_\infty}{1 + \rho_\infty} \right), \quad \alpha_f = \left( \frac{1}{1 + \rho_\infty} \right). \quad (5.61)$$

The spectral radius of the amplification matrix at an infinitely large time step,  $\rho_\infty \in [0, 1]$ , which controls the high-frequency damping, was set to 0.5, which results in  $\alpha_f = 0.66\bar{6}$  and  $\alpha_m = 0.83\bar{3}$  and hence, satisfying Eq. (5.60) for unconditionally stable time integration for a system of linear ODEs. The situation is however more complicated



for nonlinear problems as the notion of stability is problem-dependent. For nonlinear phase-field problems, there is still little known about the stability of the generalized- $\alpha$  method [172, 173]. Nonetheless, based on our numerical experience, the method is *computationally* stable [174, 175] for the range of time-step sizes we considered in this paper. The nonlinear system of Eqs. (5.58) and the corresponding equations related to the other fields of interest are solved using Newton's method. For  $\Phi_1$  and  $\dot{\Phi}_1$  representing the global vectors of control variables of  $\phi_1$  and  $\dot{\phi}_1$ , the two stages Predictor-Multicorrector approach as the following:

1. Predictor stage:

$$\Phi_{1_{n+1}}^{(0)} = \Phi_{1_n} \quad (5.62)$$

$$\dot{\Phi}_{1_{n+1}}^{(0)} = \frac{\gamma-1}{\gamma} \dot{\Phi}_{1_n} \quad (5.63)$$

with the superscript in those equations is denoting the iteration index of the nonlinear solver.

2. Multicorrector stage:

Repeat the following steps for  $i = 1, 2, 3, \dots, i_{max}$ , or until convergence is reached.

- Evaluate iterates at  $\alpha$ -levels:

$$\dot{\Phi}_{1_{n+\alpha_m}}^{(i)} = \dot{\Phi}_{1_n} + \alpha_m (\dot{\Phi}_{1_{n+1}}^{(i-1)} - \dot{\Phi}_{1_n}) \quad (5.64)$$

$$\Phi_{1_{n+\alpha_f}}^{(i)} = \Phi_{1_n} + \alpha_f (\Phi_{1_{n+1}}^{(i-1)} - \Phi_{1_n}) \quad (5.65)$$

- Use  $\alpha$ -level iterates to assemble the linear system of equations corresponding to the linearization of Equation (5.54)

$$\mathbf{K}_{\phi_1 \mathbf{U}}^{(i)} \Delta \mathbf{U}_{n+1}^{(i)} + \mathbf{K}_{\phi_1 \mathbf{F}_1}^{(i)} \Delta \mathbf{F}_{1_{n+1}}^{(i)} + \mathbf{K}_{\phi_1 \phi_1}^{(i)} \Delta \Phi_{1_{n+1}}^{(i)} = -\mathbf{R}_{n+1}^{\Phi_1(i)} \quad (5.66)$$

This linearized system is solved using the GMRES method available through KSP solvers in PETSc [176–179].

- Update the solution

$$\dot{\Phi}_{1_{n+1}}^{(i)} = \dot{\Phi}_{1_{n+1}}^{(i-1)} + \Delta \dot{\Phi}_{1_{n+1}}^{(i)} \quad (5.67)$$

$$\Phi_{1_{n+1}}^{(i)} = \Phi_{1_{n+1}}^{(i-1)} + \gamma \Delta t_n \dot{\Phi}_{1_{n+1}}^{(i)} \quad (5.68)$$

Note: The Predictor-Multicorrector stages for the other global control variables are obtained in a similar manner to the first phase-field variable as in equations (5.62-5.68). The tangents matrices - for example -  $\mathbf{K}_{\Phi_1 \mathbf{U}}$ ,  $\mathbf{K}_{\Phi_1 \mathbf{F}_1}$  and  $\mathbf{K}_{\Phi_1 \Phi_1}$  in Eq. (5.66) is the partial derivative of the residual of the first phase-field variable w.r.t. the velocity field, i.e.,  $\mathbf{U}$ , first intermediate equation, i.e.,  $\mathbf{F}_1$  and the first phase-field variable, i.e.,  $\Phi_1$ , respectively. The tangent matrix  $\mathbf{K}_{\Phi_1 \Phi_1}$  w.r.t. the first phase-field variable  $\Phi_1$  is evaluated as following:

$$\begin{aligned} \mathbf{K}_{\Phi_1 \Phi_1} &= \frac{\partial \mathbf{R}^{\Phi_1}}{\partial \dot{\Phi}_{1_{n+\alpha_m}}} \frac{\partial \dot{\Phi}_{1_{n+\alpha_m}}}{\partial \dot{\Phi}_{1_{n+1}}} + \frac{\partial \mathbf{R}^{\Phi_1}}{\partial \Phi_{1_{n+\alpha_f}}} \frac{\partial \Phi_{1_{n+\alpha_f}}}{\partial \dot{\Phi}_{1_{n+1}}} \\ &= \alpha_m \frac{\partial \mathbf{R}^{\Phi_1}}{\partial \dot{\Phi}_{1_{n+\alpha_m}}} + \alpha_f \gamma \Delta t_n \frac{\partial \mathbf{R}^{\Phi_1}}{\partial \Phi_{1_{n+\alpha_f}}} \end{aligned} \quad (5.69)$$

where the iteration index  $i$  has been dropped for simplicity. We resort to the finite-difference approximation of the Jacobian within the numerical library [177–179]. This has proven sufficient accuracy as shown in [45] when compared to the hand-written Jacobian. In addition, the aforementioned formulation is obtained under the assumption that the time derivative of the coarse-scale velocity vector is zero within the domain, while the fine-scale velocity vector equals zero on the boundaries, and under the orthogonality condition of  $[\mathbf{D}(\mathbf{w}^h), (2\mu^*/Re)\mathbf{D}(\mathbf{u}')]_{\Omega} = 0$ .

## 5.5 Numerical examples

The computational implementation of the isogeometric formulation of the aforementioned weak form was conducted using the NURBS-based PetIGA [180]. PetIGA is a computational framework to approximate the solution of PDEs using isogeometric analysis. It relies heavily on PETSc [176, 177, 179], *Portable, Extensible Toolkit for Scientific Computation*, by exploiting a huge part of its algorithms, data structures, and solvers. PETSc uses Message Passing Interface (MPI) standard protocol for communication and

data exchange between multiple processes among single or multiple communicators in a given run. In the field of biomembrane mechanics and hydrodynamics, the computational load is immense, and therefore, the availability of a parallel-based framework for computational implementation of the numerical formulation is paramount, and this is where PetIGA/PETSc fits in. But all things considered, PetIGA has been used to tackle some challenging problems in a wide range of fields [20, 40, 43, 45, 173], and hence, it is extensively tested and highly reliable.

Due to the large set of parameters that can alter the outcome of this study, we are not conducting a parametric study in regards to the Reynolds and Capillary numbers, and the values were set to  $5 \times 10^{-3}$  and  $1.0 \times 10^4$ , respectively unless otherwise stated. In what follows, all examples are spatially discretized using  $\mathcal{C}^1$  quadratic NURBS elements with 6 integration points per direction, with 1 unit of length spanning over 32 elements. A convergence study was conducted using  $\varepsilon = 2h$  - where  $h$  is the element size - for different unit length to elements ratios of 1:8, 1:16, 1:32, and 1:64. Results show at this value of regularization parameter and the ratio of unit length to element numbers, that the area relative error of the system tends to converge to the values obtained using a ratio of 1:32, where a ratio of 1:64 gives a very small change in the relative error equals to 0.0024%.

In our previous work involving vesicles electromechanics [45], we have noticed that in certain situations we need to use an unequally-spaced knot vector to densify the mesh in a part of the domain engulfing the vesicle. However, a correct and accurate choice of the regularization parameter along with sufficient smoothness of the basis function will give satisfactory results. We have not noticed any “*peculiar*” behavior when vesicles are subjected to large deformations and/or coming close to each other; this is due to two factors, the first one is the implicit method we used to track the interface, which is most suitable for this class of problems, and second, is the incorporation of the interaction energy definition that maintains a certain distance between the vesicles preventing them from overlapping. With two factors in mind, we concluded – as shown later – that there is no need for adding extra control points in certain parts of the domain, especially when the phase-field model is used, which tracks the evolution of the interface on a fixed mesh, rendering the use of extra control points meaningless.

The temporal discretization is done by the Generalized- $\alpha$  method and was evenly spaced with a timestep size  $\Delta t$  of 0.0001, hence, adaptivity was disabled for most examples. For

some examples, however, the initial timestep size was set to 0.005 and the cap value was set to 0.05. When considered, the Digital Signal Processing (DSP) time adaptivity scheme [174, 175] was used. The cap is placed on the timestep controller so step size would remain within the range of the initial timestep size and the cap at any of the iterations. This is in part to maintain stability and numerical accuracy. Using the timestep-increase delay functionality in PETSc, we delay the increase in the timestep size until three consecutive steps converge successfully in order to prevent the time-controller from bouncing back and forth between two nearby timesteps which provides an additional layer of stability in reaching the maximum timestep size specified. Throughout the remainder of this section, the numerical examples are presented in 2D dimensional settings, where the reduced area  $\chi \in (0, 1]$  is defined as the ratio between the vesicle area and the area of a circle with the same perimeter as following

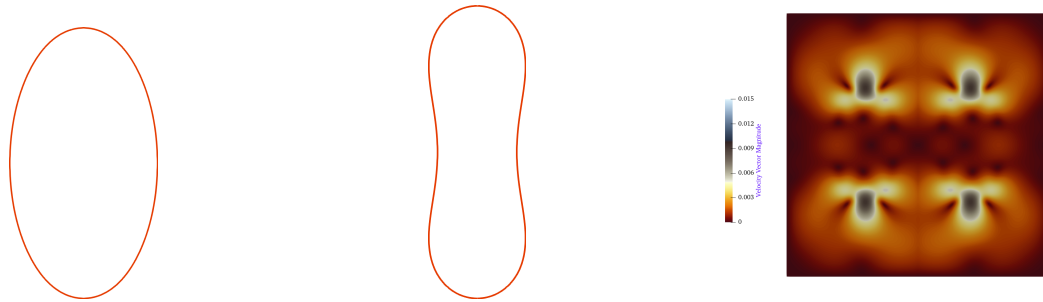
$$\chi = \frac{\mathcal{A}_0}{\pi} \left( \frac{2\pi}{\mathcal{P}_0} \right)^2 \quad (5.70)$$

where  $\mathcal{A}_0$  and  $\mathcal{P}_0$  are the area and perimeter of the vesicle, respectively. Consequently, the initial condition of the phase field variable accounting for the reduced area in the Cartesian coordinates system is generated using the hyperbolic tangent function as the following

$$\phi_0 = \tanh \left[ \frac{-\left( \frac{(x^*+y^*)^{0.5}}{(\gamma^{-2}x^*+\gamma^{-2}y^*)^{0.5}} (\sqrt{x^*+y^*} - \mathcal{R}_0) \right)}{\sqrt{2}\varepsilon} \right], \quad \text{where} \quad (5.71)$$

$$\gamma = [1 + (1 - \chi^2)^{0.5}]^{0.5}$$

Unless otherwise stated, the coefficients  $\eta_{\phi_i}$  and  $\xi$  were set to 0.1 and 1, respectively. The computational domain dimensions and the velocity profile vary depending on the numerical example to be presented. The scalar and vector absolute and relative tolerance values for the System of nonlinear equations (SNEs) context were set to  $1 \times 10^{-3}$ , which was also used for the linear Krylov subspace (KSP) solvers. In the following subsections, we are presenting a verification example. We also study the hydrodynamics of vesicle doublet in planar extensional flow with various interaction number values. In addition, we study the hydrodynamics of vesicle doublet in a shear flow, and in parabolic planar extensional flow with two inlets and two outlets with various domain, dimensions to simulate different ambient environments with various values of fluid velocities. The vesicle doublet might align vertically or might have an initial vertical displacement, i.e., an offset



(a) Vesicle spheroidal initial shape (b) Vesicle peanut-like final shape (c) Velocity vector during evolution

Figure 5.1: Temporal evolution of a single vesicle from (5.1a) the spheroidal shape to the (5.1b) well-known peanut-like shape in absence of external forces. Fig. (5.1c) shows the velocity profile during the evolution.

in the vertical direction between two centers of masses of the vesicle doublet. Aside from one example where the vesicles have an initial oblate-like shape, all examples are initialized with vesicle doublets having a prolate-like spheroid shape.

### 5.5.1 Vesicle doublet in stationary fluid

As a verification example for the proposed phase-field Navier-Stokes model, we test the system for the well-known elliptical configuration of the vesicle, which is supposed to evolve morphologically to a peanut-like shape, i.e., a biconcave shape [43, 45, 103, 194] in absence of external forces. The computational domain  $\Omega$  is defined as  $[0, 5] \times [0, 5]$  spanning over  $[160 \times 160]$  quadratic NURBS-elements. The boundary conditions for the velocity field and Lagrangian multipliers are imposed strongly, i.e.,  $\mathbf{u} = 0$ ,  $\lambda_1 = 0$ , and  $\lambda_2 = 0$ . Homogeneous natural boundary conditions are assumed for the phase-field variables  $\phi_1$  and  $\phi_2$  and the intermediate variables  $f_1$  and  $f_2$ . The velocity is set to zero on all boundaries and hence, within the domain. As shown in Fig. (5.1), each vesicle is evolving to form a peanut-like shape upon equilibrium as shown in Fig (5.1b). One interesting outcome of this verification example is the development of a velocity vector within the extra-cellular medium even though no velocity profile was defined at the initialization. This can be explained by the movement of the vesicle membrane which generates small ripples within the fluid outside the vesicle as shown in Fig. (5.1c).

### 5.5.2 Effect of Interaction Number

The value of the dimensionless Interaction Number  $\mathcal{JN}$  in Eq. (2.46) has a significant impact on vesicle doublet hydrodynamics. Conceptually, the interaction energy is inversely proportioned to the interaction number which is also inversely proportioned to the repulsion parameter  $\alpha$ . Therefore, a smaller value for  $\alpha$ , i.e., a weak repulsion, gives a large value for the interaction number, which is manifested by a strong interaction between the vesicle doublet and a higher interaction energy for the system, due to the contribution of the short-range interaction function. To test this, we chose three values for the interaction number  $\mathcal{JN}$ , i.e., 0.05, 0.5, and 5. The computational domain  $\Omega$  is defined as  $[0,5] \times [0,5]$  spanning over  $[160 \times 160]$  quadratic NURBS-elements. The reduced area  $\chi = 0.84$  and the characteristic length  $R_e = 0.863$ . The vesicle doublet was suspended in planar extensional flow in the x-direction, i.e.,  $\mathbf{u}_{left} = 10\mathbf{e}_1 + 0\mathbf{e}_2$  and  $\mathbf{u}_{right} = -10\mathbf{e}_1 + 0\mathbf{e}_2$  at the side inlets of the computational domain to simulate a *push* on both vesicles to displace as much fluid as possible from in between with the purpose of testing the interaction number effect. We consider stress-free boundary conditions on the outlet boundaries. The vesicle doublets are centered with no initial vertical displacement to prevent any sliding motion. The Reynolds number remains unchanged from the previous example. Results indicated that a larger interaction number, i.e., a small value of repulsion parameter  $\alpha$  leads to more interaction between vesicle doublet when compared to a smaller interaction number. In addition, values of  $\mathcal{JN}$  greater than 5 will result in the phase-field of the vesicle doublet overlapping, which practically does not hold any physical meaning. It can be seen from Figures (5.2a-5.2c) that the fluid velocity in the vicinity of the vesicles decreases significantly compared to the inlet fluid velocity. In addition, and as shown in Fig. (5.2f), an area of high-pressure forms on the sides of both vesicles facing the inlets, and in between the vesicles themselves. Both vesicles also experience an elongation in the direction perpendicular to the fluid flow when compared to the initial state of the vesicle doublet showed in Fig. (5.2d), which results in tension areas on both sides of the vesicle doublet and a small compression area on the tips of each vesicle as shown in Fig. (5.2). For the remainder of this work, we are considering  $\mathcal{JN}$  to be 0.5. This would allow the vesicles to get as close as possible to each other without overlapping.

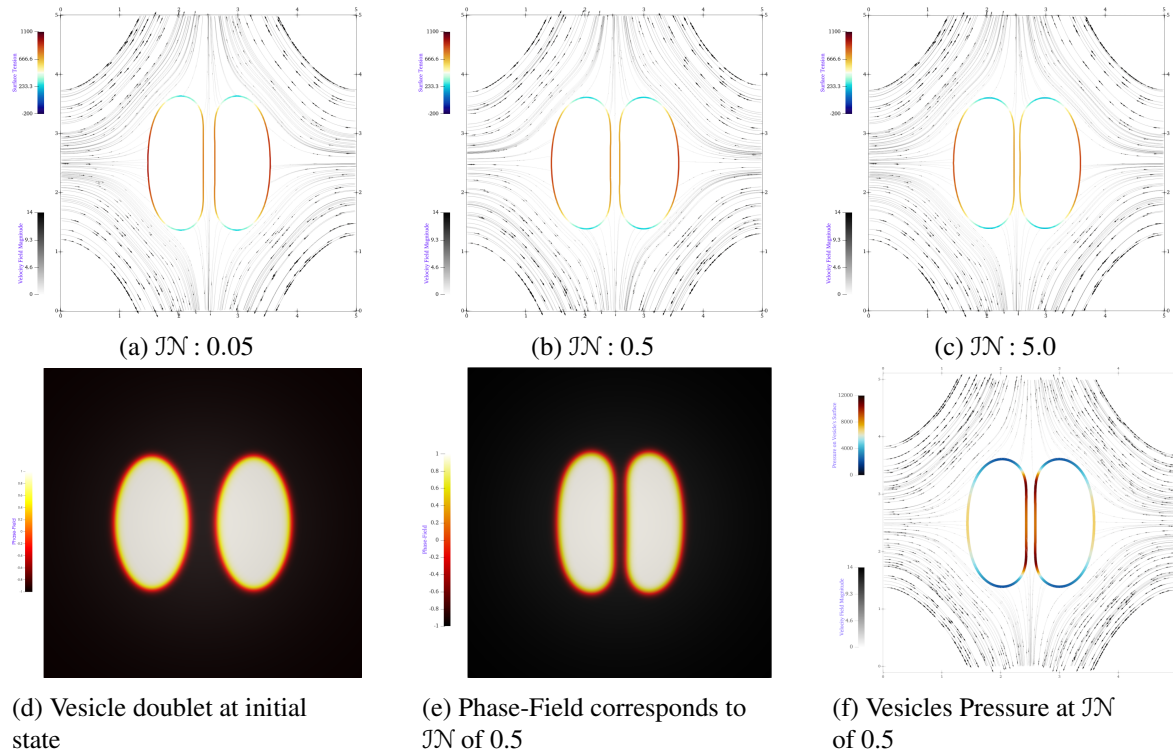


Figure 5.2: Velocity Streamlines of vesicle doublet suspended in planar extensional flow with various interaction number ( $JN$ ) of: (5.2a) 0.05, (5.2b) 0.5, and (5.2c) 5.0.  $\lambda_1$  and  $\lambda_2$  projected on the zero level-set of phase-field variables  $\phi_1$  and  $\phi_2$ , and interpreted as the surface tension on both vesicles. In figure (5.2f), the pressure projected on the zero-level set of the phase field shows increased values on both sides facing the inlet and facing the other vesicle.

### 5.5.3 Vesicle doublet suspended in a shear flow

Single vesicle hydrodynamics in a shear flow is well understood and verified. Vesicles can undergo either one of two types of motions - in a tubular channel - based on a set of factors like viscosity contrast embedded in the definition of the dynamic viscosity and Reynolds number. Those two types of motion are tank-threading and tumbling. Tumbling motion has also been observed in [123, 124]. Based on the work done by Valizadeh et. al. [43] and reported in [195, 196], single inextensible vesicles undergo tumbling motion in the Stokes limits, i.e., small Reynolds numbers and at certain viscosity ratios. When the Reynolds number is relatively large, vesicles start showing tank-treading motion with a stationary shape at a certain inclined angle. That being said, the hydrodynamics of vesicle doublet suspended in a shear flow does not fit any of those two types of motion as more dynamics emerge, as will be shown later. We start by testing two inextensible vesicles placed apart from each other. The computational domain  $\Omega$  is defined as  $[0,8] \times [0,4]$  spanning over  $[256 \times 128]$  quadratic NURBS-elements. The vesicles are 4 units length apart and

centered at (2.0,2.0) and (6.0,2.0), respectively. The interaction number is set to 0.5. We consider identical vesicles with an effective radius  $\mathcal{R}_0$  of 0,863 and a reduced area  $\chi$  of 0,840. The vesicles are suspended in a shear flow acting in the x-direction, i.e.,  $\mathbf{u}_{b_{top}} = 10\vec{\mathbf{e}}_1 + 0\vec{\mathbf{e}}_2$  and  $\mathbf{u}_{b_{bottom}} = -10\vec{\mathbf{e}}_1 + 0\vec{\mathbf{e}}_2$ . The Dirichlet boundary condition characterized by the aforementioned velocity profile defined on the top and bottom boundaries is imposed weakly using the method proposed by Bazilevs et. al. [197], which was designed to avoid oscillations in the solution especially when the boundary data is discontinuous. This is done by removing the essential boundary conditions from the trial and test functions spaces and adding the following terms to the LHS of Eq. (5.39):

$$\begin{aligned} & \sum_{A=1}^{n_b} \left( \tau_B \mathbf{w}^h \cdot (\mathbf{u}^h - \mathbf{u}_b^h) \right)_{\Omega_D} - \sum_{A=1}^{n_b} \left( \mathbf{w}^h \cdot \mathbf{S}(\mathbf{u}^h, p^h) \cdot \mathbf{m} \right)_{\Omega_D} \\ & - \sum_{A=1}^{n_b} \left[ \left( \frac{2\mu_0}{Re} \mathbf{D}(\mathbf{w}^h) \cdot \mathbf{m} + q^h \mathbf{m} \right) \cdot (\mathbf{u}^h - \mathbf{u}_b^h) \right]_{\Omega_D} \end{aligned} \quad (5.72)$$

where  $\mathbf{m}$  is the normal vector to the boundary, and  $\mathbf{u}_b$  is the velocity vector imposed on the boundary elements  $\Omega_D$  subjected to the essential boundary conditions. The stabilization parameter  $\tau_B$  is defined as:

$$\tau_B = \frac{\mathcal{C}_I^B \left( \frac{\mu_0}{Re} \right)}{h_n} \quad (5.73)$$

with the wall-normal element size parameter  $h_n$  is  $(\mathbf{m} \cdot \mathbf{G} \cdot \mathbf{m})^{-1/2}$ , and  $\mathcal{C}_I^B$  is a large positive constant, which was set to the value  $5(\mathcal{P} + 1)$ .

As shown in Fig. (5.3), the tank-threading motion of a single vesicle is reproduced. This is mainly because both vesicles are at least one semi-major axis apart, which prevents them from coming in contact when they start tilting and prolonging in the direction of the flow, and since the vesicles are apart enough for the velocity profile to be reconstructed as it was at the inlet without being obscured by any of the vesicles, then both vesicle exhibit similar dynamics. A further indication of the validity of the results presented in this example is by comparing the inclination angle for both vesicles with values in [43], where both vesicles incline to an angle of 0.423 and 0.419, respectively.

In another case, when the vesicles are placed close to each other to form a vesicle doublet, the dynamics change completely. Depending on the velocity profile and initial vertical displacement, vesicle doublet can develop two types of dynamics, i.e., separating and drifting apart or separating and sliding on top of each other. Beginning with the first case where



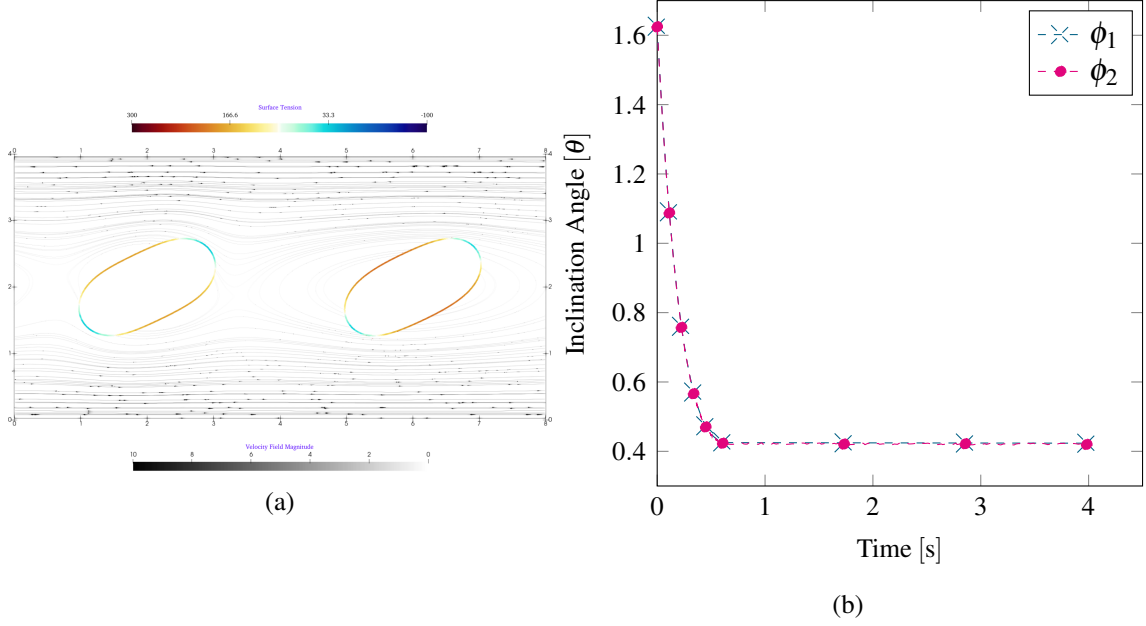


Figure 5.3: (5.3a) Vesicles suspended in a shear flow, and (5.3b) their corresponding inclination angles.  $\phi_1$  denotes the vesicle on the left and  $\phi_2$  denotes the vesicle on the right. Fluid flow motion is shown by the velocity streamlines.

the vesicle doublet is expected to separate and drift apart, we test two different settings. For both settings, we have a computational domain  $\Omega$  defined as  $[0,6] \times [0,4]$  spanning over  $[192 \times 128]$  quadratic NURBS-elements. The reduced area  $\chi = 0.84$  and the characteristic length  $R_e = 0.863$ . The vesicle doublet in the first set is centered at  $(2.2, 2.0)$  and  $(3.8, 2.0)$  and in the second set is centered at  $(2.0, 2.02)$  and  $(4.0, 1.98)$ , respectively. That means we have for the first setting no vertical displacement, while for the second set, we have a vertical displacement of 0.04 unit length, and a 1.6 unit length of horizontal displacement, center-to-center. We apply a shear flow characterized by a prescribed fluid velocity vector in the x-direction on both the top and bottom of the computational domain. For the first setting, we consider the following fluid velocity vector:  $\mathbf{u}_{b_{top}} = 10\mathbf{e}_1 + 0\mathbf{e}_2$  and  $\mathbf{u}_{b_{bottom}} = -10\mathbf{e}_1 + 0\mathbf{e}_2$ , while for the second one, we consider the following:  $\mathbf{u}_{b_{top}} = 15\mathbf{e}_1 + 0\mathbf{e}_2$  and  $\mathbf{u}_{b_{bottom}} = -15\mathbf{e}_1 + 0\mathbf{e}_2$ . The interaction and Reynolds numbers remain unchanged from the previous example, and the velocity boundary conditions are imposed weakly on  $\Gamma$  at the top and the bottom sides of the computational domain. In the first set, and as shown in Fig. (5.4), the vesicle doublet tends to tilt in the direction of the shear flow, i.e., to the right from the top and to the left from the bottom. It can be seen that after initial inclination, the vesicle doublet *lock* in position and remains so for the remainder of the temporal domain. In absence of external factors that might alter the morphology and

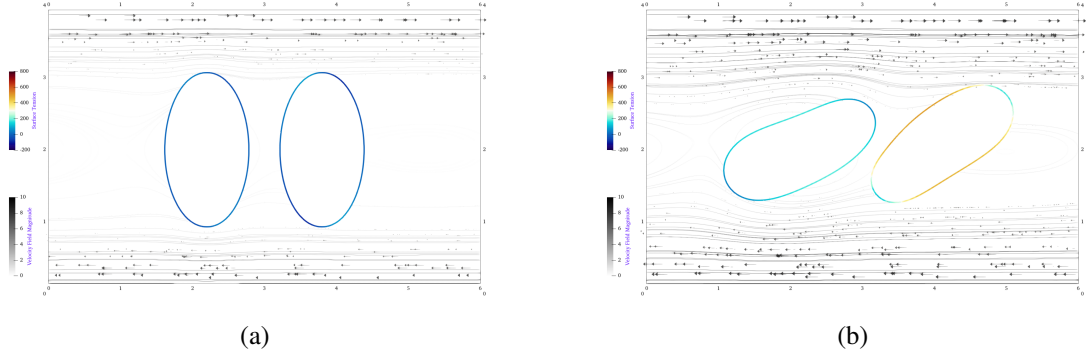


Figure 5.4: Vesicle doublet suspended in a shear flow with no initial vertical displacement at (5.4a) initial state and (5.4b) equilibrium state. Vesicle doublet *lock* in position due to the absence of initial vertical displacement. Fluid flow motion is shown by velocity streamlines.

hydrodynamics of the vesicle doublet, and when there is no initial vertical displacement, this is the equilibrium shape, in which, the hydrodynamic forces exerted by the fluid flow on the vesicle doublet are not great enough to overcome the interaction energy between two vesicles to cause a separation between them. In Fig. (5.4b), we can see that the vesicle on the right is experiencing higher values of surface tension compared to the one on the left, this is due to the fact that this vesicle is not as much inclined as the one on the left, which leaves it exposed to hydrodynamic forces from the fluid flow moving in the upper and lower regions of the computational domain, whereas the vesicle on the left is mainly inclined in the region of the fluid of low velocity.

In the second set of the first case, when the fluid velocity is increased, i.e.,  $\mathbf{u}_{b_{top}} = 10\vec{\mathbf{e}}_1$  to  $\mathbf{u}_{b_{top}} = 15\vec{\mathbf{e}}_1$  and  $\mathbf{u}_{b_{bottom}} = -10\vec{\mathbf{e}}_1$  to  $\mathbf{u}_{b_{bottom}} = -15\vec{\mathbf{e}}_1$ , and the initial vertical displacement is introduced and the horizontal distance between two vesicle increases, we notice completely different hydrodynamics. As shown in Fig. (5.5), the vesicle doublet starts to tilt in the direction of the shear flow, i.e., in the positive x-direction on the top and in the negative x-direction on the bottom. Due to a larger horizontal displacement of 2.0 unit length when compared to the previous setting, where the horizontal displacement was 1.6 unit length center-to-center, and because of the higher fluid velocity, we can see that the vesicle doublet is separating and drifting apart as shown in Figures (5.5b-5.5e). Once the vesicles start experiencing hydrodynamic forces, the surface tension starts to build up where it reaches a maximum value around  $t = 0.4$ . This is the time when vesicles come into contact with each other and the interaction energy is at maximum value as shown in Fig. (5.6a). From now on, the vesicles drift apart slowly till an equilibrium state is reached as shown in Fig (5.5f). We have also tested the vesicle doublet suspended in a

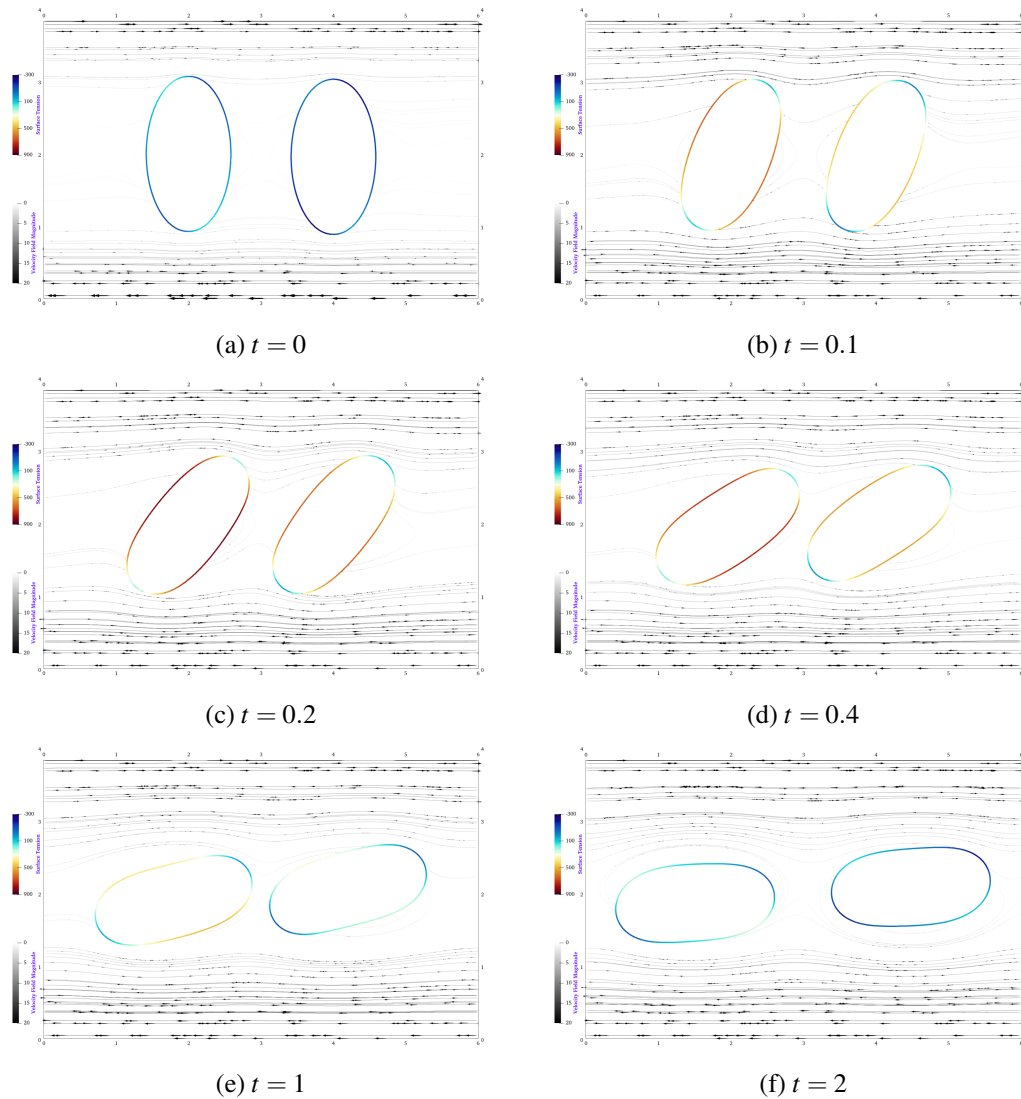


Figure 5.5: Vesicle doublet suspended in a shear flow with initial vertical displacement of 0.04 unit length at (5.5a) initial state, (5.5b)  $t = 0.1$ , (5.5c)  $t = 0.2$ , (5.5c)  $t = 0.2$ , (5.5d)  $t = 0.4$ , (5.5e)  $t = 1$ , and (5.5f)  $t = 2$ . Fluid flow motion is shown by velocity streamlines.

shear flow with a prescribed x-component velocity of 20 on top and -20 on the bottom using the same parameters and initial vertical displacement. And even with the increased velocity and shear flow intensity, the same hydrodynamics were observed where the vesicles separate and drift apart.

However, when we push the velocity a bit further to  $\mathbf{u}_{b_{top}} = 30\mathbf{e}_1$  and  $\mathbf{u}_{b_{bottom}} = -30\mathbf{e}_1$ , increase the initial vertical displacement to 0.06 unit length, and increase Reynolds number to  $5 \times 10^{-2}$ , we start seeing different dynamics. To start with, the vesicle doublet undergoes a completely different behavior where both vesicles start moving towards each other and then tumbling on top of each other. These dynamics have not been observed before when the fluid velocity and Reynolds number were smaller. In this example,

the computational domain  $\Omega$  is defined as  $[0,6] \times [0,4]$  spanning over  $[192 \times 128]$  quadratic NURBS-elements. The vesicle doublet is centered at  $(2.2, 2.03)$  and  $(3.8, 1.97)$ , respectively. Subsequently, the initial vertical displacement is 0.06 units in length, and the vesicles are 1.6 units in length, center-to-center, apart. For this example, and in order to broaden the experiment, we impose periodic boundary conditions on both left and right boundaries. The velocity boundary condition is imposed weakly on the top and bottom boundaries per Eq. (5.72). As shown in Fig. (5.7b), the vesicle doublet starts behaving like its counterpart from the previous example, however, due to the increased velocity and initial vertical displacement, and instead of sliding and drifting apart, the vesicles start tumbling on top of each other as shown in Figures (5.7c-5.7h). As seen from the hydrodynamics of Fig. (5.7), the interaction energy definition incorporated in the mathematical model and the corresponding numerical model successfully prevents the vesicle doublet from overlapping or the phase-field from collapsing at any point within the temporal domain. As shown in Fig. (5.6b), upon initial contact, the interaction energy records the highest value, this is due to the fact that the vesicle is rotating from a vertical alignment to a horizontal one, during which, the fluid flow is exerting pressure on both vesicles pushing them together. But once this configuration is attained, the interaction energy upon contact is not as high as the value recorded at the first one, and the peak value upon each consequential contact keeps dropping. In addition, when the vesicles are close to each other, or about to rotate from a semi-vertical alignment to a horizontal one, the surface tension spikes to its maximum value as shown in Fig. (5.7k), due to the hydrodynamic stretching forces exerted on both vesicles by the fluid flow in the upper and lower portions of the computational domain, but once the vesicles pass each other and drift to the mid-zone of the tubular channel, the surface tension starts to drop once again. From the results presented in this subsection, we can notice a pattern in the hydrodynamics of vesicle doublet suspended in a shear flow. At low velocities, and without any initial vertical displacement, the vesicle doublet is expected to separate and drift apart, and even when an initial vertical displacement is introduced, the vesicle doublet still separated and drifted apart. However, when the velocity increases beyond a certain threshold, i.e.,  $\mathbf{u}_{top} = 30\vec{\mathbf{e}}_1$  and  $\mathbf{u}_{bottom} = -30\vec{\mathbf{e}}_1$  in this study, as well as the initial vertical displacement and Reynolds number, we start seeing vesicles going in the direction of the shear flow and sliding on top of each other. The original tank-treading

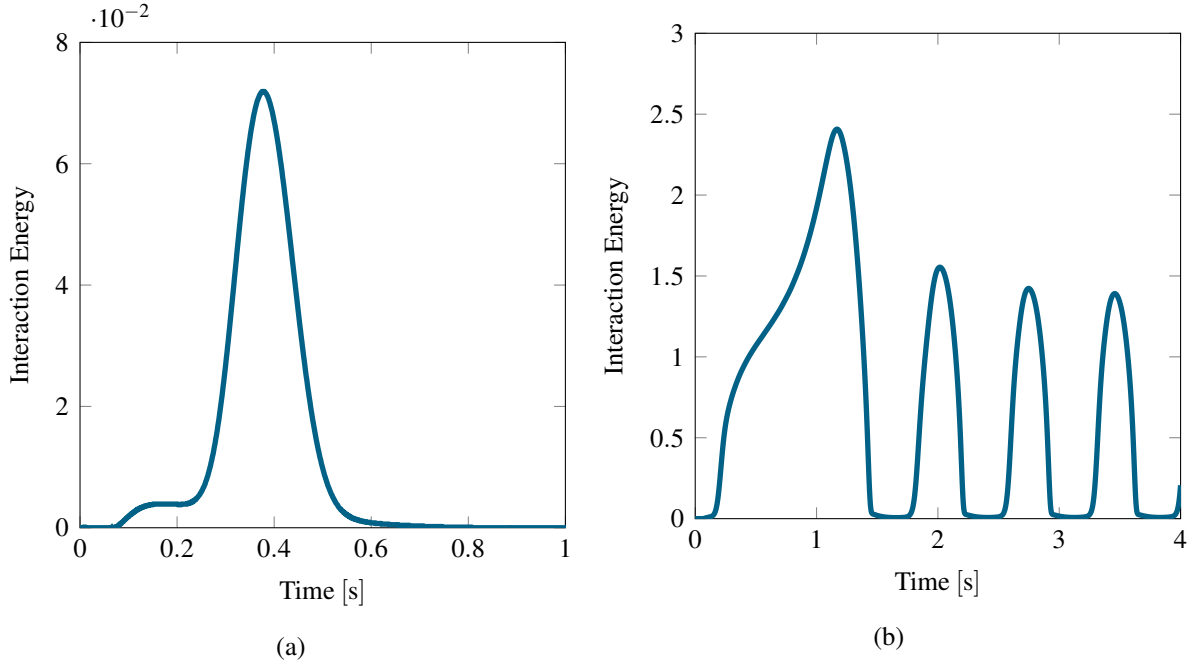


Figure 5.6: (5.6a) Interaction energy of vesicle doublet system in a shear flow with initial vertical displacement of 0.04 unit length and a velocity vector  $\mathbf{u}_{b_{top}} = 15\vec{\mathbf{e}}_1$  and  $\mathbf{u}_{b_{bottom}} = -15\vec{\mathbf{e}}_1$ , and (5.6b) interaction energy of vesicle doublet system in a shear flow with an initial vertical displacement of 0.06 unit length and a velocity vector  $\mathbf{u}_{b_{top}} = 30\vec{\mathbf{e}}_1$  and  $\mathbf{u}_{b_{bottom}} = -30\vec{\mathbf{e}}_1$ .

motion was reproduced for two vesicles placed apart from each other as a verification example for the underlying work, which agrees with the findings of Quaife et. al. [44]

#### 5.5.4 Vesicle doublet suspended in a planar extensional flow

In this subsection, we are presenting a set of examples for vesicle doublet suspended in planar extensional flow. Different from the shear flow, vesicle doublet in planar extensional flow (PEF) tend to move toward each other and collide after displacing fluid from in between the vesicles. In certain cases, a slip-like behavior is observed depending on the initial condition of the problem. We are going to test the hydrodynamics of vesicle doublet in multiple settings: at a junction, where we have two inlets on two side boundaries and two outlets on the other two side boundaries, and in a tubular channel with two inlets on two side boundaries and partial outlets on the other two side boundaries. In addition, we are presenting the results for an example, where the boundary condition was imposed strongly on a portion of a boundary. First, we consider a junction configuration, where a velocity profile is defined on two sides simulating two inlets. On the other two sides, we assume stress-free boundary conditions. The computational domain  $\Omega$  is defined as  $[0,5] \times [0,5]$  spanning over  $[160 \times 160]$  quadratic NURBS-elements. The

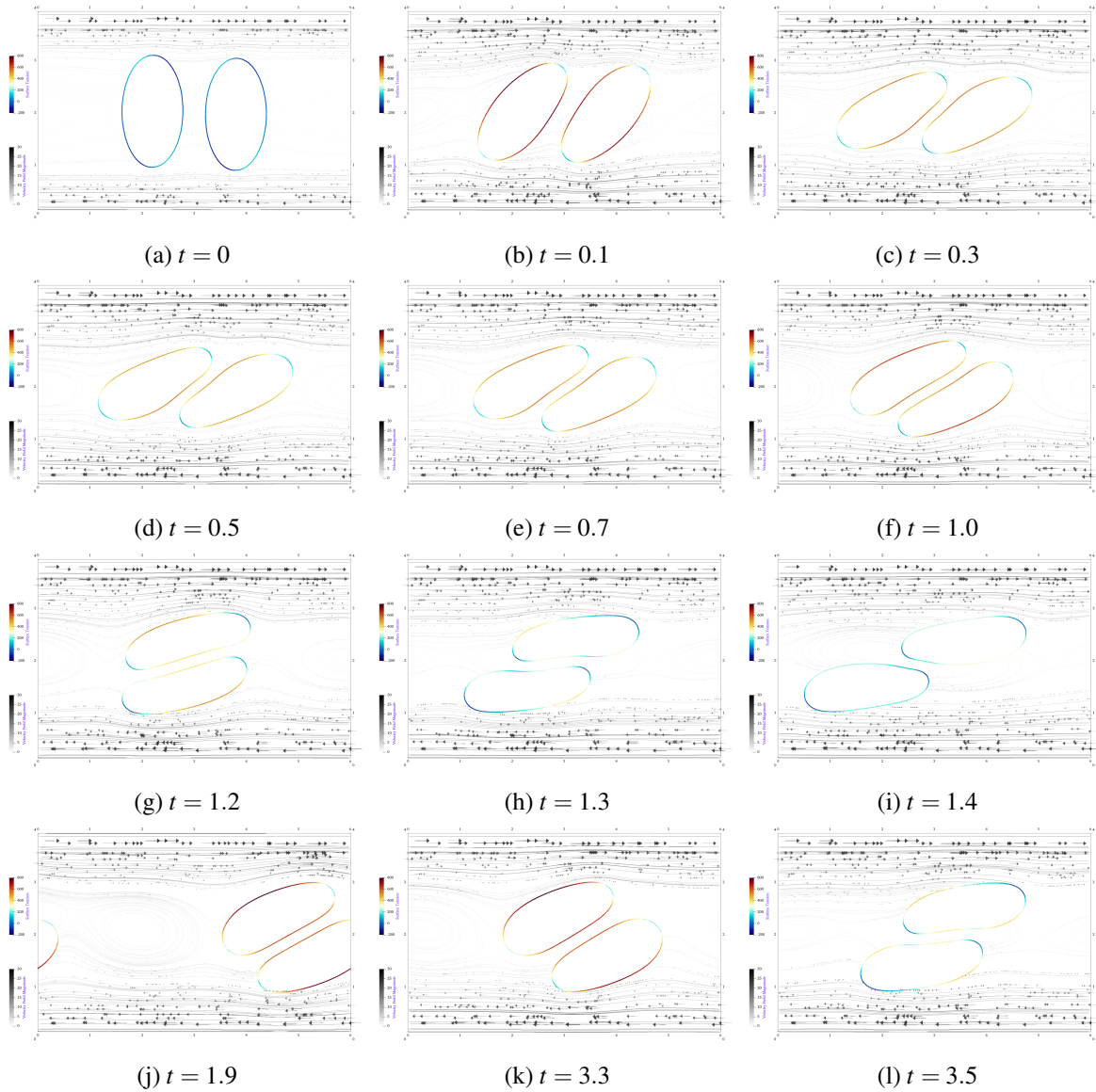


Figure 5.7: Vesicle doublet suspended in a shear flow with vertical displacement of 0.06 unit length and a horizontal displacement of 1.6 unit length at (5.5a) initial state and (5.71)  $t = 3.5$ . Fluid flow motion shown by velocity streamlines, and a velocity profile  $\mathbf{u}_{b_{top}} = 30\mathbf{e}_1$  and  $\mathbf{u}_{b_{bottom}} = -30\mathbf{e}_1$ .

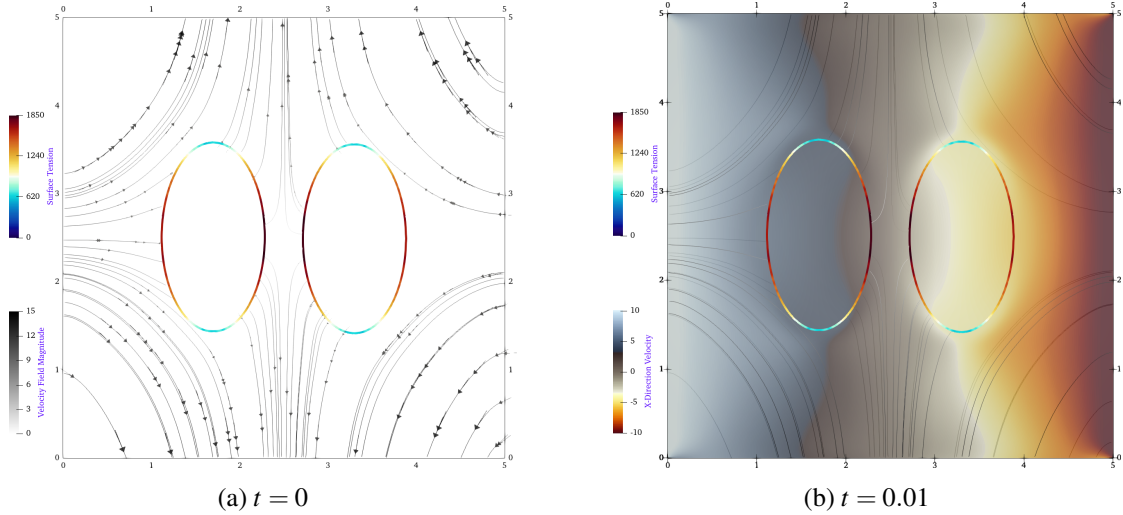


Figure 5.8: (5.8a) Initial state of vesicle doublet suspended in planar extensional flow at  $t = 0$  with velocity streamlines showing fluid flowing in the  $x$ -direction, and (5.8b) and the corresponding velocity profile at  $t = 0.01$ .

reduced area  $\chi = 0.84$  and the characteristic length  $R_e = 0.863$ . For this example, we test three initial vertical displacement values of 0.02, 0.1, and 0.2. Therefore, for the first, second, and third configurations, we have the vesicles centered at (1.7,2.51) and (3.3,2.49), (1.7,2.55) and (3.3,2.45), and (1.7,2.6) and (3.3,2.40), respectively, which gives the aforementioned initial vertical displacements. The interaction number  $\mathcal{JN}$  considered is 0.5, and the Reynolds number is  $5 \times 10^{-3}$ . The configuration of the example is depicted in Fig. (5.8), where the flow is pouring into the computational domain from both side boundaries, and leaves the computational domain from the top and bottom boundaries. The results show how the constant velocity profile for the fluid flow inlet evolves over time to form a planar extensional flow as shown in Figures 5.9a, 5.9d and 5.9g. In addition, and as shown in Figures 5.9b, 5.9e and 5.9h, the vesicle location affect the velocity of the fluid flow since the vesicle membrane acts like a barrier between the extra- and intracellular medium, which results in reducing the velocity within its vicinity significantly compared to the inlet velocity, especially when the vesicle doublet is placed in a PEF pushing on the doublet from both sides. We can also see from Fig. (5.9) the effect of the initial vertical displacement, where vesicle doublets with larger values of initial vertical displacements tend to separate faster than ones with smaller as shown visually in Figs. (5.9a) and (5.9d), where a vesicle doublet with initial vertical displacement of 0.02 is about to separate at  $t = 0.8$ , whereas the same vesicle doublet will separate at  $t = 0.52$  when the initial vertical displacement is 0.2. The results presented here agree with the

findings of Quaife et. al. [44].

However, vesicle doublet hydrodynamics when suspended in a PEF in a tubular channel is different from those presented in Fig. (5.9) since the vesicles are bound to move within a narrow channel and evolve according to the velocity profile imposed on the boundaries as shown in Fig. (5.10) before moving towards the existing outlet. Valizadeh et. al. [43] showed that when a vesicle is suspended in a parabolic flow, it evolves to form a parachute-like shape, therefore, to test the limits of our model, we are considering two vesicles suspended in a parabolic extensional flow with two side inlets and two mid-span upper and lower outlets with the same surface area in order to maintain a constant volumetric flow rate. The computational domain  $\Omega$  is defined as  $[0,16] \times [0,4]$  spanning over  $[512 \times 128]$  quadratic NURBS-elements. The reduced area  $\chi = 0.84$  and the characteristic length  $R_e = 0.863$ . The vesicles centered at  $(1.5, 2.1)$  and  $(14.5, 1.9)$ , resulting in an initial vertical displacement of 0.2. The interaction number  $\mathcal{JN}$  considered is 0.5, and the Reynolds number is 0.01. The profiles prescribed on the left and right inlets are defined as follows:  $\mathbf{u}_{left} = (8y - 2y^2)\mathbf{e}_1 + 0\mathbf{e}_2$  and  $\mathbf{u}_{right} = (-8y + 2y^2)\mathbf{e}_1 + 0\mathbf{e}_2$ , which results in a parabolic flow velocity with a maximum value of 8 in the x-direction. For this example in particular, the no-slip boundary condition is imposed strongly on the upper and lower boundary portions highlighted in red in Fig. (5.10), and since the argument for weakly imposed boundary condition was based on the use of  $\mathcal{C}^0$  basis function which might lead to oscillation in the solution [197], then this can be mitigated all together with the use of  $\mathcal{C}^1$  NURBS-basis functions. In PetIGA [182], the computational framework we are using throughout this study, the function `IGASetBoundaryValue()` is used to impose Dirichlet boundary conditions on  $\Gamma_D$  by specifying a scalar value for the entire boundary. In a parallel implementation, the computational domain  $\Omega$  is divided according to the specified communicator size to produce a structured rectangular layout, where each sub-domain is assigned to a single process with a specified rank, therefore, the boundary elements will most likely be distributed among multiple processes. In our implementation, we use the non-normalized knot vector initialization in PetIGA to specify the portion of boundary using the same unit length of the computational domain, e.g., for a boundary that starts from -4.0 and ends at 4.0, with a corresponding  $2^{nd}$  order knot vector in the parametric space of  $\{-4, -4 - 4, \dots, 4, 4, 4\}$ , we can directly specify - *for example* - all elements that span from -4 to -2 directly. In case the beginning - or the end - of the boundary portion



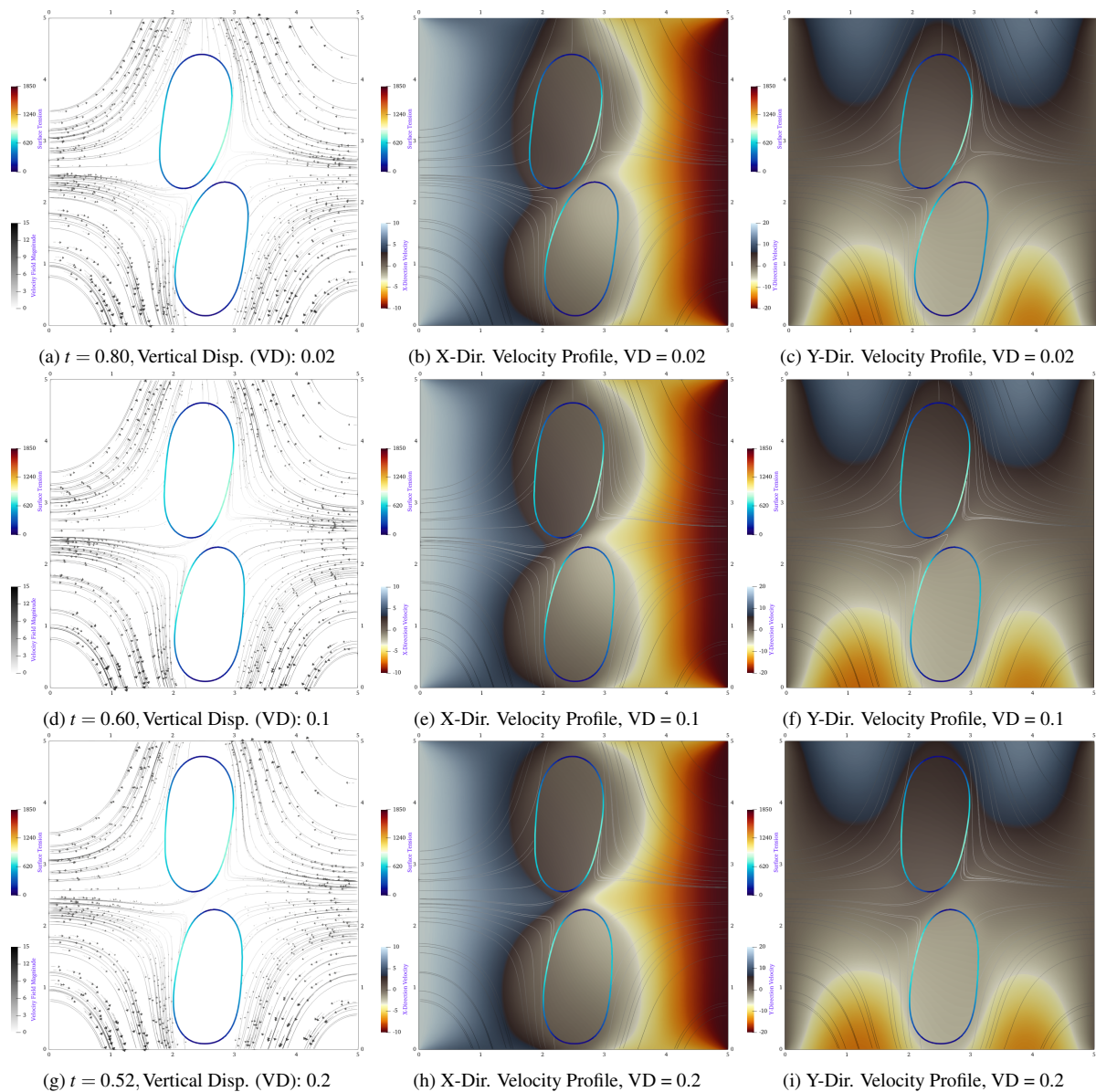


Figure 5.9: (5.9a) Vesicle doublet temporal evolution suspended in a planar extensional flow at  $t = 0.8$  with initial vertical displacement of 0.02, (5.9b) the corresponding X-Direction velocity profile, and (5.9c) the corresponding Y-Direction velocity profile. (5.9d-5.9f) Ditto, at  $t = 0.60$  with initial vertical displacement of 0.1, and (5.9g-5.9i) Ditto, at  $t = 0.52$  with initial vertical displacement of 0.2.

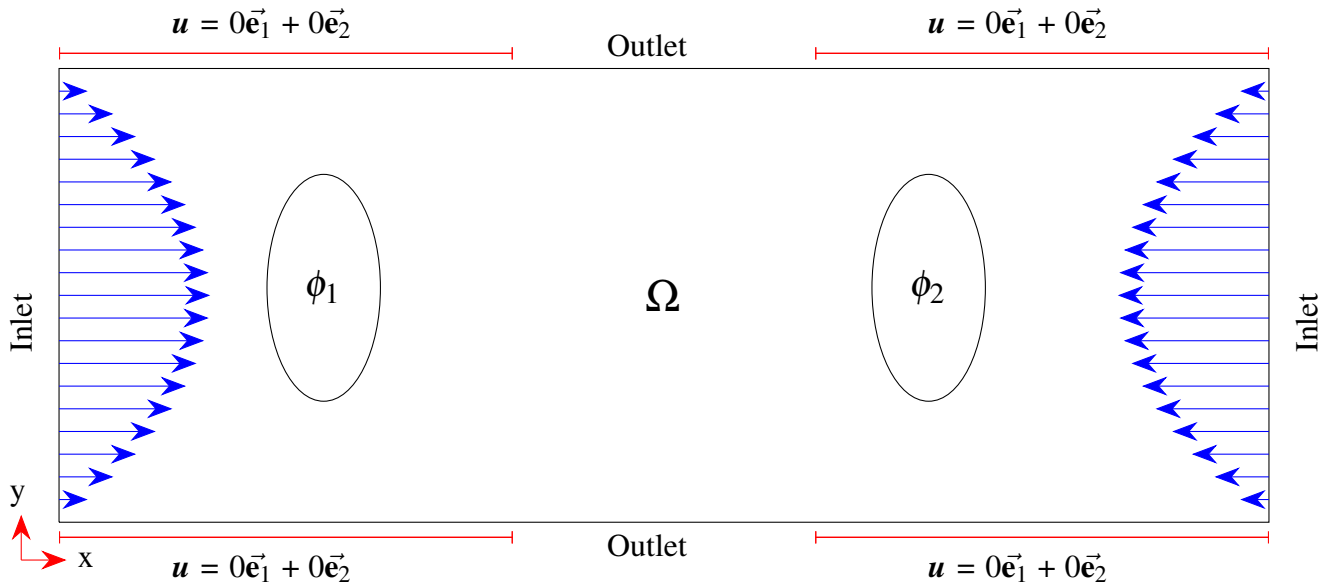


Figure 5.10: A not-to-scale representation of the computational domain with two vesicles suspended in a planar extensional flow in a tubular channel with two side inlets and two outlets.

did not coincide with a specific knot within the knot vector, we consider the nearest knot to the specific value, which results in a set of elements being subjected to strongly imposed boundary conditions. Upon the element loop during the residual vector and tangent matrix assembly procedures, each element will be checked for the possibility of being a boundary element, afterwards, if the boundary has partial boundary conditions, the element will be checked against the set of elements specified upon initialization. The element index can be obtained from a partitioning and a distribution function that specify the global indices for the set of elements on each process based on the communicator size. To summarize, we added another check to whether the boundary element has a boundary condition in case the partially strongly-imposed Dirichlet boundary condition was applied. Fig. (5.11) shows a set the elements (in blue) with strongly-imposed BC on the top and bottom boundaries distributed among multiple processes in the communicator.

Figure (5.12) shows the temporal evolution of the two vesicles suspended in a parabolic fluid flow. The parachute-like shape of the vesicles starts to develop at around  $t = 0.2$ . However, unlike the results reported by Valizadeh et. al [43], the vesicles do not show a symmetric evolution due to the fact that both vesicles are not centered around the line of the maximum velocity layer of the fluid flow, which results in the asymmetric shapes as in Figures (5.12c-5.12d). Once the two vesicles reach the domain of the outlets where the flow is not anymore characterized by its parabolic profile, they start to retract to a sharp

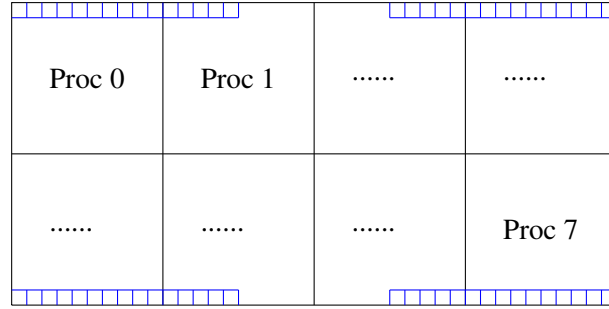


Figure 5.11: A representation of the computational domain  $\Omega$  being distributed on 8 processes, which corresponds to `mpirun -n 8`.

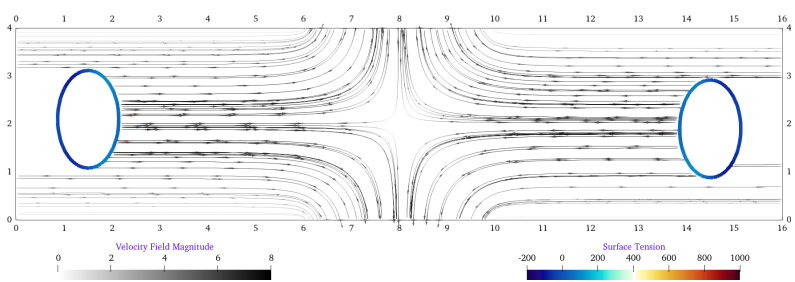
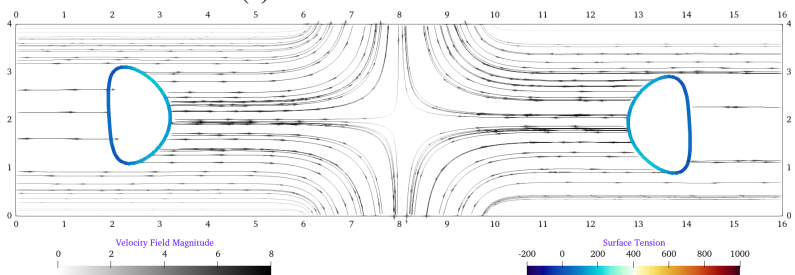
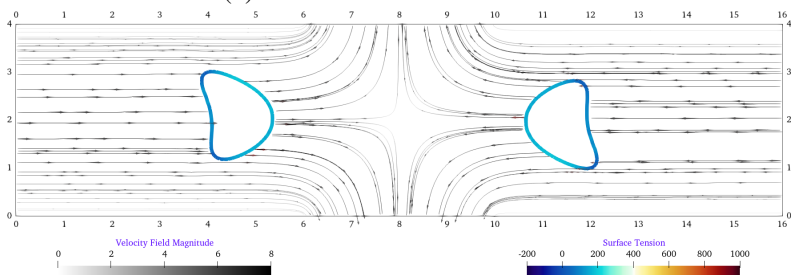
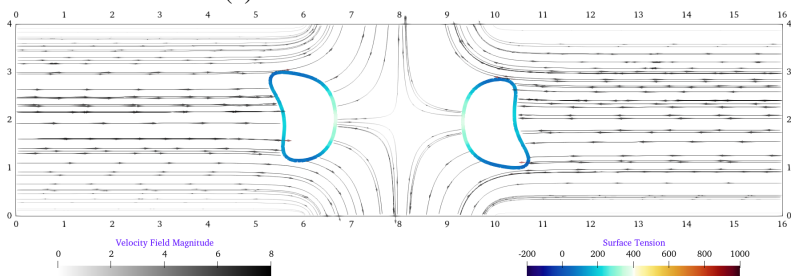
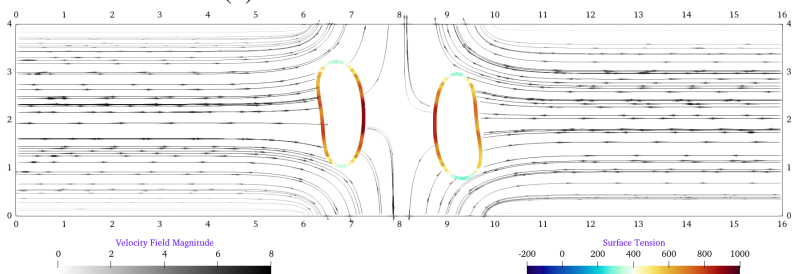
prolate spheroid shape due to the hydrodynamic forces exerted on both vesicles which result in the maximum surface tension values recorded during the temporal domain of this example as shown in Figures (5.12e-5.12g).

For a close-up inspection of those surface tension values the left vesicle in Fig. (5.12) experiences, we project those values of the zero-level set of the phase field variable  $\phi_1$  as shown in Fig. (5.13). In the beginning, we start noticing compression values on the side of the vesicle facing the fluid flow and tension values on the other side as shown in Fig. (5.13a), and as the vesicles move towards the center of the computational domain, the surface tension values intensifies as shown in Figures (5.13c-5.13d). At the point where the vesicle starts to evolve to the prolate spheroid shape as in Fig. (5.13e), it is no longer under the influence of the parabolic fluid flow, but rather, under the influence of the exiting flow which exerts hydrodynamic forces on the vesicle causing it to stretch, and hence, increasing the surface tension of the vesicle as shown in Fig. (5.13f). The aforementioned morphological evolution presented in Fig. (5.13) is compared to the morphological evolution of the same two vesicles, but in a wider tubular channel, that is, a computational domain  $\Omega$  defined as  $[0,16] \times [0,6]$ , i.e., an increase by 50% from the computational domain of vesicles in Fig. (5.13). To ensure we get the same velocity profile with a different channel height, we apply the following boundary condition:  $\mathbf{u}_{left} = [(48y - 8y^2)/9]\mathbf{e}_1 + 0\mathbf{e}_2$  and  $\mathbf{u}_{right} = [(-48y + 8y^2)/9]\mathbf{e}_1 + 0\mathbf{e}_2$ . As shown in Fig. (5.14), in the early stages, the vesicle profile is almost identical, but when hydrodynamic forces are strong enough to cause the shape transition, we can see that the vesicle in the wider tubular channel - in blue in Fig. (5.14) - does not evolve to the parachute-like shape even when suspended in a parabolic flow. The clearest distinction between the two cases can be seen in Fig. (5.14d).

Another interesting case can be observed when the vesicles have an oblate spheroid shape, i.e., a major axis in the direction of the flow. In this case, the vesicles transition from an oblate-like shape to a prolate-like shape upon coming in close proximity with each other once both vesicles enter the outlet region. The computational domain of this example and all other numerical and physical parameters are similar to that of the previous example. The vesicles were initiated with an oblate spheroid shape by tilting the phase-field profiles from the previous example by  $\pi/2$ . From Fig. (5.15), we can see the transition process from the original oblate-like shape to the prolate-like shape. Initially, the vesicle's surface starts experiencing compression as the vesicle undergoes a shape transition as in Figures (5.15a-5.15c). However, once the vesicle is in the outlet region and under the influence of the exiting fluid, it starts experiencing tension forces on its surface as shown in Figures (5.15d-5.15f).

## 5.6 Summary

In this chapter, we present a phase-field Navier Stokes model to simulate the hydrodynamics of vesicle doublets suspended in various settings of incompressible fluid flow. A crucial factor in the successful implementation of the model is the incorporation of the interaction energy defined in Eq. (2.46), as it prevents the phase-field defined vesicles from overlapping, opening the way for a wide variety of vesicle doublets hydrodynamics. The model accounts for a local inextensibility constraint within the vicinity of the zero-level set of the phase-field variables by introducing an additional equation to the system. To overcome the numerical difficulties of standard Galerkin-based finite element solutions of the Navier-Stokes equations, we apply the Residual-Based Variational Multi-Scale (RBVMS) method and solve the coupled systems using isogeometric analysis. We investigated the effect of the interaction number value on the evolution of the vesicle doublet and how this might affect its morphology. We consider vesicle doublet suspended in a shear flow, in a planar extensional flow, and in a parabolic flow. When the vesicle doublet is suspended in a shear flow, it can either slip past each other or slide on top of each other based on the value of the initial vertical displacement, that is the vertical distance between the center of masses between the two vesicles, and the velocity profile applied. When the vesicle doublet is suspended in a planar extensional flow in a con-

(a) Vesicles evolution at  $t = 0$ .(b) Vesicles evolution at  $t = 0.14$ .(c) Vesicles evolution at  $t = 0.42$ .(d) Vesicles evolution at  $t = 0.62$ .(e) Vesicles evolution at  $t = 0.75$ .

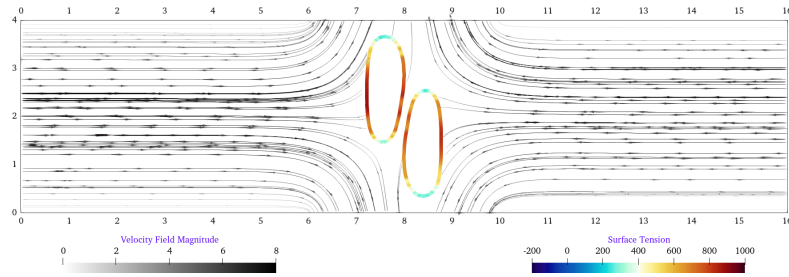
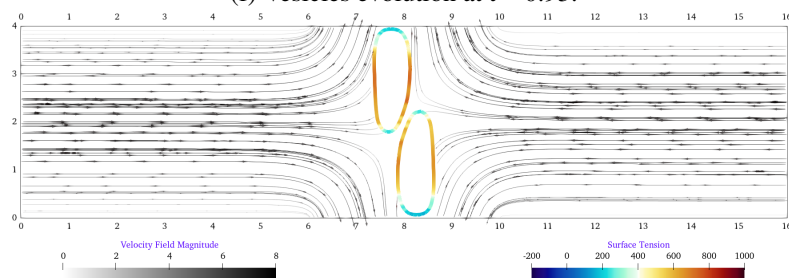
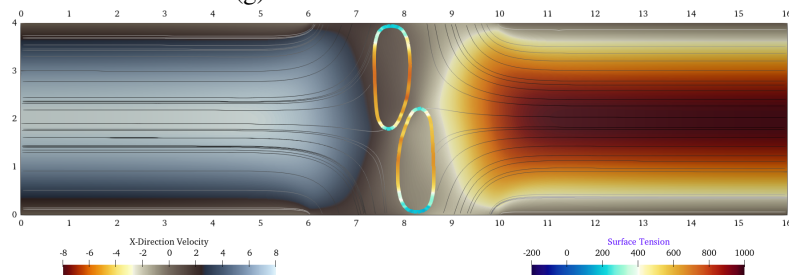
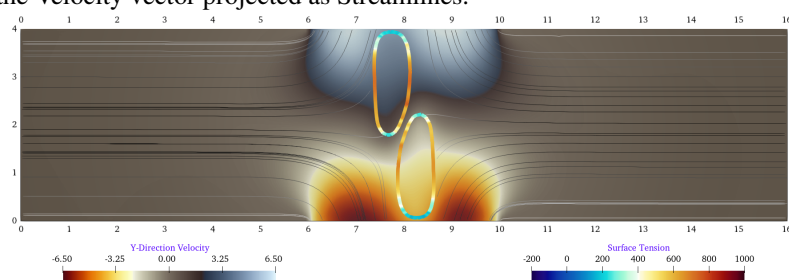
(f) Vesicles evolution at  $t = 0.93$ .(g) Vesicles evolution at  $t = 1.0$ .(h) Vesicles evolution at  $t = 1.0$  with a parabolic velocity profile. Color map shows the X-component of the velocity vector with the Velocity vector projected as Streamlines.(i) Vesicles evolution at  $t = 1.0$  with a parabolic velocity profile. Color map shows the Y-component of the velocity vector with the Velocity vector projected as Streamlines.

Figure 5.12: Snippets of the temporal evolution of two vesicles suspended in a planar extensional flow with an initial vertical displacement of 0.2. The velocity vector is projected as streamlines. The X- and Y-components of the velocity vector are shown in Figures (5.12h) and (5.12i).

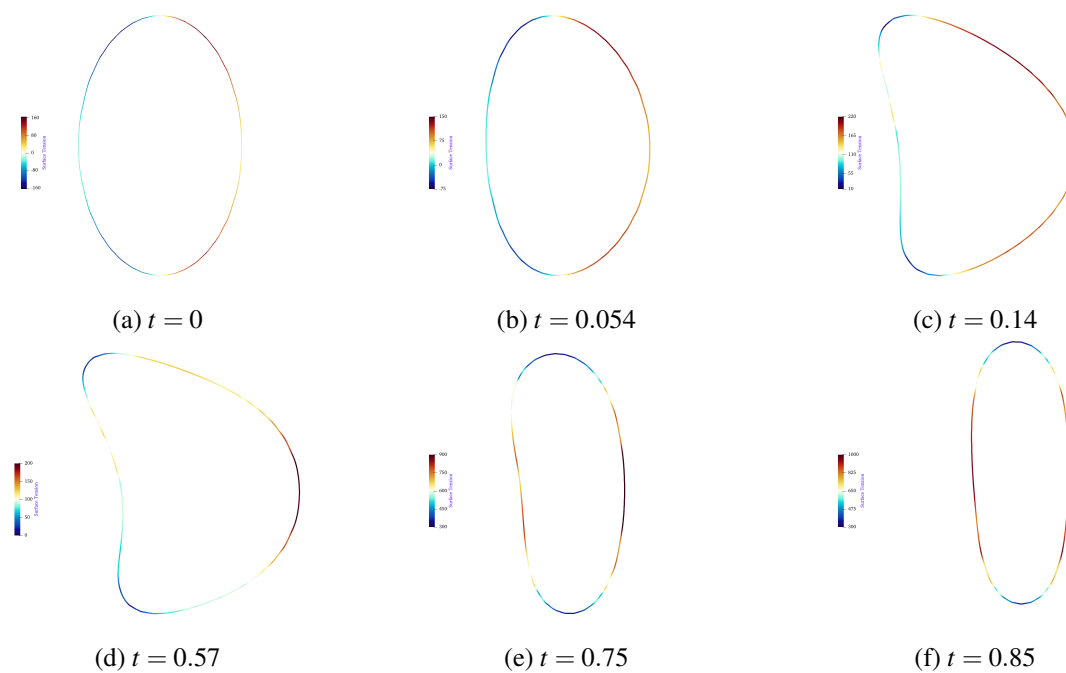


Figure 5.13: The temporal evolution of the left vesicle in Fig. (5.12) in a parabolic extensional flow with an initial vertical displacement of 0.2.

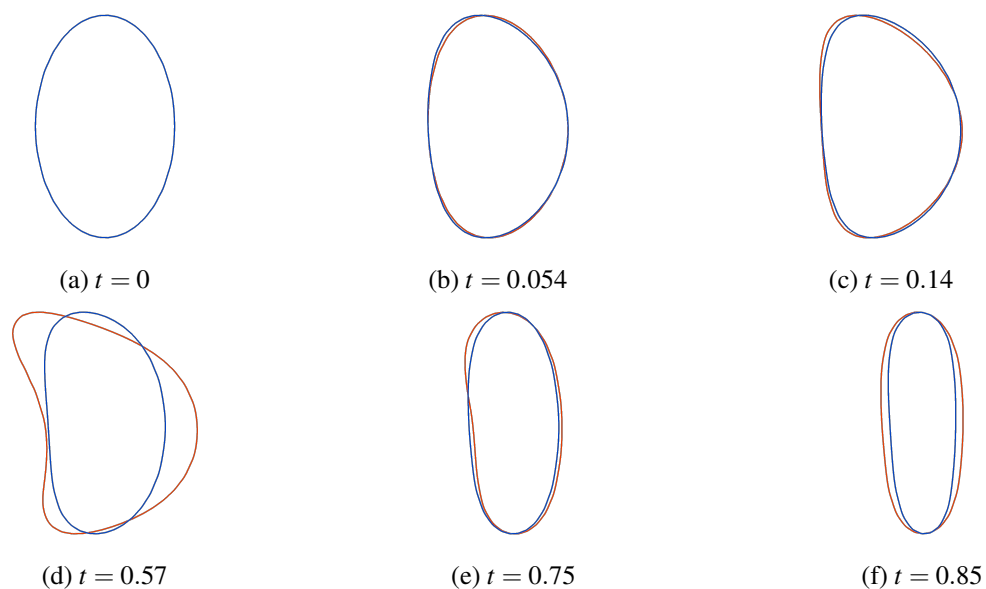


Figure 5.14: A comparison between the morphological evolution of two vesicles suspended in a planar extensional flow. The blue vesicle is suspended in a tubular channel with a width of 6 unit length, while the red one is suspended in a channel of 4 unit length.

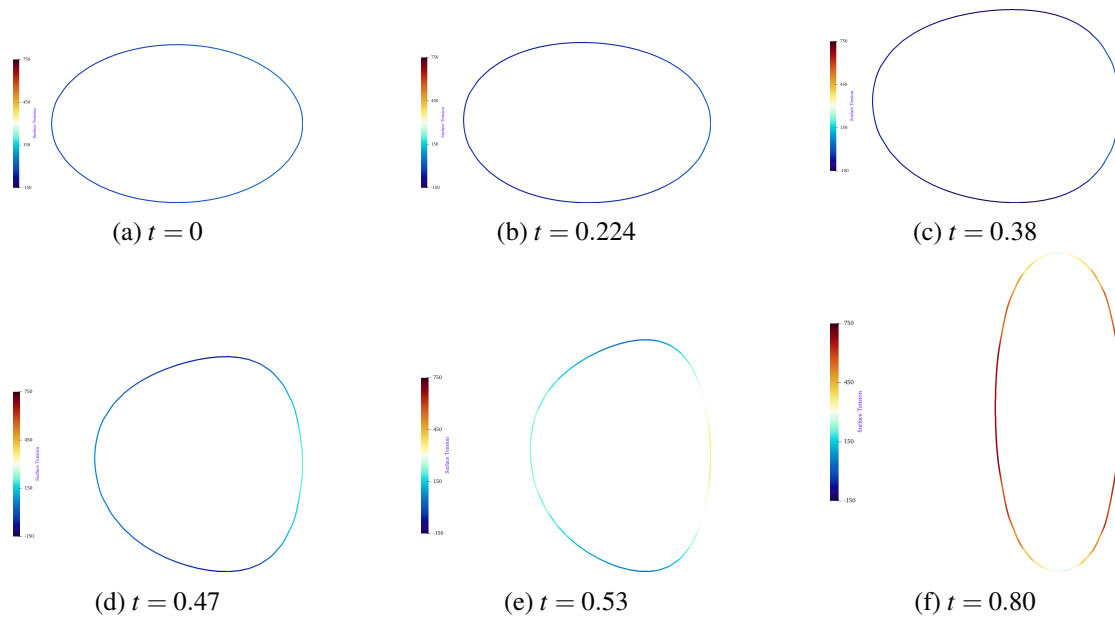


Figure 5.15: The temporal evolution of an oblate spheroid vesicle suspended in a planar extensional flow with a parabolic velocity profile. Fig. (5.15a) shows the initial oblate-like shape, while Fig. (5.15f) shows the final shape of the vesicle as it exits through the top outlet. Domain configurations are similar to Fig. (5.10).

figuration that resembles a junction, the time in which both vesicles separate depends largely on the value of the initial vertical displacement. However, when the vesicles are suspended in a tubular channel with a parabolic fluid flow, they develop a parachute-like shape upon converging towards each other before exiting the computational domain from the predetermined outlets. This shape however is affected largely by the height of the tubular channel in which the vesicle is suspended. The velocity essential boundary conditions are imposed weakly and strongly. The weak implementation of the boundary conditions was used when the velocity profile was defined on the entire boundary, while the strong implementation was used when the velocity profile was defined on a part of the boundary. The strong implementation of the essential boundary conditions was done by selectively applying it to the predetermined set of elements in a parallel-based code. This allowed us to simulate vesicle hydrodynamics in a computational domain with multiple inlets and outlets. We also investigated the hydrodynamics of oblate-like shape vesicles in a parabolic flow.





# 6

## Summary, conclusions, and future research

In this dissertation, we explore the possibility of coupling the phase-field method with isogeometric analysis to solve two of the most difficult problems related to vesicles morphology. In what follows, we summarize our work and draw our conclusions, and list the potential research direction.

### 6.1 Summary

We have addressed two main points. In the first, we study the morphology of single vesicles immersed in an electric field, and in the second, we study the morphology and hydrodynamics of vesicle doublet in an incompressible flow.

1. Vesicle morphology under static electric loads:

In this part of the research, we simulate the vesicle morphology under static electric loads. Our work is built on the electromechanical model proposed in [18, 109, 160]. We consider the Helmholtz free energy of the lipid bilayer, which accounts

for the elastic bending energy, the flexoelectric energy, and the dielectric energy for both the membrane and electrolyte. Each of those energies is recast in terms of the phase-field variable  $\phi$ . The total energy of the system is then complemented by two constraints to preserve the initial volume  $V_0$  and the surface area  $A_0$ . Using the gradient flow approach, we formulate the time evolution of the vesicle interface as the sum of the time derivative of the phase-field variable and the variational derivative of the total energy functional. Due to the need for high-order continuity basis functions, we resort to the NURBS-based isogeometric analysis to approximate the solution in a staggered scheme. This entails solving the linear Laplacian PDE describing the electric potential distribution within the computational domain and then solving for the phase-field variable by considering the electric potential that has been evaluated separately at each time step. This type of problems is extremely demanding computational-wise, and hence, we use the open-source PetIGA library. PetIGA is heavily reliant on PETSc, and provides the possibility of a parallel implementation for structured mesh problems, which is an essential part of solving this type of problems in a reasonable time-scale.

We test the response of vesicles subjected to static electric fields with varying intensities, e.g., from 10 10 kV/m to 50 10 kV/m. We also test the vesicle evolution when the flexoelectric nature of the membrane is accounted for, and the role the contrast in electrolyte conductivities inside and outside the vesicle. We intensively test the effect of the diffusive interface thickness on the stability of the solution and the overall morphology of the vesicle.

## 2. Vesicle doublet hydrodynamics in incompressible fluid flow:

In the second part of the research, we address the issue of vesicle doublet hydrodynamics. In this problem, we solve two advection-diffusion equations describing the process of advecting each vesicle by the fluid flow, in addition to the set of Navier-Stokes equations. We account for the local inextensibility by introducing a constraint equation based on the model proposed by [119] that takes effect within the vicinity of the interface. To prevent the phase-field variables representing the vesicles from overlapping, we introduce an interaction energy definition for this purpose. The proposed phase-field Navier-Stokes model has 9 degrees of freedom and is solved using isogeometric analysis in 2-D settings. We formulate the weak

form of the problem in a hybrid framework, where the set of advection-diffusion equations are weakened using the Galerkin NURBS-based IGA. Meanwhile, for the Navier-Stokes equations, we use the Residual-Based Variational MultiScale (RB-VMS) method proposed in [192]. The RBVMS is based on the idea of decomposing the fine and coarse scale equations, then approximating the fine-scale equations analytically and using the results in the coarse-scale equations, which are solved numerically. As in the previous problem, we used PetIGA to solve our numerical model, but different from it, we approximate the tangent matrix using PETSc's built-in finite-difference method.

In order to build our results on sound foundations, we started by testing the interaction number's effect on the repulsion between vesicle doublets. Then, we test the hydrodynamics of the vesicle doublet in a shear flow and how the relative proximity of both vesicles might alter the outcome of the numerical experiment. We also test the vesicle doublet hydrodynamics in a planar extensional flow in two different configurations, e.g., when the entire top and bottom sides of the boundaries were considered as outlets, and when only a portion of the top and bottom boundaries were considered as outlets (A junction configuration).

## 6.2 Conclusions

In what follows, we list our conclusions which are divided between the physics of the problems we solved and the numerical aspects of the research we have conducted.

1. The isogeometric analysis possesses the unique ability to solve higher-order PDEs, e.g., of order  $2m$ , due to the ability to obtain  $\mathcal{C}^{m-1}$  basis functions, by *tweaking* the multiplicity of any given knot within the knot vector. For any PDE in the strong form, there are certain differentiability requirements on the trial and test function spaces to obtain a smooth continuous solution within the weak form formulation; and those requirements are satisfied in the case of a basis function of  $\mathcal{C}^{m-1}$  continuous. This can be seen in the Euler-Lagrange equation of (2.3.2). In the context of the gradient flow approach, we end up with a fourth-order PDE, which necessitates the basis functions to be at least  $\mathcal{C}^1$  continuous, which is in fact the case in all of our numerical examples,

2. In the case where the electric response of the vesicle's membrane is the point of interest, the penalty method is not suitable to maintain any constraint imposed to preserve certain properties of the vesicle, like the initial volume and surface area. After intensive and lengthy testing, the penalty method in this particular type of problems suffers two deficiencies; when the penalty constant has a moderate to a large value, the vesicle interface tends to lock-on to the initial shape and not evolve over time, however, when the penalty constant is small to mitigate the lock-on problem, the phase-field variable tend to *dilute* over the entire computational domain or in another word, the diffusive interface with pre-defined width will not be maintained during the temporal domain of the problem,
3. The vesicle tends to deform due to the presence of the electric field. An increase in the electric field intensity leads to an increase in the deformation from the initial spherical shape to an oblate-like shape. When the flexoelectric nature of the vesicle's membrane is considered, the vesicle evolves to an asymmetrical shape. Besides this, the vesicle's membrane acts like a capacitor preventing charges from moving freely between intra- and extracellular medium, which leads to accumulations of charges at the top and the bottom poles of the vesicles in the direction of the electric field. The conductivity ratio,  $\sigma_{in} \setminus \sigma_{out}$ , plays also a key role in the stationary state of vesicles, where a sphere-to-prolate shape was observed on the higher end of the tested spectrum, and a sphere-to-oblate was observed on the lower end,
4. When modeling the hydrodynamics of vesicle doublet in incompressible fluid flow, the RBVMS method shows robustness, as it does not involve any *ad hoc* mechanisms. It and the standard Galerkin method for the transport equation can adequately predict the interaction between vesicles in a doublet system when a proper interaction number is chosen. In our numerical simulation, we found out that a value of 0.5 for the dimensionless interaction number would allow the vesicles to get as close as possible to each other without overlapping or locking,
5. When placed in a shear flow, the vesicle doublet can either slip past each other or slide on top of each other. This depends largely on the vertical displacement between the two vesicles and the velocity profile applied to the boundaries. However, in a planar extensional flow where the vesicle doublet system is placed at what resembles

a junction, the vesicles slip past each other but at a varying times to do so. This is also mainly affected by the vertical displacement. Different from this, a parachute-like shape develops when the vesicles are placed in a tubular channel with two inlets and two outlets. Upon converging on each other, the vesicles retract to form a prolate-like shape before exiting the channel from the side outlets. The parachute-like shape develops when the velocity profile is defined to be parabolic, and the symmetry depends on whether the vesicles are centered around the centerline of the velocity profile or not.

### 6.3 Future research

With the knowledge and experience gained over the course of this research in the fields of vesicles electromechanics and hydrodynamics, we are actively seeking to address the following points:

1. Investigate the time-varying electric and transmembrane potentials of the lipid bilayers, where due to the nature of the biomembrane as a barrier, electric charges tend to pile up on the vesicle's surface, and a concentration in the electric potential starts to develop on both sides of the membrane, and thus, the electric potential field experience a discontinuity. This discontinuity is expressed as jumps in the Maxwell stress tensor, which in turn exerts large forces on the biomembrane [91] itself, resulting in phenomenal morphological shapes of vesicles in time. A streamlines interpolation as shown in Fig. (4.7a) shows that despite an initial uniform electrical field, the vesicle membrane tends to deflect the electrical charges away from the vesicle. Additionally, there is a spike in the electric field intensity at the top and the bottom of the vesicle in the direction of the electric field, as shown in Fig. (4.7b) which depicts an accumulation of the electric charges in those regions. It is because of this reason that a comprehensive study using the phase-field method needs to be conducted to accurately calculate the electric potential across the biomembrane given its vital rule in the time-varying evolution of vesicles where the interpolating function used to approximate the conductivity within the computational domain, i.e., Eq. (2.20) does not capture the real physics of vesicles but rather consider as a simplification for this complex physical multi-fields problem.

2. In the case of vesicle doublet hydrodynamics, we conducted our research on the assumption that the fluid inside the vesicle and outside it has the same viscosity, which is not always the case [198, 199]. This simplification can be revisited by accounting for the viscosity contrast and, therefore, solving the Navier-Stokes equation in its full form. A broader image of single- and multi-vesicle systems hydrodynamics can also be built in the case where a parametric study was to be conducted to test vesicle behavior in turbulent flow at various Reynolds numbers. This can as well be extended to account for different geometrical configurations, such as channels with varying radii and curved channels, to study vesicles margination and hydrodynamics in a spatial environment similar to that in the human body. Doing so, however, requires access to a powerful high-performance computing cluster, and a highly optimized code to mitigate extra running costs. This can be implemented using PetIGA, with the need to devote more time in the preprocessing phase in order to generate the required geometries, which requires generating and manipulating a control mesh to produce the desired geometry.



## Phase-Field formulation of Bending, Flexoelectric and Dielectric energies

In his doctoral thesis, Wang [162], proposed and proved two lemmas to reformulate the sharp-interface defined bending energy surface integral to a phase-field defined bending energy volume integral. In chapter 2, we relied heavily on those two lemmas to recast the original definition of the bending, flexoelectric and dielectric energies into the phase-field form. In this appendix, we show the original transformation, and although Wang [162] models were only limited to incorporating the bending energy, we apply the lemmas to the flexoelectric sharp-interface defined energy as well as the dielectric energy.

1. The first lemma

$$\lim_{\varepsilon \rightarrow 0} \frac{1}{\varepsilon} \int_{\Omega} p\left(\frac{d(x)}{\varepsilon}\right) f(x) dx = \int_{-\infty}^{\infty} p(t) dt \int_{\Gamma} f(s) ds \quad (\text{A.1})$$

2. The second lemma

$$\int_{-\infty}^{\infty} \left[1 - \tanh^2\left(\frac{x}{\sqrt{2}\varepsilon}\right)\right]^2 dx = \frac{4}{3}\sqrt{2}\varepsilon \quad (\text{A.2})$$

The second lemma can be also further manipulated by dividing both sides of the equation by the term on the right hand side, as following:



$$\frac{3}{4\sqrt{2}\varepsilon} \int_{-\infty}^{\infty} [1 - \tanh^2(\frac{x}{\sqrt{2}\varepsilon})]^2 dx = 1 \quad (\text{A.3})$$

The phase-field variable  $\phi$  is defined by the profile of the tangent hyperbolic function and regularized by the regularization parameter  $\varepsilon$  as following:

$$\begin{aligned} \phi(\mathbf{x}) &= \tanh\left(\frac{di(\mathbf{x})}{\sqrt{2}\varepsilon}\right), \quad \text{where} \\ \nabla di(\mathbf{x}) &= \mathbf{n}, \quad \text{and} \\ \mathbf{n} &= \frac{\sqrt{2}\varepsilon}{1-\phi^2} \nabla\phi, \quad \text{and} \\ \nabla \cdot \mathbf{n} &= \frac{\sqrt{2}\varepsilon}{1-\phi^2} \left[ \Delta\phi + \frac{\phi(1-\phi^2)}{\varepsilon^2} \right] = -2H \end{aligned} \quad (\text{A.4})$$

## A.1 Bending Energy

The sharp-interface definition of the bending energy is as following:

$$\mathcal{E}_B = \int_{\Gamma} \frac{1}{2} \kappa [2H + H_{sp}]^2 d\Gamma \quad (\text{A.5})$$

Using Eq. (A.3), we can rewrite the aforementioned definition in terms of the phase-field variable  $\phi$ , as following:

$$E_B(\phi) \approx \left( \int_{\Gamma} \frac{1}{2} \kappa [2H + H_{sp}]^2 d\Gamma \right) \left( \frac{3}{4\sqrt{2}\varepsilon} \int_{-\infty}^{\infty} [1 - \phi^2]^2 dx \right) \quad (\text{A.6})$$

And using the total curvature definition from Eq. (A.4) into Eq. (A.6), then we have:

$$\begin{aligned} E_B(\phi) &= \frac{3\kappa}{8\sqrt{2}\varepsilon} \int_{\Omega} (1-\phi^2)^2 (2H + H_{sp})^2 d\Omega \\ &= \frac{3\kappa}{8\sqrt{2}\varepsilon} \int_{\Omega} (1-\phi^2)^2 \left( \frac{-\sqrt{2}\varepsilon}{1-\phi^2} \left[ \Delta\phi + \frac{\phi(1-\phi^2)}{\varepsilon^2} \right] + H_{sp} \right)^2 \\ &= \frac{3\kappa}{8\sqrt{2}\varepsilon} \int_{\Omega} \left[ -\sqrt{2}\varepsilon \left( \Delta\phi + \frac{\phi}{\varepsilon^2} (1-\phi^2) \right) + H_{sp} (1-\phi^2) \right]^2 \\ &= \frac{3\kappa}{8\sqrt{2}\varepsilon} \int_{\Omega} \left[ -\sqrt{2}\varepsilon \Delta\phi - \frac{\sqrt{2}\phi}{\varepsilon} (1-\phi^2) + H_{sp} (1-\phi^2) \right]^2 \\ &= \frac{3\kappa}{8\sqrt{2}\varepsilon} \int_{\Omega} \left[ -\sqrt{2}\varepsilon \Delta\phi - \frac{\sqrt{2}\phi}{\varepsilon} (1-\phi^2) + \frac{\sqrt{2}}{\sqrt{2}} H_{sp} (1-\phi^2) \right]^2 \\ &= \frac{3\kappa}{8\sqrt{2}\varepsilon} \int_{\Omega} [-\sqrt{2}]^2 \left[ \varepsilon \Delta\phi + \frac{\phi}{\varepsilon} (1-\phi^2) - \frac{1}{\sqrt{2}} H_{sp} (1-\phi^2) \right]^2 \\ &= \frac{3\kappa}{4\sqrt{2}\varepsilon} \int_{\Omega} \left[ \varepsilon \Delta\phi + \frac{\phi}{\varepsilon} (1-\phi^2) - \frac{1}{\sqrt{2}} H_{sp} (1-\phi^2) \right]^2 \\ &= \frac{3\kappa}{4\sqrt{2}\varepsilon} \int_{\Omega} \left[ \varepsilon \Delta\phi + \left( \frac{\phi}{\varepsilon} - \frac{H_{sp}}{\sqrt{2}} \right) (1-\phi^2) \right]^2 d\Omega \end{aligned} \quad (\text{A.7})$$

## A.2 Flexoelectric Energy

The flexoelectric energy defined on the surface of the vesicle as following:

$$\mathcal{E}_F = - \int_{\Gamma} \int_0^{d_m} \mathbf{P}^f \cdot \mathbf{E} \, dr \, d\Gamma = -2c_1 d_m \int_{\Gamma} H \mathbf{E} \cdot \mathbf{n} \, d\Gamma \quad (\text{A.8})$$

using the second lemma of Eq. (A.3) in Eq. (A.8), and substituting for the total curvature and normal vector to the surface of the vesicles from Eq. (A.4), we end up with:

$$\begin{aligned} E_F(\phi) &\approx \left( -2c_1 d_m \int_{\Gamma} H \mathbf{E} \cdot \mathbf{n} \, d\Gamma \right) \left( \frac{3}{4\sqrt{2}\varepsilon} \int_{-\infty}^{\infty} [1 - \phi^2]^2 dx \right) \\ &= -\frac{6c_1 d_m}{4\sqrt{2}\varepsilon} \int_{\Omega} \left[ (1 - \phi^2)^2 H \mathbf{n} \cdot \nabla \psi \right] d\Omega \\ &= -\frac{6c_1 d_m}{4\sqrt{2}\varepsilon} \int_{\Omega} (1 - \phi^2)^2 \left( \frac{-\sqrt{2}\varepsilon}{2(1 - \phi^2)} \left[ \Delta \phi + \frac{\phi(1 - \phi^2)}{\varepsilon^2} \right] \mathbf{n} \cdot \nabla \psi \right) d\Omega \\ &= -\frac{6c_1 d_m}{4\sqrt{2}\varepsilon} \int_{\Omega} (1 - \phi^2)^2 \left( \frac{-\sqrt{2}\varepsilon}{2(1 - \phi^2)} \left[ \Delta \phi + \frac{\phi(1 - \phi^2)}{\varepsilon^2} \right] \frac{\sqrt{2}\varepsilon}{1 - \phi^2} \nabla \phi \cdot \nabla \psi \right) d\Omega \\ &= -\frac{6c_1 d_m}{4\sqrt{2}\varepsilon} \int_{\Omega} (1 - \phi^2) \left( \frac{-\sqrt{2}\varepsilon}{2(1 - \phi^2)} \left[ \Delta \phi + \frac{\phi(1 - \phi^2)}{\varepsilon^2} \right] \sqrt{2}\varepsilon \nabla \phi \cdot \nabla \psi \right) d\Omega \\ &= -\frac{6c_1 d_m}{4\sqrt{2}\varepsilon} \int_{\Omega} \left( \frac{\sqrt{2}\varepsilon}{2} \left[ \Delta \phi + \frac{\phi(1 - \phi^2)}{\varepsilon^2} \right] \sqrt{2}\varepsilon \nabla \phi \cdot \nabla \psi \right) d\Omega \\ &= -\frac{6c_1 d_m}{4\sqrt{2}\varepsilon} \int_{\Omega} \left( \varepsilon^2 \left[ \Delta \phi + \frac{\phi(1 - \phi^2)}{\varepsilon^2} \right] \nabla \phi \cdot \nabla \psi \right) d\Omega \\ &= -\frac{6c_1 d_m}{4\sqrt{2}\varepsilon} \int_{\Omega} \left[ \varepsilon^2 \Delta \phi + \phi(1 - \phi^2) \right] \nabla \phi \cdot \nabla \psi \, d\Omega \\ &= -\frac{6c_1 d_m}{4\sqrt{2}\varepsilon} \int_{\Omega} \varepsilon \left[ \varepsilon \Delta \phi + \frac{\phi}{\varepsilon} (1 - \phi^2) \right] \nabla \phi \cdot \nabla \psi \, d\Omega \\ &= -\frac{3c_1 d_m}{2\sqrt{2}} \int_{\Omega} \left[ \varepsilon \Delta \phi + \frac{\phi}{\varepsilon} (1 - \phi^2) \right] \nabla \phi \cdot \nabla \psi \, d\Omega \end{aligned} \quad (\text{A.9})$$

## A.3 Dielectric Energy of the Membrane

The sharp-interface definition of the dielectric energy of the membrane is as following:

$$\begin{aligned} \mathcal{E}_{DM} &= -\frac{1}{2} \int_{\Gamma} \int_0^{d_m} \mathbf{D}^e \cdot \mathbf{E} \, dr \\ &= -\frac{d_m}{2} \int_{\Gamma} \mathbf{D}^e \cdot \mathbf{E} \, dA \end{aligned} \quad (\text{A.10})$$

where  $\mathbf{D}^e$  is the electric displacement defined as  $\mathbf{D}^e = \varepsilon_m \mathbf{E}$ , and  $\varepsilon_m$  is the dielectric constant of the vesicle. The term inside the surface integral of Eq. (A.10)  $\mathbf{D}^e \cdot \mathbf{E}$  can be simplified

to  $\varepsilon_m |\nabla\psi|^2$  given that  $\mathbf{E} = -\nabla\psi$ . Following this, Eq. (A.10) becomes:

$$\varepsilon_{DM} = -\frac{1}{2} \int_{\Gamma} \int_0^{d_m} \mathbf{D}^e \cdot \mathbf{E} \, dr = -\frac{d_m \varepsilon_m}{2} \int_{\Gamma} |\nabla\psi|^2 \, d\Gamma \quad (\text{A.11})$$

And by the second lemma of Eq. (A.3), the dielectric energy of the membrane can be written as following:

$$\begin{aligned} \varepsilon_{DM} &\approx \left( -\frac{d_m \varepsilon_m}{2} \int_{\Gamma} |\nabla\psi|^2 \, d\Gamma \right) \left( \frac{3}{4\sqrt{2}\varepsilon} \int_{-\infty}^{\infty} [1 - \phi^2]^2 \, dx \right) \\ E_{DM}(\phi) &= -\frac{3d_m \varepsilon_m}{8\sqrt{2}\varepsilon} \int_{\Omega} (1 - \phi^2)^2 |\nabla\psi|^2 \, d\Omega \end{aligned} \quad (\text{A.12})$$

## Bibliography

- [1] Ya'nan Lin et al. “Dynamic Behavior of Complex Coacervates with Internal Lipid Vesicles under Nonequilibrium Conditions”. In: *Langmuir* 36.7 (Jan. 2020), pp. 1709–1717. DOI: [10.1021/acs.langmuir.9b03561](https://doi.org/10.1021/acs.langmuir.9b03561).
- [2] Pia R-M Siljander et. al. “Biological properties of extracellular vesicles and their physiological functions”. In: *Journal of Extracellular Vesicles* 4.1 (Jan. 2015), p. 27066. DOI: [10.3402/jev.v4.27066](https://doi.org/10.3402/jev.v4.27066).
- [3] Rashmi Wardhan and Padmshree Mudgal. *Textbook of Membrane Biology*. Springer, 2017. DOI: <https://doi.org/10.1007/978-981-10-7101-0>.
- [4] Udo Seifert. “Configurations of fluid membranes and vesicles”. In: *Advances in physics* 46.1 (1997), pp. 13–137. DOI: <https://doi.org/10.1080/00018739700101488>.
- [5] J Käs and E Sackmann. “Shape transitions and shape stability of giant phospholipid vesicles in pure water induced by area-to-volume changes”. In: *Biophysical journal* 60.4 (1991), pp. 825–844. DOI: [10.1016/S0006-3495\(91\)82117-8](https://doi.org/10.1016/S0006-3495(91)82117-8).
- [6] Guillaume Gueguen, Nicolas Destainville, and Manoel Manghi. “Fluctuation tension and shape transition of vesicles: renormalisation calculations and Monte Carlo simulations”. In: *Soft matter* 13.36 (2017), pp. 6100–6117. DOI: <https://doi.org/10.1039/C7SM01272A>.
- [7] Hiroshi Noguchi and Gerhard Gompper. “Shape transitions of fluid vesicles and red blood cells in capillary flows”. In: *Proceedings of the National Academy of Sciences* 102.40 (2005), pp. 14159–14164. DOI: <https://doi.org/10.1073/pnas.0504243102>.
- [8] SL Das, JT Jenkins, and T Baumgart. “Neck geometry and shape transitions in vesicles with co-existing fluid phases: Role of Gaussian curvature stiffness vs. spontaneous curvature”. In: *EPL (Europhysics Letters)* 86.4 (2009), p. 48003. DOI: <https://iopscience.iop.org/article/10.1209/0295-5075/86/48003>.
- [9] Albert J Markvoort, RA Van Santen, and PAJ Hilbers. “Vesicle shapes from molecular dynamics simulations”. In: *The Journal of Physical Chemistry B* 110.45 (2006), pp. 22780–22785. DOI: <https://doi.org/10.1021/jp064888a>.

- [10] Volker Knecht and Siewert-Jan Marrink. “Molecular dynamics simulations of lipid vesicle fusion in atomic detail”. In: *Biophysical journal* 92.12 (2007), pp. 4254–4261. DOI: <https://doi.org/10.1529/biophysj.106.103572>.
- [11] Xiang Yu and Meenakshi Dutt. “A multiscale approach to study molecular and interfacial characteristics of vesicles”. In: *Molecular Systems Design & Engineering* 3.6 (2018), pp. 883–895. DOI: <https://doi.org/10.1039/C8ME00029H>.
- [12] Stefano Piotto and Fabio Mavelli. “Monte Carlo simulations of vesicles and fluid membranes transformations”. In: *Origins of Life and Evolution of the Biosphere* 34.1-2 (2004), pp. 225–235. DOI: <https://doi.org/10.1023/B:ORIG.0000009842.58634.a0>.
- [13] Satoru Yamamoto, Yutaka Maruyama, and Shi-aki Hyodo. “Dissipative particle dynamics study of spontaneous vesicle formation of amphiphilic molecules”. In: *The Journal of chemical physics* 116.13 (2002), pp. 5842–5849. DOI: <https://doi.org/10.1063/1.1456031>.
- [14] Hiroshi Noguchi and Masako Takasu. “Adhesion of nanoparticles to vesicles: a Brownian dynamics simulation”. In: *Biophysical journal* 83.1 (2002), pp. 299–308. DOI: [https://doi.org/10.1016/S0006-3495\(02\)75170-9](https://doi.org/10.1016/S0006-3495(02)75170-9).
- [15] Xuejin Li, Petia M Vlahovska, and George Em Karniadakis. “Continuum-and particle-based modeling of shapes and dynamics of red blood cells in health and disease”. In: *Soft Matter* 9.1 (2013), pp. 28–37. DOI: [10.1039/C2SM26891D](https://doi.org/10.1039/C2SM26891D).
- [16] Vincent Doyeux et al. “Simulation of two-fluid flows using a finite element/level set method. Application to bubbles and vesicle dynamics”. In: *Journal of Computational and Applied Mathematics* 246 (2013), pp. 251–259. DOI: <https://doi.org/10.1016/j.cam.2012.05.004>.
- [17] J.M. Lyu et al. “An isogeometric boundary element method for soft particles flowing in microfluidic channels”. In: *Computers and Fluids* 214 (Jan. 2021), p. 104786. DOI: [10.1016/j.compfluid.2020.104786](https://doi.org/10.1016/j.compfluid.2020.104786).
- [18] Ling-Tian Gao, Xi-Qiao Feng, and Huajian Gao. “A phase field method for simulating morphological evolution of vesicles in electric fields”. In: *Journal of Computational Physics* 228.11 (2009), pp. 4162–4181. DOI: <https://doi.org/10.1016/j.jcp.2009.02.034>.
- [19] Ebrahim M. Kolahdouz and David Salac. “Electrohydrodynamics of Three-Dimensional Vesicles: A Numerical Approach”. In: *SIAM Journal on Scientific Computing* 37.3 (2015), B473–B494. DOI: <https://doi.org/10.1137/140988966>.

- [20] Navid Valizadeh and Timon Rabczuk. “Isogeometric analysis for phase-field models of geometric PDEs and high-order PDEs on stationary and evolving surfaces”. In: *Computer Methods in Applied Mechanics and Engineering* 351 (2019), pp. 599–642. DOI: <https://doi.org/10.1016/j.cma.2019.03.043>.
- [21] Xiaoqiang Wang, Lili Ju, and Qiang Du. “Efficient and stable exponential time differencing Runge–Kutta methods for phase field elastic bending energy models”. In: *Journal of Computational Physics* 316 (2016), pp. 21–38. DOI: <https://doi.org/10.1016/j.jcp.2016.04.004>.
- [22] T.J.R. Hughes, J.A. Cottrell, and Y. Bazilevs. “Isogeometric analysis: CAD, finite elements, NURBS, exact geometry and mesh refinement”. In: *Computer Methods in Applied Mechanics and Engineering* 194.39 (2005), pp. 4135–4195. DOI: <https://doi.org/10.1016/j.cma.2004.10.008>.
- [23] J Austin Cottrell, Thomas JR Hughes, and Yuri Bazilevs. *Isogeometric analysis: toward integration of CAD and FEA*. John Wiley & Sons, 2009. DOI: <https://doi.org/10.1002/9780470749081.ch7>.
- [24] Y. Bazilevs et al. “Isogeometric analysis using T-splines”. In: *Computer Methods in Applied Mechanics and Engineering* 199.5 (2010). Computational Geometry and Analysis, pp. 229–263. DOI: <https://doi.org/10.1016/j.cma.2009.02.036>.
- [25] Ping Wang et al. “Adaptive isogeometric analysis using rational PHT-splines”. In: *Computer-Aided Design* 43.11 (Nov. 2011), pp. 1438–1448. DOI: [10.1016/j.cad.2011.08.026](https://doi.org/10.1016/j.cad.2011.08.026).
- [26] N. Nguyen-Thanh et al. “Isogeometric analysis using polynomial splines over hierarchical T-meshes for two-dimensional elastic solids”. In: *Computer Methods in Applied Mechanics and Engineering* 200.21-22 (May 2011), pp. 1892–1908. DOI: [10.1016/j.cma.2011.01.018](https://doi.org/10.1016/j.cma.2011.01.018).
- [27] N. Nguyen-Thanh et al. “Isogeometric analysis of large-deformation thin shells using RHT-splines for multiple-patch coupling”. In: *Computer Methods in Applied Mechanics and Engineering* 316 (Apr. 2017), pp. 1157–1178. DOI: [10.1016/j.cma.2016.12.002](https://doi.org/10.1016/j.cma.2016.12.002).
- [28] Andrea Bartezzaghi, Luca Dedè, and Alfio Quarteroni. “Biomembrane modeling with isogeometric analysis”. In: *Computer Methods in Applied Mechanics and Engineering* 347 (2019), pp. 103–119. DOI: <https://doi.org/10.1016/j.cma.2018.12.025>.
- [29] Gwenn Boedec, Marc Leonetti, and Marc Jaeger. “Isogeometric FEM-BEM simulations of drop, capsule and vesicle dynamics in Stokes flow”. In: *Journal of Computational Physics* 342 (2017), pp. 117–138. DOI: <https://doi.org/10.1016/j.jcp.2017.04.024>.

- [30] Navid Valizadeh. “Developments in Isogeometric Analysis and Application to High-Order Phase-Field Models of Biomembranes”. en. PhD thesis. 2022. DOI: [10.25643/BAUHAUS-UNIVERSITAET.4565](https://doi.org/10.25643/BAUHAUS-UNIVERSITAET.4565).
- [31] Nicola A Nodargi et al. “An isogeometric analysis formulation for red blood cell electro-deformation modeling”. In: *Computer Methods in Applied Mechanics and Engineering* 338 (2018), pp. 392–411. DOI: <https://doi.org/10.1016/j.cma.2018.04.038>.
- [32] Daniel Hilger et al. “A Novel Approach to Fluid-Structure Interaction Simulations Involving Large Translation and Contact”. In: *Isogeometric Analysis and Applications 2018 1* (2021), pp. 39–56. DOI: [10.1007/978-3-030-49836-8\\_3](https://doi.org/10.1007/978-3-030-49836-8_3).
- [33] Chenglong Wang et al. “Modeling of a hydraulic arresting gear using fluid–structure interaction and isogeometric analysis”. In: *Computers & Fluids* 142 (2017), pp. 3–14. DOI: <https://doi.org/10.1016/j.compfluid.2015.12.004>.
- [34] M Dinachandra and Sethuraman Raju. “Isogeometric analysis for acoustic fluid-structure interaction problems”. In: *International Journal of Mechanical Sciences* 131 (2017), pp. 8–25. DOI: [10.1016/j.ijmecsci.2017.06.041](https://doi.org/10.1016/j.ijmecsci.2017.06.041).
- [35] Yuri Bazilevs, M-C Hsu, and MA3003060 Scott. “Isogeometric fluid–structure interaction analysis with emphasis on non-matching discretizations, and with application to wind turbines”. In: *Computer Methods in Applied Mechanics and Engineering* 249 (2012), pp. 28–41. DOI: <https://doi.org/10.1016/j.cma.2012.03.028>.
- [36] Ahmed Mostafa Shaaban et al. “Shape optimization by conventional and extended isogeometric boundary element method with PSO for two-dimensional Helmholtz acoustic problems”. In: *Engineering Analysis with Boundary Elements* 113 (2020), pp. 156–169. DOI: <https://doi.org/10.1016/j.enganabound.2019.12.012>.
- [37] Ahmed Mostafa Shaaban et al. “3D isogeometric boundary element analysis and structural shape optimization for Helmholtz acoustic scattering problems”. In: *Computer Methods in Applied Mechanics and Engineering* 384 (2021), p. 113950. DOI: <https://doi.org/10.1016/j.cma.2021.113950>.
- [38] Ahmed Mostafa Shaaban et al. “An isogeometric Burton-Miller method for the transmission loss optimization with application to mufflers with internal extended tubes”. In: *Applied Acoustics* 185 (2022), p. 108410. DOI: <https://doi.org/10.1016/j.apacoust.2021.108410>.
- [39] Ahmed Mostafa Shaaban et al. “Isogeometric boundary element analysis and shape optimization by PSO for 3D axi-symmetric high frequency Helmholtz acoustic problems”. In: *Journal of Sound and Vibration* 486 (2020), p. 115598. DOI: <https://doi.org/10.1016/j.jsv.2020.115598>.

- [40] Jorge López, Navid Valizadeh, and Timon Rabczuk. “An isogeometric phase–field based shape and topology optimization for flexoelectric structures”. In: *Computer Methods in Applied Mechanics and Engineering* 391 (2022), p. 114564. DOI: <https://doi.org/10.1016/j.cma.2021.114564>.
- [41] Jorge López, Cosmin Anitescu, and Timon Rabczuk. “Isogeometric structural shape optimization using automatic sensitivity analysis”. In: *Applied Mathematical Modelling* 89 (2021), pp. 1004–1024. DOI: <https://doi.org/10.1016/j.apm.2020.07.027>.
- [42] JS Langer. “Models of pattern formation in first-order phase transitions”. In: *Directions in Condensed Matter Physics: Memorial Volume in Honor of Shang-Keng Ma*. World Scientific, 1986, pp. 165–186. DOI: [https://doi.org/10.1142/9789814415309\\_0005](https://doi.org/10.1142/9789814415309_0005).
- [43] Navid Valizadeh and Timon Rabczuk. “Isogeometric analysis of hydrodynamics of vesicles using a monolithic phase–field approach”. In: *Computer Methods in Applied Mechanics and Engineering* 388 (2022), p. 114191. DOI: <https://doi.org/10.1016/j.cma.2021.114191>.
- [44] Bryan Quaife, Shravan Veerapaneni, and Y.-N. Young. “Hydrodynamics and rheology of a vesicle doublet suspension”. In: *Physical Review Fluids* 4.10 (Oct. 2019). DOI: [10.1103/physrevfluids.4.103601](https://doi.org/10.1103/physrevfluids.4.103601).
- [45] Mohammed Ashour, Navid Valizadeh, and Timon Rabczuk. “Isogeometric analysis for a phase-field constrained optimization problem of morphological evolution of vesicles in electrical fields”. In: *Computer Methods in Applied Mechanics and Engineering* 377 (2021), p. 113669. DOI: <https://doi.org/10.1016/j.cma.2021.113669>.
- [46] Charlotte Kuhn and Ralf Müller. “A continuum phase field model for fracture”. In: *Engineering Fracture Mechanics* 77.18 (Dec. 2010), pp. 3625–3634. DOI: [10.1016/j.engfracmech.2010.08.009](https://doi.org/10.1016/j.engfracmech.2010.08.009).
- [47] Vincent Hakim and Alain Karma. “Laws of crack motion and phase-field models of fracture”. In: *Journal of the Mechanics and Physics of Solids* 57.2 (Feb. 2009), pp. 342–368. DOI: [10.1016/j.jmps.2008.10.012](https://doi.org/10.1016/j.jmps.2008.10.012).
- [48] G. Tegze, T. Pusztai, and L. Gránásy. “Phase field simulation of liquid phase separation with fluid flow”. In: *Materials Science and Engineering: A* 413–414 (Dec. 2005), pp. 418–422. DOI: [10.1016/j.msea.2005.09.045](https://doi.org/10.1016/j.msea.2005.09.045).
- [49] Yue Hou et al. “Coupled Navier–Stokes Phase-Field Model to Evaluate the Microscopic Phase Separation in Asphalt Binder under Thermal Loading”. In: *Journal of Materials in Civil Engineering* 28.10 (Oct. 2016). DOI: [10.1061/\(asce\)mt.1943-5533.0001581](https://doi.org/10.1061/(asce)mt.1943-5533.0001581).



- [50] Ingo Steinbach. “Phase-Field Model for Microstructure Evolution at the Mesoscopic Scale”. In: *Annual Review of Materials Research* 43.1 (July 2013), pp. 89–107. DOI: [10.1146/annurev-matsci-071312-121703](https://doi.org/10.1146/annurev-matsci-071312-121703).
- [51] Long-Qing Chen. “Phase-Field Models for Microstructure Evolution”. In: *Annual Review of Materials Research* 32.1 (Aug. 2002), pp. 113–140. DOI: [10.1146/annurev-matsci.32.112001.132041](https://doi.org/10.1146/annurev-matsci.32.112001.132041).
- [52] Srujan Rokkam et al. “Phase field modeling of void nucleation and growth in irradiated metals”. In: *Modelling and Simulation in Materials Science and Engineering* 17.6 (Aug. 2009), p. 064002. DOI: [10.1088/0965-0393/17/6/064002](https://doi.org/10.1088/0965-0393/17/6/064002).
- [53] Paul C Millett et al. “Void nucleation and growth in irradiated polycrystalline metals: a phase-field model”. In: *Modelling and Simulation in Materials Science and Engineering* 17.6 (Aug. 2009), p. 064003. DOI: [10.1088/0965-0393/17/6/064003](https://doi.org/10.1088/0965-0393/17/6/064003).
- [54] X.Q. Ma et al. “Phase-field simulation of hydride precipitation in bi-crystalline zirconium”. In: *Scripta Materialia* 47.4 (2002), pp. 237–241. DOI: [https://doi.org/10.1016/S1359-6462\(02\)00131-8](https://doi.org/10.1016/S1359-6462(02)00131-8).
- [55] X.Q. Ma et al. “Effect of applied load on nucleation and growth of Y-hydrides in zirconium”. In: *Computational Materials Science* 23.1 (2002), pp. 283–290. DOI: [https://doi.org/10.1016/S0927-0256\(01\)00226-9](https://doi.org/10.1016/S0927-0256(01)00226-9).
- [56] Michael Strobl and Thomas Seelig. “On constitutive assumptions in phase field approaches to brittle fracture”. In: *Procedia Structural Integrity* 2 (2016), pp. 3705–3712. DOI: [10.1016/j.prostr.2016.06.460](https://doi.org/10.1016/j.prostr.2016.06.460).
- [57] Marreddy Ambati, Tymofiy Gerasimov, and Laura De Lorenzis. “A review on phase-field models of brittle fracture and a new fast hybrid formulation”. In: *Computational Mechanics* 55.2 (Dec. 2014), pp. 383–405. DOI: [10.1007/s00466-014-1109-y](https://doi.org/10.1007/s00466-014-1109-y).
- [58] Yulan Li et al. “A review: applications of the phase field method in predicting microstructure and property evolution of irradiated nuclear materials”. In: *npj Computational Materials* 3.1 (Apr. 2017). DOI: [10.1038/s41524-017-0018-y](https://doi.org/10.1038/s41524-017-0018-y).
- [59] Y. Bazilevs et al. “Isogeometric Fluid–structure Interaction Analysis with Applications to Arterial Blood Flow”. In: *Computational Mechanics* 38.4-5 (June 2006), pp. 310–322. DOI: [10.1007/s00466-006-0084-3](https://doi.org/10.1007/s00466-006-0084-3).
- [60] J.A. Cottrell et al. “Isogeometric analysis of structural vibrations”. In: *Computer Methods in Applied Mechanics and Engineering* 195.41-43 (Aug. 2006), pp. 5257–5296. DOI: [10.1016/j.cma.2005.09.027](https://doi.org/10.1016/j.cma.2005.09.027).
- [61] Héctor Gómez et al. “Isogeometric analysis of the Cahn–Hilliard phase-field model”. In: *Computer Methods in Applied Mechanics and Engineering* 197.49-50 (Sept. 2008), pp. 4333–4352. DOI: [10.1016/j.cma.2008.05.003](https://doi.org/10.1016/j.cma.2008.05.003).

- [62] Wolfgang Helfrich. “Elastic properties of lipid bilayers: theory and possible experiments”. In: *Zeitschrift für Naturforschung C* 28.11-12 (1973), pp. 693–703. DOI: [10.1515/znc-1973-11-1209](https://doi.org/10.1515/znc-1973-11-1209).
- [63] Qiang Du and Jian Zhang. “Adaptive finite element method for a phase field bending elasticity model of vesicle membrane deformations”. In: *SIAM Journal on Scientific Computing* 30.3 (2008), pp. 1634–1657. DOI: <https://doi.org/10.1137/060656449>.
- [64] Ashkan Almasi et al. “A strong form meshfree collocation method for frictional contact on a rigid obstacle”. In: *Computer Methods in Applied Mechanics and Engineering* 357 (2019), p. 112597. DOI: [doi.org/10.1016/j.cma.2019.112597](https://doi.org/10.1016/j.cma.2019.112597).
- [65] Young-Cheol Yoon and Jeong-Hoon Song. “Extended particle difference method for weak and strong discontinuity problems: part I. Derivation of the extended particle derivative approximation for the representation of weak and strong discontinuities”. In: *Computational Mechanics* 53.6 (2014), pp. 1087–1103. DOI: [10.1007/s00466-013-0950-8](https://doi.org/10.1007/s00466-013-0950-8).
- [66] Young-Cheol Yoon and Jeong-Hoon Song. “Extended particle difference method for weak and strong discontinuity problems: part II. Formulations and applications for various interfacial singularity problems”. In: *Computational Mechanics* 53.6 (2014), pp. 1105–1128. DOI: [10.1007/s00466-013-0951-7](https://doi.org/10.1007/s00466-013-0951-7).
- [67] Young-Cheol Yoon and Jeong-Hoon Song. “Extended particle difference method for moving boundary problems”. In: *Computational Mechanics* 54.3 (Apr. 2014), pp. 723–743. DOI: [10.1007/s00466-014-1029-x](https://doi.org/10.1007/s00466-014-1029-x).
- [68] Andrea Bartzaghi, Luca Dedè, and Alfio Quarteroni. “Isogeometric Analysis of high order Partial Differential Equations on surfaces”. In: *Computer Methods in Applied Mechanics and Engineering* 295 (Oct. 2015), pp. 446–469. DOI: [10.1016/j.cma.2015.07.018](https://doi.org/10.1016/j.cma.2015.07.018).
- [69] Anna Tagliabue, Luca Dedè, and Alfio Quarteroni. “Isogeometric Analysis and error estimates for high order partial differential equations in fluid dynamics”. In: *Computers and Fluids* 102 (Oct. 2014), pp. 277–303. DOI: [10.1016/j.compfluid.2014.07.002](https://doi.org/10.1016/j.compfluid.2014.07.002).
- [70] Michele Bucelli et al. “Multipatch Isogeometric Analysis for electrophysiology: Simulation in a human heart”. In: *Computer Methods in Applied Mechanics and Engineering* 376 (Apr. 2021), p. 113666. DOI: [10.1016/j.cma.2021.113666](https://doi.org/10.1016/j.cma.2021.113666).
- [71] Sylwia Koniusz et al. “Extracellular Vesicles in Physiology, Pathology, and Therapy of the Immune and Central Nervous System, with Focus on Extracellular Vesicles Derived from Mesenchymal Stem Cells as Therapeutic Tools”. In: *Frontiers in Cellular Neuroscience* 10 (2016). DOI: [10.3389/fncel.2016.00109](https://doi.org/10.3389/fncel.2016.00109).

- [72] Robert H Edwards. “Neurotransmitter release: Variations on a theme”. In: *Current Biology* 8.24 (1998), R883–R885. DOI: [https://doi.org/10.1016/S0960-9822\(07\)00551-9](https://doi.org/10.1016/S0960-9822(07)00551-9).
- [73] A E Walsby. “Gas vesicles”. In: *Microbiological Reviews* 58.1 (1994), pp. 94–144. DOI: [10.1128/mr.58.1.94-144.1994](https://doi.org/10.1128/mr.58.1.94-144.1994).
- [74] B. Alberts et al. *Molecular Biology of the Cell 4th Edition: International Student Edition*. Routledge, 2002.
- [75] Hongyan Yuan, Changjin Huang, and Sulin Zhang. “Dynamic shape transformations of fluid vesicles”. In: *Soft Matter* 6.18 (2010), pp. 4571–4579. DOI: <https://doi.org/10.1039/C0SM00244E>.
- [76] Lindsay M. Biga et al. *Anatomy and Physiology*. OpenStax/Oregon State University, 2019.
- [77] Scott E. Feller. “Molecular dynamics simulations of lipid bilayers”. In: *Current Opinion in Colloid and Interface Science* 5.3-4 (July 2000), pp. 217–223. DOI: [10.1016/S1359-0294\(00\)00058-3](https://doi.org/10.1016/S1359-0294(00)00058-3).
- [78] Richard M. Venable, Frank L.H. Brown, and Richard W. Pastor. “Mechanical properties of lipid bilayers from molecular dynamics simulation”. In: *Chemistry and Physics of Lipids* 192 (Nov. 2015), pp. 60–74. DOI: [10.1016/j.chemphyslip.2015.07.014](https://doi.org/10.1016/j.chemphyslip.2015.07.014).
- [79] J GUMBART et al. “Molecular dynamics simulations of proteins in lipid bilayers”. In: *Current Opinion in Structural Biology* 15.4 (Aug. 2005), pp. 423–431. DOI: [10.1016/j.sbi.2005.07.007](https://doi.org/10.1016/j.sbi.2005.07.007).
- [80] Richard W. Pastor. “Molecular dynamics and Monte Carlo simulations of lipid bilayers”. In: *Current Opinion in Structural Biology* 4.4 (Jan. 1994), pp. 486–492. DOI: [10.1016/S0959-440X\(94\)90209-7](https://doi.org/10.1016/S0959-440X(94)90209-7).
- [81] Sybille Rex et al. “Experimental and Monte Carlo Simulation Studies of the Thermodynamics of Polyethyleneglycol Chains Grafted to Lipid Bilayers”. In: *Biophysical Journal* 75.6 (Dec. 1998), pp. 2900–2914. DOI: [10.1016/S0006-3495\(98\)77732-X](https://doi.org/10.1016/S0006-3495(98)77732-X).
- [82] Thomas Heimburg. “Monte Carlo simulations of lipid bilayers and lipid protein interactions in the light of recent experiments”. In: *Current Opinion in Colloid and Interface Science* 5.3-4 (July 2000), pp. 224–231. DOI: [10.1016/S1359-0294\(00\)00059-5](https://doi.org/10.1016/S1359-0294(00)00059-5).
- [83] Jocelyn M. Rodgers et al. “Understanding the Phase Behavior of Coarse-Grained Model Lipid Bilayers through Computational Calorimetry”. In: *The Journal of Physical Chemistry B* 116.5 (Jan. 2012), pp. 1551–1569. DOI: [10.1021/jp207837v](https://doi.org/10.1021/jp207837v).
- [84] Ask F. Jakobsen, Ole G. Mouritsen, and Gerhard Besold. “Artifacts in dynamical simulations of coarse-grained model lipid bilayers”. In: *The Journal of Chemical Physics* 122.20 (May 2005), p. 204901. DOI: [10.1063/1.1900725](https://doi.org/10.1063/1.1900725).

- [85] Mark J. Stevens. “Coarse-grained simulations of lipid bilayers”. In: *The Journal of Chemical Physics* 121.23 (Dec. 2004), pp. 11942–11948. DOI: [10.1063/1.1814058](https://doi.org/10.1063/1.1814058).
- [86] Lianghai Gao, Julian Shillcock, and Reinhard Lipowsky. “Improved dissipative particle dynamics simulations of lipid bilayers”. In: *The Journal of Chemical Physics* 126.1 (Jan. 2007), p. 015101. DOI: [10.1063/1.2424698](https://doi.org/10.1063/1.2424698).
- [87] G. J. A. Sevink and J. G. E. M. Fraaije. “Efficient solvent-free dissipative particle dynamics for lipid bilayers”. In: *Soft Matter* 10.28 (2014), p. 5129. DOI: [10.1039/c4sm00297k](https://doi.org/10.1039/c4sm00297k).
- [88] Julian C. Shillcock and Reinhard Lipowsky. “Equilibrium structure and lateral stress distribution of amphiphilic bilayers from dissipative particle dynamics simulations”. In: *The Journal of Chemical Physics* 117.10 (Sept. 2002), pp. 5048–5061. DOI: [10.1063/1.1498463](https://doi.org/10.1063/1.1498463).
- [89] Sajad Moradi, Amin Nowroozi, and Mohsen Shahlaei. “Shedding light on the structural properties of lipid bilayers using molecular dynamics simulation: a review study”. In: *RSC Advances* 9.8 (2019), pp. 4644–4658. DOI: [10.1039/c8ra08441f](https://doi.org/10.1039/c8ra08441f).
- [90] Eugenio Oñate et al. “The particle finite element method—an overview”. In: *International Journal of Computational Methods* 01.02 (Sept. 2004), pp. 267–307. DOI: [10.1142/s0219876204000204](https://doi.org/10.1142/s0219876204000204).
- [91] Ebrahim M Kolahdouz and David Salac. “A numerical model for the trans-membrane voltage of vesicles”. In: *Applied Mathematics Letters* 39 (2015), pp. 7–12. DOI: <https://doi.org/10.1016/j.aml.2014.08.001>.
- [92] Zhilin Li et al. “An overview of the immersed interface method and its applications”. In: *Taiwanese journal of mathematics* 7.1 (2003), pp. 1–49. DOI: [10.11650/twjm/1500407515](https://doi.org/10.11650/twjm/1500407515).
- [93] Zuo Cui et al. “A sharp-interface immersed boundary method for simulating incompressible flows with arbitrarily deforming smooth boundaries”. In: *International Journal of Computational Methods* 15.01 (2018), p. 1750080. DOI: [10.1142/S0219876217500803](https://doi.org/10.1142/S0219876217500803).
- [94] Mingyu Zhang and Xiao-Long Deng. “A sharp interface method for SPH”. In: *Journal of Computational Physics* 302 (2015), pp. 469–484. DOI: <https://doi.org/10.1016/j.jcp.2019.05.022>.
- [95] AH Rajkotwala et al. “A critical comparison of smooth and sharp interface methods for phase transition”. In: *International Journal of Multiphase Flow* 120 (2019), p. 103093. DOI: <https://doi.org/10.1016/j.ijmultiphaseflow.2019.103093>.
- [96] Charles Puelz and Boyce E Griffith. “A sharp interface method for an immersed viscoelastic solid”. In: *Journal of Computational Physics* 409 (2020), p. 109217. DOI: [10.1016/j.jcp.2019.109217](https://doi.org/10.1016/j.jcp.2019.109217).

- [97] Daniel M Anderson, Geoffrey B McFadden, and Adam A Wheeler. “Diffuse-interface methods in fluid mechanics”. In: *Annual review of fluid mechanics* 30.1 (1998), pp. 139–165. DOI: <https://doi.org/10.1146/annurev.fluid.30.1.139>.
- [98] Deepali N Bhate, Allan F Bower, and Ashish Kumar. “A phase field model for failure in interconnect lines due to coupled diffusion mechanisms”. In: *Journal of the Mechanics and Physics of Solids* 50.10 (2002), pp. 2057–2083. DOI: [https://doi.org/10.1016/S0022-5096\(02\)00019-4](https://doi.org/10.1016/S0022-5096(02)00019-4).
- [99] Junseok Kim. “Phase-field models for multi-component fluid flows”. In: *Communications in Computational Physics* 12.3 (2012), pp. 613–661. DOI: [10.4208/cicp.301110.040811a](https://doi.org/10.4208/cicp.301110.040811a).
- [100] Nele Moelans, Bart Blanpain, and Patrick Wollants. “An introduction to phase-field modeling of microstructure evolution”. In: *Calphad* 32.2 (2008), pp. 268–294. DOI: <https://doi.org/10.1016/j.calphad.2007.11.003>.
- [101] A Rosolen, C Peco, and Marino Arroyo. “An adaptive meshfree method for phase-field models of biomembranes. Part I: Approximation with maximum-entropy basis functions”. In: *Journal of Computational Physics* 249 (2013), pp. 303–319. DOI: <https://doi.org/10.1016/j.jcp.2013.04.046>.
- [102] Stanley Osher and James A Sethian. “Fronts propagating with curvature-dependent speed: Algorithms based on Hamilton-Jacobi formulations”. In: *Journal of Computational Physics* 79.1 (1988), pp. 12–49. DOI: [https://doi.org/10.1016/0021-9991\(88\)90002-2](https://doi.org/10.1016/0021-9991(88)90002-2).
- [103] D. Salac and M. Miksis. “A level set projection model of lipid vesicles in general flows”. In: *Journal of Computational Physics* 230.22 (2011), pp. 8192–8215. DOI: <https://doi.org/10.1016/j.jcp.2011.07.019>.
- [104] Vincent Doyeux et al. “Simulation of vesicle using level set method solved by high order finite element”. In: *ESAIM: Proceedings* 38 (Dec. 2012). Ed. by F. Coquel et al., pp. 335–347. DOI: [10.1051/proc/201238018](https://doi.org/10.1051/proc/201238018).
- [105] S Aland. “Phase field modeling of inhomogeneous biomembranes in flow”. In: *Modeling of Microscale Transport in Biological Processes*. Elsevier, 2017, pp. 221–242. DOI: <https://doi.org/10.1016/B978-0-12-804595-4.00009-2>.
- [106] Guillermo R Lázaro, Ignacio Pagonabarraga, and Aurora Hernández-Machado. “Phase-field theories for mathematical modeling of biological membranes”. In: *Chemistry and physics of lipids* 185 (2015), pp. 46–60. DOI: <https://doi.org/10.1016/j.chemphyslip.2014.08.001>.

- [107] Tae-Yeon Kim et al. “A Nitsche-type variational formulation for the shape deformation of a single component vesicle”. In: *Computer Methods in Applied Mechanics and Engineering* 359 (2020), p. 112661. DOI: [doi.org/10.1016/j.cma.2019.112661](https://doi.org/10.1016/j.cma.2019.112661).
- [108] David Steigmann and Ashutosh Agrawal. “Electromechanics of polarized lipid bilayers”. In: *Mathematics and Mechanics of Complex Systems* 4.1 (2016), pp. 31–54. DOI: [10.2140/memocs.2016.4.31](https://doi.org/10.2140/memocs.2016.4.31).
- [109] Ling-Tian Gao et al. “An electromechanical liquid crystal model of vesicles”. In: *Journal of the Mechanics and Physics of Solids* 56.9 (2008), pp. 2844–2862. DOI: <https://doi.org/10.1016/j.jmps.2008.04.006>.
- [110] P.B. Canham. “The minimum energy of bending as a possible explanation of the biconcave shape of the human red blood cell”. In: *Journal of Theoretical Biology* 26.1 (1970), pp. 61–81. DOI: [https://doi.org/10.1016/S0022-5193\(70\)80032-7](https://doi.org/10.1016/S0022-5193(70)80032-7).
- [111] Hui Ye and Austen Curcuru. “Vesicle biomechanics in a time-varying magnetic field”. In: *BMC Biophysics* 8.1 (Jan. 2015). DOI: [10.1186/s13628-014-0016-0](https://doi.org/10.1186/s13628-014-0016-0).
- [112] Qingchuan Li et al. “Electroformation of giant unilamellar vesicles in saline solution”. In: *Colloids and Surfaces B: Biointerfaces* 147 (Nov. 2016), pp. 368–375. DOI: [10.1016/j.colsurfb.2016.08.018](https://doi.org/10.1016/j.colsurfb.2016.08.018).
- [113] Linying Liu et al. “The Influence of Vesicle Shape and Medium Conductivity on Possible Electrofusion under a Pulsed Electric Field”. In: *PLOS ONE* 11.7 (July 2016). Ed. by Christof Markus Aegerter, e0158739. DOI: [10.1371/journal.pone.0158739](https://doi.org/10.1371/journal.pone.0158739).
- [114] Nicola A. Nodargi et al. “An isogeometric analysis formulation for red blood cell electro-deformation modeling”. In: *Computer Methods in Applied Mechanics and Engineering* 338 (Aug. 2018), pp. 392–411. DOI: [10.1016/j.cma.2018.04.038](https://doi.org/10.1016/j.cma.2018.04.038).
- [115] Martin Kraus et al. “Fluid Vesicles in Shear Flow”. In: *Physical Review Letters* 77.17 (Oct. 1996), pp. 3685–3688. DOI: [10.1103/physrevlett.77.3685](https://doi.org/10.1103/physrevlett.77.3685).
- [116] Sreejith Sukumaran and Udo Seifert. “Influence of shear flow on vesicles near a wall: A numerical study”. In: *Physical Review E* 64.1 (June 2001). DOI: [10.1103/physreve.64.011916](https://doi.org/10.1103/physreve.64.011916).
- [117] Giovanni Ghigliotti, Thierry Biben, and Chaouqi Misbah. “Rheology of a dilute two-dimensional suspension of vesicles”. In: *Journal of Fluid Mechanics* 653 (Apr. 2010), pp. 489–518. DOI: [10.1017/s0022112010000431](https://doi.org/10.1017/s0022112010000431).
- [118] Abtin Rahimian, Shravan Kumar Veerapaneni, and George Biros. “Dynamic simulation of locally inextensible vesicles suspended in an arbitrary two-dimensional domain, a boundary integral method”. In: *Journal of Computational Physics* 229.18 (Sept. 2010), pp. 6466–6484. DOI: [10.1016/j.jcp.2010.05.006](https://doi.org/10.1016/j.jcp.2010.05.006).

- [119] Sebastian Aland et al. “Diffuse interface models of locally inextensible vesicles in a viscous fluid”. In: *Journal of computational physics* 277 (2014), pp. 32–47. DOI: <https://doi.org/10.1016/j.jcp.2014.08.016>.
- [120] Wieland Marth, Sebastian Aland, and Axel Voigt. “Margination of white blood cells: a computational approach by a hydrodynamic phase field model”. In: *Journal of Fluid Mechanics* 790 (2016), pp. 389–406. DOI: <https://doi.org/10.1017/jfm.2016.15>.
- [121] Badr Kaoui, Alexander Farutin, and Chaouqi Misbah. “Vesicles under simple shear flow: Elucidating the role of relevant control parameters”. In: *Physical Review E* 80.6 (2009), p. 061905. DOI: <https://doi.org/10.1103/PhysRevE.80.061905>.
- [122] Petia M Vlahovska and Ruben Serral Gracia. “Dynamics of a viscous vesicle in linear flows”. In: *Physical Review E* 75.1 (2007), p. 016313. DOI: <https://doi.org/10.1103/PhysRevE.75.016313>.
- [123] Vasiliy Kantsler, Enrico Segre, and Victor Steinberg. “Critical dynamics of vesicle stretching transition in elongational flow”. In: *Physical review letters* 101.4 (2008), p. 048101. DOI: <https://doi.org/10.1103/PhysRevLett.101.048101>.
- [124] HONG ZHAO and ERIC S. G. SHAQFEH. “The dynamics of a vesicle in simple shear flow”. In: *Journal of Fluid Mechanics* 674 (2011), pp. 578–604. DOI: <https://doi.org/10.1017/S0022112011000115>.
- [125] Joanna B. Dahl et al. “Experimental observation of the asymmetric instability of intermediate-reduced-volume vesicles in extensional flow”. In: *Soft Matter* 12 (16 2016), pp. 3787–3796. DOI: [10.1039/C5SM03004H](https://doi.org/10.1039/C5SM03004H).
- [126] Jiandi Wan, Alison M. Forsyth, and Howard A. Stone. “Red blood cell dynamics: from cell deformation to ATP release”. In: *Integrative Biology* 3.10 (Sept. 2011), pp. 972–981. DOI: [10.1039/c1ib00044f](https://doi.org/10.1039/c1ib00044f).
- [127] Natacha Callens et al. “Hydrodynamic lift of vesicles under shear flow in microgravity”. In: *Condensed Matter* (2008). DOI: [10.48550/ARXIV.0804.0761](https://doi.org/10.48550/ARXIV.0804.0761).
- [128] M. Abkarian and A. Viallat. “Dynamics of Vesicles in a Wall-Bounded Shear Flow”. In: *Biophysical Journal* 89.2 (Aug. 2005), pp. 1055–1066. DOI: [10.1529/biophysj.104.056036](https://doi.org/10.1529/biophysj.104.056036).
- [129] Petia M. Vlahovska, Thomas Podgorski, and Chaouqi Misbah. “Vesicles and red blood cells in flow: From individual dynamics to rheology”. In: *Comptes Rendus Physique* 10.8 (Nov. 2009), pp. 775–789. DOI: [10.1016/j.crhy.2009.10.001](https://doi.org/10.1016/j.crhy.2009.10.001).
- [130] Damir Juric and Grétar Tryggvason. “A Front-Tracking Method for Dendritic Solidification”. In: *Journal of Computational Physics* 123.1 (Jan. 1996), pp. 127–148. DOI: [10.1006/jcph.1996.0011](https://doi.org/10.1006/jcph.1996.0011).

- [131] Javed Shaikh, Atul Sharma, and Rajneesh Bhardwaj. “On comparison of the sharp-interface and diffuse-interface level set methods for 2D capillary or/and gravity induced flows”. In: *Chemical Engineering Science* 176 (Feb. 2018), pp. 77–95. DOI: [10.1016/j.ces.2017.10.022](https://doi.org/10.1016/j.ces.2017.10.022).
- [132] J López et al. “A volume of fluid method based on multidimensional advection and spline interface reconstruction”. In: *Journal of Computational Physics* 195.2 (Apr. 2004), pp. 718–742. DOI: [10.1016/j.jcp.2003.10.030](https://doi.org/10.1016/j.jcp.2003.10.030).
- [133] C.W Hirt and B.D Nichols. “Volume of fluid (VOF) method for the dynamics of free boundaries”. In: *Journal of Computational Physics* 39.1 (Jan. 1981), pp. 201–225. DOI: [10.1016/0021-9991\(81\)90145-5](https://doi.org/10.1016/0021-9991(81)90145-5).
- [134] Maxime Theillard, Frédéric Gibou, and Tresa Pollock. “A Sharp Computational Method for the Simulation of the Solidification of Binary Alloys”. In: *Journal of Scientific Computing* 63.2 (Aug. 2014), pp. 330–354. DOI: [10.1007/s10915-014-9895-0](https://doi.org/10.1007/s10915-014-9895-0).
- [135] Lijian Tan and Nicholas Zabaras. “Modeling the growth and interaction of multiple dendrites in solidification using a level set method”. In: *Journal of Computational Physics* 226.1 (Sept. 2007), pp. 131–155. DOI: [10.1016/j.jcp.2007.03.023](https://doi.org/10.1016/j.jcp.2007.03.023).
- [136] RK Zeytounian and MF Platzer. “Theory and Applications of Viscous Fluid Flows”. In: *Applied Mechanics Reviews* 57.3 (May 2004), B15–B16. DOI: [10.1115/1.1760521](https://doi.org/10.1115/1.1760521).
- [137] Emmanuel Maitre et al. “Applications of level set methods in computational biophysics”. In: *Mathematical and Computer Modelling* 49.11-12 (June 2009), pp. 2161–2169. DOI: [10.1016/j.mcm.2008.07.026](https://doi.org/10.1016/j.mcm.2008.07.026).
- [138] E. Maitre et al. “Comparison between advected-field and level-set methods in the study of vesicle dynamics”. In: *Physica D: Nonlinear Phenomena* 241.13 (July 2012), pp. 1146–1157. DOI: [10.1016/j.physd.2012.03.005](https://doi.org/10.1016/j.physd.2012.03.005).
- [139] V. Doyeux et al. “Simulation of two-fluid flows using a finite element/level set method. Application to bubbles and vesicle dynamics”. In: *Journal of Computational and Applied Mathematics* 246 (July 2013), pp. 251–259. DOI: [10.1016/j.cam.2012.05.004](https://doi.org/10.1016/j.cam.2012.05.004).
- [140] Vincent Doyeux et al. “Simulation of vesicle using level set method solved by high order finite element”. In: *ESAIM: Proceedings* 38 (Dec. 2012). Ed. by F. Coquel et al., pp. 335–347. DOI: [10.1051/proc/201238018](https://doi.org/10.1051/proc/201238018).
- [141] Yulan Li et al. “A review: applications of the phase field method in predicting microstructure and property evolution of irradiated nuclear materials”. In: *npj Computational Materials* 3.1 (Apr. 2017). DOI: [10.1038/s41524-017-0018-y](https://doi.org/10.1038/s41524-017-0018-y).



- [142] Heyu Wang, Ruo Li, and Tao Tang. “Efficient computation of dendritic growth with r-adaptive finite element methods”. In: *Journal of Computational Physics* 227.12 (June 2008), pp. 5984–6000. DOI: [10.1016/j.jcp.2008.02.016](https://doi.org/10.1016/j.jcp.2008.02.016).
- [143] Nikolas Provatas, Nigel Goldenfeld, and Jonathan Dantzig. “Efficient Computation of Dendritic Microstructures Using Adaptive Mesh Refinement”. In: *Physical Review Letters* 80.15 (Apr. 1998), pp. 3308–3311. DOI: [10.1103/physrevlett.80.3308](https://doi.org/10.1103/physrevlett.80.3308).
- [144] W. J. Boettinger et al. “Phase-Field Simulation of Solidification”. In: *Annual Review of Materials Research* 32.1 (Aug. 2002), pp. 163–194. DOI: [10.1146/annurev.matsci.32.101901.155803](https://doi.org/10.1146/annurev.matsci.32.101901.155803).
- [145] Long-Qing Chen and Wei Yang. “Computer simulation of the domain dynamics of a quenched system with a large number of nonconserved order parameters: The grain-growth kinetics”. In: *Physical Review B* 50.21 (Dec. 1994), pp. 15752–15756. DOI: [10.1103/physrevb.50.15752](https://doi.org/10.1103/physrevb.50.15752).
- [146] I. Steinbach et al. “A phase field concept for multiphase systems”. In: *Physica D: Nonlinear Phenomena* 94.3 (July 1996), pp. 135–147. DOI: [10.1016/0167-2789\(95\)00298-7](https://doi.org/10.1016/0167-2789(95)00298-7).
- [147] Mark T. Lusk. “A phase-field paradigm for grain growth and recrystallization”. In: *Proceedings of the Royal Society of London. Series A: Mathematical, Physical and Engineering Sciences* 455.1982 (Feb. 1999), pp. 677–700. DOI: [10.1098/rspa.1999.0329](https://doi.org/10.1098/rspa.1999.0329).
- [148] Y. L. Li et al. “Phase-field model of domain structures in ferroelectric thin films”. In: *Applied Physics Letters* 78.24 (June 2001), pp. 3878–3880. DOI: [10.1063/1.1377855](https://doi.org/10.1063/1.1377855).
- [149] P.H. Leo and W.C. Johnson. “Spinodal decomposition and coarsening of stressed thin films on compliant substrates”. In: *Acta Materialia* 49.10 (June 2001), pp. 1771–1787. DOI: [10.1016/s1359-6454\(01\)00084-2](https://doi.org/10.1016/s1359-6454(01)00084-2).
- [150] I. S. Aranson, V. A. Kalatsky, and V. M. Vinokur. “Continuum Field Description of Crack Propagation”. In: *Physical Review Letters* 85.1 (July 2000), pp. 118–121. DOI: [10.1103/physrevlett.85.118](https://doi.org/10.1103/physrevlett.85.118).
- [151] Alain Karma, David A. Kessler, and Herbert Levine. “Phase-Field Model of Mode III Dynamic Fracture”. In: *Physical Review Letters* 87.4 (July 2001). DOI: [10.1103/physrevlett.87.045501](https://doi.org/10.1103/physrevlett.87.045501).
- [152] Mohan Mahadevan and R. Mark Bradley. “Phase field model of surface electromigration in single crystal metal thin films”. In: *Physica D: Nonlinear Phenomena* 126.3-4 (Feb. 1999), pp. 201–213. DOI: [10.1016/s0167-2789\(98\)00276-0](https://doi.org/10.1016/s0167-2789(98)00276-0).

- [153] Deepali N. Bhate, Ashish Kumar, and Allan F. Bower. “Diffuse interface model for electromigration and stress voiding”. In: *Journal of Applied Physics* 87.4 (Feb. 2000), pp. 1712–1721. DOI: [10.1063/1.372082](https://doi.org/10.1063/1.372082).
- [154] John W. Cahn and John E. Hilliard. “Free Energy of a Nonuniform System. I. Interfacial Free Energy”. In: *The Journal of Chemical Physics* 28.2 (Feb. 1958), pp. 258–267. DOI: [10.1063/1.1744102](https://doi.org/10.1063/1.1744102).
- [155] S.M Allen and J.W Cahn. “Ground state structures in ordered binary alloys with second neighbor interactions”. In: *Acta Metallurgica* 20.3 (Mar. 1972), pp. 423–433. DOI: [10.1016/0001-6160\(72\)90037-5](https://doi.org/10.1016/0001-6160(72)90037-5).
- [156] Markus Kästner, Philipp Metsch, and René de Borst. “Isogeometric analysis of the Cahn–Hilliard equation – a convergence study”. In: *Journal of Computational Physics* 305 (Jan. 2016), pp. 360–371. DOI: [10.1016/j.jcp.2015.10.047](https://doi.org/10.1016/j.jcp.2015.10.047).
- [157] Samuel M Allen and John W Cahn. “Coherent and incoherent equilibria in iron-rich iron-aluminum alloys”. In: *Acta Metallurgica* 23.9 (Sept. 1975), pp. 1017–1026. DOI: [10.1016/0001-6160\(75\)90106-6](https://doi.org/10.1016/0001-6160(75)90106-6).
- [158] A. A. Wheeler, W. J. Boettinger, and G. B. McFadden. “Phase-field model of solute trapping during solidification”. In: *Physical Review E* 47.3 (Mar. 1993), pp. 1893–1909. DOI: [10.1103/physreve.47.1893](https://doi.org/10.1103/physreve.47.1893).
- [159] Toshio Suzuki et al. “Phase-field model of dendritic growth”. In: *Journal of Crystal Growth* 237-239 (Apr. 2002), pp. 125–131. DOI: [10.1016/s0022-0248\(01\)01891-7](https://doi.org/10.1016/s0022-0248(01)01891-7).
- [160] Tu Zhanchun et al. *Geometric Methods in Elastic Theory of Membranes in Liquid Crystal Phases*. Vol. 2. World Scientific, 2017. DOI: <https://doi.org/10.1142/10645>.
- [161] Pierre-Gilles De Gennes and Jacques Prost. *The physics of liquid crystals*. Vol. 83. Oxford university press, 1993.
- [162] Xiaoqiang Wang. “Phase field models and simulations of vesicle bio-membranes”. In: (2005). DOI: [https://etda.libraries.psu.edu/files/final\\_submissions/6651](https://etda.libraries.psu.edu/files/final_submissions/6651).
- [163] Qiang Du, Chun Liu, and Xiaoqiang Wang. “Simulating the deformation of vesicle membranes under elastic bending energy in three dimensions”. In: *Journal of computational physics* 212.2 (2006), pp. 757–777. DOI: <https://doi.org/10.1016/j.jcp.2005.07.020>.
- [164] Aymen Laadhari, Pierre Saramito, and Chaouqi Misbah. “Computing the dynamics of biomembranes by combining conservative level set and adaptive finite element methods”. In: *Journal of Computational Physics* 263 (Apr. 2014), pp. 328–352. DOI: [10.1016/j.jcp.2013.12.032](https://doi.org/10.1016/j.jcp.2013.12.032).

- [165] Qiang Du et al. “Energetic variational approaches in modeling vesicle and fluid interactions”. In: *Physica D: Nonlinear Phenomena* 238.9-10 (2009), pp. 923–930. DOI: <https://ui.adsabs.harvard.edu/abs/2009PhyD..238..923D/abstract>.
- [166] Qiang Du, Manlin Li, and Chun Liu. “Analysis of a phase field Navier-Stokes vesicle-fluid interaction model”. In: *Discrete & Continuous Dynamical Systems-B* 8.3 (2007), p. 539. DOI: <http://www.aims sciences.org/article/doi/10.3934/dcdsb.2007.8.539>.
- [167] Maurice G Cox. “The numerical evaluation of B-splines”. In: *IMA Journal of Applied mathematics* 10.2 (1972), pp. 134–149. DOI: [10.1093/imamat/10.2.134](https://doi.org/10.1093/imamat/10.2.134).
- [168] Carl de Boor. “On calculating with B-splines”. In: *Journal of Approximation Theory* 6.1 (July 1972), pp. 50–62. DOI: [10.1016/0021-9045\(72\)90080-9](https://doi.org/10.1016/0021-9045(72)90080-9).
- [169] Les Piegl and Wayne Tiller. *The NURBS book*. Springer Science & Business Media, 2012. DOI: <http://dx.doi.org/10.1007/978-3-642-59223-2>.
- [170] Les Piegl and Wayne Tiller. “Rational B-spline Curves and Surfaces”. In: *The NURBS Book*. Springer Berlin Heidelberg, 1997, pp. 117–139. DOI: [10.1007/978-3-642-59223-2\\_4](https://doi.org/10.1007/978-3-642-59223-2_4).
- [171] Vinh Phu Nguyen, Stephane P. A. Bordas, and Timon Rabczuk. “Isogeometric analysis: an overview and computer implementation aspects”. In: (2012). DOI: [10.48550/ARXIV.1205.2129](https://doi.org/10.48550/ARXIV.1205.2129).
- [172] Kenneth E Jansen, Christian H Whiting, and Gregory M Hulbert. “A generalized- $\alpha$  method for integrating the filtered Navier–Stokes equations with a stabilized finite element method”. In: *Computer methods in applied mechanics and engineering* 190.3-4 (2000), pp. 305–319. DOI: [10.1016/S0045-7825\(00\)00203-6](https://doi.org/10.1016/S0045-7825(00)00203-6).
- [173] Hector Gomez and Kristoffer G van der Zee. “Computational Phase-Field Modeling”. In: *Encyclopedia of Computational Mechanics Second Edition* (2018), pp. 1–35. DOI: <https://doi.org/10.1002/9781119176817.ecm2118>.
- [174] Gustaf Söderlind. “Digital filters in adaptive time-stepping”. In: *ACM Transactions on Mathematical Software (TOMS)* 29.1 (2003), pp. 1–26. DOI: <https://doi.org/10.1145/641876.641877>.
- [175] Gustaf Söderlind and Lina Wang. “Adaptive time-stepping and computational stability”. In: *Journal of Computational and Applied Mathematics* 185.2 (2006), pp. 225–243. DOI: <https://doi.org/10.1016/j.cam.2005.03.008>.
- [176] Shrirang Abhyankar et al. “PETSc/TS: A Modern Scalable ODE/DAE Solver Library”. In: *arXiv preprint arXiv:1806.01437* (2018). DOI: <https://doi.org/10.48550/arXiv.1806.01437>.
- [177] Satish Balay et al. *PETSc Web page*. 2019.

- [178] Satish Balay et al. *PETSc Users Manual*. Tech. rep. ANL-95/11 - Revision 3.14. Argonne National Laboratory, 2020.
- [179] Satish Balay et al. “Efficient Management of Parallelism in Object-Oriented Numerical Software Libraries”. In: *Modern Software Tools for Scientific Computing*. Birkhäuser Boston, 1997, pp. 163–202. DOI: [10.1007/978-1-4612-1986-6\\_8](https://doi.org/10.1007/978-1-4612-1986-6_8).
- [180] L. Dalcin et al. “PetIGA: A framework for high-performance isogeometric analysis”. In: *Computer Methods in Applied Mechanics and Engineering* 308 (2016), pp. 151–181. DOI: <https://doi.org/10.1016/j.cma.2016.05.011>.
- [181] A.F. Sarmiento et al. “PetIGA-MF: A multi-field high-performance toolbox for structure-preserving B-splines spaces”. In: *Journal of Computational Science* 18 (2017), pp. 117–131. DOI: <https://doi.org/10.1016/j.jocs.2016.09.010>.
- [182] N. Collier et al. “The Cost of Continuity: Performance of Iterative Solvers on Isogeometric Finite Elements”. In: *SIAM Journal on Scientific Computing* 35.2 (2013), A767–A784. DOI: [10.1137/120881038](https://doi.org/10.1137/120881038).
- [183] N. Collier, L. Dalcin, and V. M. Calo. “On the computational efficiency of isogeometric methods for smooth elliptic problems using direct solvers”. In: *International Journal for Numerical Methods in Engineering* 100.8 (2014), pp. 620–632. DOI: [10.1002/nme.4769](https://doi.org/10.1002/nme.4769).
- [184] Daniel Garcia et al. “The value of continuity: Refined isogeometric analysis and fast direct solvers”. In: *Computer Methods in Applied Mechanics and Engineering* 316 (2017). Special Issue on Isogeometric Analysis: Progress and Challenges, pp. 586–605. DOI: <https://doi.org/10.1016/j.cma.2016.08.017>.
- [185] Daniel Garcia et al. “Refined Isogeometric Analysis for a preconditioned conjugate gradient solver”. In: *Computer Methods in Applied Mechanics and Engineering* 335 (2018), pp. 490–509. DOI: <https://doi.org/10.1016/j.cma.2018.02.006>.
- [186] Tadej Kotnik and Damijan Miklavčič. “Second-order model of membrane electric field induced by alternating external electric fields”. In: *IEEE Transactions on Biomedical Engineering* 47.8 (2000), pp. 1074–1081. DOI: [10.1109/10.855935](https://doi.org/10.1109/10.855935).
- [187] Miho Yanagisawa, Masayuki Imai, and Takashi Taniguchi. “Shape deformation of ternary vesicles coupled with phase separation”. In: *Physical review letters* 100.14 (2008), p. 148102. DOI: [10.1103/PhysRevLett.100.148102](https://doi.org/10.1103/PhysRevLett.100.148102).
- [188] Dayinta L Perrier et al. “The role of gel-phase domains in electroporation of vesicles”. In: *Scientific reports* 8.1 (2018), pp. 1–10. DOI: <https://doi.org/10.1038/s41598-018-23097-9>.
- [189] Rumiana Dimova et al. “Giant vesicles in electric fields”. In: *Soft matter* 3.7 (2007), pp. 817–827. DOI: [10.1039/b703580b](https://doi.org/10.1039/b703580b).

- [190] Will Schroeder, Ken Martin, and Bill Lorensen. *The Visualization Toolkit An Object-Oriented Approach To 3D Graphics*. 4.1. Kitware, 2018.
- [191] L. Dalcin and N. Collier. *Toolkit for IsoGeometric Analysis (IGA)*. 2015.
- [192] Y. Bazilevs et al. “Variational multiscale residual-based turbulence modeling for large eddy simulation of incompressible flows”. In: *Computer Methods in Applied Mechanics and Engineering* 197.1 (2007), pp. 173–201. DOI: <https://doi.org/10.1016/j.cma.2007.07.016>.
- [193] Peter Gamnitzer. “Residual-based variational multiscale methods for turbulent flows and fluid-structure interaction”. PhD thesis. Technische Universität München, 2010.
- [194] Kian Chuan Ong and Ming-Chih Lai. “An immersed boundary projection method for simulating the inextensible vesicle dynamics”. In: *Journal of Computational Physics* 408 (2020), p. 109277. DOI: <https://doi.org/10.1016/j.jcp.2020.109277>.
- [195] David Salac and Michael J Miksis. “Reynolds number effects on lipid vesicles”. In: *Journal of Fluid Mechanics* 711 (2012), pp. 122–146. DOI: <https://doi.org/10.1017/jfm.2012.380>.
- [196] Aymen Laadhari, Pierre Saramito, and Chaouqi Misbah. “Vesicle tumbling inhibited by inertia”. In: *Physics of Fluids* 24.3 (2012), p. 031901. DOI: [10.1063/1.3690862](https://doi.org/10.1063/1.3690862).
- [197] Y. Bazilevs and T.J.R. Hughes. “Weak imposition of Dirichlet boundary conditions in fluid mechanics”. In: *Computers and Fluids* 36.1 (2007). Challenges and Advances in Flow Simulation and Modeling, pp. 12–26. DOI: <https://doi.org/10.1016/j.compfluid.2005.07.012>.
- [198] Badr Kaoui and Jens Harting. “Two-dimensional lattice Boltzmann simulations of vesicles with viscosity contrast”. In: *Rheologica Acta* 55.6 (Aug. 2015), pp. 465–475. DOI: [10.1007/s00397-015-0867-6](https://doi.org/10.1007/s00397-015-0867-6).
- [199] John W. Barrett, Harald Garcke, and Robert Nürnberg. “Numerical computations of the dynamics of fluidic membranes and vesicles”. In: *Physical Review E* 92.5 (Nov. 2015). DOI: [10.1103/physreve.92.052704](https://doi.org/10.1103/physreve.92.052704).

## Mohammed H. A. Ashour

---

CONTACT INFORMATION	Marienstr. 7 Institute of Structural Mechanics (ISM) Bauhaus-Universität Weimar 99423 Weimar, Germany	mohammed.ashour@uni-weimar.de
EDUCATION	<b>PhD. Scholar</b> Institute of Structural Mechanics (ISM) Bauhaus-Universität Weimar, Weimar Deutschland  <b>Master of Science, M.Sc.,</b> Faculty of Civil Engineering Islamic-University of Gaza, Gaza Gaza Strip, Palestinian Territory  <b>Bachelor of Science, B.Sc.,</b> Faculty of Civil Engineering Islamic-University of Gaza, Gaza Gaza Strip, Palestinian Territory	Sept. 2017 - Jul. 2022  Sept. 2010 - Feb. 2015  Sept. 2005 - Feb. 2010
RESEARCH	<b>Bauhaus-Universität Weimar</b> Weimar, DE-TH, October 2017 - July 2022 Researcher and PhD. Scholar, <i>Vesicles Morphology using Phase-Field Isogeometric Analysis from Computational Mechanics Point of View</i> . Worked on: <ul style="list-style-type: none"> <li>• Vesicles morphology in Electric Fields using Phase-Field Isogeometric Analysis</li> <li>• Phase-Field Navier-Stokes model for Vesicle Doublet Hydrodynamics</li> <li>• Isogeometric Analysis and Parallel Implementation using PetIGA</li> </ul>	
PUBLICATION	<ul style="list-style-type: none"> <li>• Mohammed Ashour, Navid Valizadeh, and Timon Rabczuk. <b>“Isogeometric analysis for a phase-field constrained optimization problem of morphological evolution of vesicles in electrical fields”</b>. In: <i>Computer Methods in Applied Mechanics and Engineering</i> 377 (2021), p. 113669.</li> <li>• Mohammed Ashour, Navid Valizadeh, and Timon Rabczuk. <b>“Phase-Field Navier-Stokes model for vesicle doublets hydrodynamics in incompressible fluid flow”</b>. In: <i>Computer Methods in Applied Mechanics and Engineering (Under Review)</i>.</li> </ul>	
CONFERENCES PROCEEDINGS	<ul style="list-style-type: none"> <li>• Mohammed Ashour, Navid Valizadeh, <b>“Isogeometric analysis of a phase field model for simulating electromechanical behavior and morphological evolution of vesicles”</b>. Conference Proceedings of Data Driven Computing and Machine Learning in Engineering (DACOMA-19). <i>Advances in Computational Mechanics</i>. Volume 4, 2019. ISSN: 1940-5820 (printed). China, September 2019. [DOI: 10.32604/acm.2019.00185]</li> <li>• Mohammed Ashour, Navid Valizadeh, and Timon Rabczuk. <b>“Isogeometric Analysis for a Phase-field Model of Vesicles Under the Influence of an Electric Field”</b>. Conference Proceedings of The International Conference on Modern Mechanics and Applications (ICOMMA), <i>Modern Mechanics and Applications</i>, ISBN: 978-981-16-3238-9, December 2020 in Ho Chi Minh City, Vietnam.</li> </ul>	
EMPLOYMENT AND EXPERIENCE	<b>Supervising Site Engineer</b> Art-House Consultant Gaza Strip, Palestinian Territory	Jan. 2017 - Aug. 2017

<b>Site Engineer</b> PALCON Contracting Co. Gaza Strip, Palestinian Territory	Oct. 2016 - Aug. 2017
<b>Supervising Site Engineer</b> Universal Group for Engineering and Consulting Gaza Strip, Palestinian Territory	Apr. 2015 - Feb. 2016
<b>Finite Element Analyst</b> Universal Group for Engineering and Consulting Gaza Strip, Palestinian Territory	Mar. 2016 - May. 2016
<b>Project Manager</b> Salam Residential Building Reconstruction Committee Gaza Strip, Palestinian Territory	Oct. 2013 - Jan. 2016
<b>Structural Engineer and Quantity Surveyor</b> PALCON Contracting Co. Gaza Strip, Palestinian Territory	Sep. 2013 - Feb. 2015
<b>Site Engineer</b> Catholic Relief Services (CRS) Gaza Strip, Palestinian Territory	Jun. 2011 - July. 2012
<b>Site Engineer</b> PALCON Contracting Co. Gaza Strip, Palestinian Territory	Jan. 2012 - Aug. 2013